EPFL

Thèse n° 10 452

Filiform Variable Stiffness Technologies for Medical Robotics

Présentée le 31 mai 2024

Faculté des sciences et techniques de l'ingénieur
Laboratoire de systèmes intelligents
Programme doctoral en mécanique

pour l'obtention du grade de Docteur ès Sciences

par

Yegor PISKAREV

Acceptée sur proposition du jury

Prof. M. S. Sakar, président du jury
Prof. D. Floreano, directeur de thèse
Prof. A. Menciassi, rapporteuse
Prof. K.-J. Cho, rapporteur
Prof. J. Paik, rapporteuse

École polytechnique fédérale de Lausanne

2024

To my mother, *Mariia Piskareva*, who raised me as a free citizen of the world, my grandmother, *Nataliia Kulagina* for her care, patience and openness to new things, and my father, *Alexey Piskarev*, who taught me hard work and discipline by his example.

Эта диссертация посвящается моей маме, *Марии Пискаревой*, которая вырастила меня как свободного гражданина мира, бабушке, *Наталии Кулагиной* за ее заботу, терпение и открытость к новому , и моему папе, *Алексею Пискареву*, научившего меня своим примером трудолюбию и дисциплине.

Acknowledgements

I would like to start by expressing my deepest gratitude to my supervisor, **Prof. Dario Floreano.** I entered the Laboratory of Intelligent Systems (LIS) in the fall semester of 2016 and since then, I spent the last 7 years in different roles here: twice as a semester project student, a summer intern, a student working on a project in my free time without salary or credits, a master's project student, and finally Ph.D. student. I stayed for so long because the work environment you built at LIS and the people you are hiring are great. Here, I always felt (and still feel) that I am working on various exciting projects surrounded by top-notch people who would be happy to help me in case I am stuck. I enjoyed a lot our long project discussions during which I always tried to grasp as much as I could. Now, looking back, I realize that I learned so many things from you that are beyond research and are more important than the regular skills we are gaining at work. You taught me how to logically combine pieces of information into one coherent line of thought and how to find crucial gaps in these stories. You taught me how to present whatever I have to present and how to make the audience understand me. Now I know how to focus on essential questions and omit all the secondary aspects. Dear Dario, unfortunately, time flies so fast. If I had to choose which laboratory to do my Ph.D. in again, I would choose the LIS over and over again.

At the LIS, I am very lucky to work with **Michelle Wälti** and **Michèle Jaccoud**, our administrative assistants, who helped and kept helping me with tons of organizational challenges. I am immensely appreciative of your contribution to the daily life of the LIS because it helps us to focus on our research instead of sorting everything out on our own. I would like to thank **Martina Keddouh** for her help with all administrative questions related to the mechanical engineering department.

I also extend my deep gratitude to the thesis committee members, **Prof. Selman Sakar, Prof. Jamie Paik, Prof. Arianna Menciassi,** and **Prof. Kyujin Cho,** for assessing my research and overseeing my oral Ph.D. defense. Your dedication to reviewing my work and offering invaluable feedback is truly appreciated. An interesting fact is that I was part of the inaugural group of students in Jamie's class "Mechanical Product Design and

Development" back in 2016. It stands out as one of my favorite courses, being the first setting where I delved into soft robotics as a research discipline.

The accomplishment of my doctoral work owes much to the encouragement and guidance provided by my close friend and mentor, **Prof. Jun Shintake**. You revealed the fascinating world of science to me, and my choice to embark on this academic journey is solely a result of the valuable experience gained from working alongside you. You illuminated the excitement in science, showcasing that intricate problems can be creatively solved without the need for time-consuming calculations. Your support has been immeasurable, helping me navigate countless challenges with ease and simplicity. You are a born leader and brilliant scientist who feels when a student needs direct help, additional freedom, or even mental support. All my research results, including this thesis, represent your success as much as they do mine.

I would also like to express my gratitude to my former master's project advisor and current collaborator, **Prof. Michael Dickey.** You taught me how to work independently on my ideas, review publications, and supervise students by your own example. You are an exceptional researcher and, even more importantly, one of the kindest human beings I have ever met. During this unforgettable year at NCSU, I met many bright people, including my close friend and great scientist **Prof. Jiayi Yang.** Thank you for all our trips and conversations there and throughout all the years after.

I would also like to extend my appreciation to the LIS lab members for the wonderful moments we shared. Throughout all these years, I met three different batches of LIS employees. The first one taught me that sleeping and cooking in the lab is a part of our business (thank you Jun and **Alice Tonazzini**). With the second batch, I enjoyed our crazy cooking battles, game nights, and the enjoyment of Swiss nature via hikes and just sitting by the lake and taking in the views. Time passed, and "stressful" cooking battles transformed into friendly dinners and bouldering sessions (even though I am not heavily involved in them). In particular, thank you, **Prof. Willliam Stewart** (Go Pack!), **Prof. Krishna Digumarti, Vivek Ramachandran, Prof. Przemyslaw Kornatowski, Davide Zappetti,** and **Zhenishbek Zhakypov** for your guidance during my first years of Ph.D. William, you spent so much time with me listening to my silly project ideas and correcting my mediocre reports in English. Every time I asked for your advice, you returned with a few new ideas and multiple corrections. Your desire to truly help and the huge amount of effort you put into working with students will make you a brilliant professor, no doubt. Vivek and Davide, I started my master's program at the same time you started your Ph.D. journey, and you were always around. Thank you for our warm academic and personal discussions that always brighten my day. I would also like to express my gratitude to my coffee break buddies, **Harshal Sonar, Hritwick Banerjee, Petr Listov, Pavel Kalinin**, and **Euan Judd,** whose stories made me laugh or kept me thoughtful until the end of the day. I would also like to thank my ex-roomie **Prof. Yi Sun** for his great engineering ideas at every new step of projects and his great personality, which combines brilliant scientist, metal music and anime lover, drummer in the band, and a pens collector. A special thanks goes to **Enrico Ajanic,** not only for our warm chats and the paddleboard I borrowed but also for an exceptional sense of style. Your Ph.D. journey has been influential, reflected in my documents such as my CV, cover letters, and even this Ph.D. thesis, nearly

mirroring your works. As you know, imitation is the ultimate form of flattery. My next big thanks go to **Valentin Wüest, Simon Jeger, Benjamin Jarvis,** and **Shuhang Zhang** for everything you guys helped me with starting with my awkward pitch decks to flowers delivery. It is such a gift to enter the lab and see all of you there smiling (or crying). Thank you, **Raphael Zufferey,** for teaching me bouldering and skiing, and for your additional help in editing my thesis abstract the night before submission. I would like to thank **Markéta Pankhurst** for her guidance on my very first steps after my Ph.D. and significant contribution in my first grant writing. I express my gratitude to my entrepreneurial friends, **William Esposito** and **Martin Phelan,** for sparking my interest in developing tangible products that positively impact people. I extend my gratitude to the numerous semester students, master's students, and interns under my supervision in the preceding years. I would like to specifically thank **Tatiana Turincev** for her brilliant problem-solving skills, **Antoine Devincenti** for his independence and curiosity, **Etienne Hofstetter** for his hard work and perfectionism, and **Etienne Desbouis** for his remarkable hands-on skills. In general, there are too many remarkable beings I had the privilege to meet and spend time with. To all of you, thank you.

Expressing my gratitude becomes a challenge when thinking about those instrumental in shaping my journey to EPFL. **Prof. Sergey Vorotnikov** and **Prof. Denys Sashenko,** your care and support during and after my BMSTU studies are unforgettable. Moreover, you illustrated the influence of networking, sometimes surpassing the impact of hard skills. Till today and forever, I promise to close the feedback loops as you taught me. I extend a sincere thanks to my BMSTU mathematics teachers, **Prof. Anatoly Anikin** and **Prof. Viktor Tomashpolsky,** for introducing me to the fascinating world of mathematics and emphasizing that problems are not insurmountable (at least to a certain extent). A big thanks go to **Nataliya Belova,** who encouraged me to apply abroad at the moment when I was almost about to give in and stay in Moscow for my graduate degree. Without you, I would never have found the motivation to apply abroad and completely change my life.

I want to express my sincere gratitude to my wonderful friends who have been there for me every step of the way during my time at EPFL. Special thanks to my brothers from the "Real Boars Gang," **Alexander Shatskov, Andrey Piskunov, Vyacheslav Samokhvalov,** and **Ilia Sergachev.** Thank you for countless enjoyable evenings and meaningful conversations. Despite the inevitable passage of time and the increasing demands of our lives, I deeply cherish every moment spent with you guys. The memories of our underground parties during COVID, shared trips, and endless conversations about nothing will always hold a special place in my heart. I want to give a special shoutout to Andrey for his unwavering support - always there whenever I needed assistance. And a big thanks to Sasha for developing the dumbest hobby of "walking" that the world has ever seen. I would like to thank **Nataliia Piskunova** for her invaluable assistance with complex differential equations and physical problems that I was too dumb to solve on my own. I would also like to thank **Sofya Samokhvalova** for giving me the best "Chili con Carne" recipe, which I still use to this day.

I owe a great deal of gratitude to my friend **Shamil Gemuev**, who introduced me to the thrilling realm of competitive engineering challenges, igniting my passion for

competition and the drive to emerge victorious. Thank you for all the trips we shared filled with laughter, crazy stories, and intimate conversations.

A huge thanks goes to my oldest and best friends **Nikolaii Lukyanov, Alexandr Gavrilin, Artem Dontsov, Vladislav Spitsyn,** and **Andrei Petrukhin** from "Baklaki Gentlemen's Club". I have known most of you since I was 14 years old, which is half of my life. You are absolutely great humans and friends, and I am proud to call you friends and share the same vision and life values with you. Sasha, thank you for inspiring me with your own example of how to come to the new country and change your life by starting from zero. Kolya, you are the human with the best sense of humor I have ever met, and I think I tried to take over some of your tricks but unfortunately they do not work with me as well as you do. Thank you for all our time together, especially, trips abroad when we were young and poor (not young anymore ha ha). Tema, thank you for your support in very complicated life moments. You are a strong and wise man in addition to being a great friend. Thank you for showing me a wonderful and a bit painful thought world of banya. Vlad, I appreciate the numerous evenings spent in your "lounge bars" all over the globe, engaging in long conversations about both amusing and occasionally unnerving topics. Thank you for continually introducing me to new things up to this day. For example, I will always remember the time we were sitting somewhere, and you pulled out your phone to show me the first rap battle in my life. Andrey, thank you for being an example of kindness, support, and self-awareness. Thank you for being an example of a human who is consistently and mercilessly looking for happiness. The way you changed your life by jumping from a well-paying toxic yet medtech job into the uncertainty of the software engineering world showcases it in the best way.

In the final section, I would like to thank my beloved family. My brother, **Timofey Piskarev,** for my education in the field of contemporary music and unusual yet amusing videos. My sister, **Julia Piskareva,** for the best drawings and soft toys at my workplace. My grandfather, **Vladimir Radugin,** for his sense of humor that I definitely took over. To my grandmother, **Svetlana Radugina,** for embodying a remarkable spirit of vitality and a profound love for life. I would like to thank my godmother **Oksana Shchepochkina** and all her family for the happiest trips and summer time together. I express my heartfelt gratitude to **Nataliia Kulagina,** my grandmother, who invested a tremendous amount of time in me while I was a child (and already an adult), who helped me do my homework and cooked me delicious soups. Thank you for the time you dedicated to helping me write letters more evenly and read books faster. Lastly, my heartfelt gratitude goes to my wonderful parents, **Mariia Piskareva** and **Alexey Piskarev,** for their unwavering love and support throughout my life. You put a huge emphasis on my education and were quite demanding of me, and I appreciate it a lot. As you see, the effort paid off! Thank you for showing me the world and guiding me on the nuances of navigating life through your own example. Being with you is something I truly cherish, especially now as I continue to grow. I love you all to the moon and back.

Lutry beach, Lausanne, January 2, 2024

Yegor Piskarev

Abstract

In recent years, soft robotics has surged in applications like wearables, drones, smart fabrics, and medical instruments. Due to their compliance, these devices excel in tasks demanding dexterity and adaptability, such as manipulation, locomotion, crash resiliency, and surgical procedures. One intriguing design is the filiform structure, known as "smart fibers." They can be easily integrated into different objects and offer various functionalities such as actuation, sensing, energy generation, and adaptable stiffness.

In medical devices, like catheters and endoscopes, smart fibers enhance dexterity and compliance through variable stiffness. Variable stiffness allows reversible changes from soft to rigid states triggered by factors like thermal, electrical, magnetic, or pneumatic. Incorporating variable stiffness does bring certain drawbacks into play. These include increased design complexity, a compromise in biocompatibility due to the use of toxic components, and performance limitations stemming from slower reaction times in stiffness changes.

To overcome these limitations, we present in this thesis three filiform variable stiffness technologies that enable miniaturization, biocompatibility, and fast transition changes between soft and rigid states for medical devices used in minimally invasive surgeries. First, we propose an easily scalable filiform design made of a conductive phase-changing polymer, serving as a heater, temperature sensor, and variable stiffness substrate. We developed a new fabrication method using a dipping technique, enabling the creation of fibers with the desired thickness and electrical resistance. Then, we introduce two approaches to design filiform variable stiffness technologies with fast reaction times using phase-changing materials with active cooling and fiber jamming. Finally, we discuss their advantages and disadvantages in terms of scalability, stiffness change variation and speed.

Thanks to variable stiffness fibers, the minimally invasive devices of the future will offer doctors increased dexterity and safety previously unimaginable.

Keywords: robotics, soft robotics, medical robotics, variable stiffness, smart fibers, minimally invasive devices, catheters, remote magnetic navigation.

Résumé

Ces dernières années, la robotique molle a fait de gros progrès dans des applications telles que les appareils portables, les drones, les tissus intelligents et les instruments médicaux. En raison de leur conformité, cette technologie excelle dans les tâches exigeant dextérité et adaptabilité, telles que la manipulation, la locomotion, la résilience aux collisions et les interventions chirurgicales. Une conception particulière est la structure filiforme, connue sous le nom de "fibres intelligentes". "Elles peuvent être facilement intégrés dans différents objets et offrent diverses fonctionnalités telles que l'actionnement, la détection, la génération d'énergie et une rigidité adaptable.

Dans les dispositifs médicaux, comme les cathéters et les endoscopes, les fibres intelligentes améliorent la dextérité et la compliance grâce à une rigidité variable. La rigidité variable permet des changements réversibles de l'état mou à l'état rigide déclenchés par des facteurs tels que thermique, électrique, magnétique ou pneumatique. Malgré ces avantages particulièrement prometteurs, l'intégration de technologies à rigidité variable présente des difficultés significatives. Il s'agit notamment d'une complexité de conception accrue, d'un compromis en matière de biocompatibilité dû à l'utilisation de composants toxiques et de limitations de performances résultant de temps de réaction plus lents dans les changements de rigidité.

Pour surmonter ces limitations, nous présentons dans cette thèse technologies filiformes à rigidité variable qui permettent la miniaturisation, la biocompatibilité et les changements de transition rapides entre les états souples et rigides pour les dispositifs médicaux utilisés dans les chirurgies mini-invasives. Tout d'abord, nous proposons un design filiforme facilement évolutive constituée d'un polymère conducteur à changement de phase, servant de chauffage, de capteur de température et de substrat de rigidité variable. Nous avons développé une nouvelle méthode de fabrication utilisant une technique d'immersion, permettant la création de fibres avec l'épaisseur et la résistance électrique souhaitées. Ensuite, nous introduisons deux approches pour concevoir des technologies filiformes à rigidité variable avec des temps de réaction rapides en utilisant des matériaux à changement de phase avec refroidissement actif et blocage des fibres. Enfin, nous discutons de leurs avantages et inconvénients en termes de scalabilité, de vitesse et variation du changement de rigidité.

Grâce aux fibres à rigidité variable, les cathéters et endoscopes du futur vont offrir à nos médecins un accès étendu, une flexibilité et des possibilités d'opérations physique jusqu'ici impensable.

Contents

List of Figures

List of Tables

Chapter 1

1 Introduction

1.1 Background

Over the past years, we have witnessed the development of soft robotics devices for various applications, including wearable devices,[1–3] drones,[4] smart fabrics,[5,6] and medical instruments.[7–9] Due to intrinsic compliance, these devices find utility in tasks demanding high dexterity and adaptability,[10] like manipulation,[11–13] locomotion,[14–16] crash resiliency,[4] and surgical procedures.[17] While these devices take on various shapes and forms, one particularly intriguing design is the filiform structure. Devices adopting this form factor earn the title of "smart fibers" for their capacity to deliver diverse functionalities such as actuation, sensing, energy generation, and adaptable stiffness.[18,19] The title picture of this chapter presents a futuristic example of a smart fiber that combines all these functionalities.

Smart fibers have already found their application in the next generation of drones, enabling them to seamlessly transition between multiple modes of locomotion through morphing.[10] Smart fibers also extend their potential to smart clothing, facilitating precise temperature or humidity sensing,[20,21] additional actuation force,[22] defense against external impacts,[10] and passive or active energy generation.[23,24] Medical devices for minimally invasive surgeries, such as catheters and endoscopes, have adopted smart fibers extensively due to their matching form factor and aspect ratio.[7,25,26] Within these medical contexts, they elevate dexterity levels and offer an adjustable level of compliance, enhancing the capabilities of these essential instruments.[27] The aforementioned enhanced capabilities were achieved through the integration of segments into medical devices that can change their stiffness and locally adjust their mechanical properties.

This feature is known as variable stiffness, which allows a reversible stiffness change from a soft to rigid state and vice versa when a certain internal or external trigger such as

thermal,[28] electrical,[29] magnetic,[30] or pneumatic,[31] is applied. The reader can observe a similar functionality in their own body when intentionally flexing arm muscles from the soft to the rigid state while lifting a heavy bag of consumer goods. The same approach is used in the animal kingdom by sea cucumbers that respond to an external dangerous impact by promptly and temporarily enhancing the rigidity of their skin as a protective measure.[32] The effectiveness of this functionality inspired researchers to develop the very first filiform variable stiffness technologies that were then integrated into medical devices such as catheters and endoscopes.[25,28]

As a result, these devices gained improved performance, which came with the cost of increased design complexity caused by the integration of additional active components, which limits their scalability and miniaturization.[27] Thus, new designs and scalable manufacturing approaches are required to develop future medical devices. In addition, novel materials with smart capabilities used in these devices have to be biocompatible in terms of material composition and working temperatures to not harm human tissue while the surgery is being performed. The working speed of such medical devices plays also an important role since it determines the speed of overall surgery, which influences the cost and waiting time for the patients.[33,34] Therefore, the new generation of medical devices should have fast reaction times.

In this thesis, we introduce three filiform variable stiffness technologies that enable miniaturization, biocompatibility, and fast transition change between soft and rigid states of medical devices used in minimally invasive surgeries. A filiform variable stiffness-based device inherently qualifies as a smart fiber, as the activation of its variable stiffness mechanism requires not only a variable stiffness substrate but also a triggering mechanism, like a heater and a sensor to determine the stiffness state. Furthermore, active actuation is frequently integrated into this device. Therefore, in Chapter 1, we provide an overview of the current state of smart fibers. In Chapter 2, we propose an easily scalable filiform design made of a conductive phase-changing polymer, which is a nontoxic material that simultaneously serves as a heater, a temperature sensor, and a variable stiffness substrate. We developed a new fabrication method consisting of a dipping technique that enables the fabrication of fibers with the desired thickness and electrical resistance. Phase-changing-based variable stiffness technologies, with stiffness change times on the order of minutes, result in a procedure duration that is up to four times longer, making them unsuitable for conventional minimally invasive procedures. Therefore, in Chapters 3 and 4, we propose two approaches to design filiform variable stiffness technologies with fast reaction times using phase-changing materials with active cooling and fiber jamming. We discussed their advantages and disadvantages in terms of stiffness change speed and stiffness variation. The performance of all filiform variable stiffness technologies developed in this thesis was simulated, electromechanically characterized, and then validated in a real-case medical scenario after integration into the catheter ablation body. We believe that this new generation of medical devices has the potential to greatly improve the quality of heart surgeries, particularly cardiac ablation, thanks to their exceptional maneuverability and adaptable compliance achieved through variable stiffness.

The primary contribution of this thesis emphasizes the project on filiform variable stiffness technologies for medical devices. Alongside this, over the years, we have engaged in numerous satellite projects that significantly contribute to the field of soft robotics. These encompass the variable stiffness dielectric elastomer actuator, the soft universal gripper, and innovative methods to enhance the fabrication of soft robots. The way we envision the translation of these devices into medicine will be discussed at the end of the thesis in the Chapter 5 "Conclusion and future work".

1.2 Functionalities of smart fibers

In this subchapter, existing functionalities of smart fibers, their working principle, and advantages are discussed. Within the realm of soft robotics, there exist four essential components by functionalities: actuators (responsible for generating motion), sensors (used to perceive the surroundings), energy modules (in charge of producing energy), and variable stiffness elements (used to enhance locomotion or interaction capabilities). These components have the capability to take on the filiform structure of fibers by seamlessly integrating into various devices through techniques such as knitting or bonding, all while retaining their distinctive form factor and functionalities. From the fabrication perspective, smart fibers can be produced with diameters spanning a few millimeters and lengths extending several meters. [10] Moreover, some of the recent concept already combines multiple functionalities important for a specific application within the same fiber.[35,36] A comprehensive analysis of the various functionalities that can be, and have been, implemented within a smart fiber presented in this chapter was crucial in determining the design and fabrication approach of the devices presented later in Chapters 2 to 4.

1.2.1 Actuation

The actuation principles of fiber-based actuators can be classified into three mechanisms. The first one relies on the change of order of the molecule chains actuated by electricity, light, or thermal stimuli. The second one enables change of volume of the fibers resulting from mass exchange between fibers and the environment. The third one allows for change of distance between the twisted fibers causing contraction, rotation, and translation of the yarn/thread.[19]

Fiber actuators respond to various stimuli including electric or magnetic fields, heat, light, solvent/vapor, or pressure change enabling diverse ways to build interactions between humans and robots (Figure 1.1).[19]

Electricity is a widely available and controllable energy source that activates various types of fiber actuators. Electrical stimuli can trigger an actuation in different ways either by direct and indirect Joule heating or by generating electric field inside the material. The latter approach includes geometrical change of electroactive polymers due to electromechanical force generated via high potential difference between electrodes,[37] conductive yarns' distance change due to tensile contraction generated by the Columb force,[38] and piezoelectric strain generation (Figure 1.1a).[39,40] Electric actuation offers

advantages such as silence operation,[41] relatively high displacement with fast response,[42] low operating power, and high energy efficiency.[43] The existing shortcomings include poor performance in terms of generated strain,[42] the need of encapsulation,[44] and continuous energy consumption to maintain the deformed state.[38,45]

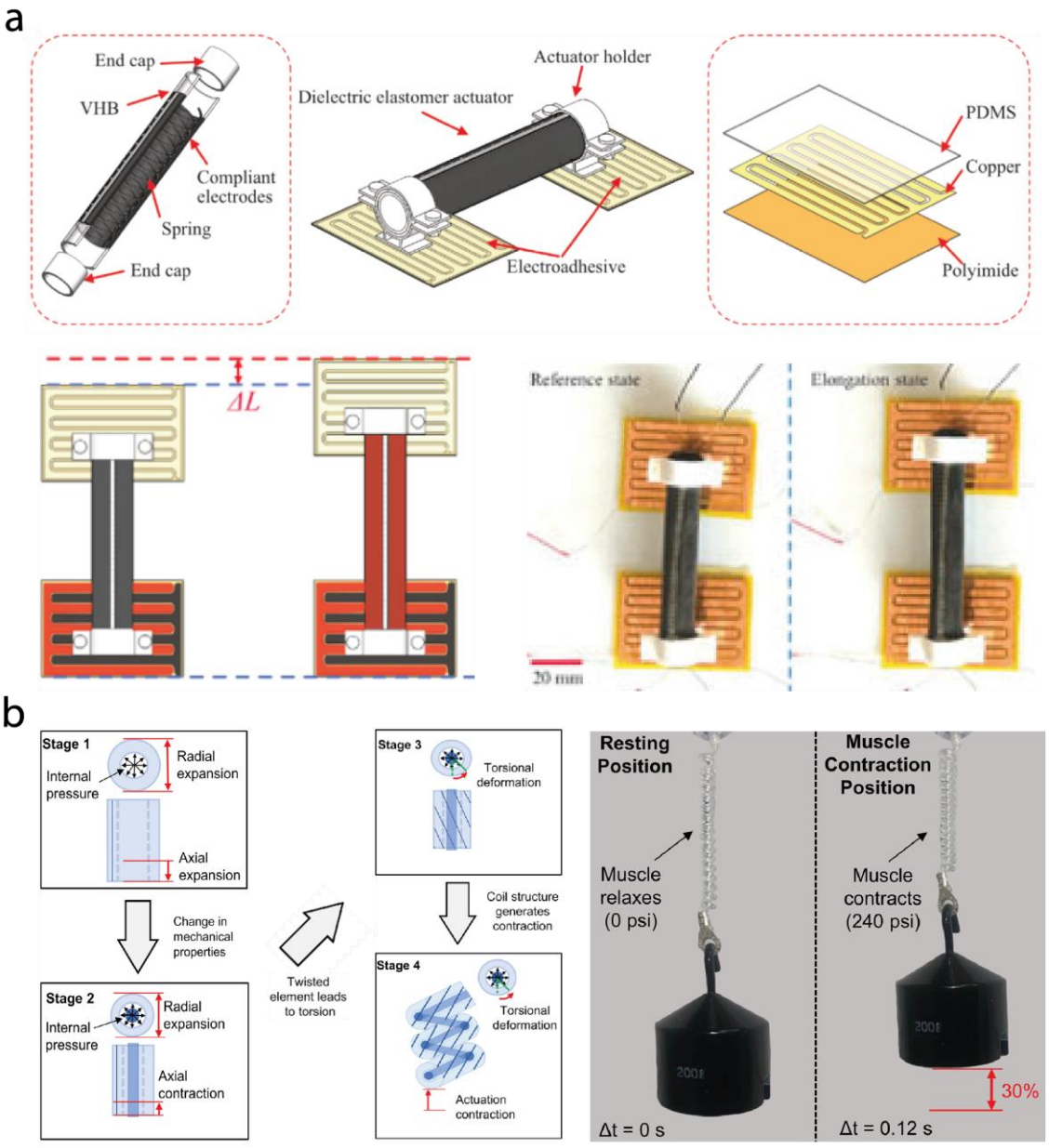

Figure 1. 1 Working principles of filiform soft actuators.
a) The soft fibers composed of rolled dielectric elastomer actuators can change the bending angle when a high potential difference is applied.[40] b) Cavatappi fluid-driven muscle-like actuator fabricated from inexpensive polymer tubes. Upon air inflation, the actuator expands radially and contracts axially. This mechanism can be used to build artificial muscles.[46]

Another actuation approach is thermal actuation, which involves materials that undergo reordering, expansion, melting, or decomposition in response to their changes in temperature. One of the most well-known material group for such actuation is shape memory polymers. They exhibit a mechanical and geometrical change when heated beyond glass transition temperature.[47] This triggering mechanism is easily implementable, thus, the shape memory polymer-based devices find applications in various fields, from medical stents and smart textiles to optical switches.[48–51]

Besides, convenience in activation, shape memory based devices suffer from small stroke and low speed that could be overcome by storing additional elastic energy inside the material.[52] Another fiber configurations with high performance and low cost leading to reversible actuation were realized by employing a bilayer structure comprising two materials with distinct thermal properties[53] or a coiled fishing line.[54] The general drawback of thermally actuated fibers lies in their elevated operating temperatures (beyond the biocompatible temperature for human body of 41°C)[55] often compromise material stability and hysteresis after multiple cycles potentially leading to discomfort and harm for humans. To overcome these limitations, low-temperature actuation (≈ 40°C) approaches have been introduced. In this case, a smart fiber was fabricated by infiltrating materials like wax or liquid metal into nanofibers, enabling reversible torsional actuation upon melting and solidification.[56] This technology provides high energy density at low required voltage applied.

An alternative method to initiate actuation involves the use of light. Light-responsive fiber actuators leverage the advantages of remote and contactless controllability, precise positioning, and a wide range of frequencies.[19] These actuators typically involve molecular order changes, such as optical chirality, amphiphilicity, conformation, and conjugation.[57,58] Liquid crystals are commonly used photoresponsive materials, with rapid and reversible deformation based on light-induced molecular realignment of the polymer network.[59] For instance, hollow fiber actuators filled with liquid slugs can be propelled by light-induced reorientation of liquid crystals molecules, enabling liquid movement and manipulation.[60] Also, aligned liquid crystal fibers exhibit phototropic behavior, bending toward light, and can be controlled by light to achieve various shapes.[61] Additionally, an artificial muscle was developed by self-assembling supramolecular motors, converting molecular motion into macroscopic movement through UV light irradiation.[62] Light-sensitive fiber actuators have the ability to help create a smart automated system. These actuators change their shape and bending angle according to where a light source, such as sun, shines on them. The light-responsive fibers face challenges in achieving optimal actuation speed, stress, and reversibility, as well as limitations in unstructured environments due to the linear path of light propagation.[19]

Magnetic fiber actuators consist of materials containing magnetic particles in their structure or permanent magnets within the fiber design.[27,63] 3D printing techniques allow for precise control of the magnetic domains, resulting in versatile soft robots capable of complex motion.[64] The actuation is achieved by influencing on the fiber with an external magnetic field causing the magnetized fiber or permanent magnets within the fiber body align with the direction of the external magnetic field.[25] These actuators offer advantages

such as fast, dexterous, and strong actuation, require, however, external magnetic field source.[65,66]

Another less common actuation mechanism involves the use of porous fibers made of hygroscopic materials.[67] These fibers can be actuated by adsorbing and desorbing substances like solvents or vapors, leading to deformations due to volume changes.[68] These fibers, with their hierarchical structure, absorb solvents due to hydrophilic properties and capillary forces, causing both contractive and rotational actuation.[69] Researchers demonstrated that carbon nanotube-based fibers respond rapidly to solvents and vapors by bending or elongating.[70,71] The actuation is reversible and can be optimized for various applications, including humidity energy harvesting and smart textiles. The high costs associated with carbon nanotubes prompted researchers to develop the more economical sheath-run artificial muscles with low hysteresis after a thousand-cycle test and higher actuation performance.[72] Potential of these fibers for in-body fluid monitoring, controlled drug release, and use as fiber robots showcases their significant promise in biomedical diagnostics and treatments.[73]

The last actuation approach involves air evacuation or inflation of the elastomer chambers in the fiber's structure (Figure 1.1b).[46] When air is evacuated from the elastomeric chamber, elements like microwires inside come into contact and exert pressure on one another. This interaction causes the fiber to bend.[74] In the case of air inflation-based filiform actuators, the bending is defined by the design of the elastomeric chamber and the constraints that are applied to it via inextensible elements such as thin nylon wires.[75,76] These elements determine the actuation's morphological information, enabling programmable motion. This method is advantageous for its fast actuation and the ability to perform bending, elongation, contraction, and twisting motions.[76] However, these pneumatically-driven actuators require the use of bulky and noisy equipment such as vacuum pumps.[77]

1.2.2 Sensing

Fiber-based sensors operate by detecting mechanical deformations, often through changes in their electrical resistance or capacitance.[78] Designed using winding, coating, or direct spinning, these sensors typically consist of a core material, like elastic rubber latex, surrounded by functional layers.[79] When subjected to strain, the sensor's structure deforms, altering the resistive properties of a functional layer. For instance, Chen et al.'s design used polyurethane fibers coated with conductive nanofibers and silver nanowires.[80] As the fiber stretches or compresses, the conductive pathways change, resulting in a measurable shift in resistance. This change is then translated into data, capturing motions or physiological signals. In the case of capacitive fiber sensors, the design typically consists of two conductive layers separated by a dielectric material.[81] When the fiber is subjected to mechanical deformation, such as stretching or compression, the distance between these conductive layers changes causing a change in capacitance. Some sensors not only use soft materials but also liquids. Recently researchers were able to print a sensor using an ionically conductive fluid as the conductor and a silicone elastomer as the dielectric encapsulant (Figure 1.2).[82] By adjusting parameters like the

inner/outer nozzle size, ink flow rates, and print speed, they were able to create a customized fiber with four concentric components. This fiber sensor was flexible and could be sewn into textiles to monitor walking gait and hand motion. To go from a centimeter length sensor to meter scale, researchers developed thermoplastic elastomer-based nanocomposites tailored for fiber processing technologies.[35,83] This innovation led to the creation of meters-long, soft, and adaptable stretchable fiber devices. Remarkably, these fibers have the precision to detect 5° bending angle in robotic mechanisms and react to minute pressing forces below a newton force. Such advancements highlight their transformative potential in fields like health diagnostics and seamless human-machine collaboration.

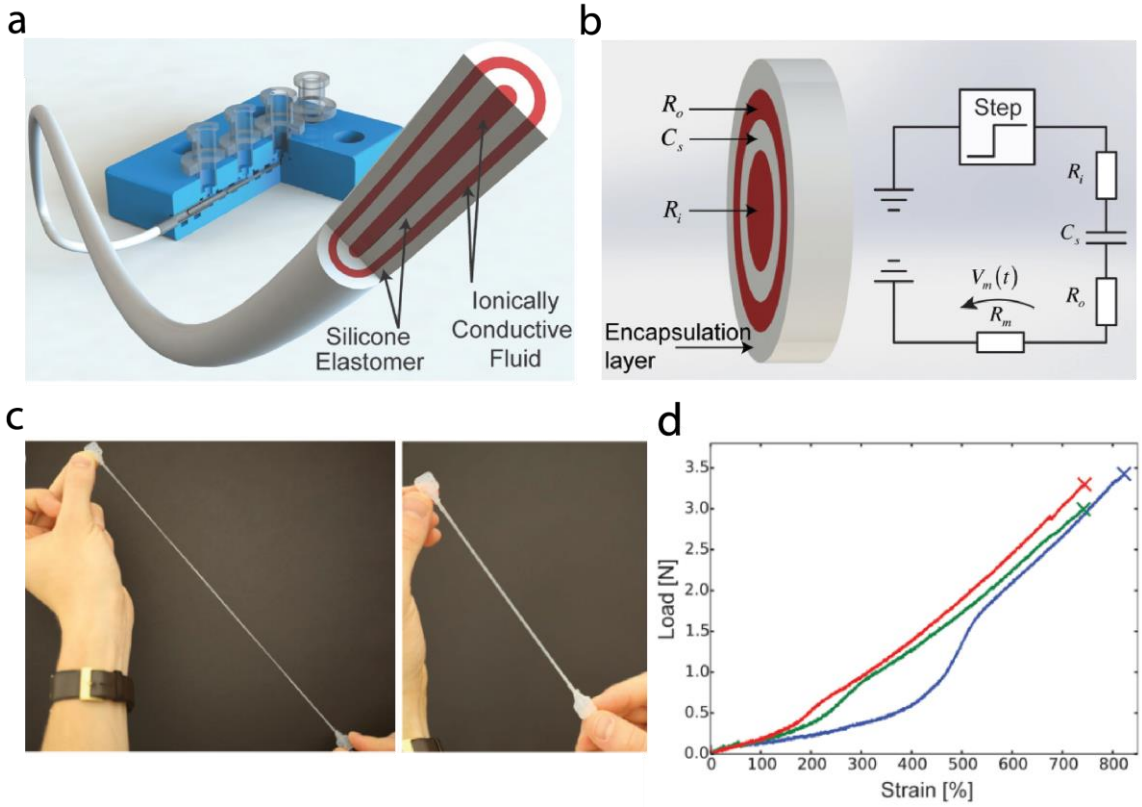

Figure 1. 2 Example of a filiform soft sensor.
a) Capacitive soft strain sensor based on multicore–shell fiber printing, which consists of four tubular layers of conductive and dielectric material.[82] b) Sensor cross-section with element properties and equivalent circuit diagram of the readout circuitry. c) Sensors strained to 0% and ≈150% strain. d) It provides accurate strain measurements without hysteresis under static and dynamic conditions.

Besides mechanical sensors, temperature sensors play a pivotal role in enabling robots and humans to detect surrounding thermal conditions and monitor health.[83–85] These sensors primarily function using thermally sensitive polymer matrices combined with conductive materials. As temperature varies, the resistance or capacitance of these materials change. One example includes a stretchable temperature sensor fabricated by coating a thread with polypyrrole, which changes conductivity with temperature variations, allowing it to detect temperatures ranging from 35 to 95°C.[86] Some designs

also incorporate semiconductors with conductivity that's temperature-dependent or materials that change light emission intensity with temperature shifts.[87] Such a sensor is made from a stretchable step-index PDMS optical fiber embedded with thermally sensitive upconversion nanoparticles. They have a specific core-shell structure and are integrated into a PDMS precursor, forming the core of the fiber. This core is then coated with another PDMS layer to create a cladding. As a result, this optical fiber sensor can effectively monitor environmental temperatures, including those of the skin, mouth, and breath.

Humidity sensors offer a unique dimension of environmental perception for soft robots and wearables. These sensors empower robots to detect and react to moisture levels, enhancing their operational accuracy.[88] For humans, integrating humidity sensors into clothing items can monitor moisture levels at the skin-textile interface, track wound recovery, and assess the comfort level of clothing on the human body against the skin where friction occurs.[19] Typically, these sensors work due to changes in electrical resistance or capacitance as aforementioned mechanical and temperature sensors. As an example, researchers developed a nitrogen-doped graphene fiber filled with platinum nanoparticles that enhance its humidity sensing capabilities.[89] Meanwhile, another type of filiform sensor was designed utilizing the wet-spinning technique to create a fiber sensitive to humidity through resistance changes, very effective for detecting water leakage or monitoring sweat levels.[90] One of the capacitance response mechanisms involves winding hydrophobic yarns on copper wire, resulting in rapid adsorption of water molecules and subsequent capacitance increases.[91] The used convergence fiber drawing approach allows scalable fabrication of highly flexible porous polymer-based capacitive sensors. Such advancements in humidity sensors in fiber form promise transformative applications in robotics, wearables, and medical fields.[92,93]

1.2.3 Energy generation

While filiform actuators and sensors are advancing, they often rely on bulky and cumbersome power sources.[94] To address this, researchers have been striving to develop filiform power units and self-powered filiform systems that harness energy directly from the human body and environment. Current innovations include biofuel cells, thermoelectric generators (TEGs), solar cells, and fiber pumps (Figure 1.3).

Filiform biofuel cells are emerging as a groundbreaking solution for energy generation.[95] Biofuel cells utilize biosecretions like sweat, tears, or saliva as electrolytes, triggering an electrochemical reaction that produces electricity.[96,97] The lactate in sweat, for instance, undergoes enzymatic oxidation, generating an electric current that can be harvested and stored for use.[98] Recently, a stretchable, wearable textile-based hybrid system was introduced that captures biochemical energy from sweat and stores it for later use.[98] However, the power generated depends on the user's perspiration rate, making energy storage crucial for consistent output. These filiform structures can simultaneously act as power sources and wearable sensors for metabolites.[96] From the fabrication side, screen printing has proven effective in creating precise, flexible electrode patterns on textiles,[99]

but the challenge lies in designing conductive inks that align with the material properties.[100]

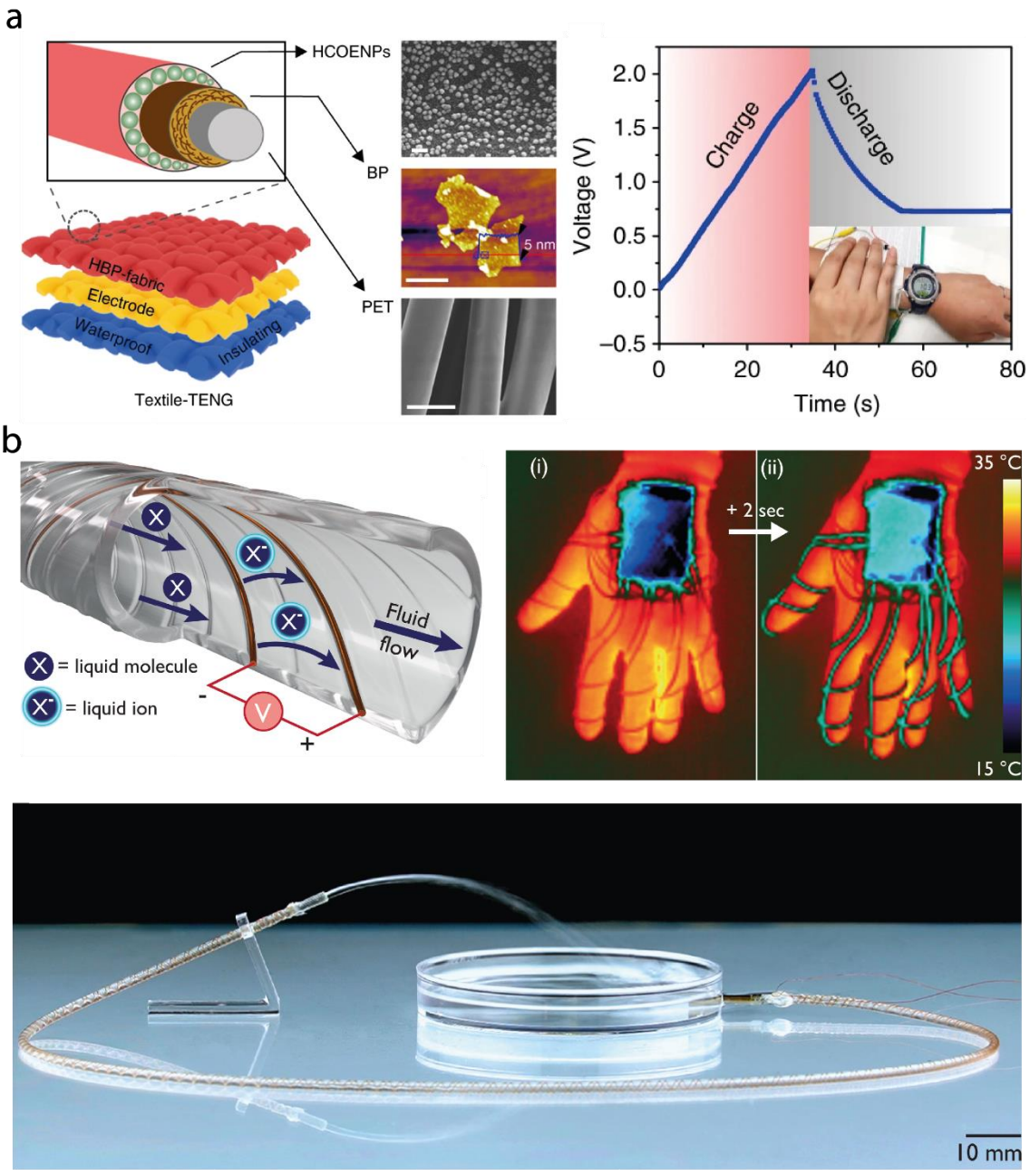

Figure 1. 3 Filiform energy generation devices that can produce electricity or create a flow of water.
a) Textile triboelectric nanogenerator operates through skin-touch activation and triboelectrification and electrostatic induction, where skin touching the device induces charges, leading to the generation of an output voltage/current signal through electrostatic induction and triboelectric effects. These devices offer advantages of washability, durability, and high triboelectricity, making it suitable for wearable devices with the capability to harvest mechanical energy from body motions.[101] b) The filiform soft pumps utilize charge injection electrohydrodynamics, with embedded helical electrodes in a polyurethane tube wall generating pressure through the ionization of a dielectric liquid, resulting in silent and efficient fluid flow. These stretchable fiber-based fluidic

pumps offer untethered wearable fluidics with high pressure generation (100 kPa/m) and efficient flow rates (55 mL/min), allowing versatile applications in wearable haptics, mechanically active fabrics, and thermoregulatory textiles.[24]

Compared to biofuel cells that derive energy from bio-secretions and provide intermittent electricity suitable for strenuous activities (sport or hard labor), filiform thermoelectric generators (TEGs) tap into a different energy source: the body's heat.[102] TEGs convert the thermal gradient, especially between the human body and its surroundings, into electrical energy.[103] The working principle of thermoelectric generators revolves around the Seebeck effect. When two different conductive materials are connected and there is a temperature difference between their junctions, voltage is generated. This voltage can then be used to drive an electric current, converting the thermal energy into electrical energy. For wearable applications, both conductive materials have to be encapsulated into a substrate, which needs to be flexible and thermally tolerant to withstand fabrication processes and ensure efficient energy conversion. However, commonly used substrates such as glass fabric or polymer films lead to significant thermal energy loss, particularly in low-dimensional TEGs, compromising their output performance.[104] To overcome these limitations, researchers developed a flexible TEG generator using screen printing technique and curing at high temperature (more than 500°C), resulting in a device that is thin, lightweight, and boasts an output power density significantly higher than previously reported flexible TEGs.[104] Thus, existing filiform TEGs can already be used to power a range of applications from sensors[105,106] to health monitoring devices.[107]

Instead of harnessing energy directly from the human body through temperature gradients or sweat, researchers are looking into using the surrounding environment, especially sunlight, as a potential energy source. It led to the development of photovoltaic self-powered fibers.[108,109] In these fibers, silicon solar cells use n-type and p-type semiconductors to create a junction. When light hits this junction, it excites electrons which move and generate an electric field.[109] This process, known as the "PV effect", produces electricity. Based on that, a filiform energy generation unit made of textile, Nickel, and conductive composite was developed using coating layer-by-layer fabrication.[110] It includes a soft flexible battery and a thin film solar cell integrated into the battery enabling recharging by light. In the scope of wearable devices, the main limitation of this technology is the lack of air permeability. The progression of this technology hinges on enhancing energy unit efficiency[110] (up to 3.67% compared to 2.6% in a previous work[111]), refining scalable production methods[112], and integrating diverse energy harvesting techniques like solar and mechanical within the same unit.[113]

Most of wearable devices operate on electricity, but exceptions exist. Devices like soft hydraulically-driven actuators[114] and haptic wearables[115] can use liquid as a power source rather than electricity. Consequently, flowing liquid serves as an energy source for such devices, in contrast to traditional electricity. To enable this liquid-powered functionality, researchers have developed filiform stretchable pumps.[24] The pumps utilize charge injection electrohydrodynamics (EHD). Two continuous helical electrodes, made of copper wire, are embedded in the polyurethane tube wall. Applying an electric field ionizes the dielectric liquid, creating charged ions that move towards an electrode,

creating fluid flow. Reversing the voltage polarity changes the flow direction. This filiform fluidic pump showcased remarkable generated pressure of 80 kPa and flow rate of 55 ml/min, which is two times better than existing rigid miniature pumps. Therefore eliminating the need for external, bulky, and rigid pumps in wearable devices by transforming the fibers into the pump itself. Moreover, the solution is scalable, simple, and stable in operation.

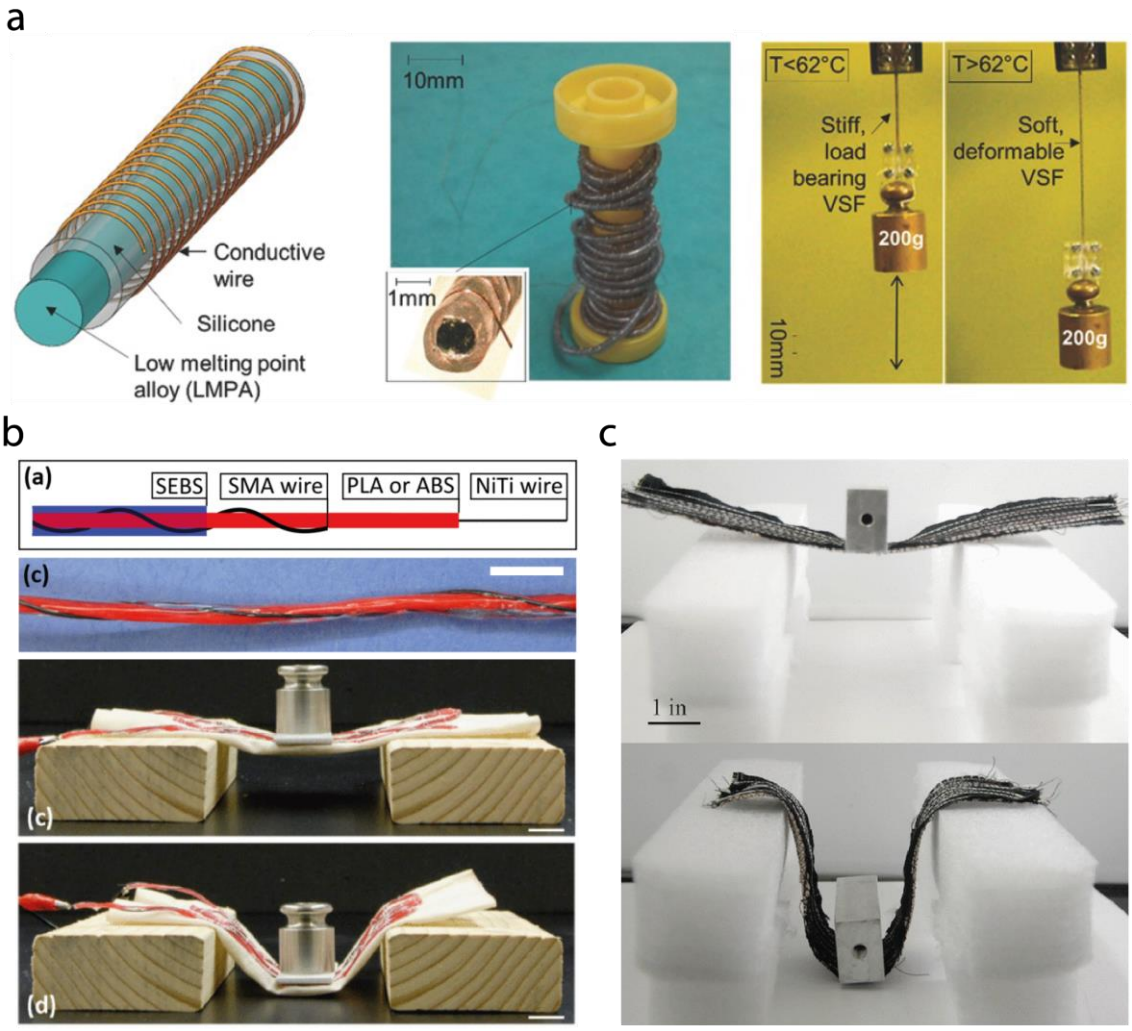

Figure 1. 4 Filiform variable stiffness technologies.
a) A filiform variable stiffness technology comprised of silicone outer tube and filled with low melting point alloy exhibits rapid softening (>700 times) and increased deformability (>400 times) when exposed to temperatures exceeding 62 °C. This versatile fiber showcases impressive self-repair capabilities of inner alloy and can be utilized in applications such as a foldable multi-purpose drone, a wearable cast for bone injuries, and a pliable multi-directional actuator, demonstrating its adaptability through clamping, knitting, and bonding.[10] b,c) Filiform variable stiffness threads and fabrics, comprising shape memory alloys and thermoplastics, integrate actuation and variable stiffness functions, enabling movement to new positions without continuous power. These devices reduce bending stiffness when the polymer is heated beyond a glass transition temperature.[5,6]

1.2.4 Variable stiffness

The natural flexibility of filiform soft actuators, sensors, and energy sources can sometimes limit their ability to exert force on surfaces or withstand mechanical stresses. The introduction of controlled stiffness plays a crucial role in overcoming this challenge, empowering soft robots and wearable devices to exert substantial forces on their surroundings and endure external pressures without compromising their shape.[18,19] Many technologies have been developed in a filiform shape for stiffness tuning in soft devices. Examples include shape-memory alloys (SMAs) and polymers (SMPs), thermoplastics, low melting point alloys (LMPAs), and layer jamming (Figure 1.4). These approaches can be categorized based on the mechanisms of material softening. In the next paragraphs, the materials are divided into two groups based on the physics of the triggering mechanism between the stiffening/softening process: temperature and pressure.

The first category encompasses materials that undergo a phase change at specific temperatures. Within this group, we find low melting point materials, glass-transition polymers, and thermally responsive elastomers. Low melting point alloys, in particular, stand out for their remarkable capacity to transition from a solid to a liquid state at slightly elevated temperatures (typically below 47°C) in less than a second, resulting in significant changes in stiffness (up to four orders of magnitude).[116] Activation of these materials involves direct or indirect Joule heating, a process enabled by low melting point[13] and shape memory alloys,[117] and external copper wiring.[10] LMPA-based filiform variable stiffness technologies experience a stiffness change of up to 700 times, allowing for extensive system adaptability. Therefore, these technologies have been applied in robotics and rehabilitation devices, facilitating versatile movement and flexible finger posture adjustments.[10] However, phase change alloys have a notable drawback due to their use of non-biocompatible or even toxic materials, posing risks to human tissue in case of leakage.[25] Additionally, the intricate design, requiring heaters, sensors, and variable stiffness substrates, constrains the scalability of these technologies.

In contrast to the sharp solid-liquid phase transition of LMPAs, glass-transition polymers are able to gradually change their stiffness over a wider temperature range from a glassy to a rubbery state due to greater mobility of polymer chains. Filiform fibers based on glass-transition polymers have been developed in the form of strands made of polylactic acid (PLA) polymer coated around conductive, nitinol wire. The state of the PLA is changed by indirect Joule heating through the nitinol wire in about 15 seconds.[5] A follow up to that work implemented SMA wire instead of nitinol wire, which brought actuation capability to the variable stiffness fiber.[6] In this configuration, SMA wire placed in the middle of the fiber works as a heating element for the surrounding glass-transition polymer and as an actuator. Apart from indirect Joule heating, direct Joule heating has been applied to propylene-ethylene elastomers by adding carbon black powder.[118] The fabricated conductive elastomer formed in a strip-like shape can be soften from 37 MPa down to 1.5 MPa in 6 seconds by applying 150 volts. The cooling time was not reported, however, its likely in a range of several minutes.[18] All examples of glass-transition polymers experience long cooling times along with LMPAs equal to 5 minutes.

The second trigger used in variable stiffness fibers is air evacuation. The use of pneumatic actuation to produce two distinct states of stiffness is widely described in the literature.[18] The most relevant implementations of these technologies in tubular form involve the controlled vacuum sealing of air chambers sealed with a flexible tube, and filled with stacked layers of flat materials.[119] The stiffness change in these studies depends on the normal force, the design of the contact region between the surfaces, and the tribological properties of the materials. These systems can produce massive changes (×100) in elastic moduli in less than a second. The rapid stiffness change of such jamming technologies is the main advantage. However, they has a few crucial disadvantages. First of all, the design is bulky because the activation mechanism needs a lot of space for the air evacuation channel. Furthermore, the process of air evacuation changes the geometrical parameters of the device. It can expand and stick or damage the surrounding environment. In addition, the elastic moduli in the soft state is two orders of magnitude higher compared to other technologies (~1000 MPa). Therefore, it is not suitable for a wide range of applications which require higher level of compliancy in the soft state. Moreover, this technology has two binary states of stiffness: soft and rigid. Therefore, it cannot be used for applications where the stiffness has to be continuously adjusted by changing between more than two states of stiffness.

1.3 Motivation

As previously outlined, filiform variable stiffness technologies encounter various challenges encompassing their design, fabrication, and performance. Some of these limitations may hold particular significance within specific applications. In this chapter, we define the focus of this thesis on the realm of medical devices used in minimally invasive surgeries, as advancements in this field have a profound impact on the general public. Every surgery has its unique characteristics that necessitate the development of highly specialized tools tailored to each surgical procedure's specific requirements. Therefore, in this thesis, we narrowed down to one specific surgery that still has tremendous challenges. We have selected cardiac ablation as our focus. Cardiac ablation is employed in the treatment of cardiac arrhythmias, a condition responsible for the deaths of approximately 300,000 people annually.[120] By enhancing the quality of this surgical procedure, we have the potential to save a significant number of lives.

1.3.1 Challenges in modern minimally invasive surgeries

Minimally invasive surgical procedures offer reduced risk and quicker recovery times compared to traditional methods. They focus on localized regions to minimize damage to healthy tissue, making them increasingly prevalent in treating conditions like cardiovascular diseases and cancer.[8,121,122] The frequently encountered cases in minimally invasive surgery included laparoscopic, gastric, and cardiac surgeries.[123,124] Modern minimally invasive medical instruments, such as catheters, are integral to these procedures.[125,126] During these surgeries, surgeons insert catheters through defined

passages in the body to perform necessary operations, such as the treatment of cardiac arrhythmias via radiofrequency ablation, where the catheter is guided through the right atrium of the heart.[127]

Some traditional catheters rely on tendon-driven mechanisms for navigation within the body,[128] while an alternative approach utilizes remote magnetic catheter navigation.[129–131] This involves embedding a permanent magnet in the catheter and controlling its movement within the body through an externally generated magnetic field.[132] During the procedure, the patient is kept inside an electromagnetic navigation system, which generates the aforementioned magnetic field across the patient's body to steer the catheter (Figure 1.5). Clinical magnetic catheters typically consist of an ablation tip, a flexible shaft with a working channel, and multiple permanent magnets determining the catheter's maximum curvature under an external magnetic field.[133] This method eliminates the need for internal actuation mechanisms, simplifying the catheter's design while enabling effective navigation to specific surgical zones.[133] Additionally, studies have demonstrated that surgeons can quickly learn remote magnetic navigation, becoming adepts with minimal training.[132]

Figure 1. 5 Electromagnetic navigation system used to remotely control magnetic catheters.
The most advanced commercial electromagnetic navigation system Genesis from Stereotaxis consists of two robotic arms with magnets on the tips, a catheter advancer Vdrive, an imaging system Model S, and a vision system Odyssey. Odyssey provides electrocardiogram, ultrasound, 3D Mapping, and fluoroscopy. The Genesis is up to 80% faster and 46% smaller in size than the previously developed system Niobe (a picture is taken from the Stereotaxis official web page: https://www.stereotaxis.com/products/).

However, compared with the manual approach, the remote method has lower success rate (60% manual vs 40% remote) and longer surgery duration (170 min manual vs 223 remote). Several reasons contribute to the below-average performance of the remote approach. In procedures like cardiac ablation for heart arrhythmias, maintaining contact between the catheter tip and the atrial wall poses challenges due to the heart's complex

anatomy and limited 3D visualization.[7,25,132,134] Also, surgical procedures, particularly in the heart, demand catheters to bend in various directions for precise positioning, while remote navigation systems typically offer a magnetic field restricted to a single direction.[135]

To address these challenges, highly dexterous catheters are required to access less accessible regions.[136–138]

1.3.2 Challenges in variable stiffness minimally invasive devices

As a solution, researchers have proposed employing segmented catheters that enable individual segments to adjust their stiffness and offer localized resistance to the magnetic field or additional applied force onto the human tissue. As a result, there has been an increase in the range of actuated bending directions, enhancing the dexterity of the catheters by adding multiple degrees of freedom.[25,27] These segments are made out of filiform variable stiffness fibers.

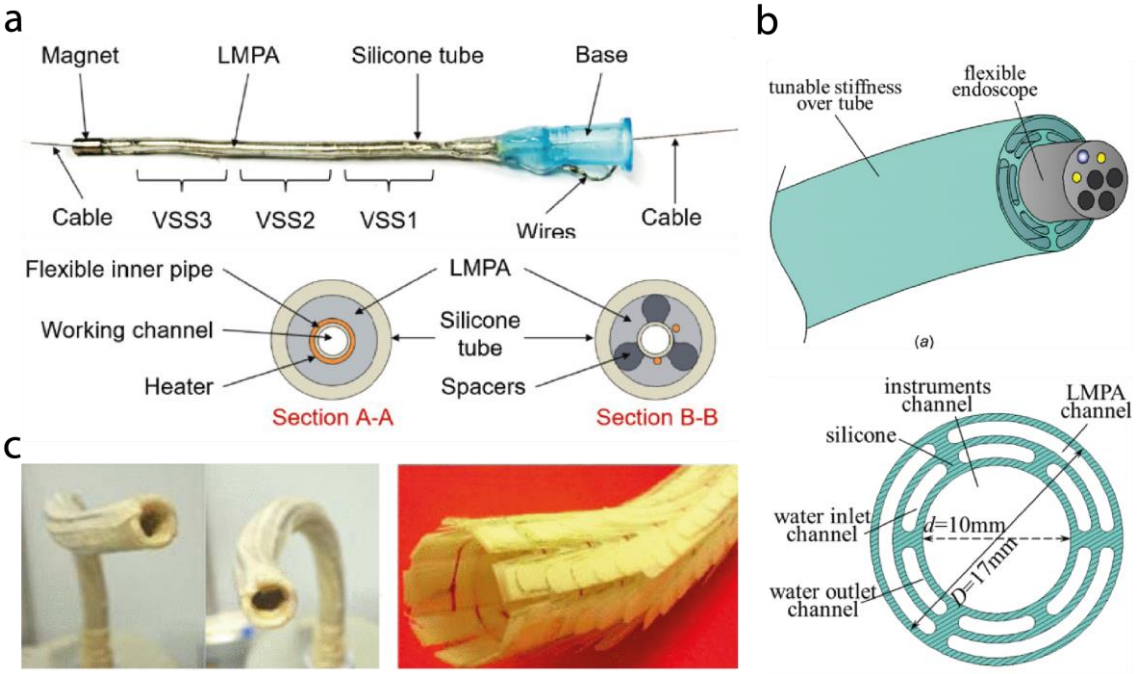

Figure 1. 6 Existing variable stiffness catheters.
a) A magnetic continuum device with three variable stiffness segments for minimally invasive surgery. Each segment consists of an external silicone sleeve, heating copper wire wrapped around the sleeve, and filled with low melting point alloy, which is rigid at room or human body temperature. After being heated up using indirect Joule heating, the alloy becomes liquid making the segment soft and compliant. In this soft state, the catheter can be externally controlled using a magnetic field.[27] b) A variable stiffness manual endoscope with a low melting point alloy that can change its state from soft to rigid and vice versa by convection heating and cooling via applying hot or cold water through the closed-loop channels. This design enables stiffness change without any voltage/current applied inside the human body. However, the addition of water channels

makes the system bulkier and limits the miniaturization.[7] c) An endoscopic device with variable stiffness capabilities achieved through layer jamming and air evacuation.[119]

Researchers have introduced a variety of technologies, including phase-change materials for variable stiffness catheters (including alloys[27] and polymers[139]), hydraulic pressure-driven systems equipped with an array of valves,[140] fiber jamming,[141] and layer jamming.[119] All these technologies have their disadvantages that limit their use in a real-use clinical scenario.

From the material selection point of view, phase-change catheters that utilize LMPA as a variable stiffness substrate suffer from toxic components such as cadmium and lead, which makes these catheters dangerous to use inside the human body in the case of any leakages.[25,27]

Jamming-based catheters can be fabricated out of biocompatible materials but they require air pressure channels, fibers, or granules that limit the miniaturization down to the size of cardiac ablation catheters. The same problem of complicated structure concerns materials-based catheters since they have to be equipped with a variable stiffness substrate, heating, and sensing systems. It leads to a laborious fabrication process, which has to be adopted for each particular catheter size by developing a new mold or encapsulation. It limits the scalability of the catheter design in terms of its stiffness and external radius for a specific application.

The next challenge is the stiffness change speed of the catheters at the scale of cardiac ablation device (2.33 mm external diameter). Catheters based on phase-change materials exhibit a stiffness change ranging from 20 to 40 times and undergo a more gradual transition in stiffness (lasting 10-100 seconds)[25,27,142,143] compared to jamming-based catheters, which undergo rapid changes in less than one second.[136,140,144] However, they possess diameters ranging from 8 to 24 mm, significantly exceeding the size of cardiac catheters (2.3 mm), rendering them inappropriate for cardiac ablation. Therefore, the development of a variable stiffness catheter with fast reaction times and acceptable stiffness change variation on the scale of cardiac ablation procedure remains challenging.

The current variable stiffness catheters utilize segmented variable stiffness fibers, each with a fixed design determined before fabrication.[25,27,142,143] This limitation restricts their versatility across various applications, including medicine, wearable devices, and robotics, as the number of segments or their length cannot be tailored to specific needs. Furthermore, repairing or replacing broken segments is a complex process. Additionally, each segment necessitates an individual wired connection to the base, altering the catheter's geometry and mechanical properties as more wires are added when new segments are introduced. Therefore, new methods to develop scalable filiform variable stiffness technologies in length, diameter, and number of independently controlled segments are needed.

1.4 Thesis outline

In this thesis, we address filiform variable stiffness challenges of bulky design, toxicity, and long reaction times in the following 3 chapters. Chapter 2 comprises the development of a nontoxic variable stiffness fiber with a scalable design in terms of diameter, resistance, and bending stiffness. In Chapter 3 and 4, we address the challenge of long stiffness change transition between soft and rigid states. We tackle this problem using two different approaches: by developing a novel variable stiffness fiber with enhanced reaction times due to the integration of an active cooling system and by developing a catheter based on fiber jamming technology, which we miniaturized down to the scale of the cardiac ablation catheter. In this section, we outline the content of the chapters and highlight their main contributions.

Publication note: The summaries are adapted from the respective publication abstracts provided in Appendix D called “Publication List”.

1.4.1 Chapter 2: A variable stiffness magnetic catheter made of a conductive phase-change polymer for minimally invasive surgery

We aim to tackle a material toxicity problem and bulky design of existing filiform variable stiffness technologies used in cardiac catheters. We developed a novel variable stiffness thread (VST) made of a conductive shape memory polymer (CSMP), which is a nontoxic material that simultaneously serves as a heater, a temperature sensor, and a VS substrate. By consolidating these three vital functions into a single layer, we streamline the design process, facilitating swift customization for any particular application. VSTs are made with a new fabrication method consisting of a dipping technique that enables the fabrication of threads with the desired thickness and electrical resistance. We validated this method through the characterization of VSTs and then demonstrated the selective bending of a multisegment catheter.

The chapter’s main contribution are:

- Development of a novel variable stiffness thread (VST) made of a conductive shape memory polymer (CSMP), which is a nontoxic material that simultaneously serves as a heater, a temperature sensor, and a VS substrate.

- Development of a scalable fabrication method for CSMP consisting of a dipping technique that enables the fabrication of threads with the desired electrical resistance and thickness with a step size of 70 μm.

- Modelling and electromechanical characterization of the VST to determine the stiffness change factor (SCF), stiffness change time, and operation settings for biocompatible surface temperature.

- Integration of two VSTs into catheter to demonstrate the selective bending of a multisegment catheter inside a hospital-compatible electromagnetic navigation system.

1.4.2 Chapter 3: Fast-response variable stiffness magnetic catheters for minimally invasive surgery

The primary limitation of the catheter developed in Chapter 2 is its extended stiffness change cycle of 126 seconds. This prolonged cycle duration results in a fourfold increase in the duration of a typical cardiac ablation procedure, which usually takes an hour. To overcome this limitation, in the Chapter 3, we developed a fast-response, multisegmented catheter for minimally invasive surgery made of variable stiffness thread (FRVST) to improve the stiffness speed from the soft to rigid state. The rapid stiffness change of the FRVST, which is composed of a non-toxic shape memory polymer, is achieved by the active cooling system that pumps water through the helical channel. Using the mechanical and thermal characterization, we demonstrated that the FRVST exhibits a stiffness-change factor of 66 and a transition time 26 times faster than the non-cooled version. We then integrated FRVSTs into multisegment catheter and characterized its bending angle change. Finally, we demonstrated the performance in a 3D-printed labyrinth and in a phantom of the human heart. The catheter has an inner working channel, which can be used for cooling the ablation tip during the procedure and for information exchange via the deployment of wires or surgical tools.

The chapter's main contributions are:

- The development of a fast-response, multisegmented catheter for minimally invasive surgery made of variable stiffness thread (FRVST) that encapsulates a helical cooling channel.

- The FRVST's mechanical and thermal characterization display a stiffness-change factor of 66 and a transition time 26 times faster than the non-cooled version.

- The integration of FRVSTs in a single- and multisegment catheter followed by bending angle characterization in a hospital-compatible eMNS in the air and water.

- The multisegmented catheter was also tested in a 3D-printed labyrinth to demonstrate how variable stiffness can help to avoid unnecessary contact with a human tissue.

- The multisegmented catheter was placed in a 3D phantom of the human heart underwater at body temperature to demonstrate an ablation procedure.

1.4.3 Chapter 4: A Fast-Response Variable Stiffness Magnetic Catheter Based on Fiber Jamming for Cardiac Ablation

While the reaction times for stiffness change were effectively decreased from 126 seconds to 17 seconds in Chapter 3, it's important to highlight that, even with this improvement, the regular cardiac ablation procedure duration still extends by 50%. This limitation hampers its practical applicability in real-world scenarios. Therefore in this chapter, we tackle the problem of slow reaction time using absolutely different variable stiffness technology compared to Chapters 2 and 3. We propose a novel approach to design variable stiffness catheters based on fiber jamming (FJ) technology, which achieves instant stiffness changes (within 300ms), enabling seamless catheter operations without delays. First, we develop a single-segment catheter by incorporating hundreds of ultrathin fibers into a slender 2.3mm catheter body. The existing fabrication approaches do not enable manufacturing a large number of ultra-thin fibers and packaging them in the scale of Ø2.33mm suitable for cardiac catheters.

To address the challenge, we introduce an innovative fabrication procedure to construct the FJ-based VS catheter. Through mechanical characterization, we showed that the catheter with a 6.5-fold stiffness change has similar performance in terms of a bending angle compared to phase-changing material-based catheters. Then, we fabricated a multisegment catheter, which achieves complex bending profiles within seconds and smooth manipulation in a simulated surgical scenario inside a hospital-compatible eMNS. In addition, the FJ-based design does not require electric currents or heating inside the human body, minimizing risks to the patients.

The chapter's main contributions are:

- We developed a novel VS catheter based on fiber jamming (FJ) that achieves instant stiffness changes (within 300ms), enabling seamless catheter operations without delays.

- We introduced an innovative fabrication procedure to construct the FJ-based VS catheter based on a precise method to produce fibers as thin as 50µm and a process to pack up to 1000 fibers within a 2mm diameter space.

- The mechanical characterization setups to determine the stiffness change factor and reaction times were built.

- The single-segment catheter was characterized in a hospital-compatible eMNS to determine the bending angle in the soft and stiff states.

- A two-segment catheter was then fabricated and tested to demonstrate a selective bending of both segments. The catheter achieves two-curvature profiles and can be manipulated inside a 3D phantom of the human heart.

- The proposed device based on fiber-jamming technology adds only a minute to the duration of a cardiac ablation procedure making the developed proof-of-concept a suitable candidate for a practical clinical use.

1.4.4 Chapter 5: Conclusions

We provide a concise overview of the thesis and delve into its implications, constraints, and prospects for future research. We also highlight some satellite robotics projects we have been working on and discuss their application in medical field.

Chapter 2

2 A variable stiffness magnetic catheter made of a conductive phase change polymer for minimally invasive surgery

Publication note: The work presented in this chapter is based on

Y. Piskarev, J. Shintake, C. Chautems, J. Lussi, Q. Boehler, B. J. Nelson, and D. Floreano, *A Variable Stiffness Magnetic Catheter Made of a Conductive Phase-Change Polymer for Minimally Invasive Surgery*, in Advanced Functional Materials, Feb. 2022.

2.1 Abstract

Variable stiffness (VS) is an important feature that significantly enhances the dexterity of magnetic catheters used in minimally invasive surgeries. Existing magnetic catheters with variable stiffness consist of sensors, heaters, and tubular structures filled with low melting point alloys, which have a large stiffness change ratio but are toxic to humans. In this paper, a variable stiffness magnetic catheter is described for minimally invasive surgery; the catheter is based on a novel variable stiffness thread (VST), which is made of a conductive shape memory polymer (CSMP). The CSMP is nontoxic and simultaneously serves as a heater, a temperature sensor, and a variable stiffness substrate. The VST is made through a new scalable fabrication process, which consists of a dipping technique that enables fabrication of threads with the desired electrical resistance and thickness (with a step size of 70 μm). Selective bending of a multisegmented VST catheter with a

diameter of 2.0 mm under an external magnetic field of 20 mT is demonstrated. Compared to existing proof-of-concept VS catheters for cardiac ablation, each integrated VST segment has the lowest wall thickness of 0.75 mm and an outer diameter of 2 mm. The segment bends up to 51° and exhibits a stiffness change factor of 21.

2.2 Introduction

Minimally invasive surgeries provide a lower risk and faster recovery time than conventional procedures since they are used to operate in targeted local regions to curtail the damage caused to healthy tissue. These procedures are increasingly being used to treat conditions such as cardiovascular disease and cancer.[8,121,122] Modern medical tools such as catheters are widely used in these surgeries.[8,125,126] The surgeon inserts a catheter through a well-defined passage in the body to perform the necessary operation.[145] An example of such an operation is the treatment of cardiac arrhythmias by radiofrequency ablation, in which the catheter passes through the right atrium of the heart.[127]

Some conventional catheters used in these surgeries make use of tendon-driven actuation for navigation within the human body.[128] An alternative approach involves the use of remote magnetic catheter navigation. In this case, a permanent magnet is embedded in the catheter, and its motion within the body is controlled by an externally generated magnetic field.[132] This eliminates the need to place actuation mechanisms within the catheter, thereby simplifying the design while still enabling effective navigation to a defined zone during surgery.[133]

Moreover, it has been shown that remote magnetic navigation can be learned quickly and that surgeons become adept at using the technology with minimal training.[132] Existing clinical magnetic catheters consist of an ablation tip, a flexible shaft with a working channel, and a given number of permanent magnets that determine the maximum curvature of the catheter under an applied external magnetic field.[133] In the scenario that involves employing a catheter to treat heart arrhythmias by cardiac ablation, it is challenging to keep the catheter tip in contact with the atrial wall to achieve ablation.[7,27,132,145,146] The complex anatomy of the human heart and lack of 3D visualization require catheters with high dexterity to reach more inaccessible regions.[136–138] Often, surgical procedures, such as those in the heart, require bending catheters in a wide variety of directions to position the tool appropriately. However, the externally generated magnetic field in a remote navigation system is typically confined to a single direction.[135]

To address this problem, researchers have suggested the use of segmented catheters in which individual segments can undergo changes in stiffness and locally resist the magnetic field. This has resulted in an increase in the number of controllable bending directions (degrees of freedom).[7,27,145] Researchers have already presented variable stiffness (VS) catheter phase-change materials (alloys[7] and polymers[139]), hydraulic pressure-driven systems with an array of valves,[140] fiber jamming,[141] granular jamming,[144] and layer jamming.[119]

Hydraulic and jamming technologies show faster reaction times (less than a second) than phase-change materials (seconds to hundreds of seconds);[139,144] however, additional air channels, layers, or granules inside the devices limit miniaturization. Existing hydraulic and jamming-based catheters with diameters of 3.0 and 5.0 mm exceed the standard diameter of cardiac catheters (2.3 mm) and cannot be used for cardiac ablation.[140,144]

The development of catheters has overcome the scaling problem with the use of low melting point alloys. These materials have a large stiffness change ratio (> 400 times) but are toxic and require encapsulation.[10,27,143,145] Moreover, the integration of additional electrical components, such as temperature sensors and heaters (needed to control the stiffness change), leads to a laborious fabrication process. This process has to be adapted for each particular catheter size by developing a new mold made of polydimethylsiloxane (PDMS) or two silicone tubes.[27,143,145] This independent integration of a large number of components also leads to a complicated design and fabrication process that results in a lack of versatility, making it difficult to match the catheter to a given specification for the application.

Here, we present a novel variable stiffness thread (VST) made of a conductive shape memory polymer (CSMP), which is a nontoxic material that simultaneously serves as a heater, a temperature sensor, and a VS substrate.

Shape memory polymers (SMPs) exhibit stiffness changes during the phase transition as well as actuation due to the shame memory effect.[147,148] The stiffness of SMPs can be tuned by varying the temperature above the glass transition temperature with the application of an external stimulus, such as photothermal or Joule heating.[149] When the polymer is heated above the glass transition temperature, it transitions from the solid-state with a high load resistance to a rubbery elastic state exhibiting easy deformation. After this transition, a stiffness change amounting to several hundred times the elastic modulus is observed.[150] If the SMP does not undergo large deformations, then the shape memory effect is not dominant and the heating or cooling of the material changes only the elastic modulus.[148] Among similar materials, polyurethane-based SMPs present several advantages, including easy processing, biocompatibility, an adjustable shape-recovery temperature, and large strain recoveries.[48,151,152] Thus, they are widely used in soft robotics applications such as variable stiffness actuators, microfluidic valves, and flexible skins.[149,153,154] The inclusion of conductive particles in SMPs enables direct Joule heating by applying a voltage difference to the material without additional heaters.[29]

The VST developed in this study is composed of three layers: a polytetrafluoroethylene (PTFE) tube with a working channel, a CSMP coating, and an encapsulation layer of silicone rubber (**Figure 2.1a**). The temperature of the CSMP layer increases from room temperature (23°C) to 80°C in 36 s via direct Joule heating with an applied power of 1.5 W and in 18 s with 2 W (Figure 2.1b). When the applied power is turned off, it takes 90 s to return to room temperature (Figure 2.1c, see Video 2.S1, Appendix A). The VST with a weight of 0.2 g withstands an applied load of 30 g in the rigid state and exhibits a large deformation in the soft state at 80°C (Figure 2.1d, see Video 2.S2, Appendix A). The thread exhibits a stiffness change factor (SCF) of 21 when heated beyond the glass transition temperature of 45°C.[29] VSTs are made with a new fabrication method consisting of a dipping technique that enables the fabrication of threads with the desired

thickness and electrical resistance. In contrast to conventional tubular VS technologies fabricated through molding or injection processes,[5,10,145] our approach allows VST thickness tuning with a step size of 70 µm.

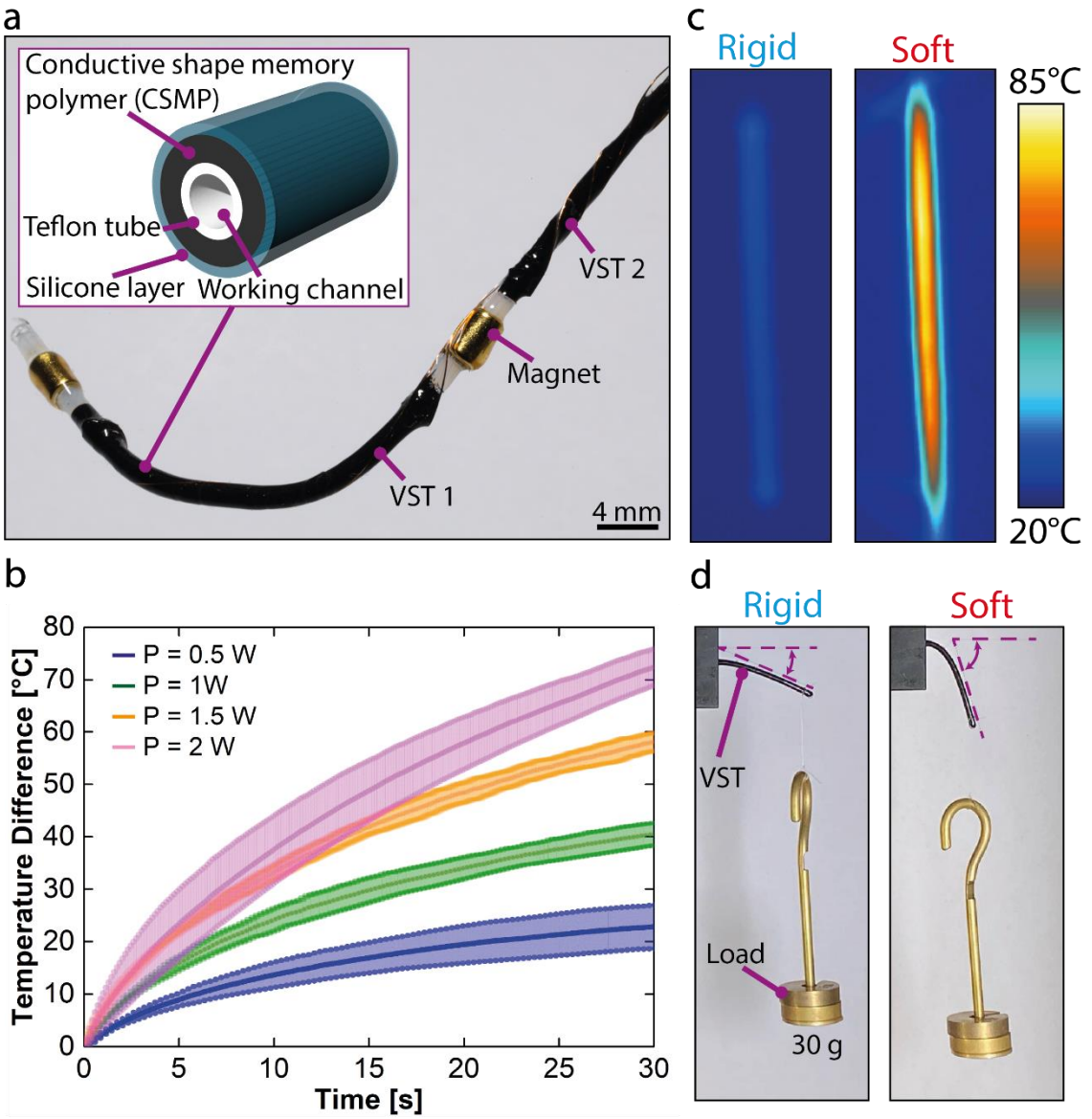

Figure 2. 1 Structure and operating principle of the variable stiffness thread (VST). a) The VST consists of a polytetrafluoroethylene (PTFE) tube with a working channel coated in a conductive shape memory polymer (CSMP) layer, which is further encapsulated in silicone. b) Heating rate of the VST from room temperature (23°C) for different applied powers. Voltages 7.6, 10.7, 13.1, and 15.1 V were applied to achieve powers of 0.5, 1, 1.5, and 2 W respectively. Three different samples were tested for each level of applied power. c) The VST can exhibit a change in the stiffness upon direct Joule heating of the CSMP layer. The device undergoes the state change from a rigid state at room temperature (23°C) to a soft state at 80°C in 27 s with an applied power of 1.5 W. d) The VST only minimally bends under a weight of 30 g in the rigid state, but freely bends under the same weight when heated to 80°C in the soft state.

We validated this method through the characterization of VSTs and then demonstrated the selective bending of a multisegment catheter (Figure 2.1a). The catheter has an external diameter of 2.0 mm and an internal diameter (i.e., working channel) of 0.5 mm, resulting in a wall thickness of 0.75 mm, which is lower than the thicknesses of other VS cardiac catheters.[27,145] In the VST catheter, each segment bends up to 51° under an 80 mT external magnetic field and has a surface temperature of 41.5°C. The working channel inside the VST can be used for incorporation of an active cooling system to enhance the reaction time and provide information flow via the deployment of wires or insertion of surgical tools.

2.3 Results and Discussion

2.3.1 Fabrication method

The VST fabrication procedure based on the dipping technique is illustrated in **Figure 2.2**. In this method, a polytetrafluoroethylene (PTFE) tube fixed on a metal rod is dipped vertically into the conductive shape memory polymer (CSMP) mixture and then cured in an oven, inducing the formation of a CSMP layer on the tube (Figure 2.2a-c). This dipping step can be repeated multiple times to achieve the desired thickness of the CSMP layer. Then, the tube with the CSMP coating is dipped into liquid silicone and cured in an oven for the purpose of encapsulation (Figure 2.2d-f). Silicone was chosen as the encapsulation material due to its low thermal conductivity (on the order of 0.2 W/m·K) and high electrical breakdown strength (on the order of 53 V/μm).[155,156] While the dipping technique itself has been widely used in industry due to its high precision control of deposit thickness,[157,158] this is the first time it has been used for coating PTFE tubes with CSMP. In previous work, the CSMP mixture was deposited only on planar surfaces.[29] Therefore, we first assessed how the number of dips affected the thickness of the CSMP layer and its resistance. As shown in **Figure 2.3a**, the thickness of the CSMP layer increased from 84 μm to 570 μm from the first to the eighth dip, with a step size of 70 μm. The data show linear behavior, suggesting that the thickness is highly controllable. For the resistance of the CSMP layer, the result shows a quadratic drop. This is because the resistance is inversely proportional to the cross-sectional CSMP area. A significant decrease in the resistance of the VST was observed after the first dip, from 891 ohm down to 374 ohm after the second dip; it ended at 96 ohm after the eighth dip at room temperature.

During the fabrication of VSTs, the CSMP coating on the PTFE tube formed four zones: a wetting zone at the top of the tube, a constant thickness zone, a dynamic meniscus, and a static meniscus.[159] The mixture's wettability (i.e., to what extent the material spreads across a substrate) is required in order to obtain uniform coating. Wettability depends on the surface tension of the liquid and on the surface energy of the substrate. On the one hand, the high surface tension of the mixture leads to strong attraction between molecules, resulting in dewetting (i.e., the rupture of a thin liquid film on a substrate and the formation of droplets). On the other hand, the high surface energy generates greater affinity of the molecules of the mixture toward the substrate, resulting in wetting. Thus,

the low surface energy of the substrate or high surface tension of the mixture can result in insufficient coating of the substrate. It is therefore essential to choose a solvent with a lower surface tension than this mixture or by changing the substrate material to one with a higher surface energy.

Existing studies have already described some of the relationships in the dipping technique. The thickness of a layer increases with a longer dipping time.[157] Additionally, the temperature of a rod dipping into the mixture influences the thickness of a coating.[160] A higher temperature for the tool leads to a thicker coating. Furthermore, an increase in viscosity results in growth of the deposit.[161]

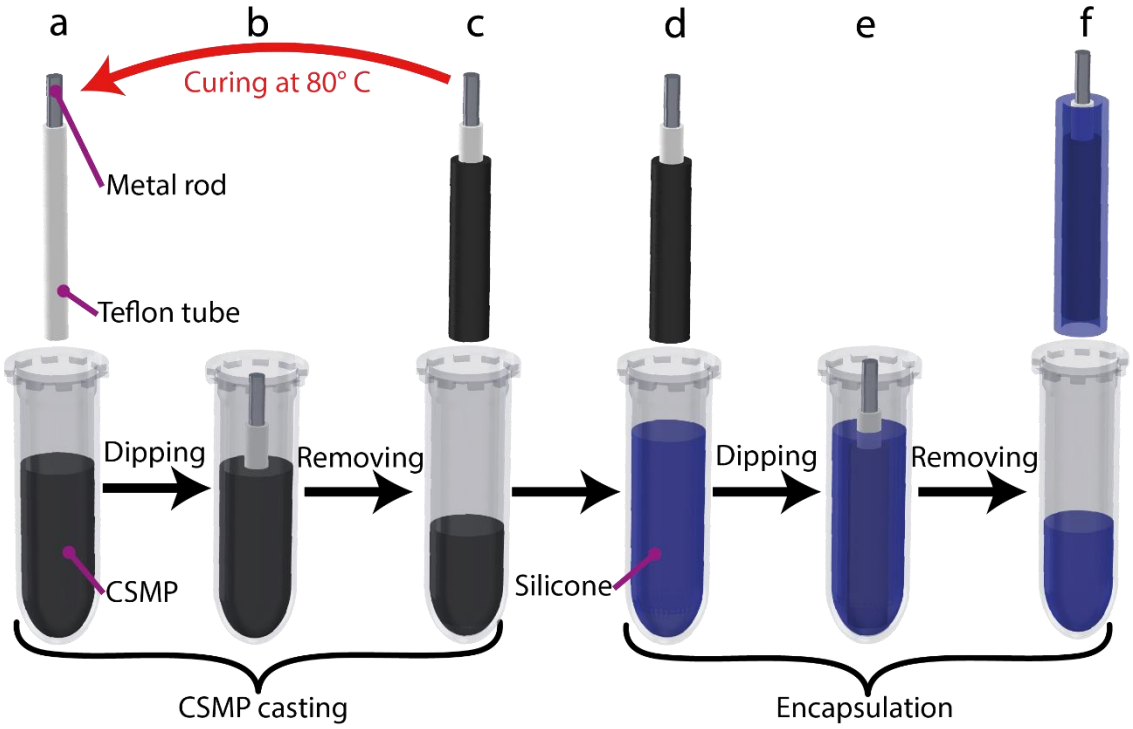

Figure 2. 2 Fabrication process of the variable stiffness threads (VSTs).
a) A PTFE tube is prepared and fixed on a metal rod. b) The tube is dipped into a conductive shape memory polymer (CSMP) mixture. c) The tube is hung vertically and cured in an oven. Steps (a)-(c) can be repeated to achieve the desired thickness of the CSMP layer. d-f) The sample is then dipped into liquid silicone, hung vertically, and cured in an oven, forming an encapsulation layer.

The base material for our VSTs was a cytocompatible polyurethane-based SMP (SMP Technologies Inc., MM4520).[162,163] SMPs are widely used in biomedical applications such as stents, drug delivery, and bone tissue engineering.[48,164,165] PDMS (Dow Corning, Sylgard 184) was applied as an outer coating on the VST due to its biocompatibility with human tissue.[9,166,167] Carbon black (Nouryon, Ketjenblack EC-600JD), a type of conductive nanofiller, was infused with the thermoplastic polyurethane to improve the mechanical and electrical characteristics without losing biocompatibility,[168] although a detailed biocompatibility study was not performed. However, carbon black has already been used for biocompatible strain sensors and flexible bioelectrodes[169,170] and the one used in this study showed high cell viability (100%) at a concentration of 32.5 µg/mL during an in vitro cytotoxicity study.[171] Additionally, as there is no evidence that the

CSMP composite is nontoxic, an in vitro cytotoxicity test was performed (according to ISO 10993-5:2009 Biological Evaluation of Medical Devices - Part 5). The results showed the cytocompatibility of the material for at least 284 minutes, the maximum time duration of a cardiac ablation procedure (Supplementary Document 2.S1, Appendix A).[172]

2.3.2 Electromechanical characterization of the VST

To quantify the VST electromechanical properties, we characterized the stiffness change factor (SCF) and resistance change at different temperatures. The SCF depends on the geometrical parameters (length and moment of inertia) and material composition of the device. The SCF is given by the relation

$$\mathrm{SCF} = \frac{K_r}{K_s} \qquad (1)$$

where K_r and K_s are the bending stiffnesses of the VST in the rigid and soft states, respectively.[13,173] The effective bending stiffness of the thread, *K*, is defined by the relation

$$K = \sum E_{\mathrm{avg}} I_i \qquad (2)$$

where E_{avg} is the Young's modulus of the entire device. I_i is the moment of inertia (second moment of area) of different layers from *i* equal to 0 to N. The moment of inertia is determined by the different layers making up the VST: the PTFE, CSMP, and silicone layer. The moment of inertia is given as

$$I_i = \frac{\pi r_e^4}{4}\left\{1 - \left(\frac{d_{\mathrm{i}}}{d_{\mathrm{e}}}\right)^4\right\} \qquad (3)$$

where r_e is the external radius, d_{i} is the internal diameter, and d_{e} is the external diameter of the layer. To calculate the Young's modulus E_{avg}, we employ the equation described in ref. [141].

$$E_{\mathrm{avg}} = \frac{E_{\mathrm{PTFE}}A_{\mathrm{PTFE}} + E_{\mathrm{CSMP}}A_{\mathrm{CSMP}} + E_{\mathrm{silicone}}A_{\mathrm{silicone}}}{A} \qquad (4)$$

where A_{PTFE}, A_{CSMP}, $A_{silicone}$, and A are the cross-sectional areas of the PTFE, CSMP, silicone, and VST, respectively. Similarly, E_{PTFE}, E_{CSMP}, and E_{silicone} are the Young's moduli of PTFE, CSMP, and silicone, respectively. In these parameters, E_{CSMP} remains uncertain due to the addition of carbon particles.[29] Thus, a thermomechanical characterization of the VST and an empirical study of the bending stiffness were performed. Dynamic mechanical analysis showed a 20-fold reduction in the elastic modulus from 2 GPa to 0.1 GPa as the temperature increased from 37 to 80°C (Figure 2.S1, Appendix A). Additionally, the infusion of carbon particles with the thermoplastic polyurethane resulted in a 4 fold reduction in the storage and loss moduli of the SMP as the temperature increased from 20 to 120°C.[149] The carbon particles also shifted the glass

transition temperature closer to the temperature of a human body from 60 to 45°C. The bending stiffness was empirically defined through a three-point flexural test, where the VST was placed in a universal testing machine equipped with a temperature box. The test was conducted at four temperatures: 22°C for the rigid state and 40°C, 60°C, and 80°C for the soft states. With this experimental condition, the deflection and reaction force of the VST were measured. The results were filtered (see Figure 2.S4, Appendix A) and plotted in Figure 2.3b. According to the Euler–Bernoulli beam theory and considering the boundary conditions, the deflection of the VST is expressed as

$$\delta = \frac{Fl^3}{48EI} \qquad (5)$$

where δ is the deflection of the VST at the point of applied force F, l is the length of the beam, E is Young's modulus, and I is the moment of inertia. The applied force F is a point load which represents a tip force during three-point flexural test. The maximum deflection was set to 3 mm to respect the assumptions of Euler–Bernoulli beam theory. The multiplication of two parameters EI represents the bending stiffness K of the device. Based on the experimental results and Equation 5, the SCFs of the VST between room temperature (22°C) and 40°C, 60°C, and 80°C were found to be 1.4, 2.4, and 21, respectively. The corresponding SCF can be defined for specific applied loads in rigid and soft states using Equations 1-5. The coating thickness of the VSTs in all experiments was 0.3 mm.

To characterize the resistance change, six samples were connected to a multimeter, placed in an oven, and heated from 22°C to 80°C with a step size of 10°C. As shown in Figure 2.3c, the VST experiences a decrease in the resistance from 115.3 ohm at 23°C to 106.6 ohm at 80°, resulting in a change of 7.6%. It also shows a significant drop in the temperature range between 23°C and 60°C. The reduction in resistance is due to the negative temperature coefficient, which occurs when the carbon black particles are small and the concentration is near the percolation threshold.[81,174–176] This effect arises from particle realignment, thermal emission of electrons between nearest carbon black particles, and oxidative crosslinking at the surface.[81,174] Overall, the VST exhibits good sensitivity to temperature changes. This means that the temperature control of the VST can be achieved based on its own resistance change without the use of additional sensing elements and associated electric components.

The VST can be heated with direct Joule heating by applying electrical power to the CSMP layer. The resistance of the device changes as it was heated in air from 23°C to 80°C in 175 s with an applied power of 1 W (Figure 2.3e). The VST can be heated to 80°C in 27 s with an applied power of 1.5 W, which reduces to 18 s with 2 W (Figure 2.1b). Then, it was cooled back to the initial temperature in 107 s. The result shows a drop of 5% between the rigid and soft states. This resistance drop can be used to sense the current stiffness of the VST. In comparison with an observed resistance drop caused by heating, the resistance change during mechanical deformation is negligible (see Figure 2.S2, Appendix A). The maximum resistance change under direct heating is 2.6% lower than that in the case of indirect heating (Figure 2.3c). This can be explained by the inhomogeneous heat distribution in the CSMP material due to variations in the dipping deposit thickness of the CSMP layers. Different thicknesses of the CSMP layer result in

local resistance differences between the top, bottom, and middle regions of the VST (Figure 2.1b).

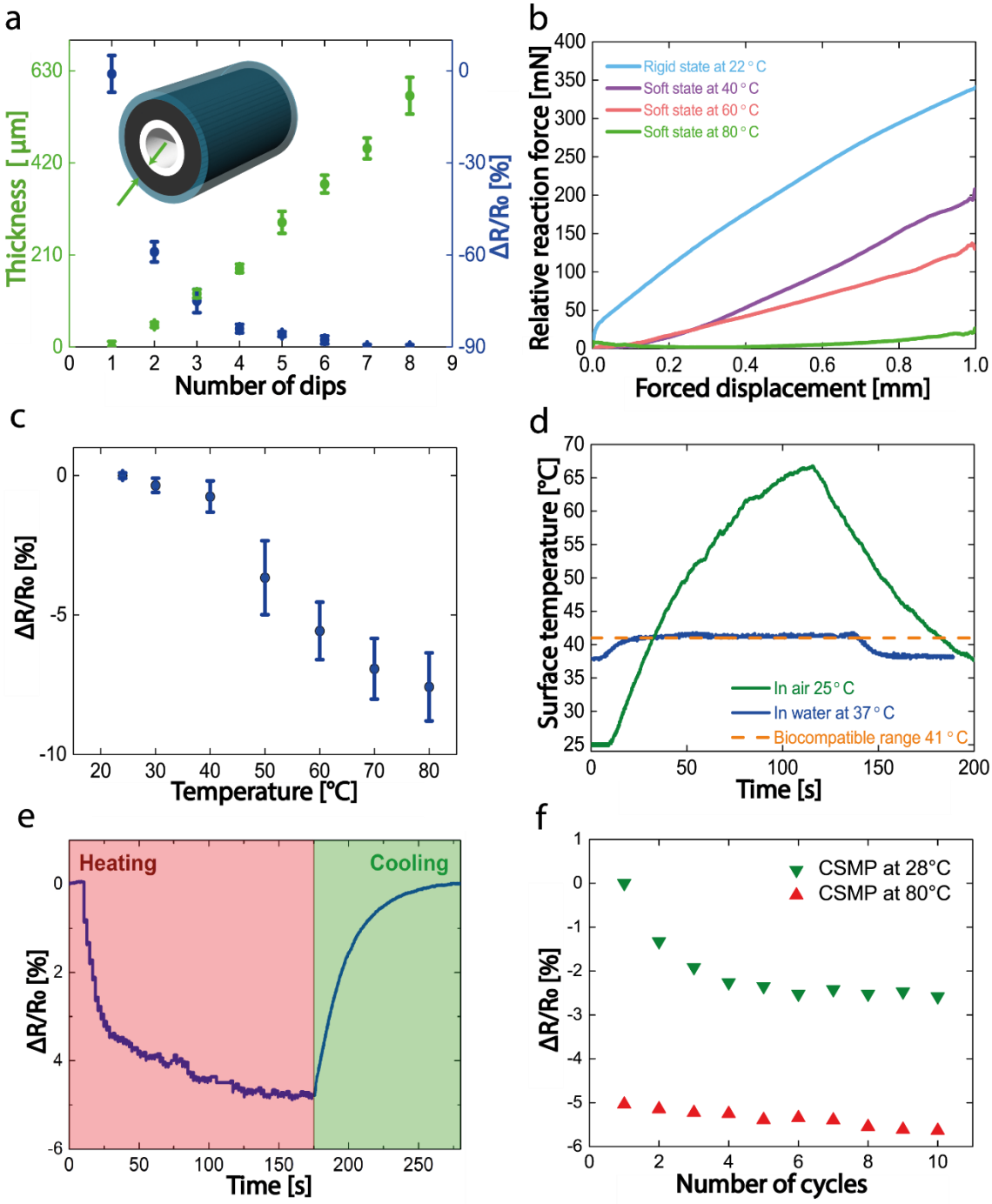

Figure 2. 3 Variable stiffness thread (VST) characterization.
The coating thickness of the VSTs was 0.3 mm. a) Thickness and electrical resistance of the conductive shape memory polymer (CSMP) layer as functions of the number of dips. The thickness changes from 84 µm after the first dip to 550 µm after the eighth dip. The resistance decreases from 891 ohm for the first dip to 91 ohm after the eights dip. b) Reaction force of the VST against forced displacement under a three-point flexural test. c) Electrical resistance of the CSMP layer as a function of the temperature change under indirect Joule heating. The resistance decreases from 115.3 ohm at 23°C to 106.6 ohm at 80°C, with a significant drop in the range between 23°C and 45°C due to the change in

state from solid to rubbery. d) VST with the CSMP layer heated to 80°C, reaching a surface temperature of 66°C in air and 41.5°C in water at 37°C without flow. e) The state of the VST can be seen with the resistance drop caused by the temperature difference for the cold and hot states. Direct Joule heating under 1 W of applied power increases the VST temperature from room temperature (23°C) to 80°C in 175 s in air. Then, the thread cools back down to room temperature in 107 s. During this heating-cooling cycle, the VST experiences a relative resistance change equal to 5%. f) Resistance change in the VST for 10 heating-cooling cycles under direct Joule heating. The green and red triangles represent the resistance change in the rigid state at 28°C and soft state at 80°C, respectively. After passing the first three cycles, the resistance change remains almost constant.

Regions with higher resistance generate more heat; thus, the temperature is higher in these regions, which leads to a higher resistance difference. As shown in Figure 1b, the temperature of the CSMP layer varies from 80°C in the middle to 50°C close to the top and bottom regions of the VST during direct Joule heating. Thus, the temperatures of the CSMP regions at the top and bottom are lower and cause less resistance change difference than the middle. In contrast, for the case of indirect heating, the VST was homogeneously heated in the oven. The VST heating time from 28°C to 80°C is 6 times longer for 1 W than for 1.5 W (Figure 2.1b) due to the lower applied power. During the cyclic thermal loading test, the resistance showed a significant drop after the first 3 cycles (Figure 2.3f). This effect is typical for conductive polymers and occurs due to the irreversible change in carbon black aggregation during heating.[174] This aggregation becomes stabilized after the first few cycles and does not return to the initial state after cooling. After passing the first three cycles, the resistance change remains almost invariant for the following seven cycles.

To determine the maximum safe temperature of the CSMP layer in the soft state, we characterized the surface temperature in air at room temperature (23°C) and in water at 37°C without forced flow. The temperature of the water was set to mimic the thermal behavior of a VST inside the human body due to its similar heat-transfer properties.[27] Three thermistors were glued on the surface of the VST, covering both ends and the middle. The thermistors were isolated against the water with a layer of glue. The surface temperature was measured by thermistors when heat was applied. The resistance of the CSMP layer was used to define its own temperature during direct Joule heating. First, the CSMP layer was heated to 80°C in air with an applied power of 1 W (applied voltage 10.7 V). The temperature was controlled using a thermal camera and by monitoring the resistance change of the CSMP layer. When submerged in water, the applied power was 1.16 W which corresponds to an applied voltage of 12.5 V. The power was turned off when a relative resistance change of 5% was achieved. The result is displayed in Figure 3d. The surface temperature of the VST reached 66°C in air and 41.5°C in water when the CSMP layer was heated to 80°C. The surface temperature in the water was 0.5°C higher than the required biocompatible surface temperature.[55] This was a result of the fact that the test was conducted in stagnant water. In minimally invasive surgery, the VST will be surrounded by flowing fluid, which will reduce the surface temperature below the safe temperature. A further reduction in surface temperature can be achieved by

increasing the thickness of the silicone layer by 65 μm or by modifying the material composition of the insulating layer (see Figure 2.S3, Appendix A).

2.3.3 Electromechanical characterization of a single-segment VST catheter

We assessed the performance of a single segment of a VST catheter in terms of the bending angle in the soft and rigid states under external magnetic fields. The bending angle in the soft state determines the level of dexterity of a catheter. In the VST rigid state, the bending angle defines the magnetic torque the catheter can withstand, thus governing the level of shape fixity that can be achieved. The external magnetic field *B* applied on a permanent magnet with a dipole moment *m* at position *p* generates a magnetic torque T_m

$$\boldsymbol{T_m(p) = m \times B(p)} \qquad (6)$$

The maximum magnetic torque is achieved when the magnetic field is perpendicular to the dipole moment and is minimal when they are aligned. On the other hand, the magnetic torque can be tuned by choosing permanent magnets with higher dipole moments.

The design of the single-segment VST catheter is illustrated in **Figure 2.4a-i**. It consists of a VST attached to a base on one end and is equipped with a permanent magnet on the other. An electrode is connected to one end of the VST and wrapped around and down to the base to deliver power to the CSMP layer. The entire structure is encapsulated in silicone. It has a length of 44 mm, an outer diameter of 2.0 mm, and an internal diameter, i.e., the working channel, of 0.5 mm (Figure 2.4a-ii). This design has the same working channel size but a lower wall thickness of 0.75 mm compared to a previously developed low melting point alloy-based catheter with a wall thickness of 0.92 mm and outer diameter of 2.3 mm.[27]

The deflection of a single-segmented catheter is characterized inside the electromagnetic navigation system with a magnetic field magnitude of 80 mT and varying magnetic field orientations. The catheter can bend up to 90° in the desired direction in the soft state under 80 mT (Figure 2.4b). The motion of the device can be observed in Supplementary Video 2.S3, Appendix A. The characterization results, plotted in Figure 4c, show that the VST catheter can withstand the applied magnetic moment and bend only up to 1.5° at the maximum magnetic field of 80 mT.

In the soft state, the device exhibits a linear change in the bending angle up to 51° at an inclination angle of 90° and a magnetic flux density of 80 mT. As shown in Figure 2.4d, the device also demonstrates high repeatability with a low hysteresis for five cycles. Note that the values in Figure 2.4c and d represent three tested catheters and five cycles per device. Compared with existing models that can bend up to 110°, the maximum bending angle in the current system is 90°.[27,145] In terms of performance repeatability, fatigue was not observed after 10 cycles of testing. [27]

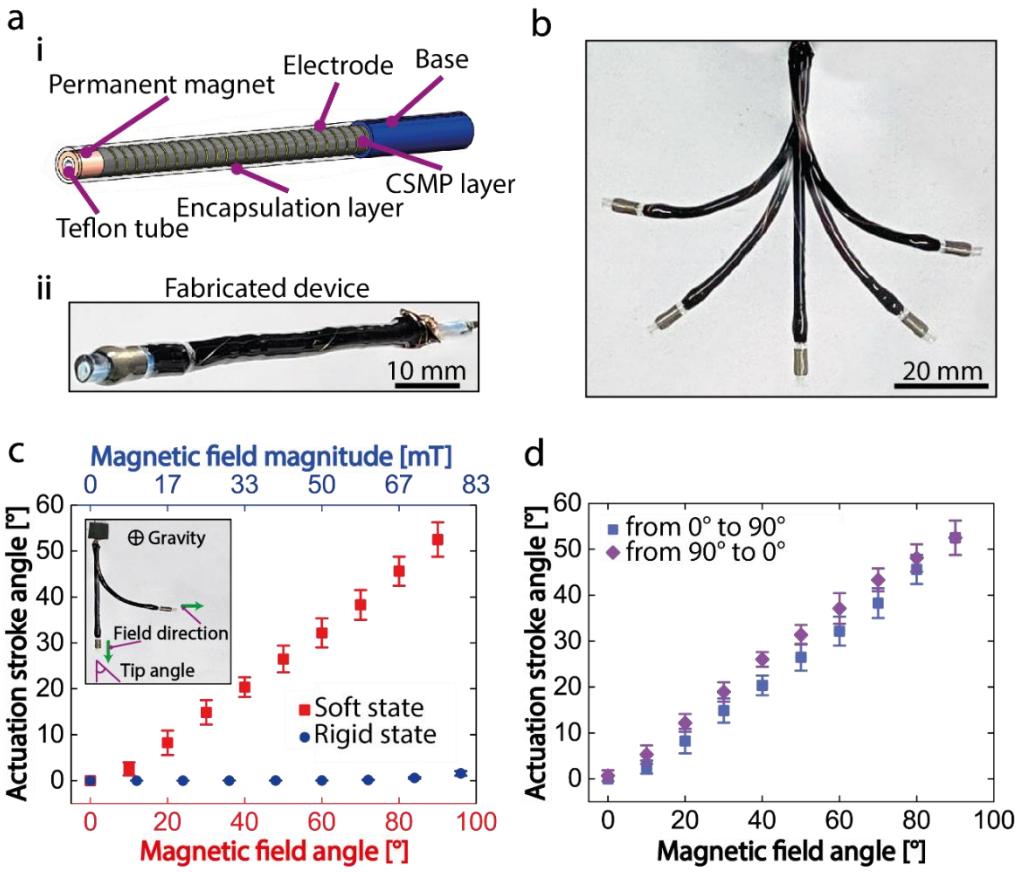

Figure 2. 4 Single-segment catheter with variable stiffness thread (VST) and characterization results.
a) (i) The catheter consists of a VST, permanent magnet, base part, and electrode wire wrapped around the conductive shape memory polymer (CSMP) layer. The entire structure is encapsulated in silicone. (ii) The catheter has a length of 44 mm and a diameter of 2.0 mm with a working channel of 0.5 mm. b) Bending actuation of the VST catheter. c) Actuation stroke angle as a function of the magnetic field angle and magnitude. The values represent three tested catheters and five cycles per device. The maximum actuation angle in the rigid state under a magnetic field magnitude of 80 mT is 1.5°. In the soft state, the actuation angle exhibits the maximum value of 51° under a magnetic field angle of 90°. d) Actuation stroke angle as a function of the magnetic field angle in the soft state. The values represent three tested catheters and five cycles per device.

2.3.4 Multisegmented catheter for cardiac ablation

To better illustrate the possible application of VST, we developed a multisegmented catheter with two integrated VSTs for use in medical scenarios such as cardiac ablation (**Figure 2.5**). The device consists of two variable stiffness segments with two permanent

magnets (Figure 2.1a and Figure 2.5a). The VSTs were fabricated separately and mounted on the PTFE tube together with magnets. Then, the whole structure was encapsulated by dipping it into silicone. Our objective is to demonstrate that a multisegmented catheter composed of two VSTs can be manipulated with a magnetic field as low as 20 mT. Thus, according to Equation 6, the induced magnetic torque for a two-segmented VST catheter is lower than that for a single-segmented catheter, where an external magnetic flux density of 80 mT is applied. Therefore, permanent magnets with a four times higher dipole moment *m* are selected to provide the same magnetic torque for the two-segmented catheter.

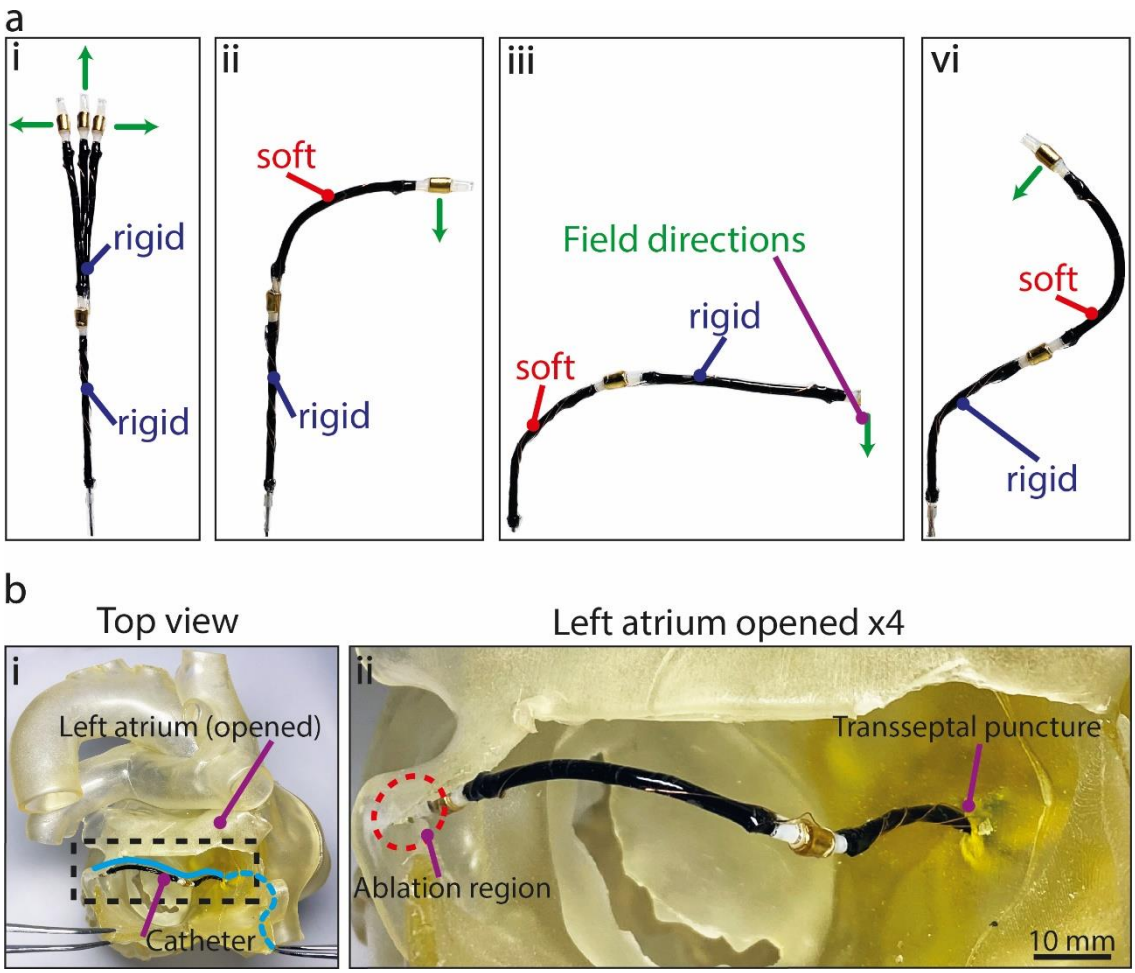

Figure 2. 5 Two-segmented catheter design, performance, and application.
a) The catheter consists of two variable stiffness threads (VSTs) and two permanent magnets fastened on the same PTFE tube. The catheter is placed in an electromagnetic navigation system (i) when both VSTs are solid and (ii-iv) when one of them is sequentially soft. b) An illustration of catheter application in the cardiac ablation procedure. The path of the catheter is shown in blue: it goes through the right femoral vein and inferior vena cava into the right atrium, through which, with a transseptal puncture, it reaches the left atrium. In the left atrium, the catheter reaches one of the four pulmonary veins (i-ii).

The catheter was first placed in the electromagnetic navigation system with rigid VSTs (Figure 2.5a-i). Magnetic flux was applied perpendicular to the length of the catheter to generate deflection of the tip in the rigid state (see Video 2.S4, Appendix A). Then, the VSTs were heated up and bent to realize catheter deflection. As shown in Figure 2.5a-ii, iii, and iv, the selective activation of VSTs enables different deformations of the device. Each of the segments can be bent up to 90°, while the second segment withstands an applied magnetic torque (Figure 2.5a-ii and iii). The catheter achieves complex curvatures by inducing sequential stiffening/destiffening of each VST segment (Figure 2.5a-iv). Thus, the device is more dexterous than the single-segmented catheter due to additional degrees of freedom obtained with two integrated VSTs. When both VSTs are in a rigid state, the workspace of the catheter consists of rotation in a circular trajectory with a diameter of 8 mm. Reducing the stiffness of the segments increases the workspace by 41 mm when the top VST is heated and by 78 mm when the bottom VST is in the soft state.

To illustrate the medical application, the catheter was inserted into a 3D printed model of a human heart (Figure 2.5b-i) made of an elastomeric material. The device was placed in the final position of the desired path (shown in blue) to reach the ablation region in one of the pulmonary veins (in red). In Figure 2.5b-i and ii, an example of an ablation location around one of the four pulmonary veins is presented. Monitoring the position of the catheter's tip can be achieved using an X-ray machine to detect a magnet on the tip and electrodes running along the catheter's length.[177]

2.4 Conclusion

We have described a method for creating tubular variable stiffness devices made of conductive shape memory polymers (CSMPs), namely, variable stiffness threads (VSTs). Our method relies on a dipping technique, which enables the fabrication of VSTs with the desired thickness and electrical resistance. The CSMP layer in the VST is nontoxic and simultaneously serves as a variable stiffness substrate, heater, and temperature sensor. Using this technique, we developed multisegmented VST catheters with integrated permanent magnets. The device demonstrated stiffness control and selective bending of each segment. Stiffness control is realized thanks to a resistance drop in the CSMP layer of up to 7.6%. In the soft state, each of the VS segments can bend up to 51°. When switched to the rigid state, the catheter can withstand applied magnetic fields up to 80 mT due to the 21× increase in the bending stiffness of VSTs. Our catheter design has the lowest wall thickness of 0.75 mm and outer diameter of 2 mm compared to existing proof-of-concept VS catheters for cardiac ablation.[27]

In addition to their application in very constrained procedures such as cardiac ablation, magnetically driven VS catheters are being used in other procedures in organs such as the stomach, lungs, and brain.[178] The scalable fabrication process of a simple three-layer VST that we presented can easily be adapted to produce catheters with various thicknesses suitable for these applications.

The VST was fabricated using nontoxic materials including polytetrafluoroethylene (PTFE), carbon particles,[151] and polyurethane-based SMP,[48] as well as PDMS, where

the latter is biocompatible.[166] However, biocompatibility of the VST is not guaranteed by using nontoxic materials in the CSMP layer and therefore further testing is required. The VST should be therefore investigated in accordance with the International Organization for Standardization (ISO) 10993 for medical devices, which include tests for factors such as irritation, sensitization, and hemolysis.[179]

The working channel inside the VST can be used for incorporating an active cooling system to enhance the reaction time, since this was already presented for variable-stiffness soft pneumatic actuators.[180] The VST sensitivity to temperature can be controlled by adapting the quantity of conductive filler.[174] The temperature of the external surface can potentially be decreased by increasing the thickness of the outer silicone layer or changing the isolation material to perfluoropolyether (PFPE), which has a lower thermal conductivity and is already used for medical applications.[143] Further interface tests between the VST and human tissue will shed light on the fouling rate and thrombi formation caused by heating of the CSMP layer. Mixing time, speed, and temperature affect the resistivity of a final conductive composite. In addition, the volume resistivity and Mooney viscosity influence the absolute stiffness and thickness of a polymer.[29,81,174–176] The robustness of the electrical and mechanical properties of CSMPs under thermal and mechanical loadings in intermediate stiffness regimes should also be investigated. The precision of the dipping technique could be improved by decreasing the viscosity of the liquid CSMP mixture. Automation of the fabrication process is another way to enhance precision. The VST could be useful not only in endoscopic devices with different mechanical and geometrical specifications but also in the development of smart fabrics that would require weaving the VSTs into a textile.[5,10,18] The stiffness and size of VSTs used in rehabilitation fabrics can be easily scaled up or down due to the simplicity of the dipping technique. We believe that the capabilities of VSTs enable their use in applications beyond medicine, where the size and weight of the system play a crucial role. Such applications include incorporation into space or flying vehicles to achieve, for example, different locomotion modes.[10]

2.5 Methods

2.5.1 Fabrication of the Variable Stiffness Thread (VST)

The fabrication of VSTs consists of three main steps: preparation of a conductive shape memory polymer (CSMP) mixture, fabrication of CSMP tubes through a dipping technique, and encapsulation of the tube. For the CSMP mixture, commercially available pellets of polyurethane (PU) SMP (MM4520, SMP Technologies) were mixed with a solvent (dimethylformamide: DMF, Sigma–Aldrich) in a weight proportion of 1 to 4 and stirred without heating for 8 h. Then, 1.2 g of carbon black powder (Nouryon, Ketjenblack EC-600JD) and 36 g of DMF were added to 30 g of homogenous SMP mixture. The mixture was then and milled together with 6 metal balls (diameters of 10 mm) where the generated shear forces break down the agglomerations of carbon black powder and disperses it homogeneously in the polymeric matrix.[181–183] A polytetrafluoroethylene (PTFE) tube with an inner diameter of 0.5 mm and an outer diameter of 0.9 mm was

dipped vertically in an already-prepared conductive mixture. Thereafter, the tube was hung vertically and cured in an oven at 80°C for an hour. The dipping process was repeated 5 times to obtain a 300 μm thickness of the CSMP layer used in the VST catheter. After completing the 5 dips, the samples were cured in an oven at 80°C for 8 h to evaporate the remaining solvent. Finally, the manufactured tube was vertically dipped in liquid polydimethylsiloxane (PDMS, Dow Corning, Sylgard 184) and cured in an oven for 30 min.

2.5.2 Reaction Force Measurement

A three-point flexural test was used to determine the SCF of the VSTs, which were placed in a universal testing machine (Instron 5965) equipped with a temperature control box. The testing machine was equipped with 3D printed acrylonitrile butadiene styrene (ABS) support parts and a rail manufactured based on the standard ISO178:2019, which defines the conditions for three-point flexural tests on universal testing systems. A rail was moved down at a constant speed of 1 mm/min until the middle point of a specimen exceeded 3mm deflection in the middle point of a thread. The tests were conducted at four temperatures of 23°C (room temperature) for the rigid state and 40°C, 60°C, and 80°C for the soft state to collect the deflection and reaction force of the VST. The raw data of reaction force against forced displacement were filtered using the infinite impulse response (IIR) filtering tool in Origin Pro 2016. A Butterworth filter with a pass frequency of 10 Hz was applied.

2.5.3 Heating and cooling times characterization

Temperature readings were sampled using a thermal camera (FLIR, E8xt) that was placed 100 mm from the VST. Three samples were collected for each of the four applied voltages 7.6, 10.7, 13.1, and 15.1 V which resulted in the applied powers of 0.5, 1, 1.5, and 2 W respectively. The VST was cooled to room temperature between each measurement and the heating profile of the VST was processed using FLIR ResearchIR Software.

2.5.4 Resistance change measurement

The VST was heated using direct Joule heat generated by a power supply (BK Precision, 9141) with a constant applied voltage. The resistance change of the VST was measured using an electric circuit consisting of a power supply, a resistor of 2.2 Kohm, and the VST connected in series. In parallel to the VST, two resistors of 8 kohm and 4 Kohm were connected. The voltage on the resistor of 4 Kohm was red using a digit multimeter (BK Precision, 5493C).

2.5.5 Cyclic Thermal Loading Measurement

The temperature of the VST was monitored with a thermal camera (FLIR, T911098) when heated through a power supply (BK Precision, 9141). The resistance was measured with a digit multimeter (BK Precision, 5493C).

2.5.6 Surface Temperature Measurement

The surface temperature was measured by placing TDK thermistors on the outer silicone layer of the VST while the temperature was increased via direct Joule heating. The VST was heated by applying 10.7 V with a power supply (BK Precision, 9141) when in air and 12.5 V when in water. Each of the applied powers resulted in a relative resistance change of 5% in the CSMP layer. The thermistor data were collected with multifunction data acquisition hardware (LabJack, U3-HV).

2.5.7 Actuation Stroke Angle Measurement

The one-segment catheter was placed in the working area of the remote magnetic navigation system CardioMag and was mounted with a holder screw to the bottom of the working area. The catheter in the rigid state was placed with the magnetic field orientation perpendicular to the permanent magnet field attitude to maximize the bending moment of the permanent magnet. At the same time, the device was placed parallel to the ground to prevent a gravitational effect on the bending performance. The catheter was deflected under an external magnetic field with a flux density from 20 mT to 80 mT. The magnetic field density and direction were controlled by regulating the currents in each of the eight electromagnets, which were placed in a hemispheric arrangement. We used three cameras and image processing in MATLAB to determine the tip angle deflection of the devices and characterize the actuation stroke angle during multiple cyclic tests.

2.6 Acknowledgments

The authors thank William Stewart and Krishna Manaswi Digumarti for their help with the manuscript and “UFAG LABORATORIEN” for their support with the cytotoxicity experiments. This work was supported by the SNSF Bridge project 20B2-1 180861 and JSPS KAKENHI Grant-in-Aid for Scientific Research on Innovative Areas “Science of Soft Robot” project (grant number 21H00324).

Chapter 3

3 Fast-response variable-stiffness magnetic catheters for minimally invasive surgery

Publication note: The work presented in this chapter is based on

Y. Piskarev, Y. Sun, M. Righi, Q. Boehler, C. Chautems, C. Fischer, B. J. Nelson, J. Shintake, and D. Floreano, *Fast-response variable-stiffness magnetic catheters for minimally invasive surgery*, in Advanced Science (accepted 22.12.2023).

3.1 Abstract

In minimally invasive surgery, such as cardiac ablation, magnetically steered catheters made of variable-stiffness materials can enable higher dexterity and higher force application to human tissue. However, the long transition time between soft and rigid states leads to a significant increase in procedure duration. Here, we describe a fast-response, multisegmented catheter for minimally invasive surgery made of variable-stiffness thread (FRVST) that encapsulates a helical cooling channel. The rapid stiffness change in the FRVST, composed of a nontoxic shape memory polymer, is achieved by an active cooling system that pumps water through the helical channel. The FRVST displays a 66 times stiffness change and a 26 times transition enhancement compared with the noncooled version. The catheter allows for selective bending of each segment up to 127° in air and up to 76° in water under an 80 mT external magnetic field. The inner working channel can be used for cooling an ablation tip during a procedure and for information exchange via the deployment of wires or surgical tools.

3.2 Introduction

Various segmented catheter and enddoscope designs made of variable-stiffness threads have been explored based on jamming technologies (fibers,[141] granules,[144] and layers[119]) and phase-change materials (alloys[27,143,184] and polymers[142,185]). In jamming technologies, the transition from soft to rigid is caused by the application of negative pressure, which causes friction between internal particles. Existing catheters based on jamming technologies display a maximum stiffness change of 50 times[119,141,144] but have a diameter between 8 and 24 mm, which is much larger than that of cardiac catheters (2.3 mm), making them unsuitable for cardiac ablation. In phase-change materials, the stiffness can be tuned by applying electrical stimulation to increase the temperature beyond the glass transition point, thus changing the state from rigid to soft or liquid.[5,10] Existing phase-change catheters display a stiffness change of 20-40 times, with a slower stiffness change (7-100 s)[27,142,185,186] than jamming-based catheters (< 1 s)[141]; however, phase-change catheters can be miniaturized down to the size of standard cardiac catheters because they do not require air pressure channels, multiple fibers, and granules.

While the stiffness transition from a rigid to soft state can be fastened by tuning the resistance of a heating element and the amount of applied heat,[185] the reverse transition from soft to rigid remains challenging for phase-changing catheters. To address this problem, in the endoscopic surgery domain, which can use catheters that are up to ten times larger than those used in heart surgery, researchers have integrated an active cooling mechanism with liquid or air into catheters consisting of thermoplastic and low-melting-point alloys.[7,26,28] Active cooling can decrease the reaction time by 8 times for catheters with a 15-17 mm external diameter and 25× stiffness change.[26,28] At the smaller scale, the preliminary study on the control strategy for endoscopic catheters of 2.5 mm external diameter showed that active cooling can decrease the reaction time by a factor of 7.[186] However, in the cardiac ablation domain, the integration of active cooling for fast stiffness transition into a variable-stiffness substrate with heaters, actuators, and a working channel without sacrificing the bending performance, remains a challenge.[187]

Here, we report a method to design and manufacture a fast-response variable-stiffness thread (FRVST) made of a nontoxic shape memory polymer (SMP) with an active cooling system, which is suitable for cardiac ablation **(Figure 3.1)**. The FRVST displays a stiffness change of 66× with a 26× faster cooling rate when the active cooling system is used. The FRVST is composed of an outer SMP tube with an encapsulated copper electrode serving as a heater to warm up the SMP tube and change its stiffness from a rigid to soft state (Figure 3.1a). A helical channel comprising fluorocarbon wire is placed inside the SMP tube to guide the water flow when active cooling is turned on. The helical channel is wound around an inner tube, which is used as the second independent cooling system to cool the tip of the catheter during ablation surgery (Figure 3.1b).

The temperature of the SMP tube increases from room temperature (25 °C) to 80 °C in 13 s via indirect Joule heating with an applied power of 2.5 W. When the applied power is turned off, it takes 115 s to naturally return to room temperature, but only 4.4 s with active cooling (0.17 L/min cooling rate), which results in a 26-fold transition enhancement (Figure 1c and Video 3.S1, Supporting Information). An FRVST segment

with a 2.3 mm diameter, 25 mm length, and 0.2 g weight can withstand a 60 g applied load in a rigid state but can undergo large deformation in a soft state at 40 °C (Figure 3.1d and Video 3.S2, Supporting Information). The FRVST exhibits a stiffness change factor (SCF) of 66 times when heated from room temperature (25 °C) to 80 °C. The FRVST is precisely fabricated by means of two automated methods: the first method is used to fabricate SMP tubes with a thickness step size of 65 μm, and the second method is used to wind fluorocarbon and copper electrodes with a 1 mm pitch size (Video 3.S3, Supporting Information).

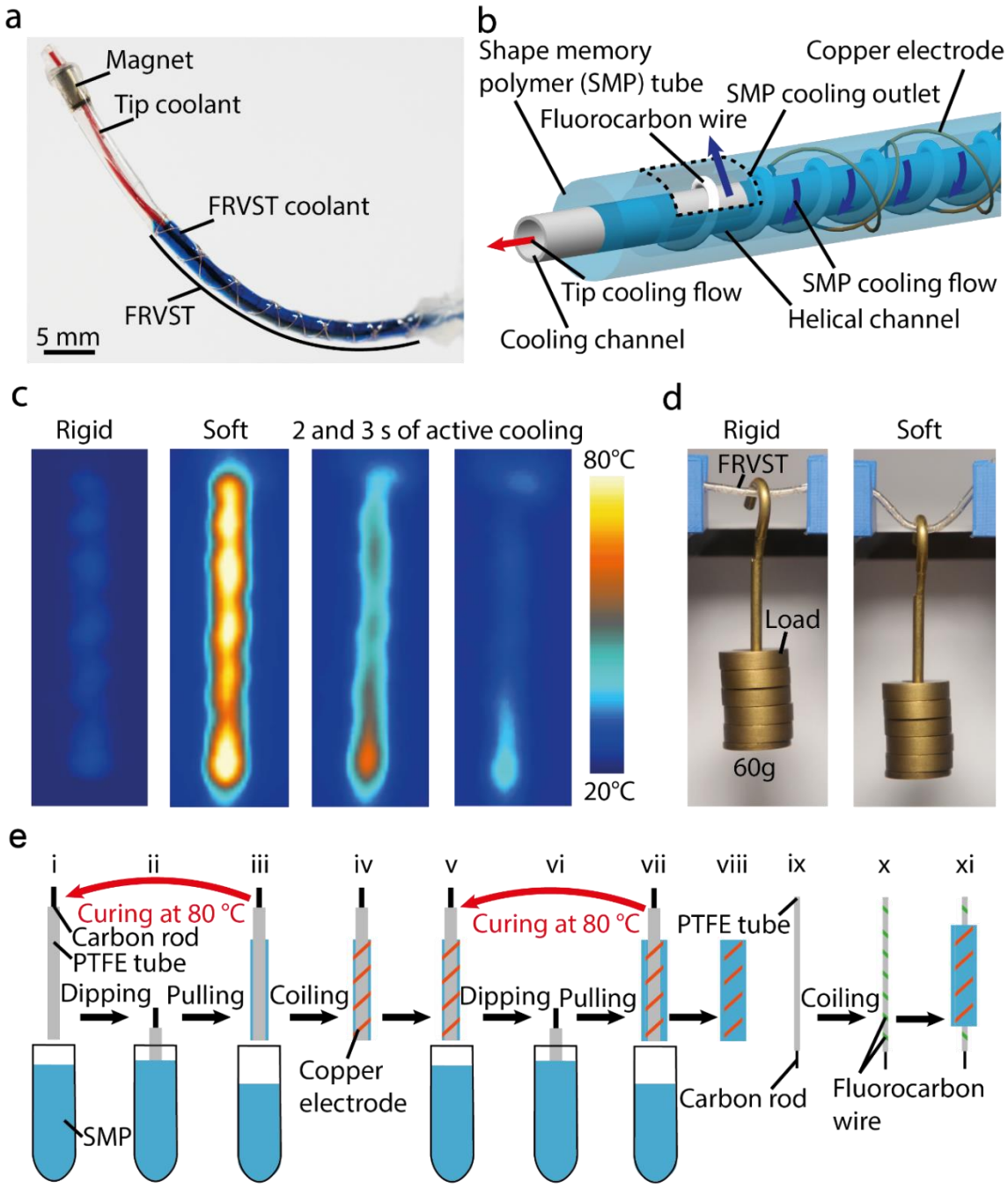

Figure 3. 1 Structure, operating principle, and fabrication process of the fast-response variable-stiffness thread (FRVST).

a) The FRVST can be integrated into a catheter for a cardiac ablation procedure. Water (in red) can be pumped through a working channel to cool down an ablation tip at the end of the catheter during surgery. Independently, water flow (in blue) can be pumped through the helical channel, enabling active cooling of the SMP layer. b) The FRVST consists of a polytetrafluoroethylene (PTFE) tube with a working channel, a helical channel made of a fluorocarbon wire, and an outer SMP tube with an encapsulated electrode used as a heater. c) The FRVST can exhibit a change in the stiffness upon indirect Joule heating of the heating electrode encapsulated into the SMP layer. d) The FRVST holds a weight of 60 g with minimal bending in the rigid state but freely bends under the same weight when heated to 80 °C in the soft state. e) The fabrication process of the FRVSTs.

We validated the proposed method through the mechanical and thermal characterization of FRVSTs integrated into a single-segment catheter. The results showed that the segment is able to bend up to 127° in air (23 °C) and up to 76° in water (36 °C) under an 80 mT external magnetic field. Then, the selective bending of a multisegmented catheter was demonstrated to achieve complicated bending curvatures in different planes. The multisegmented catheter was also tested in a 3D-printed labyrinth to demonstrate how variable stiffness can help to avoid unnecessary contact with human tissue. Finally, the multisegmented catheter was placed in a 3D phantom of a human heart underwater at body temperature to demonstrate an ablation procedure.

3.3 Results and Discussion

We first characterized the SMP so that its material properties could be incorporated into a finite element model, which guides the design of catheters by predicting the thermal and mechanical behavior. By varying the wall thickness of the SMP tube, we performed a coupled thermoelectrical FE analysis for the FRVST to determine the heating and cooling times at different wall thicknesses. Then, by varying the wall thickness of the SMP tube, we performed a coupled thermomechancal analysis for the FRVST to determine the minimal thickness, which allows high bending in the soft state and acceptable deflection in the rigid state under external magnetic field. Based on these results, we fabricated and characterized FRVSTs in terms of wall-thickness tunability, bending stiffness, heating-cooling rates, and surface temperature under different conditions. We compared the results of reaction times modelling with the empirical data to validate our model. After integrating the FRVST into a single-segment catheter, we analyzed its performance with respect to bending angle and repeatability in rigid and soft states for both air and underwater. Finally, we integrated two FRVSTs with 25 mm lengths and a tubular permanent magnet with a 4 mm length into the tip of a multisegmented catheter with a 2.3 mm external diameter and a 0.4 mm internal diameter for the working channel. This was used in our demonstration to cool down an ablation tip during the procedure and, in tandem, enable information exchange via the implementation of wire deployment or surgical tool insertion.

3.3.1 Thermomechanical Characterization of the SMP Material

The thermomechanical behavior of the SMP material, such as the stiffness change ratio and heating/cooling time, determines FRVST performance. Therefore, it is essential to assess the thermomechanical characteristics for designing FRVSTs. We characterized the behavior of SMP and then built the model to clarify the resulting performance, which was then used to design the final device For this purpose, a tensile test at different temperatures and dynamic mechanical analysis (DMA) of the SMP material were performed to determine the suitable material model, which was later incorporated into finite element simulation.

We investigated the temperature-dependent stiffness variation of the SMP by conducting uniaxial tensile tests via a tensile testing machine (Instron 5965) at a constant speed of 50 mm/min until the specimen fractured or exceeded 200% strain (**Figure 3.2a** and **Figure 3.S3** in the Supporting Information). As a result, the SMP exhibits a linear stress–strain behavior with a modulus of 3.4 GPa at a room temperature of 25 °C. The stiffness dramatically decreases to 640 and 5.6 MPa at 36 and 80 °C, respectively, followed by a modeled nonlinear stress–strain behavior (Figure 3.2b and c). These results indicate an SMP stiffness change similar to other phase-changing materials used in variable-stiffness catheters, making it a suitable candidate for this study.[27,185,186] The Yeoh model was chosen because it provides a good fit with the SMP data in the soft state and has been previously used to model polyurethane elastomers for biomedical applications (Section 3.S4 in the Supporting Information).[188,189] For our thermomechanical model, we decided to use a linear model for a rigid state (21 °C) and a Yeoh model for SMP temperatures of 36, 50, 60, and 80 °C because they provide the closest fit at these temperatures (**Figure 3.S5** in the Supporting Information).

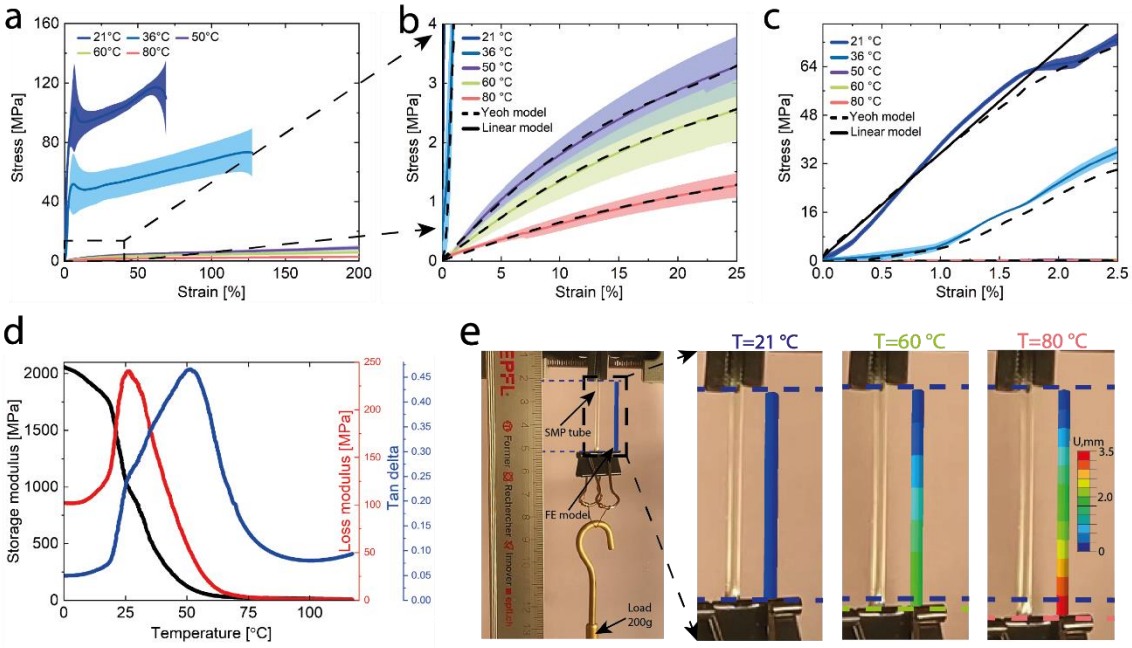

Figure 3. 2 Temperature-dependent mechanical behavior of the SMP material.
a) Stress–strain behavior of the SMP material at different temperatures. b-c) The linear and Yeoh models are well aligned with the experimental results at all temperatures. d)

The storage moduli (black), loss moduli (red), and tangent delta (blue) of the SMP as the temperature was increased from 0 to 120 °C with a ramp of 3 °C/min. e) The SMP material model verification of the displacement at different temperatures.

To determine the stiffness variation of the SMP material at different temperatures, we evaluated the thermomechanical behavior of MM5520 by performing a dynamic mechanical analysis (DMA) test by heating the sample from 0–120 °C with a ramp of 3 °C/min under tension (Figure 3.2d). The glass transition temperature (Tg) was determined as the temperature at which the tanδ (the ratio of the loss modulus (in red) to the storage modulus (in black)) curve reaches its maximum and is equal to 52 °C.[190] The increase in temperature from 0–120 °C resulted in a 200-fold decrease in stiffness. The current material reaches a tanδ pike of 0.48, which is larger than that of carbon-infused SMP (0.28).[185] As discussed for polymer–carbon nanotube interactions, the energy dissipation decreases with increasing carbon loading, leading to a decrease in the tanδ peak height.[191] The tanδ pike of the current SMP is wider than in the case of pure and carbon-infused SMPs used in soft robotics applications,[149,185] revealing higher interfacial interactions that are typical for some polyurethane (PU) polymers.[191,192] The stiffness variation and absolute values observed from the uniaxial tensile tests agree well with the results from the DMA tests.

We performed the finite-element (FE) simulation of the SMP tube using ABAQUS (V6.14, Dassault Systèmes Simulia Corp., USA) and then compared the results with an experiment (Figure 3.2e). The boundary conditions for the thermomechanical model were consistent with the experiment (Section 3.S6 in the Supporting Information). The model accurately predicts an elongation of the rigid and soft SMP tubes with a length, inner and outer diameters of 30, 0.7, and 2.2 mm under a dead load of 0.2 kg. The modeled elongations (1.9 and 3.3 mm) and experimental elongations (2 and 3.2 mm) at 60 and 80 °C were observed.

3.3.2 Fabrication Method of FRVST: Description and Characterization

The base material for our FRVSTs is a polyurethane-based SMP (SMP Technologies Inc., MM5520). We chose an SMP material because SMPs are widely used in biomedical applications such as stents, drug delivery, and bone tissue engineering[8,48,165] due to their thermoplastic properties (ability to change the stiffness under applied thermal stimuli), low cost, high recoverable strain levels (300% vs. 10% compared to other programmable materials such as shape memory alloys), and ease of manufacturing, which allows the fabrication of scalable and complex soft medical devices.[185,193,194] Compared to MM4520 used in a previous study,[185] MM5520 demonstrates excellent biocompatibility attributes defined by in vitro cytotoxicity, cytocompatibility, inflammation, thrombogenesis, and platelet adhesion tests.[193,195] All the aforementioned results were obtained within a time duration surpassing the length of a cardiac ablation procedure (284 min), making MM5520 a suitable material candidate for minimally invasive devices.[172] However, since its thermomechanical behavior is not discussed in the literature, in this study, we also perform material characterization.

The FRVST fabrication procedure starts with the formation of an SMP layer on the PTFE tube by means of our previously described dipping method (for details, see [185]). In this method, a PTFE tube with an external diameter of 1.4 mm is fixed on a carbon rod and dipped vertically into the SMP mixture. Curing in an oven induces the formation of an SMP layer on the tube (Figure 3.1e-i and ii). This dipping step can be repeated multiple times to achieve the desired thickness of the SMP layer (Figure 3.1e-iii). However, that previously described method relied on manual dipping without precise control of retraction and spin speeds of the PTFE tube with an SMP layer, resulting in poor thickness control. Here, we address the problem by developing an automated dipping setup (**Figure 3.S1** in the Supporting Information), which allows precise definition of SMP thickness by controlling the number of dips, extraction, and spin speeds.

After two dipping steps, a copper electrode wire is wound around the SMP tube using an automated winding machine (Figure 3.1e-iv and **Figure 3.S2** in the Supporting Information). This wire will be used to heat up the SMP layer during catheter operation. The wired SMP tube is then dipped again in the SMP mixture two times to encapsulate the copper electrode and attain the intended thickness (Figure 3.1e-v-vii). Finally, the fabricated SMP tube is removed from the PTFE tube (Figure 3.1e-viii) and placed aside. To form a cooling system inside the FRVST, we selected a new thin PTFE tube with an external diameter of 0.6 mm and a working channel of 0.48 mm, which matches well as a lumen for cardiac ablation catheters. Then, a fluorocarbon wire is wound around the PTFE tube to form a helical channel, which will be used as an active cooling mechanism to guide the water flow through the catheter (Figure 3.1e-ix and x).[196] As the final assembly step, the fabricated SMP tube is slipped onto a working channel tube with a helical channel (Figure 3.1e-xi).

The FRVST in this study is fabricated through an automated setup where a PTFE tube is dipped into a mixture of SMPs (Video 3.S3, Supporting Information). After extraction, the PTFE tube starts spinning to form an even layer of the SMP coating on the surface of the PTFE tube. The resulting thickness of the SMP layer depends on the number of dips and spinning speed. As shown in **Figure 3.3a**, the thickness of the SMP layer increases from 40, 50, and 90 to 355, 535, and 890 µm from the first to the eighth dip for a spin speed of 20 deg/s and dip speeds of 5, 25, and 50 mm/s, with maximum step sizes of 70, 90, and 130 µm, respectively. For spin speeds of 20, 100, and 200 deg/s, the thickness of the SMP layer increases from 90, 60, and 45 to 890, 620, and 480 µm from the first to the eighth dip at a dip speed of 50 mm/s, with maximum step sizes of 130, 75, and 65 µm, respectively (Figure 3.3b). For each experiment, the extraction speed is the same as the dipping speed. All data sets show the same behavior for all speeds, which coincides with the literature, suggesting that the thickness is highly controllable.[197] Ten times higher dip and 10 times lower spin speeds allow fabrication of a 2.5 times thicker SMP coating, which results in a 2 times higher standard deviation.

Then, we characterized the fabrication of a helical channel using an on-custom-made winding setup (Figure 3.3c and Figure 3.S2 in the Supporting Information). The generated pitch distance between two windings of a fluorocarbon wire depends on the speed ratio between the top and bottom motors of the setup. The pitch distance increases linearly from 1 to 25 mm under speed ratios from 0.2 to 5.

3.3.3 Thermomechanical Characterization of the FRVST

Before assembling a single-segment catheter, we performed thermomechanical characterization of the FRVST to ensure that its characteristics matched the requirements for cardiac catheters. We started by assessing the variable-stiffness performance of the FRVST by characterizing the bending stiffness through a three-point flexural test, where the FRVST was placed in a universal testing machine equipped with a temperature box. The test was conducted at five temperatures: 20 °C for the rigid state, and a human body temperature of 36 °C, and 40, 60, and 80 °C for the soft states. During the test, the deflection and reaction force of the FRVST were measured. The results of three measurements for three devices are plotted in Figure 3d. Based on the Euler–Bernoulli beam theory, boundary conditions, and geometrical parameters, the SCFs of the FRVST between the rigid state (20 °C) and 36, 40, 60, and 80 °C were found to be 5.6, 23.4, 45.2, and 66.1, respectively (Section 3.S7 in the Supporting Information).

We then investigated the effect of the applied power on the heating rate by measuring the temperature of the FRVST under 1, 1.5, 2, and 2.5 W (Figure 3.3e) to characterize the heating time. The FRVST can be heated in air from 25 °C (room temperature) to 80 °C in 25 and 13 s under 2 and 2.5 W, respectively. Increasing the current can shorten the heating time, but the impact is restricted since the diffusion between the heating wire and the SMP layer requires time. Moreover, further amplifying the current may lead to circuit burnout from overheating. The FRVST utilizes the helical open loop cooling system to greatly enhance the cooling speed, whereas existing VSTs for cardiac ablation devices rely on slow convection cooling.[27,142,145,185]

We measured the cooling rate of the FRVST under natural convection and different flow rates equal to 0.03, 0.08, and 0.17 L/min, which are in the same range as currently utilized for cardiac ablation surgeries.[198] The water temperature was equal to room temperature. The FRVST was heated to 80 °C under 2 W, and after reaching the desired temperature, the heat was turned off, and active cooling was turned on. Active cooling was performed using an automated syringe pump (**Figure 3.S8** in the Supporting Information). Compared with passive cooling, which requires approximately 115 s, using water coolant at 0.03, 0.08, and 0.17 L/min takes only 6.6, 6.3, and 4.4 s to decrease the temperature down to 28 °C, which improves the cooling rate by 17, 18, and 26 times, respectively (Figure 3.3f). To achieve the temperature of a human body (36 °C), it takes 46, 3, 2.65, and 1.8 s under natural conditions, and coolant rates of 0.03, 0.08, and 0.17 L/min, therefore enhancing the cooling rate by 15, 17, and 25 times, respectively.

The use of the FRVST in minimally invasive devices requires an ability to bend up to 90° without causing a change in the cross section to execute cooling at the same cooling rate. Thus, a test to measure the cooling speed at bending angles of 30, 45, 60, and 90° was performed (Figure 3.3g). The room-temperature water was pumped through the helical channel at a rate of 0.17 L/min. The FRVST cools from 80 °C to a human body temperature of 36 °C in the straight and bent configurations in 1.8 and 1.9 s, which indicates the good performance of the cooling system in the bent state.

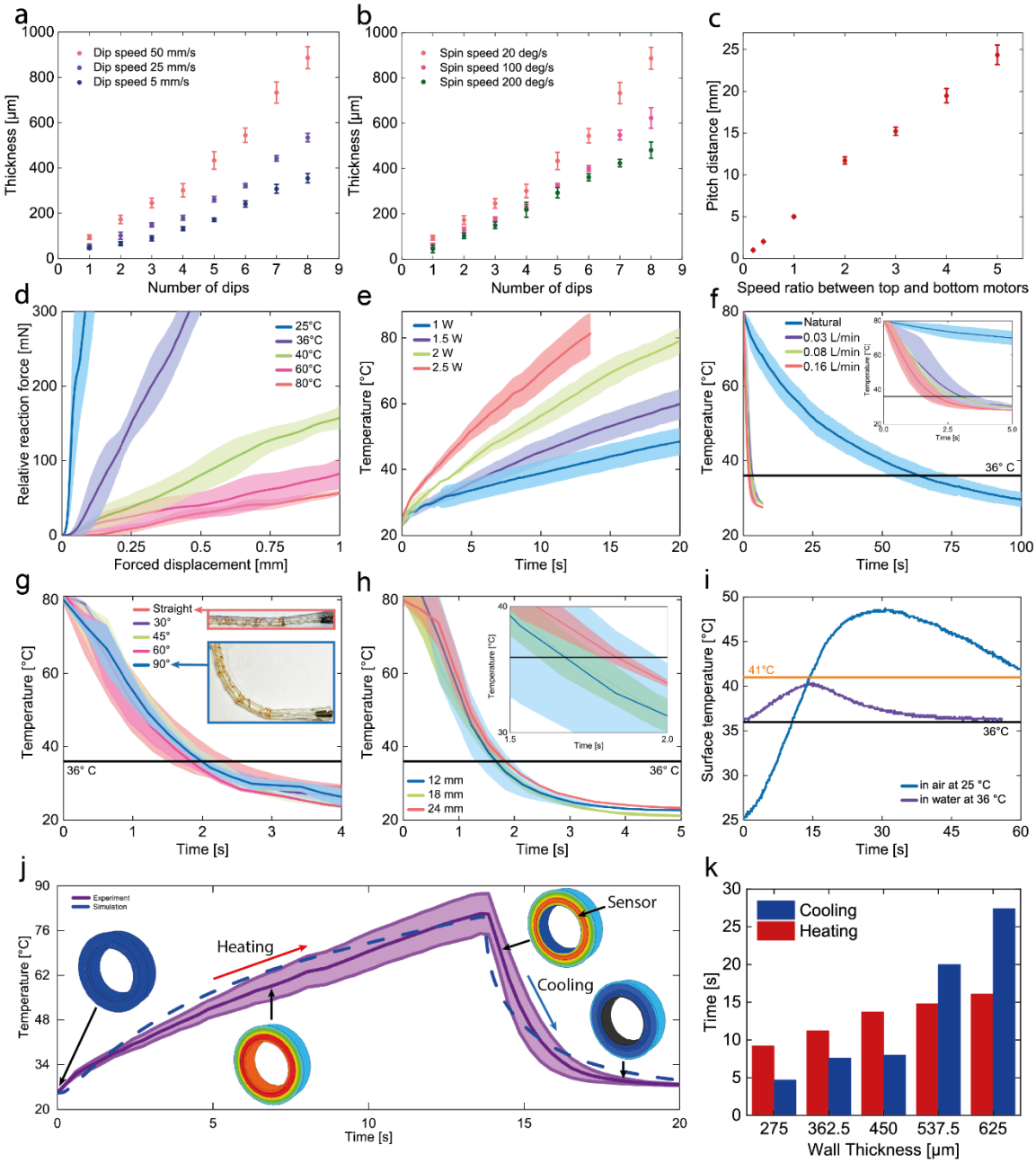

Figure 3. 3 Variable stiffness thread (FRVST) characterization.
The coating thickness of the FRVSTs was 0.45 mm. Three measurements were collected for three different samples in all the tests. a) Thickness of the shape memory polymer (SMP) layer as a function of the dip speed and number of dips. b). Thickness as a function of spin speed. c) The pitch distance between two turns of heating or fluorocarbon wires as a function of the speed ratio between the winding machine's motors. d) Reaction force of the FRVST against forced displacement under a three-point flexural test at different temperatures. e) Heating rate of the FRVST from room temperature (25 °C) for different applied powers. f) Cooling rate of the FRVST from 80 °C to room temperature for different cooling rates. g) Cooling rate of the FRVST from 80 °C to room temperature for different bending angles. h) Cooling rate of the FRVST for different cooling channel designs. i) FRVST with the SMP layer heated to 80 °C, reaching a surface temperature of 49 °C in air and 40.3 °C in water at 37 °C without flow. j) Comparison of the simulated

and measured heating-cooling cycles of the FRVST. k) Simulated heating and cooling times for the FRVST with different SMP wall thicknesses.

The dimensions of the cooling channel can be a parameter that determines the cooling rate of the FRVST. To clarify the influence of the channel dimensions, we prepared three FRVSTs with cooling channel pitch distances of 12, 18, and 24 mm. They were evaluated to clarify the effect of the helical channel on the cooling performance (Figure 3.3h). The FRVSTs with helical channel step sizes of 12 and 24 mm cool from 80 °C to a human body temperature of 36 °C in 1.65 and 1.8 s, respectively. Using a 12 mm helical channel results in a 0.15 s shorter cooling time but requires twice the length of the cooling wire, which makes the FRVST stiffer and reduces the SCF between the rigid and soft states. As a result, a 24 mm helical channel was used in the study.

When integrated in a minimally invasive device such as a catheter, the surface temperature of the FRVST must stay in a biocompatible temperature range (below 41 °C) to ensure safe operation inside the body. Thus, we determined the maximum temperature of the outer SMP layer in the soft state by characterizing the surface temperature in air at room temperature (25 °C) and in water at 36 °C without forced flow. The water temperature was set to replicate the thermal characteristics of a device in the human body, as both have comparable heat-transfer properties.[145] A thermistor was glued in the middle of the FRVST surface and was isolated against the water with a layer of glue. The surface temperature was measured by thermistors when heat was applied. In addition to the copper electrode used for heating, we wound the second copper electrode closer to the surface of the SMP layer. This electrode was used to control the stiffness of the FRVST by measuring its resistance, which changes at different temperatures of the SMP layer (**Figure 3.S9** in the Supporting Information). The use of a copper wire as a sensor was already utilized to control the state of phase-change materials with a precision of 0.2 °C.[142,143]

First, the FRVST was heated to 80 °C in air with an applied power of 2 W (applied voltage 2 V). The temperature was controlled using a thermal camera and by monitoring the resistance change in the sensing wire (**Figure 3.S9** in the Supporting Information). When submerged in water, the applied power was 4.5 W, which corresponds to an applied voltage of 3 V. The power was turned off when a sensing wire relative resistance change of 20% was achieved (Figure 3.3i). This value corresponds to the resistance change of the sensing wire when the SMP body is heated to 80 °C. The surface temperature of the FRVST reached 49 °C in air and 40.3 °C in water when the SMP body was heated to 80 °C. These results indicate that the FRVST can be operated under a biocompatible temperature range of 41 °C.[55] During minimally invasive surgery, the FRVST will be exposed to fluid flow, which increases the heat dissipation and lowers the surface temperature even more. The surface temperature differs from the FRVST body temperature because of the well-studied thermal gradient caused by the heating system and the environment.[143] The encapsulation of the FRVST consists of an SMP material, whose thermal conductivity of 210 W/mm*K is one order of magnitude lower than that of silicone with a thermal conductivity of 2730 W/mm*K used in previous studies.[27]

The FRVST stiffness change factor can be tuned by changing the thickness of the SMP layer. Thus, we performed a thermal-electrical simulation of the heating-cooling cycle using ABAQUS to later understand how the heating and cooling durations are affected by the increase in layer thickness (Section 3.S7 in the Supporting Information). The information regarding the material properties of the SMP is limited; thus, we determined the material constants of the SMP needed for the simulation, including density, specific heat capacity, thermal conductivity, and electrical conductivity (Section 3.S10,12 and **Figure 3.S11** in the Supporting Information). The simulated and measured temperature–time relationships during a heating-cooling cycle showed a good fit (Figure 3.3j). The measured heating-cooling cycle was performed under 2.5 W of power in the heating phase and under a cooling rate of 0.17 L/min in the cooling phase. With the help of this verified model, additional projections were made about the heating and cooling process of the FRVST when the thickness of its SMP layer varies (Figure 3.3k). If the thickness of the SMP layer increases from 0.275 to 0.625 mm, then the duration of heating increases from 9 to 16 s, and the duration of cooling increases from 4.7 to 27.4 s. Later in the paper, a trade-off between reaction times and bending stiffness in the rigid and soft states at different SMP layer thicknesses is discussed.

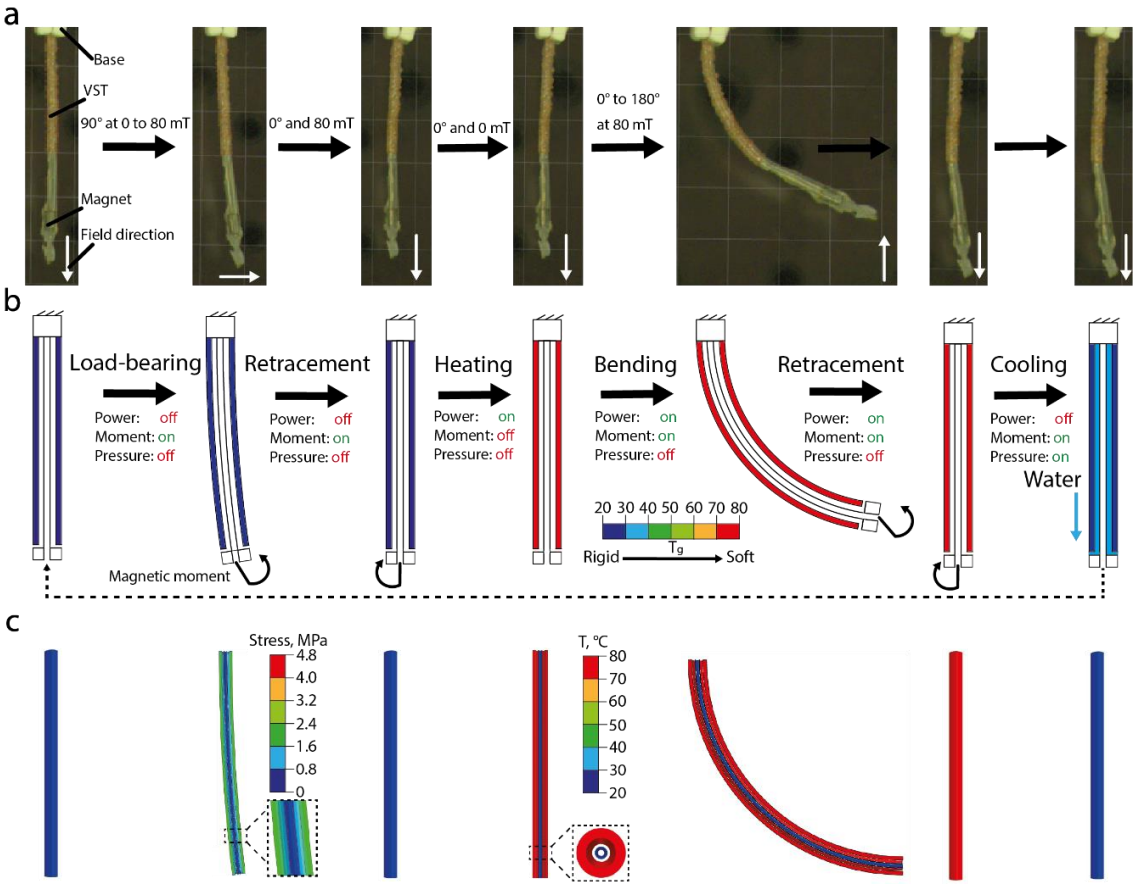

Figure 3. 4 Working principle of the single-segment catheter with the variable-stiffness thread (FRVST).
a) Images of the working cycle under an applied external magnetic field. b) Working principle of the standard working cycle of the single-segment catheter. The catheter can withstand an applied magnetic moment in the rigid state during the load-bearing phase.

In the soft state, it bends when the magnetic field is applied. c) FE simulation results in a typical working cycle. The boundary conditions for the simulation are the same as in the experiment.

A working principle of the single-segment FRVST catheter is illustrated in Figure 3.4b. In the rigid state, when power is not applied, the catheter can withstand an applied magnetic torque generated by an external magnetic field from 0 to 80 mT. When the power is applied and the SMP layer becomes soft, the catheter can be freely bent in the direction dictated by the magnetic torque from 0 to 180° at 80 mT. Once the shape of the catheter is fixed, the cooling system is turned on, and the SMP layer becomes rigid. To further investigate the actuation capabilities of the single-segment catheter in the rigid and soft states, we performed an FE simulation by implementing the Yeoh hyperelastic model into the SMP layer of the catheter. (Section 3.S6 in the Supporting Information). Figure 3.4c depicts that the FE simulation accurately matches the experiment. During the loading-carrying stage, both the experiment and simulation show a small catheter deformation. Furthermore, the simulation indicates that the SMP layer bears the majority of the load and that there is negligible stress on the soft section of the catheter.

3.3.4 Characterization of a Single-Segment FRVST Catheter

After characterizing the FRVST, we integrated it into the single-segment catheter, the design and working cycle of which are illustrated in **Figure 3.4a**. It consists of an FRVST attached to a base on the top end and is equipped with a tubular permanent magnet with a 4 mm length and 2 mm external diameter at the tip. The catheter has a 55 mm length, a 2.3 mm outer diameter, and a 0.48 mm working channel. The permanent magnet is inserted and glued inside the SMP tube. The working channel passes through the lumen inside the cylindrical magnet and can be used to deliver coolant to the tip of the catheter, for example, during an ablation procedure. The active cooling system of the SMP layer, cooling system of the tip, heating, and sensing wires are plugged into the power supply and multimeter at the base to deliver power and control the state of the SMP layer. The catheter was designed with the same size as existing cardiac ablation catheters.[196]

We evaluated how well a single segment of a FRVST catheter performs by examining its bending angle in both the soft and rigid states in the air and water when exposed to external magnetic fields by a hospital-compliant electromagnetic navigation system (eMNS). The bending angle in the soft state determines how flexible the catheter is, affecting its dexterity. Conversely, in the FRVST rigid state, the bending angle determines the magnetic torque that the catheter can resist, thereby determining the level of shape fixity that can be achieved. A permanent magnet with a dipole moment m at position p under external magnetic field B generates a magnetic torque T_m equal to $T_m(p) = m \times B(p)$.[185] When the magnetic field is perpendicular to the dipole moment, the maximum magnetic torque is attained, while the torque is minimal when they are aligned. However, selecting permanent magnets with higher dipole moments or different volumes allows for the magnetic torque to be adjusted. First, we characterized the deflection of a single-segmented catheter in a soft state by varying the magnetic field

angle from 0 to 180° in air at 20 °C and water at a human body temperature of 36 °C (**Figure 3.5a**). The catheter can bend up to 127° and 76° in the air and water under a magnetic field magnitude of 80 mT. In the rigid state, the catheter can withstand the applied magnetic moment of 80 mT perpendicular to the catheter direction and bend only up to 3.3° and 19° in the air and water, respectively (Figure 3.5b). Note that the values in Figure 5a andb represent three tested catheters and three cycles per device. In the soft state, the device also demonstrates high repeatability with a low hysteresis for five cycles in both air and water (Figure 3.5c).

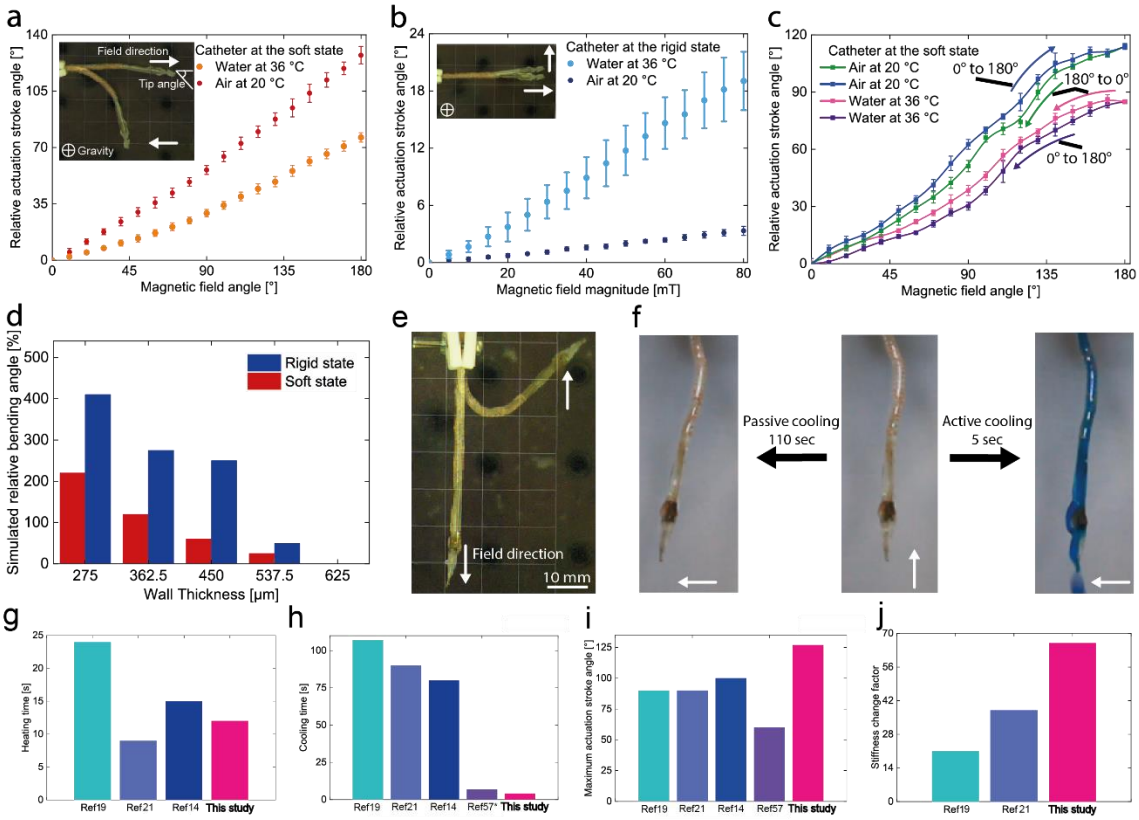

Figure 3. 5 Characterization results of the single-segment catheter with a variable stiffness thread (FRVST).
a) Actuation stroke angle as a function of the magnetic field angle in the soft state. b) Actuation stroke angle as a function of the magnetic field magnitude in the rigid state. c) Actuation stroke angle as a function of the magnetic field angle in the soft state. The values represent three tested catheters and five cycles per device. d) Simulated actuation stroke angle as a function of the SMP wall thickness in the rigid and soft states. e) Bending actuation of the FRVST single-segment catheter in the soft state. f) Demonstration of the active cooling of the single-segment catheter. g-j) Comparison of heating-cooling times, maximum actuation stroke angle, and stiffness change factor with relevant works in the literature.

We used the FE thermomechanical model discussed previously to investigate the influences of the SMP layer thickness on the resulting bending performance in the rigid and soft states in air (Figure 3.5d). The simulated results indicate that by decreasing the

SMP layer thickness from 0.625 to 0.275 mm, an increase of four and two times in the bending angle in the rigid and soft states can be achieved. Therefore, reducing the catheter's wall thickness from 0.625 mm to 0.275 mm results in a heating-cooling cycle that is 2.6 times faster but comes at the cost of a 4 times decrease in load-bearing capabilities.

The catheter can bend up to 130° in the desired direction in the soft state under 80 mT (Figure .5e). We demonstrated the soft-to-stiff state transition by cooling down the catheter with and without active cooling while the catheter was rotated by applying a rotated magnetic field from 0 to 180°. The catheter changes the state from soft to rigid in 110 and 5 s with passive and active cooling (Figure 3.5f). The motion and stiffness change rate of the device can be observed in Video 3.S4, Supporting Information. Compared with other variable-stiffness catheters with passive cooling in the literature, our catheter has a comparable heating rate, 20× faster cooling rate from 80 down to 25°C, 30° larger actuation stroke angle, and, at the same time, 1.7× higher SCF (Figure 3.5g-j).[27,142,145] Compared with the smallest endoscopic variable stiffness catheter with active cooling system, our catheter has a 2× larger actuation stroke angle and 7× faster cooling rate from 51 down to 37°C.[186] Moreover, multiple FRVSTs can be integrated into the same catheter body to achieve more dexterous positioning of the catheter's tip.

3.3.5 Multisegmented Catheter for Cardiac Ablation

Using the previously described method and materials, we developed a multisegmented catheter with two independently controlled segments and demonstrated its use for cardiac ablation in a 3D-printed model of the human heart at body temperature (**Figure 3.6**). The catheter consists of a permanent magnet at the tip, a working channel, which can be used to cool an ablation tip during the surgery, and two heating coils that can independently heat a part of the FRVST (Figures 3.1 and 3.6a). Each of the heating coils covers 25 mm of the FRVST length with a total length of 75 mm. The device structure was encapsulated by dipping it into the SMP material.

The catheter was first placed in an aquarium in the middle of the eMNS working area. The magnetic field was applied perpendicular to the length of the catheter to demonstrate the deflection of the tip in the rigid state (Figure 3.6a-i). Then, the FRVST was locally heated by applying power to one of two heating coils and bent to realize catheter deflection. The selective activation of heating coils of the FRVST enables different deformations of the multisegmented catheter (Figure 3.6a-ii and iii). Each of the segments of the catheter can be flexed up to an angle of 90 degrees, while the second segment can resist an applied magnetic torque (Video 3.S5, Supporting Information). The catheter is capable of producing complex curvatures in different planes by inducing sequential stiffening and softening of individual segments (Figure 3.6a-iv). Consequently, the catheter is endowed with greater dexterity than a single-segment catheter, owing to the additional degrees of freedom afforded by the integration of two heaters in the FRVST. When both segments are in a rigid state, the workspace of the catheter consists of a circular trajectory with a diameter of 7 mm. Reduced stiffening of the segments increases

the workspace by 28 mm when the heater closer to the permanent magnet is heated and by 42 mm when the bottom heater closer to the base is activated.

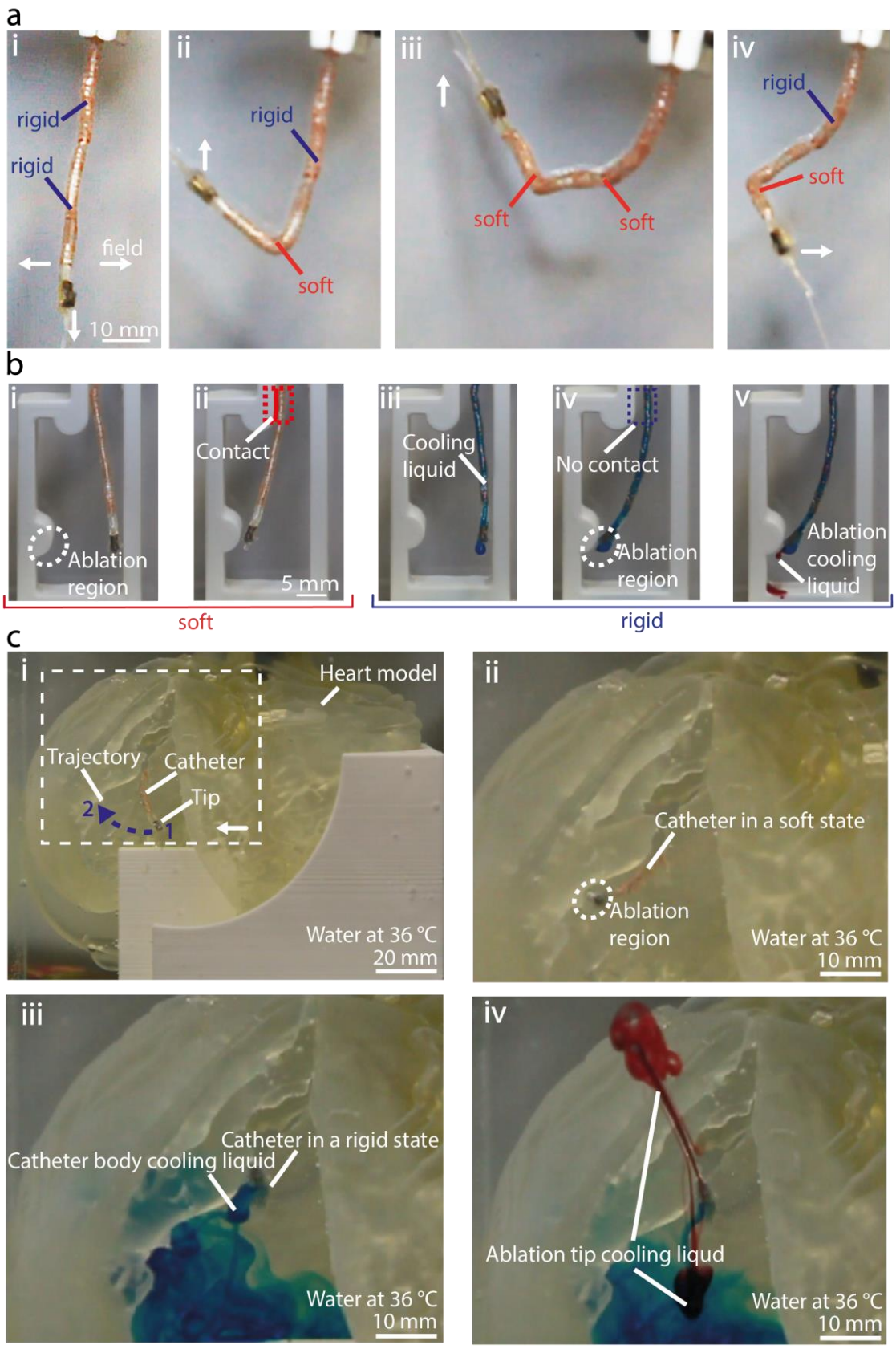

Figure 3. 6 Multisegmented catheter design, performance, and application.

a) The catheter consists of a variable-stiffness thread (FRVST) with two heating coils winded in series, allowing an independent stiffness change in two segments from the same FRVST. The catheter is placed in an electromagnetic navigation system (eMNS) i) when both FRVSTs are solid and ii–iv) when one of them is successively soft. b) A demonstration of the variable-stiffness capabilities of the multisegmented catheter. i) The catheter can be navigated to a specific ablation point by an external magnetic field. ii) In the soft state, it cannot hold the shape and avoid physical contact. iii) After cooling, iv) the stiff catheter can be accurately navigated to a specific region without applying any pressure on other regions. v) The working channel can be used to cool an ablation tool independently from the cooling of the FRVST. c) A demonstration of catheter application in the cardiac ablation procedure. The demonstration is performed underwater on a 3D phantom of the human heart placed in an eMNS. i) The catheter is magnetically steered from the point 1 to the point 2. ii) After reaching the ablation region, iii) blue cooling liquid is pumped through the helical channel to cool down the segments and lock the shape of the catheter. iv) Then, the red cooling liquid is pumped through the working channel to demonstrate the cooling process at the interface between the ablation tip and human tissue.

To illustrate the potential use case of the catheter in medical applications, the 3D-printed labyrinth was placed in the aquarium under the catheter (Figure 3.6b). In the soft state, the catheter cannot avoid contact with the channel walls while being steered to the potential ablation region (Figure 3.6b-i and ii). This contact causes frictional forces by the catheter on the blood vessel wall, which can lead to vasoconstriction, injury, and complications such as reactive intimal proliferation or distal embolization, potentially resulting in end-organ ischemia and infarction.[199,200] However, by changing the state of the top segment from soft to rigid through active cooling (blue liquid), an ablation region can be achieved without any contact with the channel walls (Figure 3.6b-iii and iv). The catheter remains in its position while the demonstration of an ablation procedure is shown with the red ablation cooling liquid (Figure 3.6b-v and Video 3.S6, Supporting Information).

Finally, to demonstrate the catheter's navigation capability in reaching ablation target regions within the heart chambers, it was guided through a 3D-printed model of a human heart submerged underwater at body temperature (Figure 3.6c-i and Video 3.S7, Supporting Information). The device was placed in the left ventricle and then steered, being in the soft state, from the initial point 1 to the final point 2 to the ablation region as it is done during a real surgery (Figure 3.6c-i,ii).[201]

The FRVST inside the catheter was cooled to lock the shape by pumping cooling liquid (in blue) through the helical channel (Figure 3.6c-iii). Finally, we demonstrated the use of a working channel to pump coolant (in red) to lower the temperature at the interface between the human tissue and the ablation tip (Figure 3.6c-iv). The motion of the multisegmented catheter in a 3D-printed model of the human heart can be observed in Supplementary Video 3.S7

3.4 Conclusion

We have described a method for designing fast-response and stiffness-tunable variable-stiffness devices made of shape memory polymers (SMPs), namely, variable-stiffness threads (FRVSTs). When heated from 25 to 80 °C, the current design can provide a 66× stiffness change. We integrated a helical channel in the FRVST design that enables open irrigated active cooling of the nontoxic SMP layer, which decreases cooling times by 26× from the soft to the rigid state compared to passive cooling. We performed material characterization of the SMP and developed an FE thermomechanical model to discuss the trade-offs among cooling/heating rates, bending performance, and SMP wall thickness. Fabrication of the FRVST utilizes a dipping and winding technique to produce SMP layers and helical channels with a predetermined thickness and pitch distance, respectively. Using this technique, we developed single-segment and multisegmented FRVST catheters with integrated permanent magnets. We demonstrated selective bending of each of the segments by controlling the stiffness of each of the segments in the hospital-compliant electromagnetic navigation system (eMNS). In the soft state, the catheter can bend up to 127° and 76° in air and water under a magnetic field magnitude of 80 mT. When switched to the rigid state, the catheter can withstand applied magnetic fields up to 80 mT and bend only up to 3.3° and 19° in the air and water. An integrated active cooling mechanism allows the shortening of the stiffening process from 117 to 4.4 s. Our catheter design has a 7× faster cooling rate, 30° larger actuation stroke angle, and 1.7× higher stiffness change factor (SCF) compared to existing proof-of-concept multisegmented variable stiffness catheters for cardiac ablation.

While variable-stiffness catheters with previous designs can simplify tip positioning and increase applied force,[27,143] they may also prolong the procedure duration because of a long 90-second heating-cooling cycle.[185] The current design with a heating-cooling cycle of 17 s can significantly decrease the duration of surgery, making variable-stiffness catheters more feasible for practical use.

In addition to its potential utility in minimally invasive devices across various medical procedures, the FRVST holds promise for incorporation into smart fabrics, where it could be woven into textiles.[18] Compared to previously developed phase change material-based variable-stiffness threads, our FRVST can change its state faster without limiting the motion of the user.[5,6] Another potential application is flying vehicles, where the rapid state change in our FRVSTs can enable faster morphing between different locomotion modes.[10]

3.5 Methods

3.5.1 Tensile Test Sample Fabrication

The SMP mixture was prepared by dissolving 10 g of pellets of a shape memory polyurethane (SMP Technologies, MM 5520) in 60 g dimethylformamide (DMF) for 8 h via a magnetic stirrer at 60 °C. The SMP mixture was poured onto a glass substrate on an

automated film applicator coater (ZAA 2000-Zehntner-Automatic film applicator). The thickness of the gap height of the applicator was adjusted to 700 µm, and the mixture was spread at a drawing speed of 2 mm/s. Afterward, the SMP mixture on the glass substrate was placed in an oven for a minimum of 8 h at 80 °C to evaporate excess DMF. The same procedure was followed for the second and third layers of the SMP with an increase in the gap height by 50 µm at every step to account for the thickness of the previous layer. The sheet was delaminated from the glass substrate using a sharp razor blade. The specimens were then cut from the SMP sheet according to ISO standard 527-3 for the determination of tensile properties of plastic films and sheets (Figure 3.S3 in the Supporting Information).

3.5.2 Tensile Test of the SMP Samples

Tensile tests were conducted to obtain the stress–strain relationships of the SMP at room temperature (25 °C), human body temperature (36 °C), 50, 60, and 80 °C. A tensile testing machine (Instron 5965) equipped with a 500 N load cell and a thermal chamber was used. A sample with a dog-bone shape and a thickness of 0.15 mm was moved at a constant speed of 50 mm/min until the specimen fractured or exceeded 200% strain (Figure 3.S3a). The collected load and elongation data were converted to a stress–strain curve to obtain Young's modulus by applying a linear or Yeoh model. The elongation and width changes before and after the tensile test were measured using a caliper and micrometer to determine the Poisson's ratio µ of the SMP using the following formula for large deformations:

$$-\frac{h_{final}-h_0}{h_0}=1-\left(1+\frac{l_{final}-l_0}{l_0}\right)^{-\nu} \qquad (S1)$$

where h_0, h_{final}, l_0, and l_{final} are the initial, final width, initial, and final length of the dog-bone sample, respectively. The determined Poisson's ratio ν of the SMP is equal to 0.48. Thus, the material was modeled as incompressible.

3.5.3 Dynamic Mechanical analysis (DMA) of the SMP Material

The DMA test for the SMP MM5520 was performed in the tension film mode on three strip samples (dimension 30 mm × 5 mm × 0.2 mm) fabricated via the layer deposition technique with a dynamic mechanical analyzer (TA Instruments DMA Q800). The sample was heated from 0–120 °C with a ramp of 3 °C/min under tension. Initially, the sample was cooled to 0 °C and stabilized for 5 min to reach thermal equilibrium. The strain oscillated at a frequency of 1 Hz with a peak-to-peak amplitude of 0.2% of strain.

3.5.4 Helical Channel Design Characterization using an On-Custom-Made Winding Machine

An on-custom-made winding machine consists of two step motors located along the same axis with drilling chucks at each of the tips serving as grippers (Figure 3.S2 in the Supporting Information). An SMP or PTFE tube was inserted between the motors and held by chucks in the horizontal position. The motors provide rotation of the tube. A coil with a winded wire (a copper or a fluorocarbon wire) stays on the linear stage, which is located under the motors. The linear stage provides movement of the coil along the length of the held SMP or PTFE tube. The control of step motors and the linear stage was performed using an Arduino Uno and step motor drivers in the control box. The rotation speed of the top step motors was fixed. The linear speed of the linear stage varied to provide a different pitch of the helical channel. Thus, the speed ratio between the two top motors and the bottom motor of a linear stage varied in the experiment. The experiment was conducted three times for three SMP tubes under speed ratio coefficients of 0.2, 0.4, 1, 2, 3, 4, and 5.

3.5.5 Automated Dipping Setup Design

The automated dipping setup has three degrees of freedom: one degree in translation to perform the dipping motion, and two degrees in rotation to perform the operations to tilt and spin the forming tool (Figure 3.S1 in the Supporting Information). The tilt degree of freedom was not used in this study. The setup consists of a translation stage (with a stepper motor Nema-17) and two stepper motors (Sanyo Denki, 103H5208-5210). System control was performed by using an Arduino Uno R3 microcontroller and three motor drivers (MotionKing, 2L415B). 3D-printed elements were used to connect parts with each other. Donau drilling chucks were used to hold the carbon rods with PTFE tubes while dipping.

3.5.6 Fabrication of the Variable-Stiffness Thread (FRVST)

The fabrication of FRVSTs began with the preparation of a shape memory polymer (SMP) mixture using commercially available pellets of polyurethane (PU) polymer (MM5520, SMP Technologies). Pellets were dissolved in a solvent (dimethylformamide: DMF, Sigma–Aldrich) in a weight proportion of 1 to 6 and stirred at 50 °C for 8 h. A polytetrafluoroethylene (PTFE) tube with an inner diameter of 1 mm and an outer diameter of 1.4 mm was dipped vertically in an already prepared SMP mixture using an on-custom-made dipping setup. Thereafter, the tube was hung vertically and cured in an oven at 80 °C for an hour. The dipping process was repeated one more time to obtain a 66 μm thick SMP layer. Then, a heating wire made of copper with a 0.1 mm diameter was wound around the SMP tube using an automated on-custom-made winding machine with a pitch distance of 1 mm. Afterward, the SMP tube with a heating wire was dipped 5 more times in the SMP mixture and cured in the oven. The sensing copper wire with a

0.052 mm thickness was wound around with a pitch distance of 1 mm. In the last fabrication step of the SMP tube, it was dipped into the SMP mixture to encapsulate the structure and achieve an external diameter of 2.3 mm. In parallel with SMP tube fabrication, a fluorocarbon wire with a 0.4 mm diameter was wound around the inner PTFE tube with a working channel and external diameters of 0.48 and 0.6 mm, respectively. The pitch distance in the cooling channel was 24 mm. Finally, the working channel with a helical channel was inserted into the SMP tube and glued from both sides. The silicone pipes were glued to the bottom part of the FRVST to provide cooling to the SMP layer and working channel.

3.5.7 Three-Point Flexural Test of the FRVST

To determine the SCF of the FRVSTs, a three-point flexural test was conducted using a universal testing machine (Instron 5965) that had a temperature control box. The machine was equipped with 3D printed support parts made of acrylonitrile butadiene styrene (ABS) and a rail designed according to the ISO178:2019 standard that outlines the conditions for three-point flexural tests on universal testing systems. A rail was moved down at a constant speed of 1 mm/min until the middle point of a specimen exceeded 3mm deflection in the middle point of a thread. The tests were performed at five temperatures, that is, 25 °C (room temperature) for the rigid state and 36, 40, 60, and 80 °C for the soft state, to obtain the deflection and reaction force of the FRVST. The raw data obtained from the reaction force against forced displacement were filtered using the Origin Pro 2016 infinite impulse response (IIR) filtering tool. A Butterworth filter with a pass frequency of 400 Hz was used for filtering.

3.5.8 Characterization of the Heating and Cooling Times

For the characterization of the heating time, temperature readings were sampled using a thermal camera (FLIR, E8xt) that was placed 150 mm from the FRVST. Three samples with an SMP wall thickness of 0.45 mm were tested for each of the four applied voltages of 1.3, 1.7, 2, and 2.4 V, which resulted in applied powers of 1, 1.5, 2, and 2.5 W, respectively. The FRVST was cooled to room temperature between each measurement, and the heating profile of the FRVST was processed using FLIR ResearchIR software. For the characterization of the cooling time, the FRVST was heated to 80 °C at 2 W. After reaching the desired temperature, the heat was turned off, and active cooling was turned on. Active cooling was performed using an automated syringe pump (**Figure 3.S7** in the Supporting Information) under natural conditions (passive cooling) and three different rates equal to 0.03, 0.08, and 0.17 L/min. All the cooling rates inside the FRVST were calculated using the parameters of the syringe pump, continuity law, and volume rate flow. For the cooling time characterization at different bending angles, the device was held in metallic grippers throughout the test.

3.5.9 Surface Temperature Measurement

The surface temperature was measured using a previously presented method[145,185] by placing a TDK thermistor on the outer SMP surface while the temperature of the FRVST body was increased via indirect Joule heating. The FRVST was heated by applying 2 W with a power supply (BK Precision, 9141) when in air and 4.5 W when in water. The current was set to 1.5 A. Each of the applied powers resulted in a relative resistance change of 20% in the sensing wire. The sensing wire data were monitored with a digital multimeter (BK Precision, 5493C). The thermistor data were collected with data acquisition hardware (LabJack, U3-HV).

3.5.10 Actuation Stroke Angle Characterization of the Single-Segment Catheter

The single-segment catheter was placed in the transparent aquarium in the working area of the electromagnetic navigation system (eMNS) CardioMag.[202] The magnitude and direction of the magnetic field were controlled by adjusting the currents in the eight electromagnets, which were arranged in a hemispheric arrangement. The catheter was mounted with a 3D-printed holder to the upper edge of the aquarium. For the actuation stroke angle measurement, to avoid any impact from gravity on device flexibility, the device was positioned parallel to the ground. In the rigid state, to maximize the bending moment of the permanent magnet, the catheter was positioned perpendicular to the attitude of the external magnetic field with a flux density from 0 mT to 80 mT with a step size of 5 mT. In the soft state, the external magnetic field magnitude was fixed to 80 mT, and the direction was changed from 0 to 180° with a step size of 10°. The time step for the flux density or magnetic field direction was set to 3 s. An experiment was repeated three times for three single-segment catheters in air and water. Three cameras were used to collect the actuation stroke angle videos, and then the video was processed to determine the tip angle deflection of the catheters.

3.5.11 Reaction Time Demonstration of the Single-Segment Catheter

For the reaction time demonstration, the single-segment catheter was placed upside down inside the aquarium in the middle of the working area of the eMNS. A repeatable magnetic field with a magnitude of 80 mT and shifting direction from 0 to 180° was applied.

3.5.12 Multisegmented Catheter Demonstration

For the demonstration scenarios, the multisegmented catheter was placed upside down inside the aquarium in the middle of the working area of the eMNS. Each of the segments was stiffened and softened to demonstrate bending in different planes. A labyrinth

demonstration was performed under the same conditions. Then, the aquarium was filled with human body temperature water. The water state was controlled with a thermometer. The catheter was inserted inside the 3D-printed phantom of the human heart and omitted in water (**Figure 3.S13** in the Supporting Information). The heart is held in the 3D-printed support. Blue and red waters were used to cool down the SMP layer and demonstrate the ablation procedure, respectively.

3.6 Acknowledgments

The authors thank Yann Lavanchy from the Polymers Laboratory at EPFL for help with the specific heat capacity determination. The authors thank Looten Alexandre Achille, Varanges Vincent Marc, and Prof. Michaud Véronique from Processing of Advanced Composites (LPAC) for help with the dynamic mechanical analysis. The authors thank Dr. Shunichi Hayashi from SMP Technologies for providing the SMP material and elaboration on the thermal properties. The authors thank SCITAS team for their expertise and help with High Performance Computing for Abaqus simulations. The authors express their gratitude to Wawrinka Djanaée and Titouan Veuillet who contributed by capturing photographs of final devices. The authors thank Benjamin Jarvis for the manuscript correction.

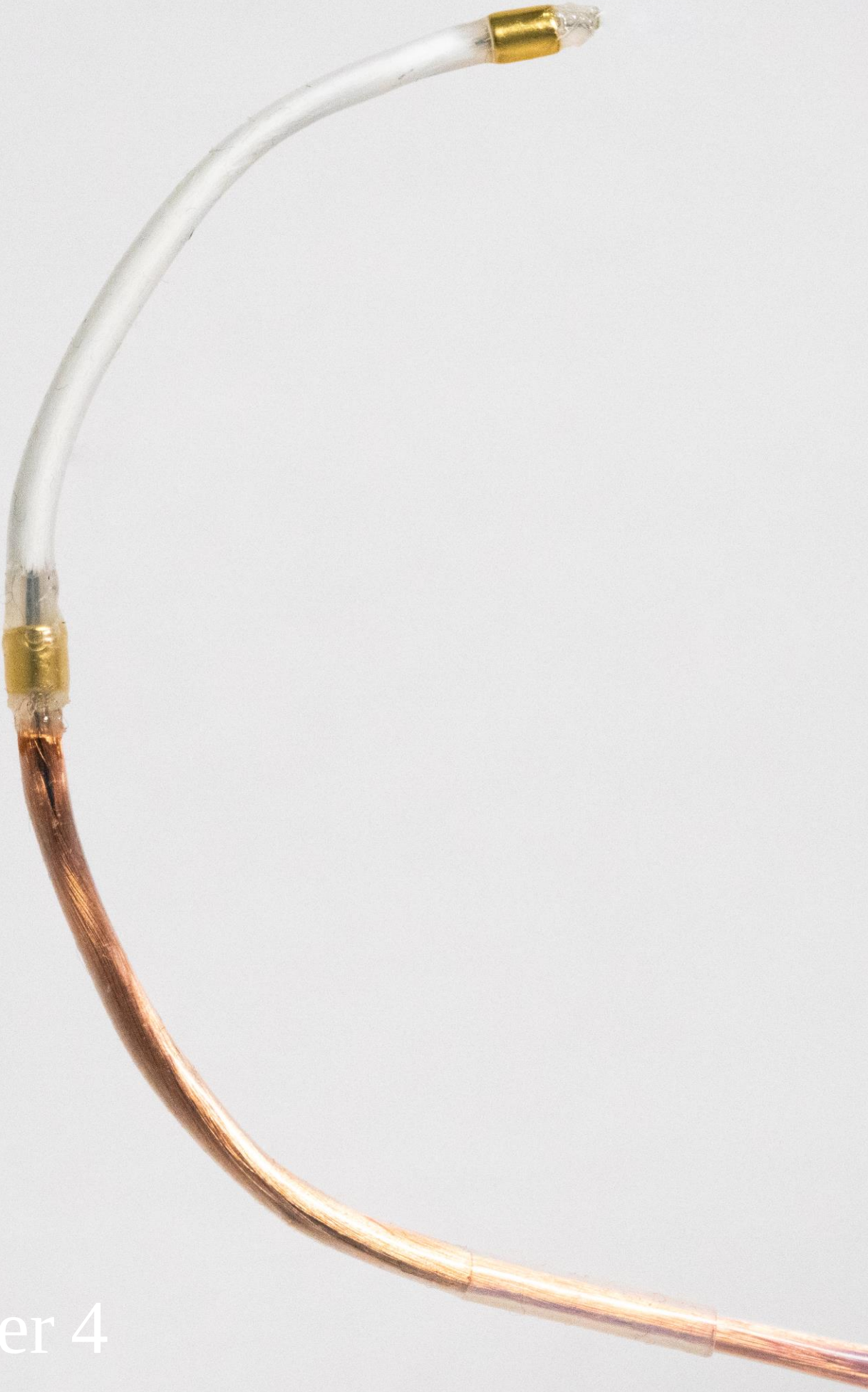

Chapter 4

4 Instant Variable Stiffness in Cardiovascular Catheters Based on Fiber Jamming

Publication note: The work presented in this chapter is based on

Y. Sun, **Y. Piskarev**, E. H. Hofstetter, C. Fischer, Q. Boehler, B. J. Nelson, and D. Floreano, *Instant Variable Stiffness in Cardiovascular Catheters Based on Fiber Jamming,* in Science Advances (under major revision).

4.1 Abstract

Variable stiffness (VS) has revolutionized miniature surgical instruments, including cardiovascular catheters for minimally invasive surgeries (MISs), enabling advanced capabilities in stiffness modulation, multi-curvature bending, and force control. However, existing VS catheters are made of phase-changing materials with slow softening and stiffening rates (up to 90 seconds) that can lead to significant increase in surgery duration. To address the slow stiffness change, we propose a novel VS catheter based on fiber jamming (FJ) that achieves instant stiffness changes (within 300ms), enabling seamless catheter operations without delays. Moreover, our catheter, incorporating hundreds of ultrathin fibers into a slender 2.3mm catheter body, achieves up to 6.5-fold stiffness changes. With adequate stiffness change, a two-segment catheter is fabricated and

achieves complex bending profiles within seconds and smooth manipulation in a simulated surgical scenario. In addition, the FJ-based design does not require electric currents or heating inside the human body, thus minimizing patient risks. This FJ-based VS catheter, with instantaneous response, adequate stiffness change and enhanced safety, can potentially establish new benchmarks in MIS, allowing medical practitioners to effectively address formidable diseases.

4.2 Introduction

Despite the high stiffness change factors (SCFs) of phase-changing-based devices including the catheters developed in Chapter 2 and 3, their complete stiffness change cycle from the rigid to soft state and vice versa can take up to 5 minutes due to the slow heating and cooling rates of the materials.[142,143,145,185] As a result, the doctor must wait a few minutes for the next manipulation of the catheter, which substantially prolongs the surgical procedure. In the case of cardiac ablation surgery, which usually involves multiple ablation sites and dozens of ablation points per site, the catheter must be re-positioned many times.[130,203,204] With repeated slow heating and cooling processes, the accumulative waiting time can extend to hours when such variable stiffness (VS) catheters with phase-changing materials are used, compromising the surgical efficiency, increasing the costs and limiting patient access to treatments. In addition, the use of electric power for heating inside the human body imposes a heavy concern for patient safety.

Here, we present a VS catheter based on fiber jamming (FJ) that can undergo rapid stiffness changes within 0.3 seconds. This catheter consists of two VS segments filled with fibers of different materials (polylactide acid (PLA) and copper fibers) and two magnets to manipulate the two segments via a controllable magnetic field from a hospital-compatible remote magnetic navigation (RMN) system (**Fig. 4.1a,b**). Upon selective vacuum application, one segment can be stiffened while the other segment remains soft for manipulation. In our FJ configuration, the copper segment has a higher stiffness range, whose stiff state provides strong anchoring for the manipulation of the distal PLA segment which has a lower stiffness range. When the catheter forms the desired curve, the two segments can be locked in shape upon vacuum application for the ablation procedure to proceed. The stiffness change processes require only the on-off switches of the vacuum application with instant stiffness change in the catheter, making this process significantly faster than that of the existing VS catheters that rely on phase-changing mechanisms.

FJ devices comprise a slender sleeve containing numerous fibers that can freely move inside the sleeve (Fig. 1c).[141,205–207] When air is evacuated from the sleeve via vacuum application, the external pressure squeezes the fiber bundle and increases the mutual friction of the fibers. This increased friction impedes the relative sliding of the fibers, resulting in an increase in the bending stiffness.[141,205,206] FJ technology has recently emerged as a promising VS mechanism with potentials in different robotic applications, such as robotic manipulators, grippers, wearable devices, etc.[141,208–211] In particular, FJ

is suitable for surgical instruments with tubular structures that require omnidirectional bending stiffness changes.[141,207] Recent studies have reported FJ-based devices with SCFs up to 20 by exploring different materials, roughness, shapes, and arrangements of the fibers.[205–207,211] However, the existing FJ prototypes are 10 times larger than the size of the cardiovascular catheters which typically have diameters of 2.33mm. This dimension requirement imposes formidable challenges in catheter fabrication with FJ integration to achieve desirable SCF performance.

To make the catheter body ultra-slim, packing conventional fibers with circular cross-sections in a soft sleeve, as opposed to those with square cross-sections or rough surfaces, remains feasible. However, the SCF of such FJ configuration is below 3,[205,206] which is not sufficient for the cardio-vascular catheter applications as they require an SCF of at least 4 (section 4.S1). To overcome this challenge, our strategy for achieving a high SCF is to incorporate as many thin fibers as possible (section 4.S2). The existing FJ-based devices are filled with less than 100 fibers with diameters of at least 500µm in a thicker sleeve.[141,208–211] Therefore, the existing fabrication approaches do not enable manufacturing a large number of ultra-thin fibers and packaging them in the scale of Ø2.33mm suitable for cardiac catheters.

To address this challenge, we introduce an innovative fabrication procedure to construct the FJ-based VS catheter. The proposed procedure includes a precise method to produce fibers as thin as 50µm and a process to pack up to 1000 fibers within a 2mm diameter space. With our fabrication, we conducted parametric optimization experiments on FJ and obtained the optimal SCFs up to 6.5, possibly the maximum SCF achievable for FJ at the catheter scale. To tune the catheter stiffness range for the magnetic field magnitude, which differs for various surgery applications, we also explored the use of hybrid fiber bundles consisting of PLA and copper fibers with different material ratios. Furthermore, we created a method to measure the stiffness change time of FJ, which has not yet been achieved in the prior arts. The measurements show the FJ stiffness changes occur within 300ms, which is two orders of magnitude faster than the change rate of the existing VS catheters. Tests under the RMN system show that the single-segment FJ catheters can bend smoothly in the soft state upon the application of a magnetic field, and maintain minimal deflection in the rigid state when the fibers are jammed. A two-segment catheter is then fabricated and tested with the RMN system, which allows selective bending to achieve two-curvature profiles and manipulation inside a 3D phantom of the human heart. Compared to the existing VS catheters, the proposed FJ catheter achieves adequate and ultra-fast stiffness changes with safe materials and simple control. In addition, it eliminates the need for heating or electric power working inside the human body. Furthermore, our novel fabrication can be adopted to produce other FJ catheters for different specific minimally invasive surgery (MIS) procedures. Therefore, our proposed FJ-based VS catheter has strong potential to refine MIS by reducing procedure time and costs, and enhancing safety for both patients and surgeons.

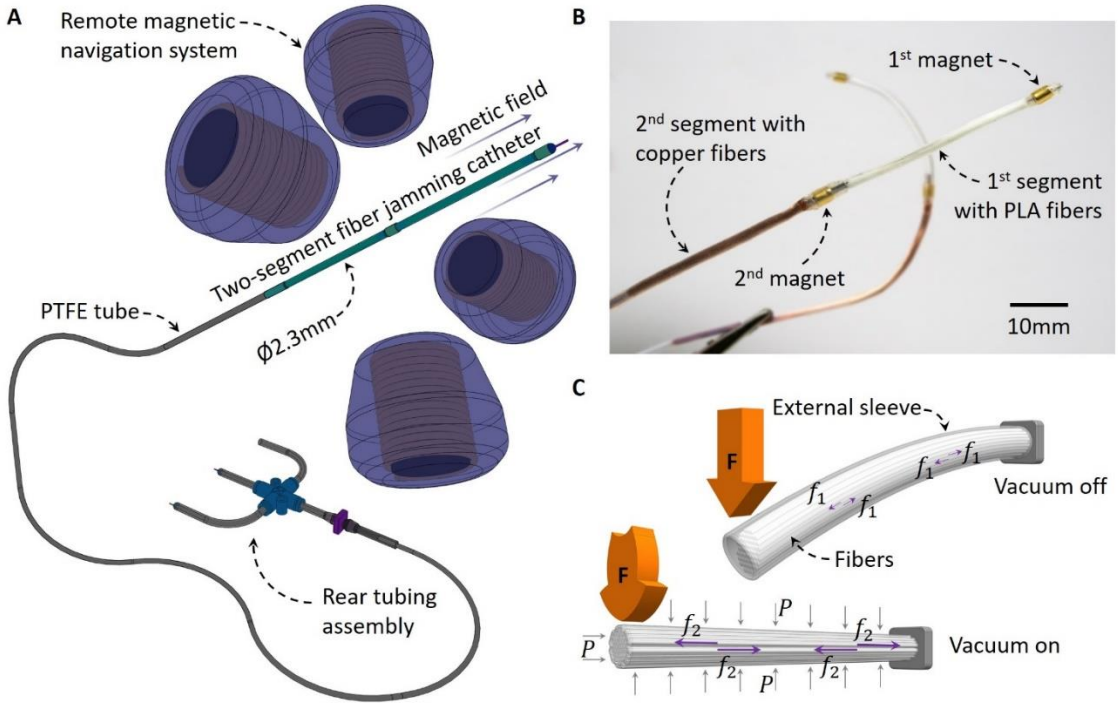

Figure 4. 1 Overview of the FJ VS catheter.
a) Schematic view of the two-segment catheter working with the RMN system. The catheter is connected to the rear tubing assembly via a PTFE tube. The rear tubing assembly provides interfaces for the vacuum application and surgical tools (e.g. ablation head). b) Actual prototypes of the catheter with two FJ segments and magnets. c) FJ working principle. The orange arrows represent the external force to bend the FJ beam; the purple arrows represent the mutual frictional forces (f) between the fibers and f1<<f2; the grey arrows represent the external pressure (P) applied to the external sleeve upon vacuum application.

4.3 Results and Discussion

4.3.1 Design and fabrication of the catheter

The FJ VS catheter has two segments, connected by a long Polytetrafluoroethylene (PTFE, for the material acronyms, please refer to Table 4.S1) tube to the rear tubing assembly (Fig. 4.1a, figs. 4.S1a and 4.S2b). The two segments have similar structures with a magnet at the tip of each segment followed by the fibers (fig. 4.S1a). They are encapsulated inside a silicone sleeve with silicone glue at the tip to fix the fibers and seal the segments (figs. 4.S1a and 4.S2b,c). In addition, one tube (purple) serving as the working channel is placed through the two segments for future installation of the ablation tip, and another tube (green) is positioned up to the first/PLA segment for vacuum application (figs. 4.S1a and 4.S2c,d). The vacuum application for the second/copper segment is served through the long PTFE tube (figs. 4.S1a and 4.S2d). At the rear tubing, the PTFE tube, the working and vacuum channels are decoupled into three independent outlets (fig. 4.S2a,e). Between the two segments, there is a supporting carbon fiber (CF)

rod extending from the tip of the second segment into the PLA fibers of the first segment to serve as a stiff support (figs. 4.S1a and 4.S2c). Detailed component information is given in fig. 4.S1 and Table 4.S1, while the anatomy of the catheter with its true proportions is illustrated in fig. 4.S2.

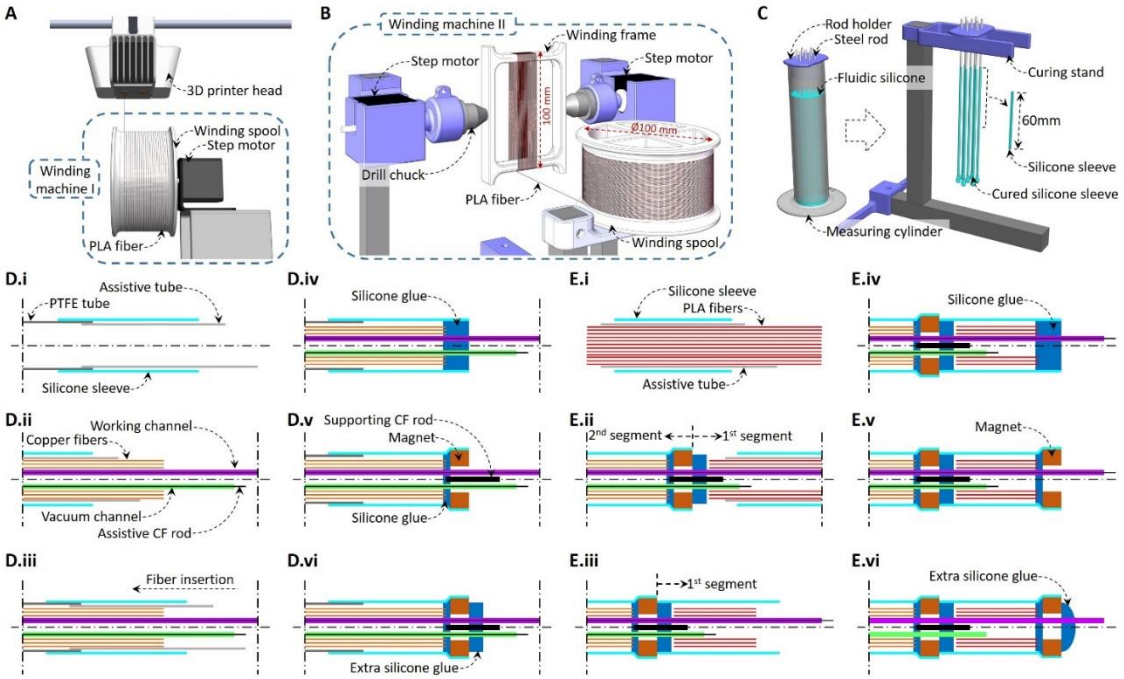

Figure 4. 2 Fabrication of the FJ VS catheter.
a) Ultra-thin PLA fibers are produced via winding machine I which pulls the melted PLA filament through its spinning spool. b) Fiber bundles with specific numbers of fibers are prepared on winding machine II. c) Fabrication of the silicone sleeve via a dipping and curing process. d) Fabrication of the second FJ segment. The silicone sleeve is first inserted into the right side of the PTFE tube, followed by the insertion of the assistive tube on the right side into the PTFE tube (i). Then the copper fiber bundle is inserted from the right, followed by the insertion of the working and vacuum channels reinforced with Ø0.3mm assistive CF rods inside (ii). By further pushing the two reinforced channels, the copper fibers are fully placed inside the silicone sleeve (iii). With the removal of the assistive tube, silicone glue is then applied at the right tip (iv), followed by the immediate insertion of the magnet and then the supporting CF rod (v). Extra silicone glue is then applied to seal the second segment (vi). e) Fabrication of the first FJ segment. The assistive tube is first inserted into the silicone sleeve, followed by the insertion of the PLA fiber bundle (i). The halfway first segment is inserted onto the tip of the second segment along the working channel (ii). The silicone sleeve is then rubbed leftwards and fixed at the tip of the second segment with silicone glue (iii). With the removal of the assistive tube, the right end of the PLA fibers is fixed with silicone glue (iv), followed by the immediate insertion of the magnet (v). The tip of the first segment is then sealed with extra silicone glue, followed by the removal of the two assistive CF rods from the working and vacuum channels (vi).

To fabricate the catheter we first obtain a large quantity of ultra-thin fibers of two material types. We select enameled copper wires (Ø50, 75, 100μm), and PLA fibres (Ø50 μm) extracted from a 3D printer (Ultimaker S5, Ultimaker B.V.) using winding machine I to pull the heated PLA filament (**Fig. 4.2a**, section 4.S3 and movie 4.S1). Once the fibers are prepared, the winding spool will be mounted onto winding machine II which reformats the fibers into a fiber bundle (Fig. 4.2b). By applying specific numbers of rotations of the winding frame, a bundle with the desired number of fibers is obtained. The second step involves preparing the external sleeve for packing the fiber bundle. We choose silicone rubber (DragonSkin 0020, Smooth-On, Inc. Elastic modulus at 100% strain: 0.34MPa) which, in the form of thin skin, is neither too brittle to break during manipulation, nor too stiff to affect the jamming effect. A dipping-curing process is employed to form silicone sleeves with a consistent wall thickness (≈150μm) (Fig. 4.2c).

With all the components ready, the catheter fabrication proceeds with copper fiber segment construction (Fig. 4.2d) followed by the PLA fiber segment (Fig. 4.2e). Both of the segments are fabricated similarly, involving the insertion of the fibers via an assistive tube, the insertion of the working and vacuum channels, the glue application and the magnet insertion. The main difference of the two segment fabrication lies with the supporting CF rod at the tip of the second segment (Fig. 4.2d(v)) and the location of the vacuum channel tip which stays in the first segment (Fig. 4.2e(vi)). The whole fabrication process is elaborated in the Materials and Methods section and movie 4.S1. Some key relative positions for the catheter fabrication process are provided in fig. 4.S3 which illustrates the components with their true proportions. For the rear tubing assembly, please refer to fig. 4.S4.

4.3.2 Fiber jamming characterization and optimization

To investigate FJ performance in terms of stiffness variation at the catheter scale and determine the optimal FJ configuration, we conducted detailed characterization using the 3-point bending tests by varying different parameters: filling rate, fiber diameter and fiber material. Moreover, the FJ reaction times are also measured via our novel method. With the focus on the FJ performance, all characterizations are implemented using the single-segment catheters with 40mm-long FJ segments (fig. 4.S5).

Prior to the investigation, the force profiles are firstly obtained to understand the FJ behavior (**Fig. 4.3a**) via the 3-point bending tests (fig. 4.S6). The initial steeper slope of the curve (0 to 0.2mm deflection) represents the high stiffness of the fiber bundle with the static friction preventing the relative sliding of the fibers. The lower stiffness observed from 0.4 to 1mm deflection is attributed to the lower kinetic friction of the fiber sliding after overcoming the static friction. The overall stiffness of FJ in the stiff state is calculated using linear fitting of the force curves within 1mm deflection. By increasing the vacuum level, the FJ stiffness and the SCF both increase (Fig. 4.3a), demonstrating that the stiffness of the catheter could be continuously modulated.

The first parameter investigated is the filling rate with Ø50μm PLA fibers at maximum vacuum (-95kPa). As the filling rate is increased from 20%, the average SCF initially

increases, peaks at a filling rate of approximately 40% and then drops (Fig. 4.3b). The standard deviations (SDs) of the SCFs are greater than 1 at low filling rates, representing a poor repeatability of the VS performance of the catheter (Fig. 4.3b).

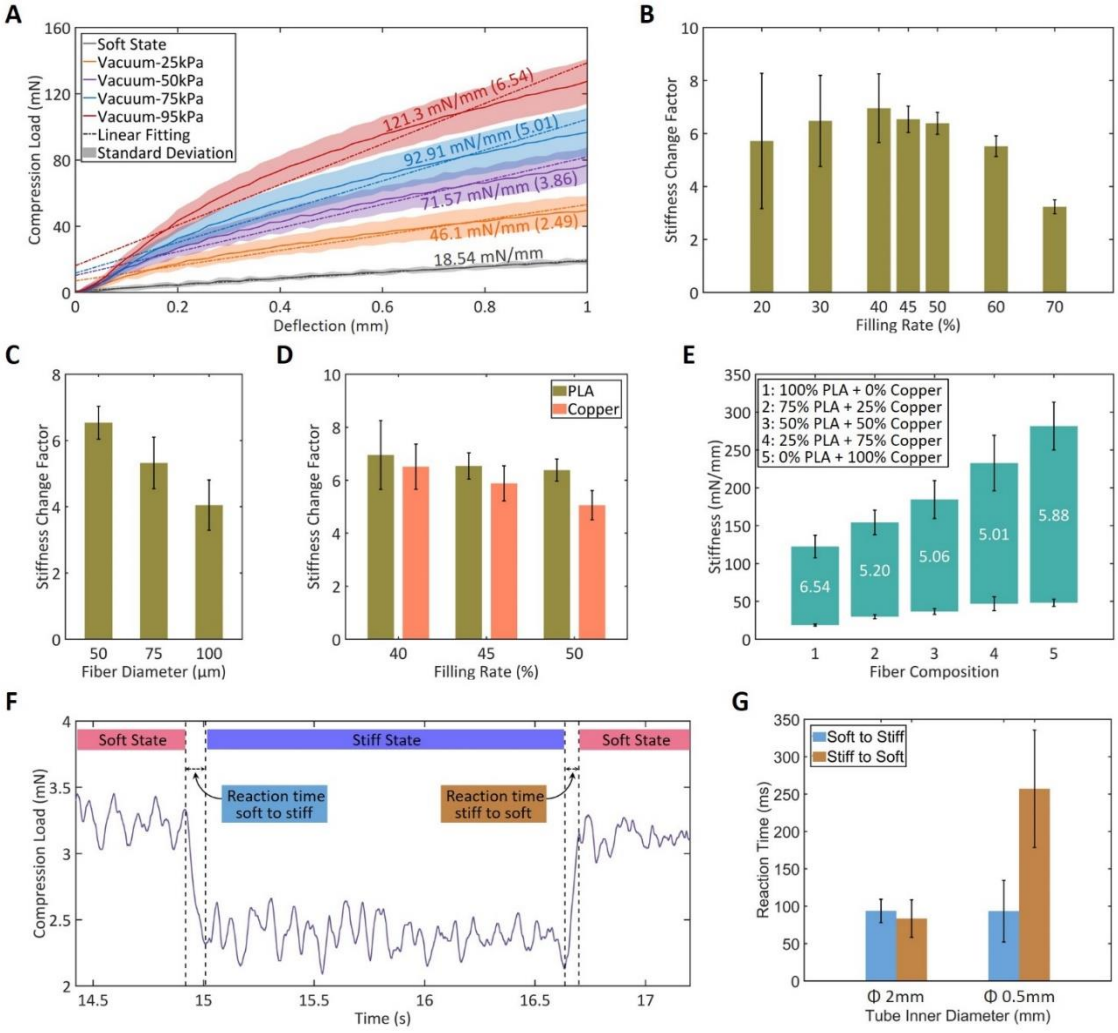

Figure 4. 3 Stiffness and reaction time characterization of FJ at the catheter scale. a) The force-deflection curves of the FJ segments with 45% filling rate and Ø50μm PLA fibers at different vacuum levels. The slopes of the individual linear fitting lines, representing the stiffness, are annotated with matching colored values. The SCF values are in parentheses. b) The SCFs of FJ with Ø50μm PLA fibers at different filling rates. c) The SCFs of FJ with PLA fibers of different diameters at 45% filling rate. To reach 45% filling rate, the numbers of fibers with 50, 75 and 100μm diameters are 720, 320 and 180, respectively. d) The SCFs of FJ with Ø50μm Copper and PLA fibers at the optimal filling rates. e) The stiffness and SCFs (white numbers) of FJ at 45% filling rate using the hybrid Ø50μm fiber bundles with different PLA-copper compositions. f) One typical force profile of the FJ transition from soft to stiff and from stiff to soft states (FJ sample: 45% filling rate with Ø50μm PLA fibers). High and low force levels represent the soft and stiff states of the FJ, respectively. The transition times in between the two force levels indicate the FJ reaction times. g) FJ reaction time measured from the catheters with Ø50μm PLA fibers at 45% filling rate using 2m long tubes with 2 mm and 0.5mm IDs to connect the

vacuum source. In (b)-(g), the results are all obtained using a -95kPa vacuum. All error bars represent one SD.

At the low filling rates, the FJ segment is somewhat hollow and, upon vacuum application, the cylindrical FJ segment is squeezed into a flattened body (fig. 4.S7a,b). Consequently, testing the FJ segments at different orientations (fig. 4.S6b) results in SCFs that can range from 3.6 to 8.2 (Fig. 4.3b). As the filling rate is increased to more than 45%, the SD drops below 0.75, representing consistent FJ performance (Fig. 4.3b). At high filling rates, the FJ segment becomes more densely packed with the fibers, and, therefore, its cross-section remains circular after vacuum application (fig. 4.S7c,d), which yields similar SCFs at different orientations (Fig. 4.3b). However, the higher filling rates come with higher stiffness in the soft state due to the increased initial friction caused by fiber congestion (fig. 4.S8a), resulting in lower SCFs (Fig. 4.3b). By comparison, the best filling rate for the catheter is determined to be 45% as this value leads to a relatively high SCF (6.54) and low SD (0.5).

With the optimal filling rate at 45%, the fiber diameter is then investigated with PLA fibers at -95kPa vacuum. The results show that increasing fiber diameters from 50 to 100µm reduces the SCF from 6.5 to 4 (Fig. 4.3c). The decrease in the SCFs is primarily due to the reduced stiffness in the stiff state as the fiber diameter increases (fig. 4.S8b). At the same filling rate, fewer fibers can be included in the sleeve when using thicker fibers. The reduced number of fibers leads to fewer contact points between the fibers, resulting in reduced friction and thus lower bending stiffness in the stiff state. Therefore, Ø50µm is chosen as the optimal fiber diameter for the catheter.

Copper fibers are also tested at the best three filling rates using -95kPa vacuum. The SCF and SD of the catheters with copper fibers also decrease with increasing filling rate (Fig. 4.3d). Due to the smoother surface, the copper fibers exhibit SCFs 0.2, 0.66 and 1.32 lower than those of the PLA fibers at 40, 45 and 50% filling rates, respectively. However, the absolute stiffness of the copper fiber catheter in the stiff state is approximately double that of the PLA fiber catheter (fig. 4.S8c). Thus, the copper fiber is a potential option for making high-stiffness catheters. Based on these experiments optimizing the three variables, the best FJ configuration is determined to be a filling rate of 45% with 50µm fiber diameter, applicable to both PLA and copper fibers.

The utilization of the two materials (PLA and copper) with different stiffness provides the possibility to customize catheter stiffness by mixing them with different ratios into hybrid fiber bundles. Therefore, hybrid fiber bundles with 75%-25%, 50%-50% and 25%-75% PLA-copper ratios are prepared and tested. The stiffness ranges of the hybrid fiber bundles gradually shifted from that of a 100% PLA bundle to that of a 100% copper bundle as the percentage of copper fibers increases and the percentage of PLA fibers decreases (Fig. 4.3e). However, the SCFs of the hybrid bundles remain stable, averaged at 5.1, as the fiber ratio changes. Importantly, this stiffness customization allows us to configure the stiffness of the multi-segment catheters, as explained in section 4.S4.

FJ technology is known for its fast reaction upon vacuum application. However, the actual reaction time (time required for a complete stiffness change from the soft to the stiff state

or vice versa) has not been previously reported due to the lack of a precise measurement method. Here, we devised a method to measure the FJ reaction time (see Methods section). We first obtain the force profile during vacuum switching which yields different force levels in the vacuumed/rigid and non-vacuumed/soft states (Fig. 4.3f). By measuring the transition times between the two force levels, the reaction (stiffening and softening) times of FJ are obtained (Fig. 4.3f). Vacuum tubes of different diameters (2 and 0.5mm for the PTFE tube and the vacuum channel, respectively) with 2m length are attached to the catheters for testing. The results show that the reaction times are mostly below 100ms, except for the softening times with Ø0.5mm tube, which reach approximately 250ms. Despite the variation, the FJ reaction is very fast with most stiffness transitions occurring within 300ms, which is at least two orders of magnitude faster than the reaction times of the existing VS catheters.

4.3.3 Bending tests of the catheter under the RMN system

After determining the optimal configuration for the FJ segment (45% filling rate, Ø50μm) and the FJ reaction times, we performed bending characterization of the catheters with five different fiber compositions used in Fig. 4.3e with a hospital-compatible RMN system (CardioMag) to investigate how the catheters respond to the magnetic field in terms of bending angles in their soft and stiff states and the speed of shape locking. In the stiff state, the single-segment catheters are tested under an increasing magnetic field density (MFD) with a fixed direction perpendicular to the catheter to assess their rigidity (**Fig. 4.4a**). Subsequently, to investigate their bending range in their soft state, the catheters are tested under their corresponding MFDs which is rotated from 0° (parallel to the catheter) to 150°(Fig. 4.4b). The MFDs for testing the catheters in their soft states are different due to different stiffness decided by their fiber material compositions, which are 40, 50, 60, 70 and 80mT for 100% PLA, 75% PLA – 25% copper, 50% PLA – 50% copper, 25% PLA – 75% copper and 100% copper, respectively, (section 4.S4 and Table 4.S3).

In the stiff state, the catheters remain rigid at their recommended MFDs, with minimal deflections of 15.1°, 11.3°, 12.1°, 10.1°, and 6.4° at 40, 50, 60, 70 and 80mT for the five fiber compositions, respectively (the highlighted dots in Fig. 4.4c and fig. 4.S9, and movie 4.S2). In the soft state, with the magnetic field turning 150°, the catheters with the five types of fiber bundles achieve significant bending angles of 107°, 100°, 98°, 94° and 92° for the five fiber compositions as compared to their deflections in the rigid state (Fig. 4.4c, fig. 4.S9 and movie 4.S2). In addition, a hysteresis of approximately 10° is observed in the cyclic bending tests (Fig. 4.4d and movie 4.S2) which is primarily attributed to the fiber rearrangement during bending.

To demonstrate the instant stiffness change of the catheters, another cyclic bending is performed, in which, the catheter is stiffened and softened multiple times (movie 4.S3). We can see that the freezing and releasing actions of the catheter occur immediately upon turning the valve knob (movie 4.S3). Overall, the calculation in section 4.S4 gives accurate predictions of the MFDs for the single-segment catheters with different fiber compositions. The catheters under the RMN system, despite slight hysteresis, exhibit

strong performance with small deflections in the stiff state, substantial bending in the soft states and ultra-high speed in stiffness change.

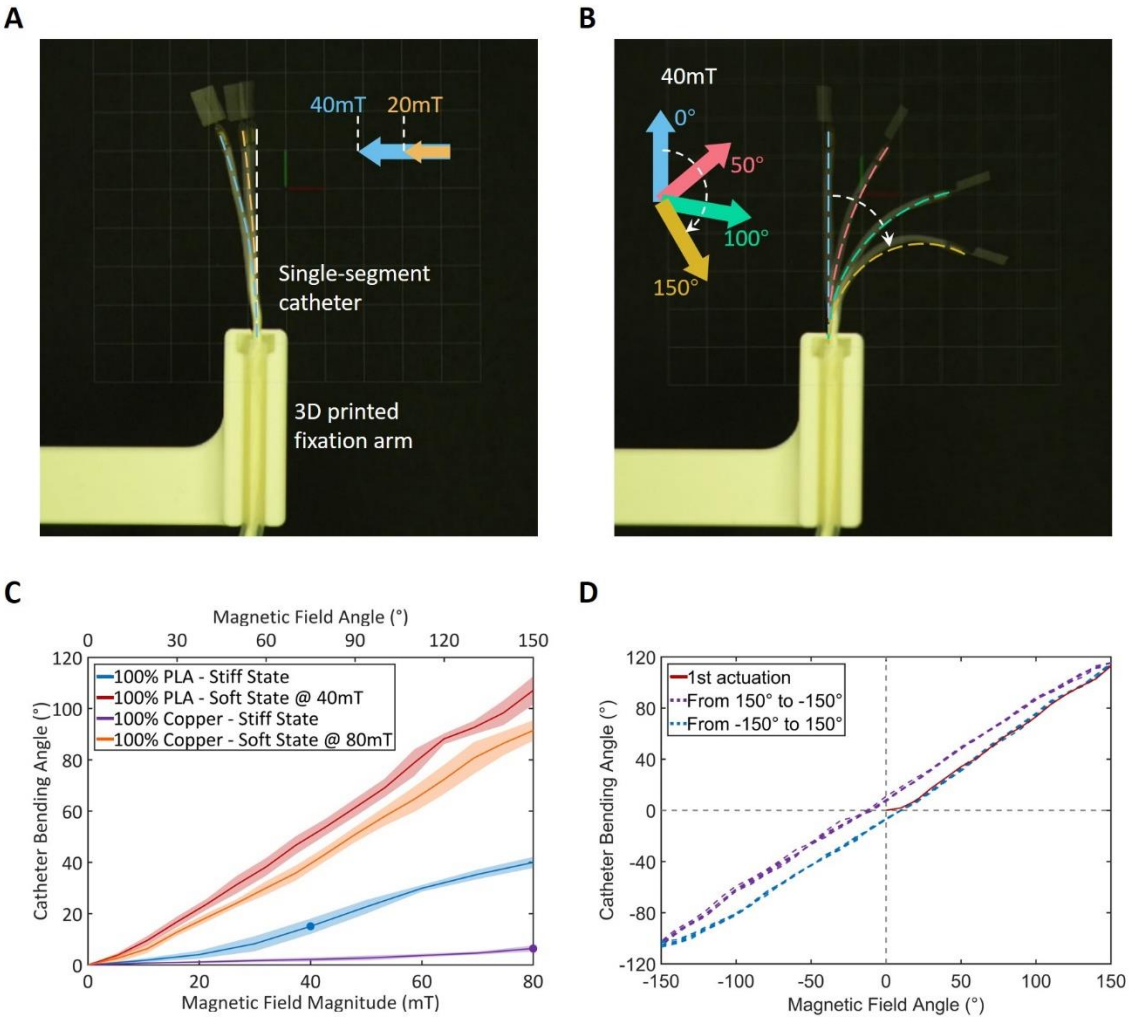

Figure 4. 4 Single-segment catheter tests with the RMN system.
a) Catheter (100% PLA fibers of Ø50µm, 45% filling rate) in the stiff state tested under increasing MFD with a fixed direction. The direction of the magnetic field is perpendicular to the initial orientation of the catheter body, generating maximum bending moments for the assessment of catheter rigidity. b) The same catheter in the soft state tested under a fixed MFD with changing direction from 0 to 150°. c) Bending results of the catheters with 100% PLA and 100% copper fibers from the tests (a) and (b). The colored dots highlight the small deflections of the catheters in the stiff state using their corresponding MFDs. (d) Cyclic bending test result of the catheter with 100% PLA fibers to reveal its bending hysteresis.

4.3.4 Two-segment catheter for cardiac ablation

During open-volume surgeries, such as those involving the heart or stomach, the precise positioning of surgical tools requires two degrees of freedom. Thus, we develop a two-segment FJ catheter to address this need effectively. The first segment uses the 100% PLA fiber bundle with a low stiffness range to allow a wide bending range, while the second segment is filled with the 100% copper fiber bundles with a high stiffness range not only to allow adequate motion range but also to provide rigid anchoring for the first segment manipulation (section 4.S4). Both segments use a 45% filling rate and Ø50μm fibers. This two-segment catheter is then tested in the RMN system with the goals of demonstrating the selective manipulation of the two segments to achieve multi-curvature bending and examining whether the stiffened segment can remain unaffected when the other segment is being manipulated. Then, to simulate a real surgical scenario, the two-segment catheter is also tested in a 3D phantom of a human heart for manipulation by the RMN system.

In the demonstration, the catheter is initially positioned vertically with the two segments stiffened (**Fig. 4.5a(i)**). Then the first segment is softened for manipulation by changing the direction of a 40mT magnetic field. While the first segment is moved leftwards, the second segment remains still, which validates the sufficient rigidity of the 100% copper fiber bundle in the vacuumed state (Fig. 4.5a(ii) and movie 4.S4). In the second test, the second segment is manipulated to the right in an 80mT magnetic field and the stiffened first segment stays straight during the procedure (Fig. 4.5a(iii) and movie 4.S4). Although the rigid first segment cannot withstand the 80mT MFD, the movement of the softened second segment occurs quickly before any deformation of the first segment occurs (movie 4.S4). The second segment is then stiffened, followed by the softening of the first segment for upward manipulation with a 40mT MFD, resulting in a multi-bending curve (Fig. 4.5a(iv) and movie 4.S4). In addition to the multi-segment curving capability, the overall actions of the catheter are performed fluently with a whole set of curve forming, including three rounds of stiffness switching and individual bending of the two segments, taking less than 10s. While the other VS catheters using phase-changing materials require at least 10 minutes to accomplish the set of movements.[142,143,145,185]

In the final demonstration, the two-segment catheter is inserted into a 3D phantom of the human heart via the right atrium, through the wall puncture between the left and right atriums, to the left ventricle. At first, we stiffen the second copper segment and manipulate the soft first segment using a 40mT magnetic field for potential ablation procedure (Fig. 4.5B and movie 4.S5). Next, the catheter is withdrawn to the left atrium and then, with the second segment frozen, the soft first segment is bent to different positions by the magnetic field (Fig. 4.5C and movie 4.S5). The multi-segment bending tests and simulated surgery tests both validate the superior motion capability, correctness of stiffness configuration in the two segments and rapid VS function of the two-segment catheter, demonstrating the promising feasibility of applying this catheter in cardiac ablation surgeries.

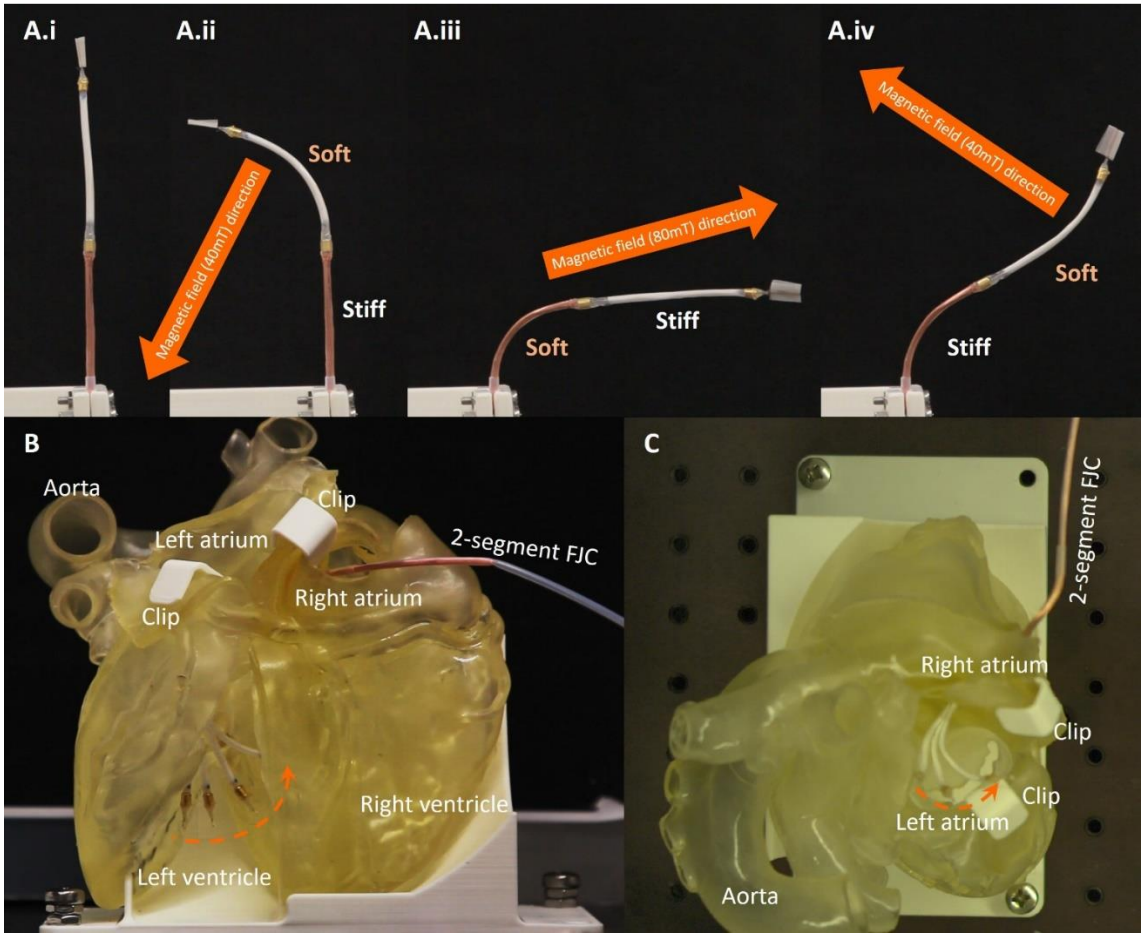

Figure 4. 5 Two-segment catheter tests with the RMN system.
(a) Selective manipulation of the two catheter segments to form a multi-curvature body. The initial state of the catheter is straight (i). The first segment is softened and manipulated, with the stiffened second segment staying still, in a 40mT MFD magnetic field (ii). The second segment is softened and manipulated, with the stiffened first segment staying straight, in an 80mT MFD magnetic field (iii). Following (iii), the second segment is stiffened, and the first segment is softened for manipulation to form a multi-curvature body in a 40mT MFD magnetic field (iv). (b, c) Catheter manipulation in a human heart phantom with the stiffened second segment supporting the manipulation of the first segment in the left ventricle (front view) (b) and left atrium (top view) (c).

4.3.5 Applied force characterization in a real clinical setting

A quality of lesion formation during a cardiac ablation procedure is determined by a number of factors including amount of power applied to the ablation tip, duration of ablation, and amount of force applied to the human tissue with the ablation tip.[212] Currently, doctors apply at least 15 g of force onto the human tissue with existing manually-driven catheters to enable high-quality lesion formation.[213] Existing clinical magnetically-driven catheters can apply 6g of force only, which results in a longer surgery duration and higher cases of cardiac arrhythmia recurrence.[134,214,215] Therefore, variable stiffness catheters have potential to enhance the force applied onto the human tissue, resulting in a high-quality lesion formation and higher success rate of the procedure.

Thus, we performed the first applied force characterisation of a variable stiffness catheters in a real clinical setting using commercially available remote magnetic navigation system Niobe, Stereotaxis at the St. Anne's University Hospital Brno, Czech Republic. Moreover, we also compared its performance with existing devices used for cardiac ablation procedure on a daily basis.

To measure the applied force we used a custom-made load cell, which allows force measurement inside the magnetic field with a precision of 0.01 g (**Figure 4.6a**). To control the orientation, every catheter was fixed in a custom-made holding setup placed inside the working area of Niobe. The setup connects together a catheter advancer, support shaft, and the catheter. A catheter advancer (Quick-CAS, Stx) moves a catheter forward and backward inside the working area. A catheter advancer is then connected to a steerable introducer (Agilis, NxT), which is used as a support sheath to deliver a catheter to a target zone inside the heart with desirable inclination angle. It also provides additional rigidity to the system since it has a larger diameter and higher stiffness compared to a catheter. By extending or retracting a catheter from the support sheath, doctors can tune the force applied onto the human tissue during ablation.[215] A catheter can be bent in any direction with magnetic field generated by permanent magnets located from the left and right sides of the patient with a magnetic field amplitude of 80 or 100 mT.

We used three commercially available certified catheters (Celsius and Navistar RMT ThermoCool, Biosense Webster; MagnoFlush, Acutus Medical) and a variable stiffness catheter presented before in a soft and rigid state with both segments activated.

We performed a characterization for three force application scenarios used by clinicians at any surgery: perpendicular push onto the human tissue using a catheter advancer only (Figure 4.6b-i,ii), a lateral touch with an object parallel to the catheter using a magnetic torque generated by permanent magnets at the tip of the catheter and Niobe's magnetic field (Figure 4.6c-i,ii), and a lateral touch with an object parallel to the catheter using both a magnetic torque and forward motion due to catheter advancer (Figure 4.6c-iii). During all experiments, catheters' tip was pressing onto the load cell till it is bent and the force is constant. The bent configuration of the catheter mimics a real case contact during the procedure but it does not represent the optimized configuration to apply maximum force with the device. We performed 20 measurements per each scenario and device. The mean values are presented in Table 4.1.

For the perpendicular push scenario, variable stiffness allows to apply two times more force onto the human tissue. The variable stiffness catheter in the rigid state outperforms all commercial catheters while in the soft state the force is the lowest. It indicates that the variable stiffness catheter can be even safer in the soft state than existing certified devices due to its low stiffness and, at the same time, can apply more force onto the human tissue while stiffened. For the later touch scenario, all certified devices show a force performance of 2g compared to 0.4 and 0.76 g for a variable stiffness device. It indicates a low dipole momentum of the magnets used in a variable stiffness catheter. By integrating magnets with larger volume, the generated magnetic torque, thus, applied force can be improved. For the third scenario when both lateral touch due to the magnetic field and forward movement due to the catheter advancer are applied, Celsius and variable

stiffness catheter in the rigid state show similar performance of 3.25 and 3.34 g of force. In this scenario, the variable stiffness increases the applied force by 40%.

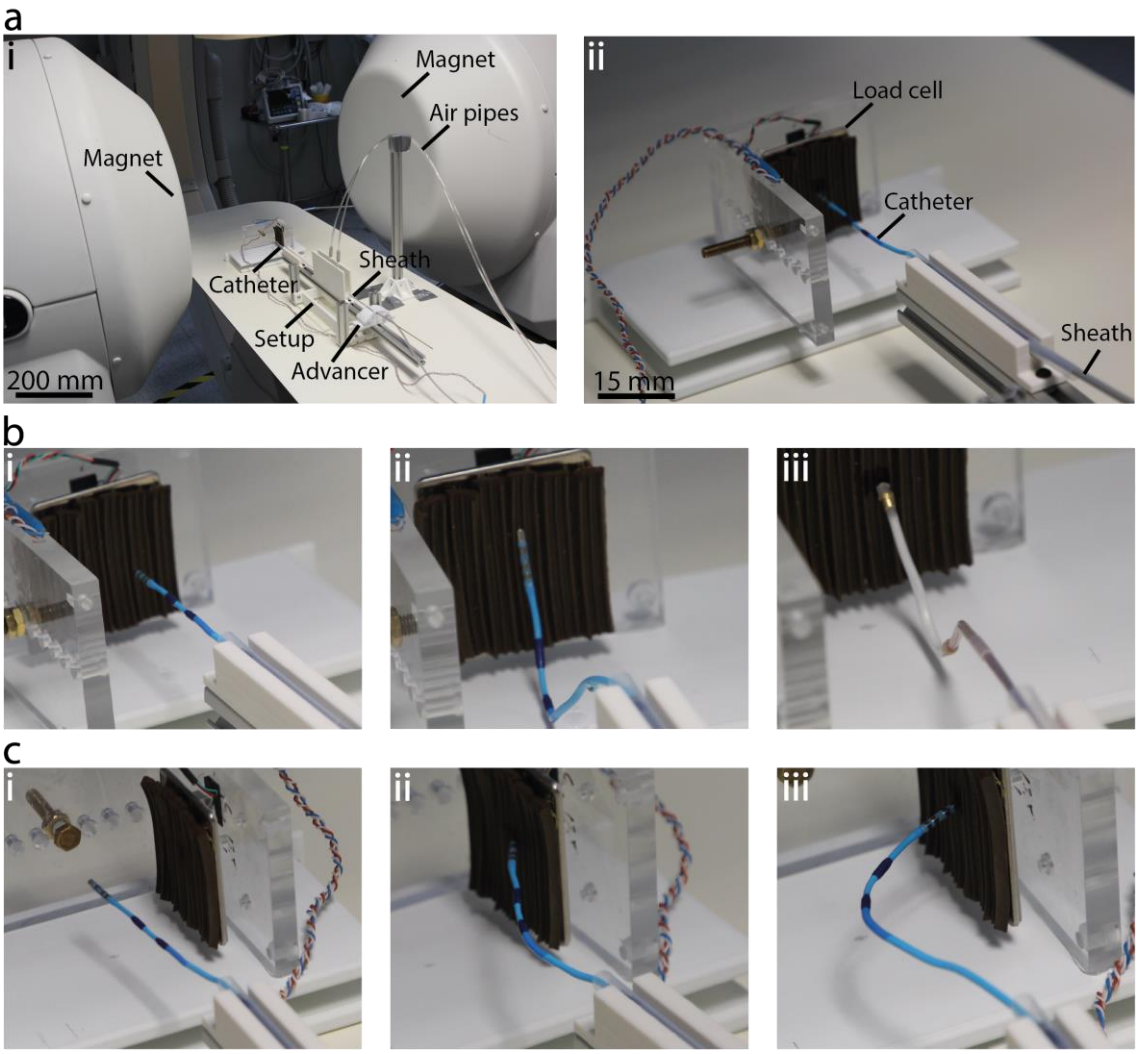

Figure 4. 6 Characterization of applied force in a remote magnetic navigation system Niobe, Stereotaxis.
a) The test setup placed in the working area of Niobe, Stereotaxis. b) Perpendicular push onto the human tissue using a catheter advancer only. b-i) Catheter is moving towards the load cell. b-ii) Certified catheter in a bent state. b-iii) Variable stiffness catheter in a bent state. c) The lateral touch with a load cell parallel to the catheter using a magnetic torque. c-i) Catheter before the magnetic torque causes bending. c-ii) Bent catheter due to magnetic field only. c-iii) The bent catheter was then pushed with a catheter advancer. It demonstrates the third testing scenario: lateral touch and push.

To conclude, variable stiffness technology integrated into a catheter enhances the applied force up to two times in all scenarios. Our variable stiffness catheter already outperforms all existing certified devices in all scenarios where the applied force was generated due

to the use of catheter advancer. It indicates that variable stiffness allows to better transfer external forces to the tip of the catheter without sacrificing its steering capabilities.

	Scenario		
Catheter's name	Perpendicular push, g	Lateral touch, g	Lateral touch and Push, g
VS catheter soft state	4.0165	0.4255	2.3175
VS catheter rigid state	8.199	0.7635	3.2475
Celsius	5.8475	2.0295	3.3375
Magnoflush	7.2685	2.0835	3.073
Navistar	7.2955	2.048	2.848

Table 4. 1 Force characterization of three certified catheters and a variable stiffness (VS) catheter in the soft and rigid states.

4.4 Conclusion

Here we proposed and characterized a novel multi-segment variable stiffness catheter based on fiber jamming that can be used in remote magnetic navigation procedures. Importantly, the proposed catheter can reversibly change stiffness up to 6.5 times in only 600ms, which is 300 times faster than other variable stiffness catheters.[142,143,145,185]

Although the stiffness change factor of this catheter is three times lower than that of existing variable stiffness catheters that use phase-changing materials, the experimental results described here indicate that its bending performance in rigid and soft states is comparable.

The proposed fabrication method can be adapted for manufacturing catheters of different lengths, thicknesses, stiffness, and segment numbers that are suitable for other types of medical procedures, such as monitoring and surgery of the abdominal or of the otorhinolaryngological pathways that require catheters of different diameters, lengths, and segment numbers.[28,216]

Cardiac ablation surgeries are intensive procedures that typically consist of dozens of ablation points at multiple sites (30). Although multi-segment variable stiffness catheters could facilitate the positioning of the ablation tip at the desired location, the transition time of existing variable stiffness catheters[142,143,145,185] requires approximately 1.5 minutes for one stiffness change cycle and 3 minutes for one curve formation, which requires the sequential stiffness change of each segment.

A typical surgery performed with conventional catheters of up to 80 ablations requires approximately 65 minutes.[217] Existing variable stiffness catheters would increase this length by 240 minutes (90s per stiffness transition cycle × 2 segments × 80 ablations). Instead, the catheter described here would add only 1.6 minutes (600ms per stiffness

transition cycle × 2 segments × 80 ablations) to today's procedure. Taken together, these results indicate that the proposed catheter not only offers performance comparable to other variable stiffness catheters and is compatible with the remote magnetic navigation system, but also does not significantly increase operation time. Surgery duration is indeed a critical factor for the adoption of variable stiffness technologies in minimally invasive surgeries and in other medical procedures.

4.5 Methods

4.5.1 Catheter fabrication

The first consideration in the fabrication is the ultra-thin fiber. The only off-the-shelf fibers with different diameters are the enameled copper wires which have an elastic modulus of 110GPa. The other type of fiber is obtained by thinning the filament from a 3D printer (Ultimaker S5, Ultimaker B.V.) using winding machine I (Fig. 4.2a). Since the various filaments have similar elastic moduli of around 3GPa, PLA is chosen due to its biocompatibility. During PLA fiber production, winding machine I pulls the melted PLA filament with its spinning spool. With a spinning speed of 12.5πrad/s, the winding spool (Ø100mm) can pull the melted PLA filament from the printer nozzle into Ø50μm fibers, while other fiber thicknesses can be achieved via different spinning speeds (section 4.S3 and Table 4.S2). This fiber production method is fairly precise with around 5μm SD in the fiber diameters. PLA fibers thinner than Ø50μm can also be produced via the aforementioned process, but they are too brittle for later operation. To prepare fiber bundles with specific numbers of fibers, the winding frame from winding machine I is mounted on winding machine II which rotates the winding frame at a slow speed (0.4πrad/s) to avoid breaking the ultra-thin fibers (Fig. 4.2b).

The silicone sleeve is prepared via a dipping-curing process (Fig. 4.2c). Multiple Ø2mm steel rods fixed on the rod holder are slowly dipped into the freshly mixed silicone (DragonSkin 0020, Smooth-On, Inc) in the measuring cylinder for 5s and then pulled out for 2-hour curing at room temperature on the curing stand. With the gravity effect, the dipping and curing process results in a consistent wall thickness (≈150μm) on the silicone coating, which is a proper thickness for the sleeve. The silicone coating is rubbed off from the steel rod and the upper 60mm segment is kept as the sleeve for the FJ segment.

With all the components ready, the fabrication starts with the construction of the second FJ segment (Fig. 4.2d and fig. 4.S3a). The silicone sleeve is first inserted into the right side of the PTFE tube, followed by the insertion of the assistive tube from the right into the silicone sleeve and then PTFE tube (Fig. 4.2d(i) and fig. 4.S3a(i)). This assistive tube with a wedged tip is to facilitate the insertion of the fiber bundle due to its smooth inner surface. Then the copper fiber bundle is inserted from the right, followed by the insertion of the working and vacuum channels (Fig. 4.2d(ii) and fig. 4.S3a(ii)). The two thin channels, due to their softness, are internally reinforced by Ø0.3mm assistive CF rods for easy insertion. The insertion of the two channels is done with the copper fibers held on

the right end. Then, the copper fibers are released to fully enter the silicone sleeve along with the further insertion of the two channels (Fig. 4.2d(iii) and fig. 4.S3a(iii)). With the removal of the assistive tube, silicone glue is then applied at the right tip of the silicone sleeve (Fig. 4.2d(iv) and fig. 4.S3a(iv)), followed by the immediate insertion of the magnet and then the supporting CF rod (Fig. 4.2d(v) and fig. 4.S3a(v)). Extra silicone glue is then applied to seal the second segment (Fig. 4.2d(vi) and fig. 4.S3a(vi)).

The next procedure is to produce the first FJ segment (Fig. 4.2e and fig. 4.S3b). The assistive tube is first inserted into the silicone sleeve, followed by the insertion of the PLA fiber bundle (Fig. 4.2e(i) and fig. 4.S3b(i)). The halfway first segment is inserted onto the tip of the second segment with the working channel passing through the first segment (Fig. 4.2e(ii) and fig. 4.S3b(ii)). The silicone sleeve is then rubbed leftwards to reach the tip of the second segment. After removing the assistive tube, the silicone sleeve is fixed to the tip of the second segment with silicone glue (Fig. 4.2e(iii) and fig. 4.S3b(iii)). The right end of the PLA fibers is fixed with silicone glue (Fig. 4.2e(iv) and fig. 4.S3b(iv)), followed by the immediate insertion of the magnet (Fig. 4.2e(v) and fig. 4.S3b(v)). The tip of the first segment is then sealed with extra silicone glue (Fig. 4.2e(vi) and fig. 4.S3b(vi)). By removing the two assistive CF rods in the working and vacuum channels, the catheter fabrication is completed.

The other end of the catheter, which is the PTFE tube with the working and vacuum channels inside, is connected to the rear tubing assembly (fig. 4.S4). For making the rear tubing assembly, the silicone tube, PU tube, barb fitting and the cross fitting are first assembled (fig. 4.S4a). Then, the working and vacuum channels inside the PTFE tube are inserted through the silicone tube, the barb fitting and the PU tube. When they reach the cross fitting, the vacuum channel goes straight across the cross fitting, while the working channel is diverted to the fitting port pointing downwards (fig. 4.S4b), followed by the insertion of the PTFE tube into the silicone tube. Another three PU tubes are then plugged into three fitting ports and the assembly is finished with silicone glue sealing the tips of outlet 1 and 2 (fig. 4.S4c).

4.5.2 Catheter stiffness measurement

For the stiffness measurement, the single-segment catheter is placed on a 3D printed 3-point bending setup with two supporting bars at two ends (gap: 35mm) and one indenter in the middle (fig. 4.S6a). The indenter is connected to the loadcell of the Instron machine (Instron5965, Instron. Inc) which moves the indenter to press on the catheter. The catheter is connected to one channel of the dual-channel vacuum controller (fig. 4.S6a). This vacuum controller, with two individual channels, can switch the vacuum channels on and off with two switch valves (VHK3, SMC. Ltd), regulate the vacuum levels with two vacuum regulators (IRV20, SMC. Ltd), and display the vacuum pressures with two vacuum indicators (ZSE20A, SMC. Ltd) (fig. 4.S6a). Due to the cross-section deformation upon vacuum application (fig. 4.S7), the catheters are tested at four orientations with 45° intervals. This is achieved via a 3D printed fixation setup including the catheter fixation and fixation housing that is placed next to the 3-point bending setup (fig. 4.S6b). The catheter fixation has an octagonal body with four orientation indicators

to allow the testing of different catheters at four orientations (fig. 4.S6b). During the test, the catheter is pressed by the by 3mm indenter at a compression rate of 0.2mm/s. The compression distance, which is also the deflection of the catheter, and force data are recorded by the Instron machine at a 10Hz sampling rate (fig. 4.S6c).

For each catheter configuration with specific filling rates, fiber diameters and fiber materials, three samples are fabricated. For each testing configuration with specific vacuum levels and fixed orientation, the tests are repeated three times for each catheter sample. After the tests, the force-deflection data within 1mm deflection is used to calculate the stiffness via linear fitting. By dividing the stiffness in the stiff state by the stiffness in the soft state, the SCF is then calculated.

4.5.3 Catheter reaction time measurement

The catheter reaction time measurement is also implemented on the 3-point bending setup (fig. 4.S6). During the test, the catheter is firstly compressed by the indenter by 3mm (fig. 4.S6c) and then, in this bent state of the catheter, the vacuum is turned on and off for five cycles. The force profile of the catheter transition between the soft and stiff states is obtained from the loadcell recording of the Instron machine (Fig. 4.3f). The force profile shows that the soft state gives higher force, while the stiff state yields lower force (Fig. 4.3f). This is because the vacuum inside the catheter shrinks the catheter body, which decreases its pressure to the indenter/loadcell. The vacuum also freezes the catheter body, which ensures that the catheter body does not lose its bent shape and thus maintains the low pressure on the loadcell. Therefore, the gaps between the last peak in the soft state and the first trough in the stiff state, and vice versa, represent the stiffening and softening times, respectively (Fig. 4.3f). The last three cycles of the force-time data are used to measure the reaction times. During the tests, the sampling rate is set at 1000Hz to ensure precise time measurement.

For the reaction time measurement, 2m long tubes with different IDs (2 and 0.5mm) are used to connect the catheters and the vacuum controller as, in the actual surgeries, the catheter should be long enough to extend from the vacuum controller to the ablation sites in the human heart, while 2 and 0.5mm IDs are the ones used in the two-segment catheter to apply vacuum to the two segments. When using the 2mm ID tube, the reaction times are measured from catheter samples with different filling rates, fiber diameters and fiber materials. When using the 0.5mm ID tube, only the three catheters with Ø50μm PLA fibers at 45% filling rate are tested.

4.5.4 Catheter bending test under RMN system

The bending tests of the single-segment catheters are implemented with the CardioMag RMN system. Five types of fiber bundles (100% PLA, 75% PLA – 25% copper, 50% PLA – 50% copper, 25% PLA – 75% copper and 100% copper) are used in the catheters with three samples for each fiber bundle type. All catheters are constructed with the

optimal FJ configuration: 45% filling rate and 50μm fiber diameter. Before the start of the tests, the catheter is adjusted into a straight body with the rear tube fixed on a 3D-printed fixation arm (Fig. 4.4a,b). In the rigid/vacuumed state, the catheters are tested with the magnetic field directed perpendicular to the initial catheter body, representing the maximum bending moment that can be generated by each MFD. With camera recording, the MFD is increased from 0 to 80mT with an incremental rate of 10mT/3s to bend the catheters. In the soft state, the catheters are tested with specific MFDs corresponding to different fiber bundle types: 40, 50, 60, 70 and 80mT for 100% PLA, 75% PLA – 25% copper, 50% PLA – 50% copper, 25% PLA – 75% copper and 100% copper, respectively. During the tests, the magnetic field is initially aligned to be parallel to the catheter body, representing a 0 bending moment. The magnetic field is then rotated by 10° every 3s until reaching an angle of 150° from its initial angle. When the magnetic field is rotating, the magnetic field direction misaligns with the catheter magnet, resulting in a bending moment to bend the catheter. Therefore, the bending of the catheter follows the rotation of the magnetic field. The bending processes are also recorded by a camera. For the cyclic bending tests to access the hysteresis, the catheters are tested in the soft state with their MFDs. With the camera recording, the magnetic field is rotated from its initial direction parallel to the initial catheter orientation, and then oscillates five times between -150° and 150° with a rotation rate of 10°/3s. For each catheter sample, all the tests are repeated three times each. All the recorded videos are then processed by motion analysis software (Tracker, physlets.org) to measure the bending angles.

4.6 Acknowledgments

This work was partially funded by the Swiss National Science Foundation, Bridge project 20B2-1 180861.

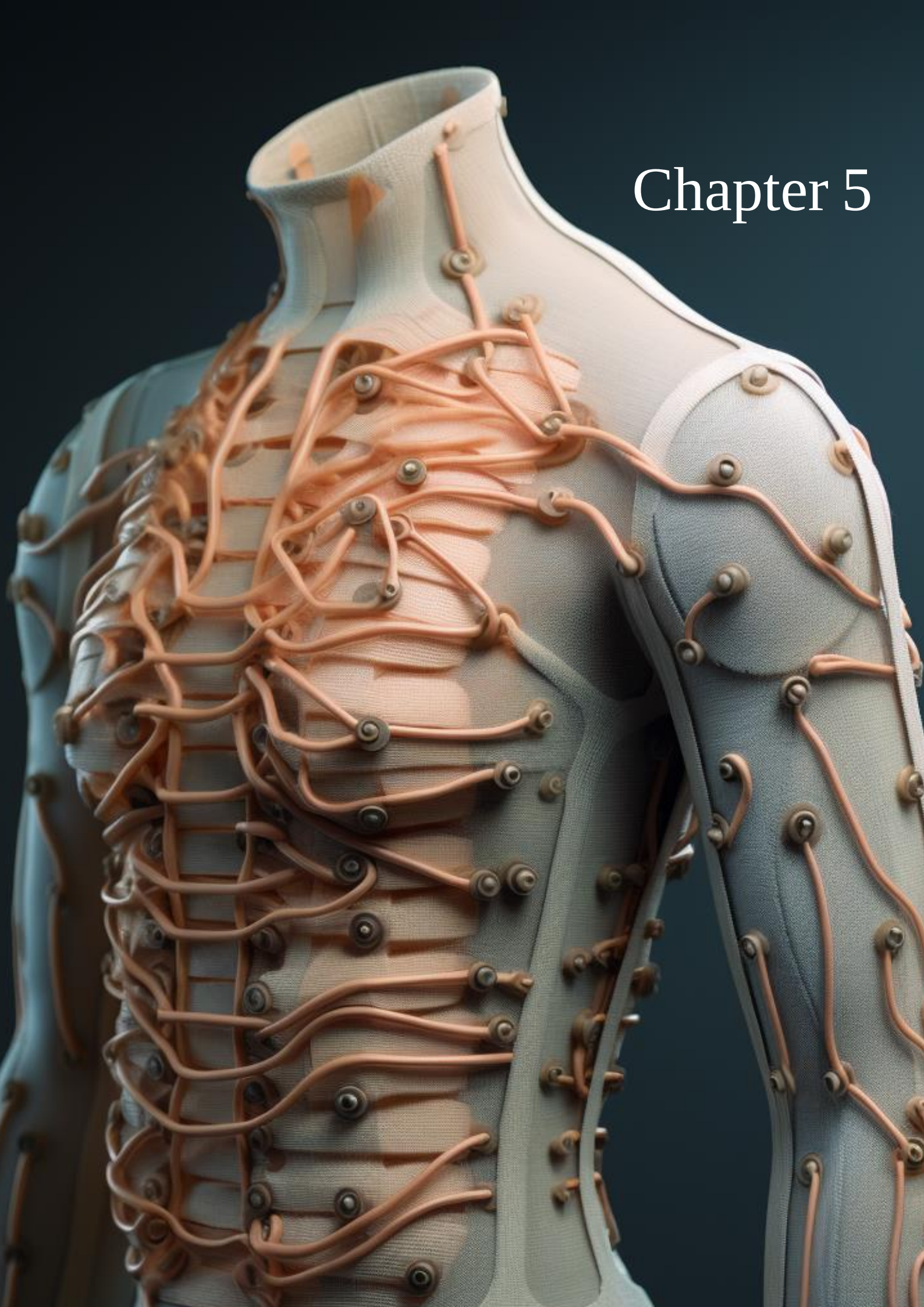

Chapter 5

5 Conclusions and future work

Within the introduction, we presented the current state of the art for smart fibers used in robotics and medicine, their functionalities, and limitations. Then, we narrowed down the focus of this thesis to one specific application, cardiac ablation, by discussing the currently used methods and their limitations. Based on the identified challenges, we proposed three novel filiform variable stiffness technologies for cardiac ablation catheters that overcome existing limitations.

Here, we summarized the main results and limitations of each of the chapters, followed by a discussion of potential avenues for future research.

Finally, we briefly describe soft robotics satellite projects that were done and published during last four years and how they can be potentially translated into the medical field.

5.1 Variable stiffness catheter made of a CSMP-based filiform fiber

5.1.1 Summary

In Chapter 2, we propose a method for creating filiform variable stiffness devices using conductive shape memory polymers (CSMPs), specifically variable stiffness threads (VSTs). Our approach involves a dipping technique, allowing us to manufacture VSTs with the desired thickness and electrical resistance. The CSMP layer within the VST serves multiple functions, including acting as a variable stiffness substrate, a heater, and a temperature sensor, while also being non-toxic. Utilizing this technique, we have developed single-segment and multisegmented catheters by integrating VSTs and permanent magnets into the catheter body. These catheters offer precise stiffness control and individual bending of each segment. Stiffness adjustments are achieved through a 7.6% reduction in resistance within the CSMP layer. In their soft state, each VST segment can bend up to 51°, and when switched to the rigid state, the catheter can withstand

magnetic fields up to 80 mT, thanks to a 21-fold increase in bending stiffness. Our catheter design boasts minimal dimensions, with a wall thickness of just 0.75 mm and an outer diameter of 2 mm, outperforming existing proof-of-concept VS catheters for cardiac ablation in this regard.[27] Furthermore, magnetically driven VS catheters are not limited to cardiac ablation procedures; they find applications in various organs, including the stomach, lungs, and brain.[178] The scalable fabrication process for a simple three-layer VST, as demonstrated here, can be easily adapted to produce catheters with different thicknesses to suit these diverse applications.

5.1.2 Limitations

In this study, we used a CSMP as a variable stiffness substrate, which is a phase-changing material. These materials suffer from long stiffness change time needed to reach the soft state by heating them up and then the rigid state by cooling them down. The primary limitation of the catheter developed in this chapter is its long stiffness change cycle of 126 seconds. This prolonged cycle duration results in a fourfold increase in the duration of a typical cardiac ablation procedure, which usually takes an hour. Such a long transition time can limit the use of this technology in applications that prioritize time components. As an example, fast reaction time is needed in wearable devices since the stiffness change of human muscles equals 1 second. The proposed design of a multisegmented catheter is not scalable. First, because each CSMP segment is powered through two copper electrodes. Therefore, the introduction of additional segments will lead to increase number of electrodes winded around the catheter body and going down to the base leading to an increase in the diameter and stiffness of a catheter. Secondly, proposed design has a monolithic structure where both segments are fixed and cannot be removed or other segments added.

5.1.3 Future work

Apart from the long reaction times that are tackled in Chapter 3 and 4, there are a few more improvements that can be made. The VST sensitivity to temperature is represented as a 7.6% reduction in resistance. The sensitivity can be controlled by adapting the quantity of conductive filler if a higher resistance change is required for a specific application.[174] The robustness of the electrical and mechanical properties of CSMPs under thermal and mechanical loadings in intermediate stiffness regimes should also be investigated. The precision of the dipping technique could be improved by decreasing the viscosity of the liquid CSMP mixture. Automation of the fabrication process and decrease of the CSMP mixture viscosity can be done to enhance the dipping technique's precision. The specifically designed controller can be developed to control the stiffness state in the intermediate states in addition to the soft and rigid states.[143] Further interface tests between the VST and human tissue will shed light on the fouling rate and thrombi formation caused by the heating of the CSMP layer. The VST was created using non-toxic materials like PTFE, carbon particles, polyurethane-based SMP, and biocompatible

PDMS. However, its biocompatibility is not assured solely based on non-toxic materials, so it underwent testing according to ISO 10993 standards for medical devices, including irritation, sensitization, and hemolysis tests.[179] The design should be significantly modified to provide a scalable solution. An design idea for such design is provided in the Appendix D.

5.2 Fast-response catheter made of an SMP-based variable stiffness fiber

5.2.1 Summary

In Chapter 3, we tackled the main shortcoming of Chapter 2, long transition times between soft and rigid states of a variable stiffness catheter. Therefore, we introduce an approach for the development of filiform variable stiffness technologies with fast transition times and large stiffness change, specifically termed as fast-response variable-stiffness threads (FRVSTs). When subjected to a temperature increase from 25 to 80 °C, our current design demonstrates an impressive 66-fold change in stiffness. Within the FRVST design, we incorporated a helical channel that allows for active cooling of the non-toxic shape memory polymeric (SMP) layer. This active cooling mechanism reduces the cooling time by 26 times when transitioning from the soft to the rigid state, compared to passive cooling methods. We conducted an extensive assessment of SMP materials and developed a finite element thermomechanical model to analyze the trade-offs among cooling/heating rates, bending performance, and SMP wall thickness. The fabrication process of FRVSTs involves a precise dipping and winding technique to create SMP layers and helical channels with predetermined thickness and pitch distances, respectively. Utilizing this technique, we successfully engineered both single-segment and multisegmented FRVST catheters, featuring integrated permanent magnets. Within the hospital-compliant electromagnetic navigation system (eMNS), we demonstrated the ability to achieve selective bending in each of the segments by fine-tuning the stiffness of each segment. In its soft state, the catheter exhibits a remarkable bending capacity of up to 127° in the air and 76° in water, all under the influence of a magnetic field with a magnitude of 80 mT. Upon transitioning to the rigid state, the catheter maintains structural integrity even when exposed to applied magnetic fields up to 80 mT, displaying only modest bending angles of 3.3° in the air and 19° in water. Our innovative integration of an active cooling mechanism significantly shortens the stiffening process, reducing it from 117 seconds to just 4.4 seconds. This catheter design boasts a 20-fold faster cooling rate, a 30° larger actuation stroke angle, and, concurrently, a 1.7-fold higher stiffness change factor (SCF) when compared to existing proof-of-concept multisegmented variable-stiffness catheters used in cardiac ablation. While prior variable-stiffness catheter designs, including the catheter in Chapter 2, have shown promise in simplifying tip positioning and increasing applied force, they have often extended procedure durations due to lengthy 90-second heating-cooling cycles. In contrast, our current design, featuring a brief 17-second heating-cooling cycle, offers a substantial reduction in surgical

procedure duration, making variable-stiffness catheters more practical for some real-world applications.

5.2.2 Limitations

The current fabrication procedure has already been semi-automized. However, the assembly is fully manual and consists of multiple steps, demanding a considerable level of expertise to achieve consistently high-quality results. The temperature control and heating were performed manually without an on-purpose-designed control unit, which led multiple times to the overheating of a heating wire and the destruction of a catheter. The stiffness change cycle of 17 seconds is still long for clinical real world applications including minimally invasive procedures such as catheter ablation or endoscopy with biopsy. Also, the proposed design is not scalable since both cooling systems are mutual for all SMP segments. Moreover, both segments are made of a single bulk SMP tube with two integrated heating systems.

5.2.3 Future work

As mentioned in the limitations, the manual assembly process is complex and demands experience, making it time-consuming and less robust. A new automated assembly method will enable fast batch fabrication of the catheters with a high level of accuracy. The development of a control unit capable of measuring the current stiffness state through the resistance change of the sensing wire and adjusting the applied power accordingly will enable robust use of the catheter without overheating. In Chapter 3 we performed a 5-cycle test for our catheters in air and water to assess the bending deviation after multiple actuations. The hysteresis of the actuation stroke angle after 5 cycles remains low. As a continuation, the 1 to 10 thousand-cycle test is needed to better assess the repeatability of the bending. Also, in this work, we focused our demonstration on the steering capabilities of the catheter, thus, it was not equipped with any medical procedure devices such as an ablation tip. In future research, the integration of an ablation catheter will enable the use of the catheter in in vitro tests to characterize its effectiveness on artificial human tissue.

5.3 Instant variable stiffness in cardiovascular catheters based on fiber jamming

5.3.1 Summary

Although the response times for stiffness change were successfully reduced from 126 seconds to 17 seconds in Chapter 3, it's crucial to emphasize that, despite this enhancement, the standard duration of a cardiac ablation procedure still increases by 50%. This constraint impedes its practical application in real-world scenarios. Consequently, in the chapter 4, we address the challenge of slow reaction time using

an entirely distinct variable stiffness technology compared to Chapters 2 and 3. Therefore we developed and characterized a novel multi-segment variable stiffness catheter based on fiber jamming technology, which has variable stiffness capabilities. The final catheter is suitable for remote magnetic navigation surgeries. Notably, this catheter can rapidly change its stiffness, up to 6.5 times, in just 0.6 seconds. Although the stiffness change factor of this catheter is three times lower than that of existing variable stiffness catheters utilizing phase-changing materials, experimental results demonstrate comparable bending performance in both rigid and soft states. The fabrication method we propose can be adapted to manufacture catheters of varying length, thickness, stiffness, and segment numbers, catering to diverse medical procedures like abdominal monitoring and otorhinolaryngological pathway surgeries that require catheters of different dimensions.[28,216] In a typical surgery employing conventional variable stiffness proof-of-concept catheters with up to 80 ablations, the duration is approximately 65 minutes.[217] The fastest existing variable stiffness catheter presented in Chapter 3 would extend this time by 45 minutes (17s per stiffness cycle × 2 segments × 80 ablations). Conversely, the catheter described here would only add 1.6 minutes (600ms per stiffness cycle × 2 segments × 80 ablations) to the procedure. These findings highlight that the proposed catheter not only matches the performance of other variable stiffness catheters and is compatible with remote magnetic navigation but also does not significantly prolong operation time. Minimizing surgery duration is pivotal for the adoption of variable stiffness technologies in minimally invasive procedures and other medical applications.

5.3.2 Limitations

The fast stiffness transition of our solution comes with a cost of at least three times lower SCF compared to other variable stiffness catheters based on phase-changing materials presented in Chapter 2 and 3. Also, the air evacuation leads to a geometrical change in the external sleeve. These limitations can be significant for some applications, for example, when the system has to withstand a high external impact. For other applications, such as smart clothes, the fast stiffness transition (less than 1 second) is crucial to not limit the motion of the human body.[18] To enable the fabrication of a catheter filled with a thousand fibers, we developed a novel precise manufacturing method for fibers based on pulling and winding. Due to the manual processes in the fabrication, there are tangible variations among the catheters in terms of stiffness and reaction time. Additional concern is buckling of a catheter in a rigid and soft states. It can result in instability, diminished load-carrying capacity, and as a result, leads to low applied force on the human tissue during ablation.[215] It can lead to low-quality ablation and cardiac arrhythmia recurrence. Also, the scalability of the proposed design is challenging since every segment requires its own evacuation channel with a diameter multiple times larger than the size of a single fiber in a segment. Therefore, addition of new segments leads to decrease of a number of fibers at the same filling rate, which results in lower stiffness change between soft and rigid states.

5.3.3 Future work

To ensure consistent performance of all the devices, the fabrication procedure can be standardized with full automation to eliminate manual processes. Aiming at precise steering capabilities, Hall sensors will be developed and integrated into the catheter body to enable position and orientation feedback. Animal tests will be conducted to further validate the efficacy of the catheter under more challenging conditions such as blood flow.

5.5 Outlook

Filiform variable stiffness technologies developed in this thesis increases the dexterity and applied force of cardiac ablation catheters. The same technologies can be then translated into endoscopes to provide additional support during human tissue sample removal (biopsy). We believe that the filiform variable stiffness technologies developed in this thesis can be used beyond cardiac ablation catheters and medical devices in general. A flexible design adaptation in terms of diameter, stiffness, length, and resistance enables the development of medical devices with different mechanical and geometrical specifications such as endoscopic devices Furthermore, with a continuously growing number of surgeries, medical devices have to be able to adjust their size or even functionality for a specific surgery and patient by minor design modifications that can be done on the spot right before the surgery starts. Thus, it is important to develop medical devices with a scalable and modular design that can be rapidly assembled. Therefore, in Appendix D “Scalable variable stiffness technology”, we introduce early results on a scalable method to develop modular variable stiffness fibers, whose length and number of active components can be adjusted for a specific application.

The simplicity of the dipping technique allows for effortless adjustment of variable stiffness fibers used in rehabilitation fabrics, enabling easy scaling up or down as needed. We anticipate that fabrication and functional fiber capabilities make them suitable for applications other than medicine, particularly in scenarios where system size and weight are pivotal factors. These potential applications encompass integration into space or aerial vehicles, facilitating diverse modes of locomotion.[10] Furthermore, these filiform technologies offer potential for integration into smart fabrics, allowing for weaving into textiles. We envision that in the future smart fabric can replace conventional materials in ordinary clothes to enhance human performance in daily tasks. Imagine a pullover (the title page of Chapter 5) that can help you lift heavy bags by using in-fabric-integrated actuators. It could be propagated beyond the aforementioned scenario to more complex cases that involve the use of in-fabric-integrated sensors, actuators, variable stiffness elements, and power sources together.

5.6 Additional Soft Robotics Projects

Publication note: The work presented in this sub chapter is based on

Y. Piskarev, J. Shintake, V. Ramachandran, N. Baugh, M. D. Dickey, and D. Floreano, *Lighter and stronger: Cofabricated electrodes and variable stiffness elements in dielectric actuators*, in Advanced Intelligent Systems, Vol. 2, No. 10, p. 2000069, Oct. 2020.

Y. Piskarev, E. Desbouis, V. Ramachandran, J. Yang, N. Baugh, J. Shintake, M. D. Dickey, and D. Floreano, *Enhancement of Pressure-Sensitive Adhesive by CO2 Laser Treatment*, in Advanced Engineering Materials, Vol. 24, No. 10, p. 2200355, Oct. 2022.

Y. Piskarev, A. Devincenti, V. Ramachandran, P.-E. Bourban, M. D. Dickey, J. Shintake, and D. Floreano, *A Soft Gripper with Granular Jamming and Electroadhesive Properties*, in Advanced Intelligent Systems, Vol. 2200409, Mar. 2023.

As the main contribution of this thesis, we highlighted the project on filiform variable stiffness technologies for medical devices. In addition to medical devices and due to my interest in soft robotics, throughout these years we worked on many satellite projects in collaboration with other research groups. These projects include the variable stiffness dielectric elastomer actuator, the soft universal gripper, and the method to improve the fabrication of soft robots. In the following paragraphs, we briefly introduce these works and then discuss why and how these devices can be translated into medicine.

As we discussed before, variable stiffness in soft actuators is crucial because the inherent compliance of soft robots often makes it difficult for them to exert forces on surrounding surfaces or withstand mechanical loading.[148] Therefore, variable stiffness soft actuators were introduced. Existing variable stiffness devices have a limitation where the actuation component and the variable stiffness component are fabricated separately, adding complexity to both the device structure and the manufacturing process.[13,29] To address this, we introduce a new design that integrates both functionalities into a compact device. This device uses a shared electrode made of low-melting-point metal for electrostatic actuation and stiffness variation, simplifying the structure and expanding design possibilities. It has a compact and lightweight structure with a thickness of 930 μm and a mass of 0.7 g. It exhibits a stiffness change of 183×, a bending angle of 31°, and a blocked force of 0.65 mN. Thanks to the lightweight feature, the stiffness change per mass of the

actuator (261× g−1) is 2.6 times higher than that of the other type of variable stiffness dielectric elastomer actuators.

While working on the variable stiffness actuator, we serendipitously discovered a new method to enhance the adhesion of the well-known "Very High Bond" (VHB) tape using CO_2 laser treatment. VHB is a widely recognized pressure-sensitive adhesive (PSA), which is a polymeric film that adheres to surfaces upon pressure and can be removed without leaving residues.[218–220] They are valued for their convenience, affordability, and versatility in applications ranging from domestic use to aerospace and medical robotics, with VHB being particularly favored for its elasticity in soft and stretchable devices.[221–223] Our novel treatment method cleaved the polymer network on the surface of theVHB, improving adhesion without altering the bulk material. We conducted tests on various substrates, assessing mechanical properties like tackiness, surface viscosity, and peeling forces. Results showed a higher concentration of non-crosslinked materials in VHB after treatment, leading to better adhesion. This study presents a straightforward and characterized method to increase the adhesion of the widely-used VHB using a readily accessible laboratory machine, without adding extra chemical substances. This approach facilitates the development of more effective connective layers for experimental soft robotics devices or domestic purposes and can be potentially used for other pressure-sensitive adhesives.

In the last satellite project, inspired by the human hand's softness, which lets humans handle various objects, we worked on a new versatile soft gripper. There is a rising interest in creating universal soft grippers for objects of different shapes, textures, and fragility.[31,180,224,225] However, designing a single gripper that can manage objects with varying surfaces and properties, including flat or fragile items, remains a challenge. In this project, we introduce a soft gripper designed to handle objects of varied shapes, surface conditions, and mechanical properties (stiff, fragile, soft, and deformable). Our design merges two distinct technologies: granular jamming (GJ) for stiffness modulation and electroadhesion (EA) for adhesion control. This combination not only addresses the individual shortcomings of each technology but also equips the gripper to execute complex grasping tasks involving different materials, textures, and geometries. For instance, the gripper can grasp and turn a book's hardcover and also flip its individual pages. Moreover, we demonstrated how the gripper can be used to make tea by grasping and moving a cup and teabag.

The aforementioned soft gripper and variable stiffness actuator, which offer robotic conformability and adaptivity, can be translated into medicine and greatly benefit from their soft nature, allowing force-tunable and safe interactions with the human body both ex vivo and in vivo.[143,226] Similar soft actuators have already been used as biomedical assistive devices to recover heart function after heart failure by providing additional actuation.[227] Moreover, soft grippers, especially miniaturized ones that can adapt to the shape of any soft tissue, have the potential to revolutionize methods for measuring the stiffness of small tumors and enhance drug delivery efficiency.[228]

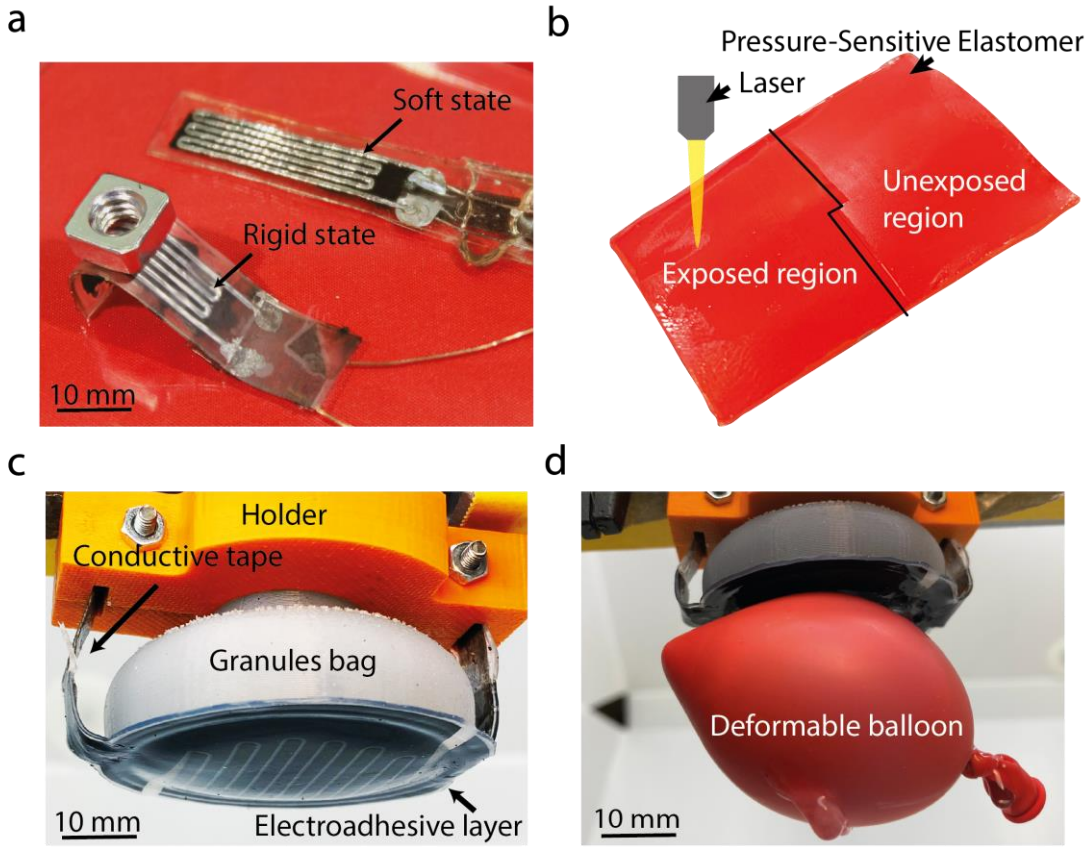

Figure 5. 1 Soft robotics satellite projects.
a) The variable stiffness dielectric elastomer actuator with simplified design.[173] b) The method to enhance the adhesion of the "Very High Bond" (VHB) tape using CO_2 laser treatment.[229] c-d) A soft gripper with granular jamming and electroadhesive properties.[230]

To enable a smooth transition of existing actuators and grippers into medicine, crucial challenges have to be overcome including the precise fabrication using only biocompatible materials and the engineering of untethered soft devices by integration of portable or remotely chargeable power sources.[226] We believe that our surface treatment method could improve the bonding of different soft elastomeric components and increase the robustness and durability of novel medical soft robotic devices.

A Appendix of Chapter 2

Supplementary Videos

All videos can be downloaded and viewed through one of the links:

https://drive.switch.ch/index.php/s/sO7oa40S6iuGsGu

https://drive.google.com/drive/folders/1ehJ_AjNNBe4Ox2kjiUmhPrPMEZe0T3hn?usp=sharing

Supplementary Video 2.S1: VST heating/cooling times

Supplementary Video 2.S2: VST bending at different temperatures

Supplementary Video 2.S3: One-segmented catheter characterization under an external magnetic field

Supplementary Video 2.S4: Demonstration of two-segmented catheter performance

Supplementary Document 2.S1

Supplementary document 2.S1, which presents the results of cytotoxicity study of the CSMP material can be downloaded and viewed through one of the links:

https://drive.switch.ch/index.php/s/sO7oa40S6iuGsGu

https://drive.google.com/drive/folders/1ehJ_AjNNBe4Ox2kjiUmhPrPMEZe0T3hn?usp=sharing

Supplementary Figures and Notes

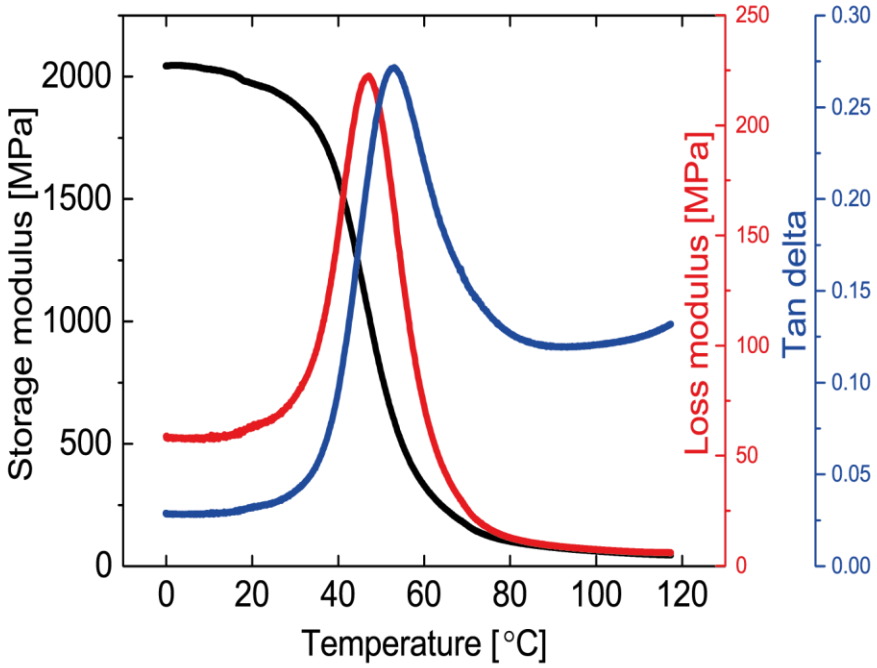

Figure 2.S 1 Thermomechanical characterization of CSMP.
The storage moduli (black), loss moduli (red), and tangent delta (blue) of CSMP as the temperature was increased from 0 to 120°C. The increase in temperature resulted in a 47-fold increase in stiffness. The stiffness change of the three samples was tested using a dynamic mechanical analyzer (TA Instruments DMA Q800).

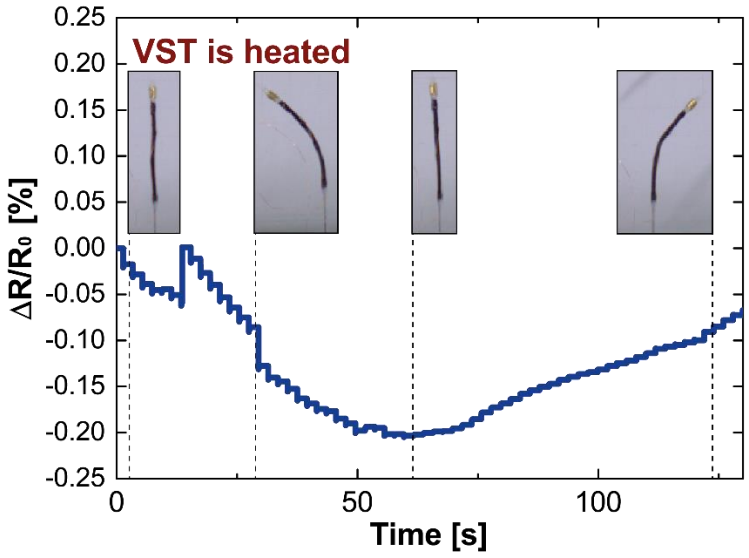

Figure 2.S 2 The VST resistance change when bent.
The VST was heated to a temperature of 80°C and bent while the resistance was recorded. The percentage change in resistance was 0.2% for a 5% increase in temperature.

Modeling the surface temperature of an insulation layer

The thickness of the insulating layer was modeled based on the rate of heat flow through a cylindrical wall. In this study, we modeled the temperature behavior in three different environments: air, water, and blood. The heat flow rate (Q) is proportional to the temperature difference across an object (T_1 and T_2), the area available for heat to flow through (A), and the thermal conductivity of the material (k), and it is inversely proportional to the thickness of the PDMS insulation layer (x):

$$Q = kA\frac{T_1 - T_2}{x}$$

where the area A for the cylindrical case is given as

$$A = 2\pi l$$

and the thickness x is given as

$$x = \ln\frac{r_2}{r_1}$$

Based on this model, we can calculate the surface temperature of the insulating layer for different thicknesses of a silicone layer expressed in terms of the radius of a VST. The biocompatibility requirements will be fulfilled if the insulating layer thickness is increased by 65 µm (see Figure 2.S3a, Supporting Information). Changing of material from PDMS to PFPE will also lead to fulfilment of the biocompatibility requirements without any design changes (see Figure 2.S3b, Appendix A).

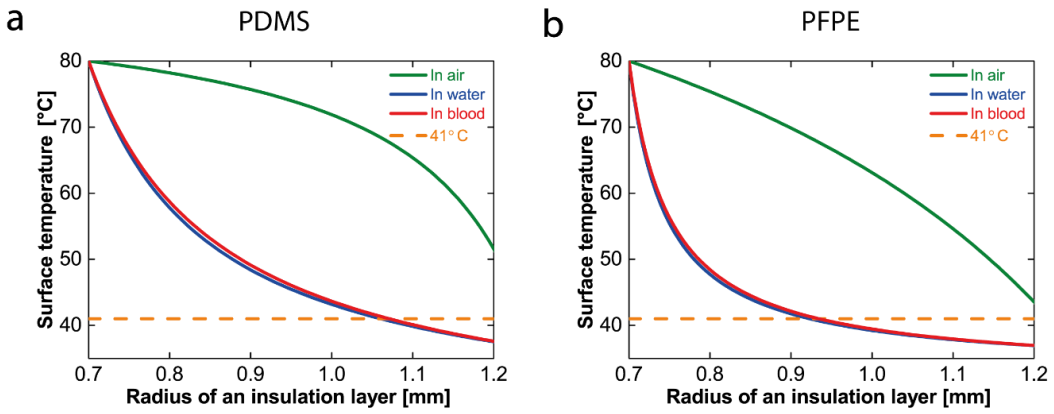

Figure 2.S 3 Modeling of the surface temperature of the insulating layer under different environmental conditions and thicknesses.
a) The thickness of the PDMS insulating layer fulfills the biocompatibility requirements (surface temperature equal to or less than 41°C – dashed orange line) in blood at a thickness of 315 µm. b) The thickness of the PFPE insulating layer fulfills the biocompatibility requirements of blood at a thickness of 215 µm due to the lower thermal conductivity.

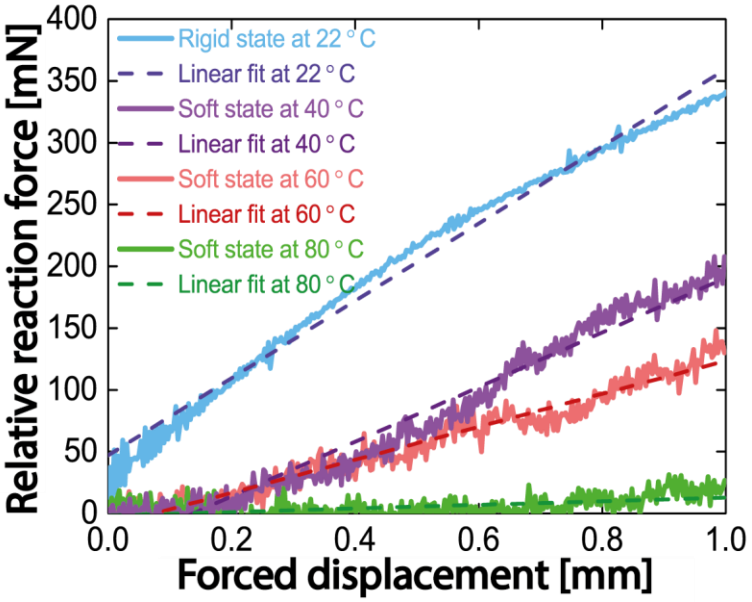

Figure 2.S 4 The nonfiltered reaction force of the VST against forced displacement in a three-point flexural test.
Linear fittings are used to calculate the stiffness change coefficients.

B Appendix of Chapter 3

Supplementary Videos

All videos can be downloaded and viewed through one of the links:

https://drive.switch.ch/index.php/s/ovVTG3rknqLpWPC

https://drive.google.com/drive/folders/1iG2MaZDYwULD-uI4UddiDiSxTQlf6nGT?usp=sharing

Supplementary Video 3.S1: Heating-cooling cycle of the FRVST using active cooling.

Supplementary Video 3.S2: FRVST load-bearing performance at different temperatures.

Supplementary Video 3.S3: Fabrication process steps of the FRVST using on-custom-made dipping and winding machines.

Supplementary Video 3.S4: Fast stiffness change in the single-segment catheter under an external magnetic field.

Supplementary Video 3.S5: Selective stiffening of two FRVSTs in the multisegmented catheter.

Supplementary Video 3.S6: Multisegmented catheter avoids wall contact due to the stiffening of the FRVST.

Supplementary Video 3.S7: Underwater demonstration of multisegmented catheter performance inside the 3D phantom of the human heart.

Supplementary Figures and Notes

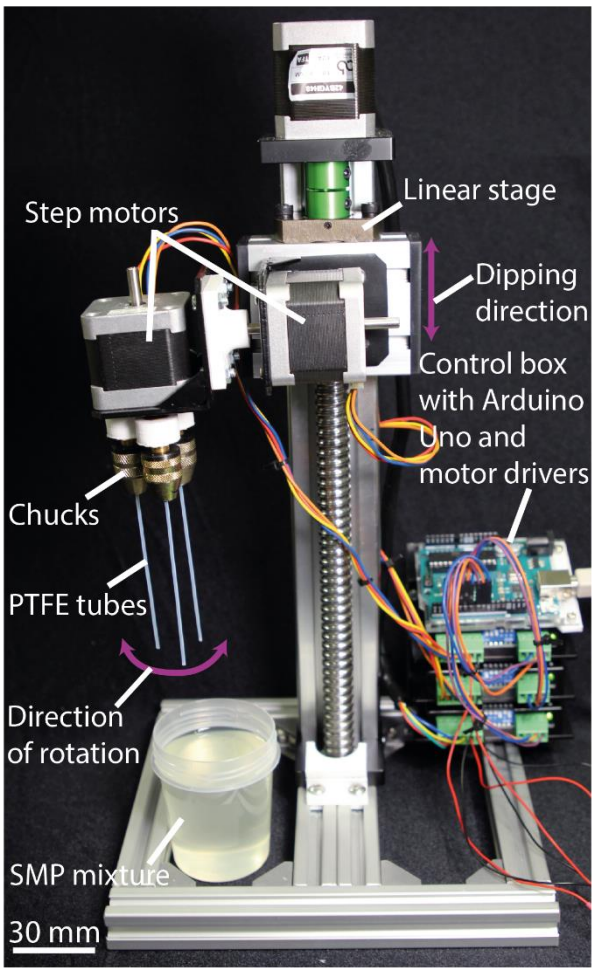

Figure 3.S 1 An automated custom-made dipping setup.

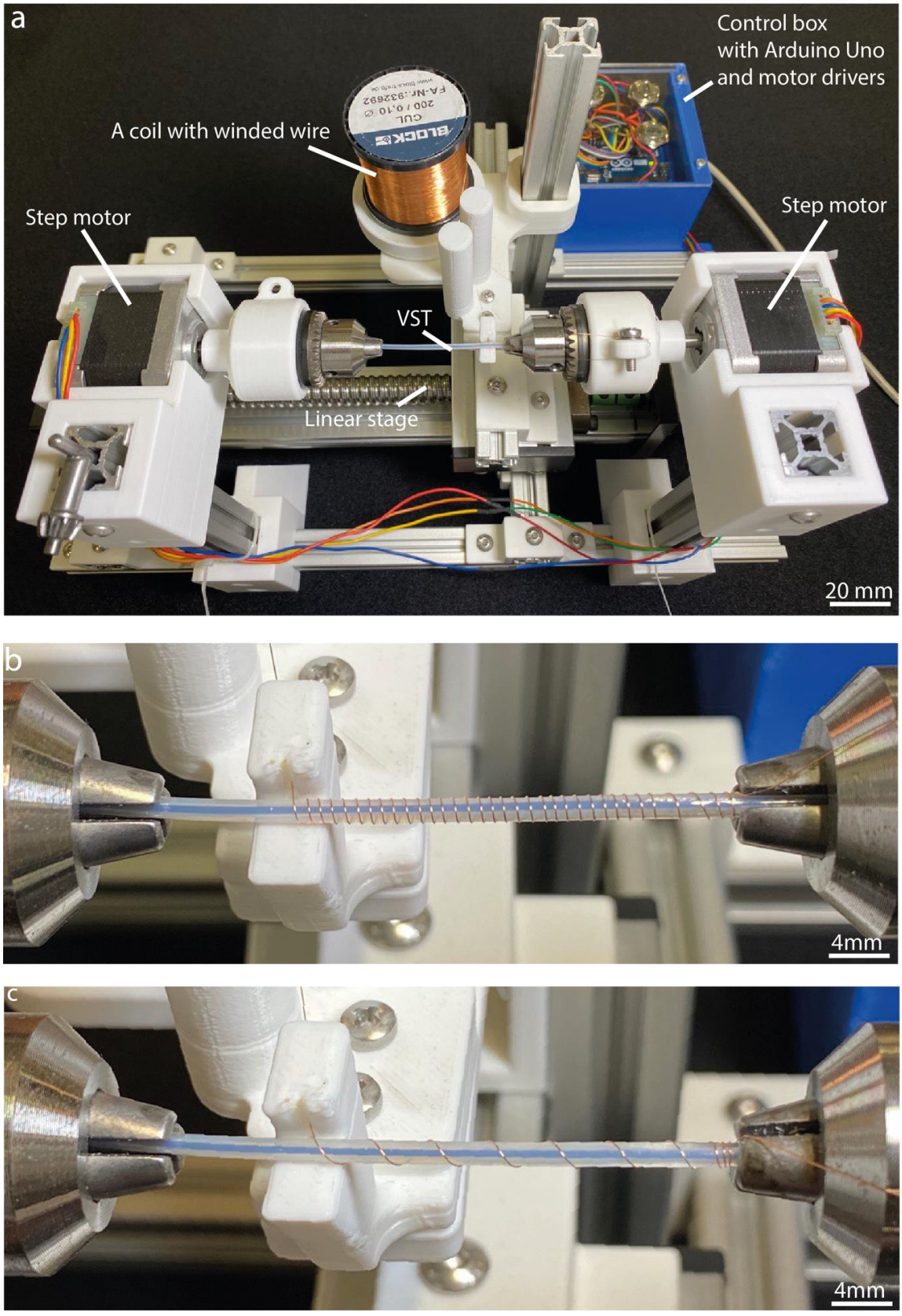

Figure 3.S 2 Winding machine.
a) On-custom-made winding machine. b-c) The helical shape at speed ratios between the top and bottom motors of 0.2 and 1, respectively.

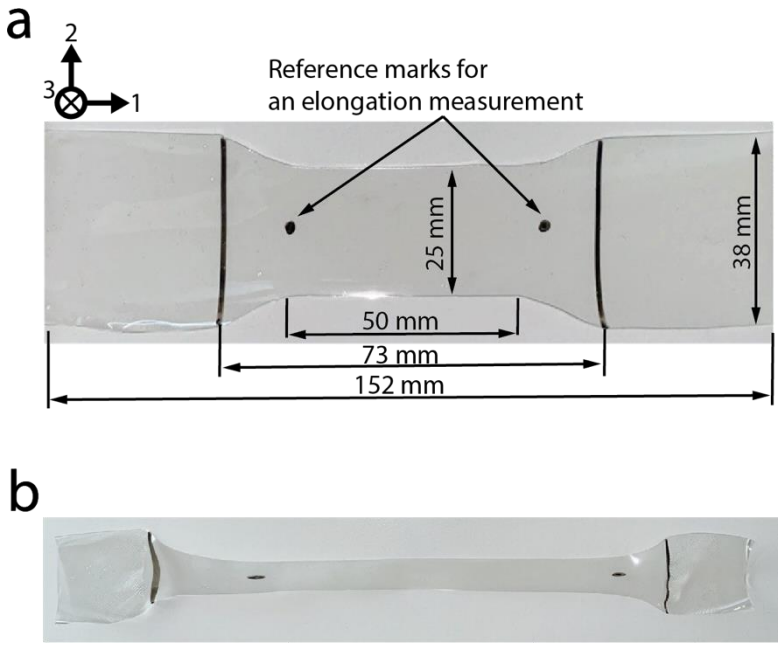

Figure 3.S 3 Dog-bone sample design for a tensile test.
a) Schematics and sizing of the SMP sample. b) The sample shape after elongation up to 200% strain.

3.S4. Parameter identification for the linear and Yeoh models

The data acquired from the tensile test were analyzed to determine the mechanical properties of the SMP samples. We applied the linear and Yeoh models to the SMP samples at all temperatures (21, 36, 50, 60, and 80 °C) to investigate the Young's modulus and material constants of the hyperelastic material models. A linear model was applied using a standard function in OriginPro 2022 (Academic), OriginLab Corporation. This model showed a good fit with the data collected for the samples at 21 °C at a strain of 2.5% with a Young's modulus equal to 3400 MPa. For all the remaining temperatures and higher strains, the Yeoh hyperelastic material model showed a better fit with the experimental results. We selected this model because it provides the best fit for the entire range of experimental data for polyurethane elastomers used in biomedical applications, including large deformations (> 150% strain).[188,189] The strain energy density function of the Yeoh model is written as follows:

$$W = \sum_{i=1}^{3} C_i (I_1 - 3)^i , \qquad (S2)$$

where C_i is a material constant and I_1 is the strain invariant ($I_1 = \lambda_1^2 + \lambda_2^2 + \lambda_3^2$). λ_1, λ_2, and λ_3 are the stretch ratios in the length, width, and thickness directions, respectively. The stretch ratios are defined as:

$$\lambda_1 = \frac{l_{final}}{l_0}, \qquad \lambda_2 = \frac{\omega_{final}}{\omega_0}, \qquad \lambda_2 = \frac{h_{final}}{h_0}, \qquad (S3)$$

where l_0, l_{final}, ω_0, ω_{final}, h_0, and h_{final} are the initial length, final length, initial width, final width, initial thickness and final thickness of the dog-bone sample, respectively. Assuming that the material is incompressible ($\lambda_1\lambda_2\lambda_3 = 1$), the stress along the length direction (tensile direction) is expressed as follows:

$$\sigma_1 = \lambda_1 \frac{\partial W}{\partial I_1} = 2\left(\lambda_1^2 - \frac{1}{\lambda_1}\right)\sum_{i=1}^{3} iC_i\left(\lambda_1^2 + \frac{2}{\lambda_1} - 3\right)^{i-1}. \quad (S4)$$

Eq. (S4) was fitted to the determined stress–strain relationship to obtain the material constants C_1, C_2, and C_3. The shear modulus was then obtained based on the consistency condition for the Yeoh material model ($\mu = 2C_1$). Young's modulus Y of the material was determined as:

$$Y = 2\mu(1 + \nu), \quad (S5)$$

where the Poisson's ratio ν of the SMP, determined via Eq. S1, is based on the tensile test data and is equal to 0.48.

Table 3.S4. Fitted parameters of the Yeoh model

Temperature (°C)	Young's modulus (MPa)	C1 (MPa)	C2 (MPa)	C3 (MPa)
21	3762	600	-41200	1790000
36	774	130.7	-682.3	1518.8
50	19.7	3.33	-6.42	11.47
60	14.3	2.42	-3.58	5.3
80	6.8	1.1492	-1.587	2.5877

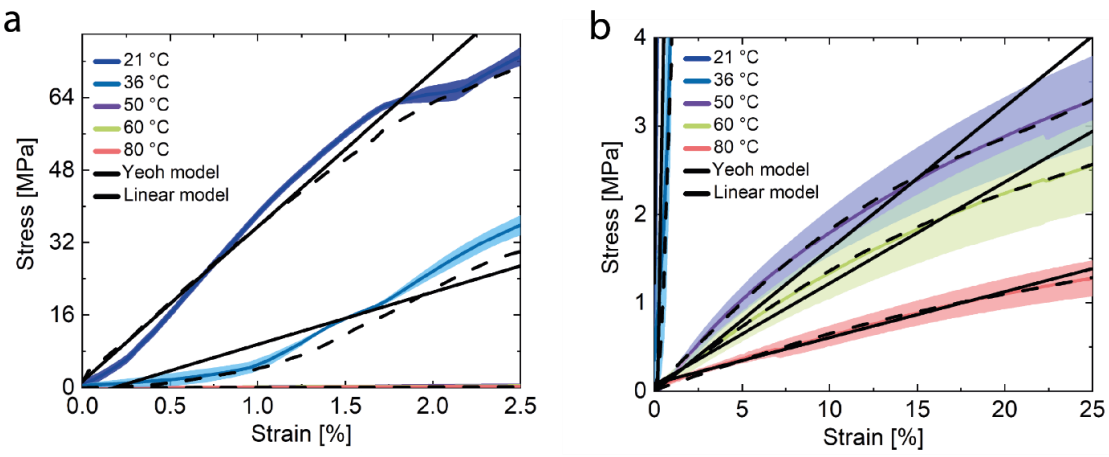

Figure 3.S 4 Stress–strain curves with fits using the linear and Yeoh models. The Yeoh model shows a better fit with empirical data for all temperatures from 36 to 80 °C than the linear model.

3.S6. Finite element simulation of elongation and bending at different material temperatures

To discuss the bending performance of catheters with different SMP wall thicknesses and mechanical properties, two finite element models were built using the commercially available software package ABAQUS.

First, a simplified three-dimensional deformable model of the SMP tube was developed and verified by an experiment (Figure 3.2e). The SMP material was modeled using a thermal-dependent Yeoh hyperelastic material model (Table 3.S4 in the Supporting Information). Ten-node quadratic tetrahedron elements (ABAQUS element type C3D10H) were used to mesh the parts with a node size of 0.00013 m. The model accurately predicts an elongation of the rigid and soft SMP tubes with a length and inner and outer diameters of 30 mm and 0.7 mm and 2.2 mm under a dead load of 0.2 kg, respectively. The dead load was applied to the diameter center point, which was coupled with all diameter nodes. The modeled elongations (1.9 and 3.3 mm) and experimental elongations (2 and 3.2 mm) at 60 and 80 °C were compared. The boundary conditions for the model were consistent with the experiment.

Second, the catheter bending model of a typical actuation cycle was built. The catheter model consists of an outer SMP layer and an inner silicone layer. The geometric parameters of the SMP and silicone layers as well as the boundary conditions were consistent with the experiment. The SMP material was defined and assigned to the outer catheter tube using the thermal-dependent Yeoh hyperelastic material model to simulate the glass transition behavior of the SMP (Table 3.S4 in the Supporting Information). The silicone layer was also modeled using the Yeoh material model with coefficients C1 and C2 equal to 110,000 and 20,000 Pa, respectively.[231] The thermal dependence was not used for the silicone layer due to the low mechanical property change in the temperature range from 20 to 80 °C. Ten-node quadratic tetrahedron elements (ABAQUS element type C3D10H) were used to mesh both parts with a node size of 0.00005 m. The bending model consists of several steps, namely, bending of the catheter in the rigid state with an applied external moment of 0.000946 Nm, heating of the SMP layer from 20 to 80 °C, bending of the catheter in the soft state, cooling of the SMP layer to 20 °C, and recovery to the initial shape by heating and applying an opposite external momentum. The momentum was calculated as a product of the external magnetic field magnitude of 80 mT, dipole moment of a permanent magnet on the tip of the catheter of 0.118 A*m2, and the angle between these two vectors equals 90°. In this model, a constant and uniform temperature distribution of 20 and 80 °C was applied to the SMP and silicone tubes. To better understand how the SMP Young's modulus and thickness influence the bending performance in the rigid and soft states, we simulated catheter bending with SMP layer thicknesses of 0.275, 0.362, 0.45, 0.537, and 0.62 mm. The same thicknesses were used to simulate the heating and cooling processes described in Section 3.S12 in the Supporting Information.

3.S7. Stiffness change factor determination

The stiffness change factor (SCF) of the device can be tuned by changing the geometrical parameters (second moment of area) and the average Young's modulus of the cross-sectional area. The SCF is given by the following relation:

$$\mathrm{SCF} = \frac{K_r}{K_s} \tag{3.1}$$

where K_r and K_s are the bending stiffnesses of the FRVST in the rigid and soft states, respectively.[13] The effective bending stiffness of the FRVST, K, is defined by the following relation:

$$K = \sum E_{\mathrm{avg}} I_i \tag{3.2}$$

where E_{avg} is Young's modulus of the entire device. I_i is the second moment of area (moment of inertia), which is determined by the different layers making up the FRVST, that is, an internal hollow PTFE tube, a helical channel made of a fluorocarbon wire, and an SMP external layer with a helical copper heating wire.

The bending stiffnesses in rigid and soft states were empirically determined using a three-point flexural test and Euler–Bernoulli beam theory. Considering the boundary conditions, the deflection of the FRVST is expressed as:

$$\delta = \frac{F l^3}{48 E I} \tag{3.3}$$

where δ is the deflection of the FRVST at the point of applied force F, l is the beam length, E is Young's modulus, and I is the moment of inertia. The point load F was applied in the middle of the FRVST. The multiplication of two parameters EI represents the bending stiffness K of the device (Equation 3.2). The corresponding SCF was defined for all temperatures using Equations 3.1-3 and empirical data from Figure 3.3d.

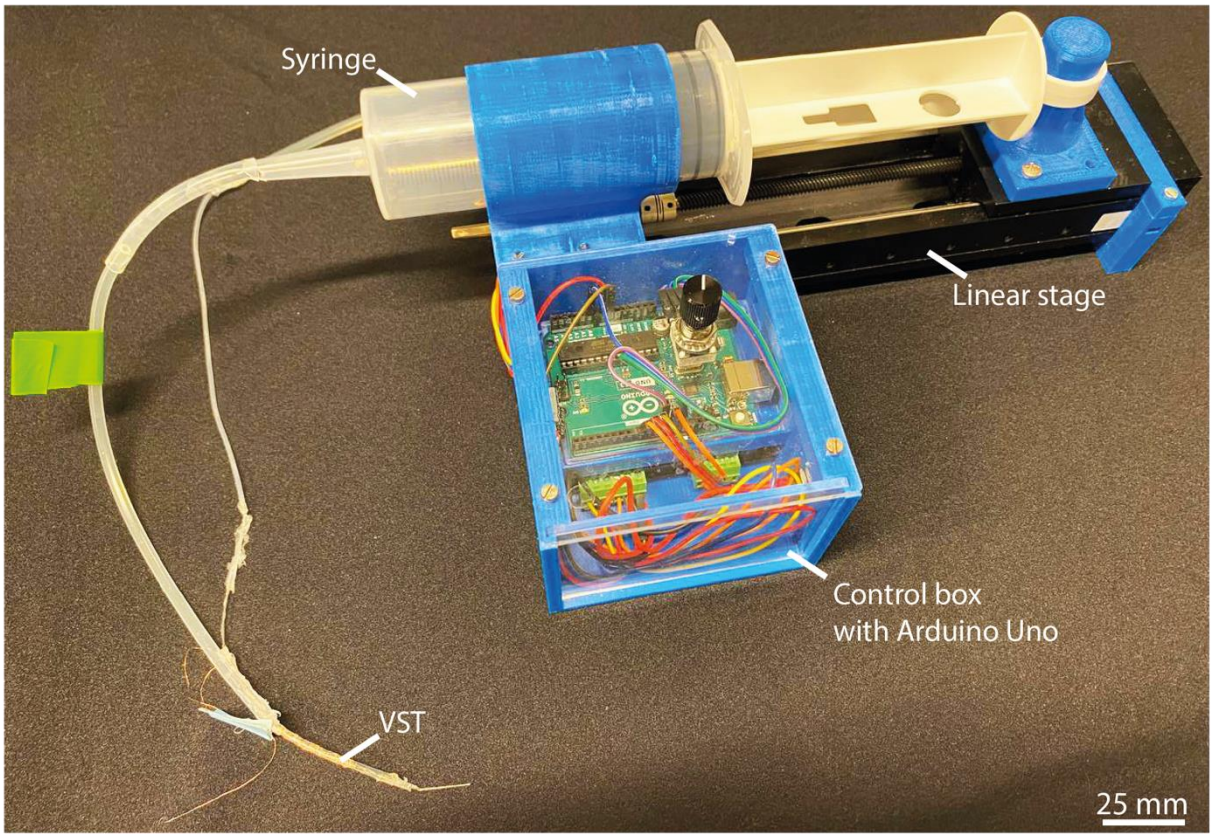

Figure 3.S 5 On-custom-made syringe pump.

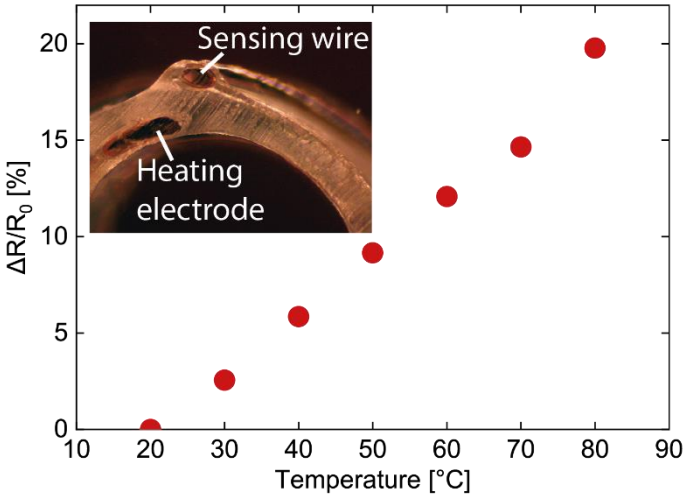

Figure 3.S 6 Resistance characterization.
A cross-sectional area of the FRVST and characterization of the resistance drop of the sensing wire at different temperatures. The initial resistance is equal to 2.73 Ohms.

3.S10. SMP Specific heat capacity characterization

Differential scanning calorimetry (DSC 8000. PerkinElmer) was used to measure the specific heat capacity of polyurethane (PU) SMP (MM5520. SMP Technologies). Specific heat capacity measurements by DSC require the use of a well-characterized

reference material to obtain satisfactory results. The instrument was calibrated with indium and lead calibration standards. First, a blank (empty furnace) measurement was made to determine the instrument baseline. Then, 4 mg of SMP was encapsulated in an aluminum pan. The material was heated from 0 °C to 100 °C at a rate of 10 °C/min in a 20 mL/min N2 flow. The experiment was performed utilizing three samples. Heat flow data collected from the DSC experiment were averaged and used to calculate the resulting specific heat capacity of the SMP. The specific heat capacity varied from 2–2.2 J/g*°C in the working range from 20-80 °C. To simplify the modeling of SMP, we assumed that the specific heat capacity was constant and equal to 2.1 J/g*°C.

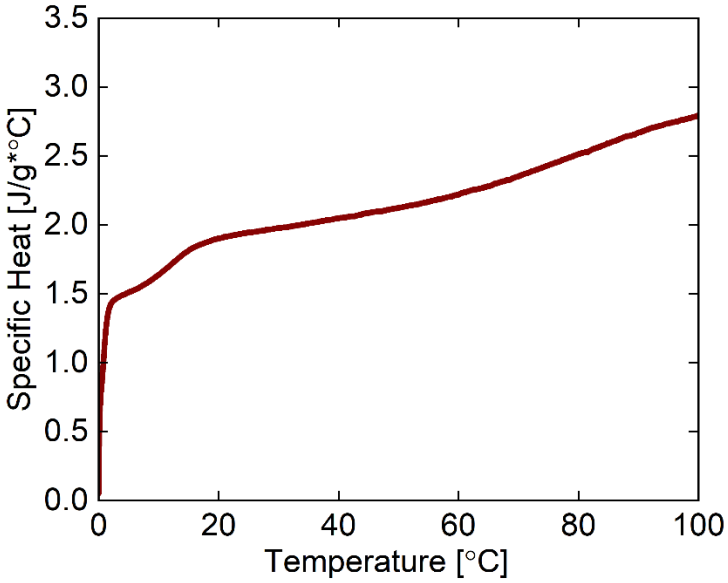

Figure 3.S 7 Specific heat capacity of SMP
Specific heat capacity of SMP MM5520, SMP Technologies.

3.S12. Finite element simulation of heating and cooling processes

To estimate the duration of the heating-cooling cycle of the catheter and heat distribution inside the SMP layer, coupled thermal-electrical analyses using ABAQUS were conducted.

To develop the model, the material properties of the SMP, including density, electrical conductivity, specific heat capacity, and thermal conductivity, were identified. The density was determined to be 81.15*10-6 kg/mm3 by dividing the mass by the volume of three samples. Electrical conductivity was defined as 0.11*10-3 1/Ohms*mm at 1 A applied. The specific heat was measured using DSC (Section 3.S10 in the Supporting Information) and was equal to 2100 J/kg*K. A thermal conductivity value of 210 W/mm*K was provided by SMP Technologies. The density, electrical conductivity, specific heat, and thermal conductivity of the copper were 8.96*10-6 kg/mm3. 58.8*103 1/Ohms*mm. 389 J/kg*K. and 0.4 W/mm*K, respectively.

The model represents a three-layer tubular structure, which consists of an inner SMP tube, a heater, and an outer SMP tube. The inner and outer SMP tube thicknesses were defined as 0.1 and 0.25 mm, respectively. The heating circuit's design was approximated as a

hollow cylinder with a wall thickness of 0.1 mm, an internal radius of 0.8 mm, and a length of 0.5 mm. Both the SMP tubular structures and a heater were modeled using twenty-node quadratic coupled thermal-electrical brick elements (ABAQUS element type DC3D20E). A hexahedral mesh with an approximate global size of 0.5 was applied. Three control points were placed on the outer and inner surfaces of the SMP layers and on the outer surface of the heating layer.

Each simulation in air consists of three intervals: initial convection between a catheter and ambient environment, heating of the heater, and active cooling by convection between water in the cooling channel and the catheter. The entire tubular structure was initially subjected to a uniform temperature field of 25 °C, which equals room temperature. For ambient conditions, the convective heat transfer coefficients for air and water in the cooling channel were defined as 5*10-6 and 5800*10-6 W/(mm2*K).[232–234] A sink temperature of 25 °C was applied to all convection interactions.

To investigate the transient heating process with a power of 2-2.5 W applied to the heating wire of the catheter (the voltage and current were equal to 2-2.4 V and 1.5-1.66 A in the empirical experiment), we imposed a surface current of 55 A/mm2, which corresponds to the same emitted power over a heating layer as a winded heating wire with a 0.1 mm diameter in a real-case scenario. The thicknesses of the inner SMP layer varied from 0.05 to 0.15 mm with a step size of 0.025 mm. The thickness of the outer SMP layer was determined to be 2.5 of the inner thickness at each of the simulations. After the heating step, the surface current was removed, and the cooling convection step was initiated. Transient analysis was used for all three modeling steps.

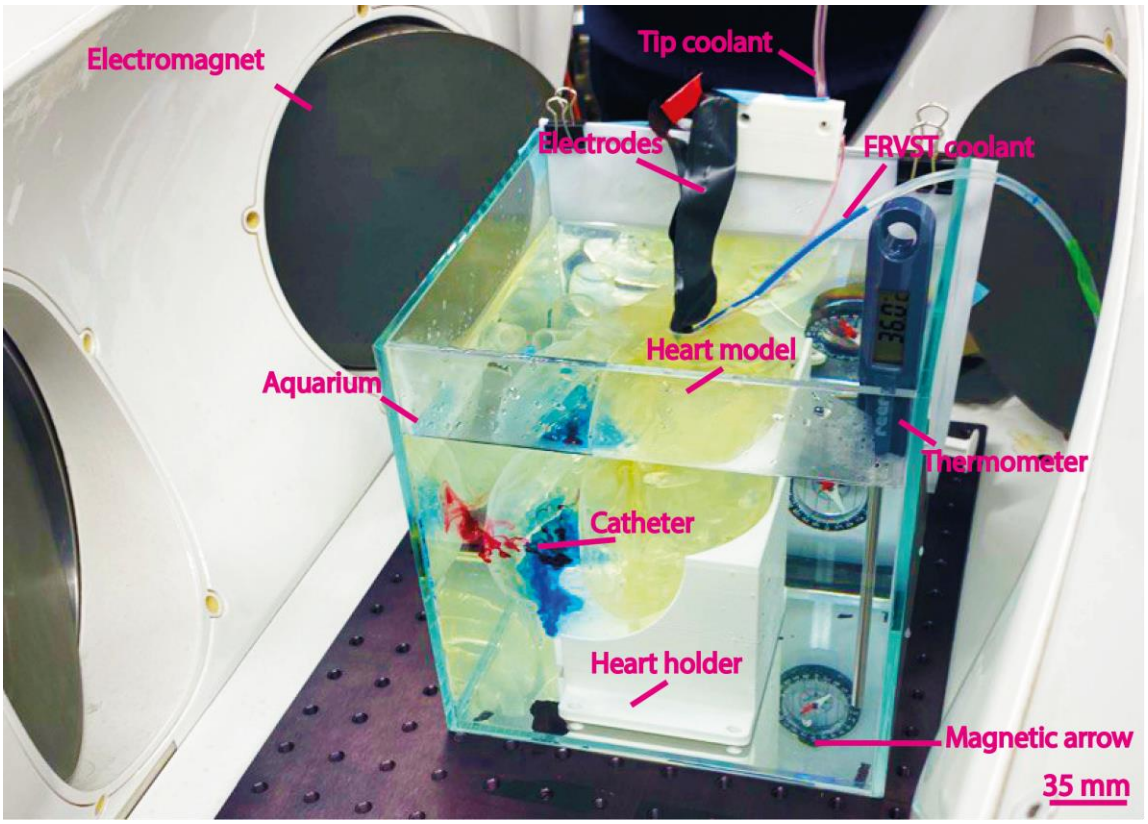

Figure 3.S 8 Setup for catheter characterization.
Setup for the underwater demonstration of the catheter performance in the 3D printed phantom of the human heart performed in the electromagnetic navigation system (eMNS).

C Appendix of Chapter 4

Supplementary Videos

All videos can be downloaded and viewed through one of the links:

https://drive.switch.ch/index.php/s/6GtpELKITKuFtvG

https://drive.google.com/drive/folders/1gZ47bvtABoLDvwnvdoS6Xf1bB6bFq7Tj?usp=sharing

Supplementary Video 4.S1: Fabrication of two-segment catheter.

Supplementary Video 4.S2: Single-segment catheter characterization.

Supplementary Video 4.S3: Demonstration of fast stiffness change of the catheter.

Supplementary Video 4.S4: Two-segment catheter bending demonstration.

Supplementary Video 4.S5: Two-segment catheter demonstration with 3D phantom of a human heart.

Supplementary Figures and Notes

4.S1. SCF requirement for VS catheter

SCF is used to define the VS performance, which is given as

$$SCF = \frac{K_r}{K_s} \quad (4.S1)$$

where Kr and Ks are the stiffness of the VS catheter in the stiff/rigid and soft states, respectively.

The stiffness of the catheter is obtained using the 3-point bending test (fig. 4.S10a).

$$K = \frac{F}{y} = \frac{48EI}{L^3} \quad (4.S2)$$

where F is the point force applied to the catheter. L is the distance between the two lateral supports of the 3-point bending test setup. y, E and I are the middle deflection, elastic modulus and second moment of area of the catheter, respectively.

Therefore,

$$SCF = \frac{K_r}{K_s} = \frac{\frac{48EI_r}{L^3}}{\frac{48EI_s}{L^3}} = \frac{I_r}{I_s} \quad (4.S3)$$

where Ir and Is are the second moment of area of the catheter in the rigid and soft states, respectively.

When the catheter is placed in the magnetic field, the bending moment of the magnetic field M will cause deflection δ in the catheter (fig. 4.S10b).

$$\delta = \frac{Ml^2}{2EI} \quad (4.S4)$$

where l is the length of the catheter.

Therefore,

$$SCF = \frac{I_r}{I_s} = \frac{\frac{Ml^2}{2E\delta_r}}{\frac{Ml^2}{2E\delta_s}} = \frac{\delta_s}{\delta_r} \quad (4.S5)$$

where δr and δs are the deflections of the catheter in the rigid and soft states, respectively.

The general requirement for the VS catheter is that, under the same magnetic field, its deflection in the rigid state δr should be less than 25% of the deflection in the soft state δs. Therefore, the desirable SCF the VS catheter should achieve is 4 and above.

$$SCF = \frac{\delta_s}{\delta_r} \geq 4 \quad (4.S6)$$

4.S2. Simplified FJ modeling of the relation between SCF, fiber size and fiber number.

When bending the catheter in the stiff and soft states with the same method, for example, the 3-point bending method (fig. 4.S10a), the SCF will be the ratio of the second moments of area of the catheter in the stiff and soft states as given in equation 4.S3.

For the FJ catheter, we can simplify it as a fiber bundle with N fibers confined in a cylindrical space with a circular cross-section area at A. In the stiff state, we assume there is no relative sliding between the fibers, and therefore the fiber bundle can be considered a solid beam. Therefore,

$$I_r = \frac{\pi R^4}{4} \tag{4.S7}$$

where R is the radius of the cross-section circle of the FJ beam, which is $\sqrt{\frac{A}{\pi}}$.

In the soft state, we assume that the fibers in the fiber bundle can bend freely around their own central axes. Therefore,

$$I_s = N \cdot \frac{\pi r^4}{4} \tag{4.S8}$$

where N is the number of fibers and r is the radius of the single fiber, which can be estimated as $\sqrt{\frac{A}{N\pi}}$.

Therefore,

$$SCF = \frac{I_r}{I_s} = \frac{\frac{\pi R^4}{4}}{N \cdot \frac{\pi r^4}{4}} = \frac{\frac{\pi \sqrt{\frac{A}{\pi}}^4}{4}}{N \cdot \frac{\pi \sqrt{\frac{A}{N\pi}}^4}{4}} = N \tag{4.S9}$$

Therefore, a higher SCF of the FJ beam can be achieved with a larger number of fibers with thinner thickness.

4.S3. PLA fiber production

PLA fibers are produced by winding machine I pulling melted PLA filament from the nozzle of an Ultimaker 3D printer. The printer does not have the function to extrude PLA, however, during the material loading process, the printer will extrude melted filaments at a fixed speed for up to 3 minutes, which allows us to obtain enough amount of fibers. When the printer head starts to extrude the PLA filaments, the initially extruded filament will be quickly attached to the spool of winding machine I. Then winding machine I is started and the spool starts spinning from 0rad/s to the set velocity with a 5s linear acceleration. Without this gentle acceleration, the high speed of the spinner will immediately break the soft filament.

Due to the high speed of the spool and the slow extrusion of the melted PLA filament, the spool will pull the initially thick strand into very thin fibers. By changing the spinning speed of the spinning spool (Ø100mm), PLA fibers of different diameters can be obtained. Through testing different spool spinning speeds and measuring the resultant fiber

diameters (Table 4.S2), we obtained fibers with diameters of 50μm, 75μm and 50μm for making the catheters that are used in the characterization.

4.S4. Stiffness configuration of the FJ segments of the multi-segment catheter

The FJ VS catheter will be equipped with two segments to achieve multi-curvature bending to reach more challenging surgical sites. When the stiffened catheter with two segments made of the same fiber configuration is placed in the magnetic field, the first segment is subject to one bending moment M, while the second segment is subject to a tripled moment 3M (fig. 4.S10c). Due to the relatively low stiffness of FJ segment, when the first segment is just stiff enough to withstand the bending moment, the second segment will not be able to withstand the tripled moment. Therefore, the two segments cannot have the same stiffness range and it is necessary to customize the stiffness ranges of FJ segments. A viable choice is to assign a low stiffness range to the first segment and endow the second segment with a high stiffness range.

Hybrid fiber bundles by mixing fibers of two different materials and stiffness with different ratios provide a solution for stiffness customization, and the experimental results show that the stiffness ranges of the fiber bundles change with different PLA and copper fiber percentages (Fig. 4.3e). The characterization results from the pure PLA and copper bundle along with the three hybrid fiber bundles will be used to evaluate their potential performance in the RMN system and then to design the two FJ segments in the two-segment catheter.

To build the connection between 3-point bending and the RMN performance of the FJ catheter, we can use the flexural rigidity EI of the catheter as both performances rely on the same EI. The deflection-force relation of the 3-point bending is given as

$$y = \frac{FL^3}{48EI} \tag{4.S10}$$

where y, F and L are the middle deflection of the catheter, the force applied by the middle indenter, and the distance between the two lateral supporting points in the 3-point bending tests, respectively (fig. 4.S10a); E and I are the overall elastic modulus and second moment of area of the catheter, respectively. EI makes the flexural rigidity.

Therefore, with the experimental results from the 3-point bending tests, we can calculate EI using the equation below:

$$EI = \frac{FL^3}{48y} \tag{4.S11}$$

The deflection of the catheter in the magnetic field is given as

$$\delta = \frac{Ml^2}{2EI} \tag{4.S12}$$

where δ is the deflection at the tip of the catheter; M is the torque generated by the magnetic field that is applied to the magnet; l is the length of the catheter; and EI is the flexural rigidity that has been obtained from the 3-point bending.

The magnetic torque can be calculated as

$$M = m \times B \tag{4.S13}$$

where m is the dipole moment of the permanent magnet mounted at the tip of the catheter, which is 0.01187Am2; B is the MFD generated by the RMN system, which ranges from 0 to 80mT.

Therefore we can calculate the MFD needed to achieve a given deflection.

$$B = \frac{2EI\delta}{ml^2} \tag{4.S14}$$

The experimental results of the 3-point bending of the five types of fiber bundles and their estimated performance in the RMN system are given in Table 4.S3. For the soft and stiff states of the five types of fiber bundles, we calculate the MFDs needed to achieve small deflection (5mm) and large deflection (15 and 20mm). Please note that the equations are only valid for small deflections and the MFD calculations for two large deflections (15 and 20mm) are given as a rough reference.

To analyze the results, we take the 100% PLA fiber bundle as an example. Ideally, the FJ catheter needs to be bent with large deflections in the soft state under the magnetic field and stay within small deflections in the stiff state. From Table 4.S3, we can see that the soft 100% PLA bundle needs an MFD of around 26 to 35mT to achieve large deflections, while its stiff state requires 58mT to reach 5mm deflection, which is larger than 35mT. Therefore, the 100% PLA fiber bundle is eligible for the catheter application, and so are the other four types of fiber bundles as their MFDs needed for small deflection in their stiff states are higher than the MFDs for large deflections in their soft states. With the calculation, the recommended MFDs for each fiber bundle type in the soft state are given as 30, 50, 60, 70 and 80mT for 100% PLA, 75% PLA – 25% copper, 50% PLA – 50% copper, 25% PLA – 75% copper and 100% copper, respectively.

The next is to consider the material configuration for the two-segment catheter. As suggested at the beginning of section 4.S4, the first segment should have a low stiffness range, therefore, the 100% PLA fiber bundle can be assigned to the first segment. The second segment, when stiffened, needs to be rigid enough to support the manipulation of the first segment with minimal deflection. In this scenario, the second segment is subject to a tripled moment which is equal to the condition when placed in the magnetic field with a tripled MFD (fig. 4.S10c). Therefore, the stiff second segment needs to withstand an MFD three times stronger than that needed for the soft 100% PLA bundle to achieve a large deflection, which is around 90mT. Therefore, only 25% PLA – 75% copper and 100% copper fiber bundles are qualified for the second segment. For guaranteed performance, the 100% copper fiber bundle is used in the second segment of our two-segment catheter.

As mentioned above, the 100% PLA fiber bundle is chosen for the first segment of the two-segment catheter. In the surgical scenario, the first segment will be in direct contact with the surgical points and thus prioritize larger bending angles for more working space and higher dexterity. Therefore, although the recommended MFD is 30mT, 40mT is chosen for the testing of the single-segment catheter with 100% PLA fiber bundle in the

RMN system as 40mT will yield a larger deflection in the soft state of the catheter despite a slight compromise in the deflection in the stiff state.

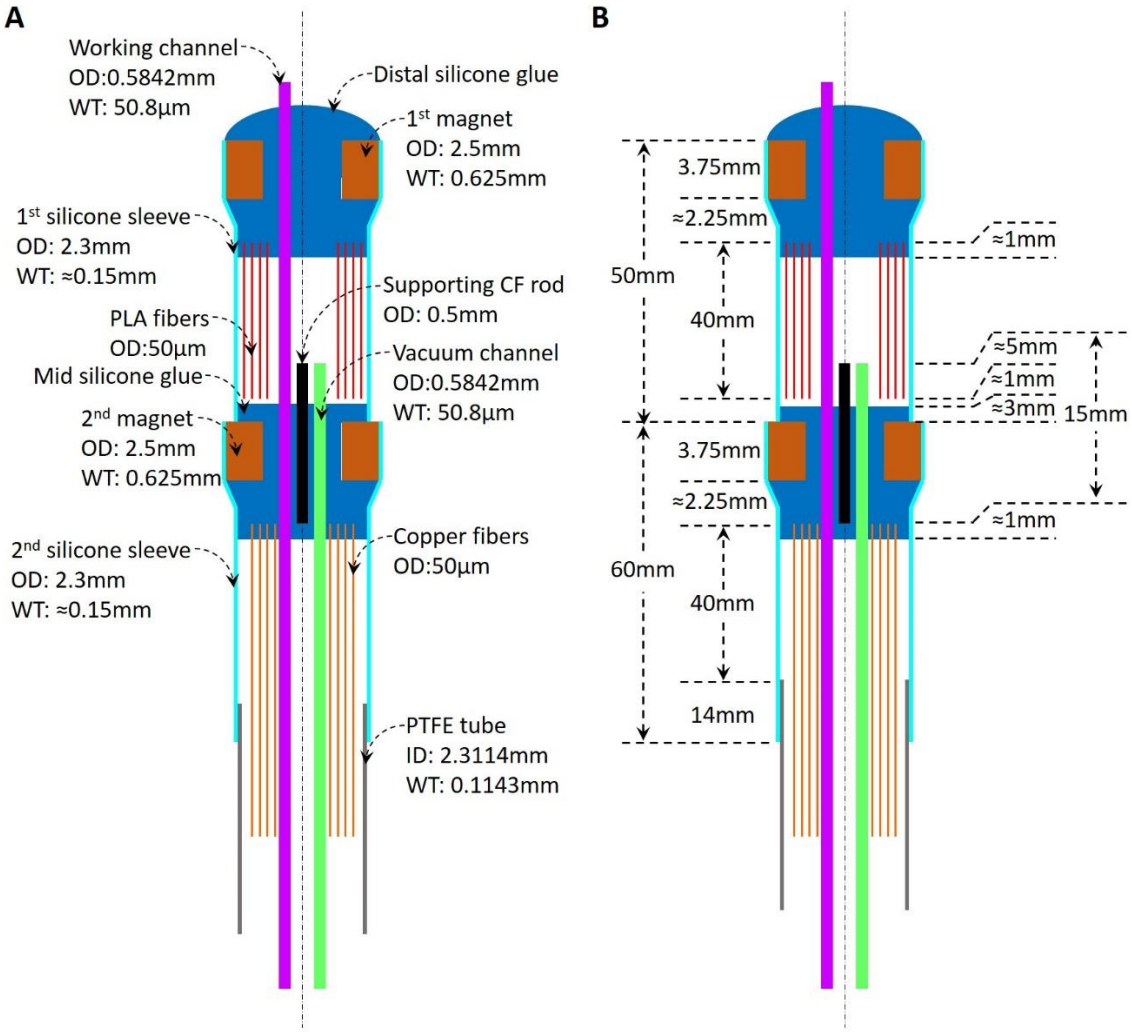

Figure 4.S 1 The structure of the two-segment FJ VS catheter.
a) Illustration of components with diameters and wall thicknesses. b) Component lengths and their relative positions.

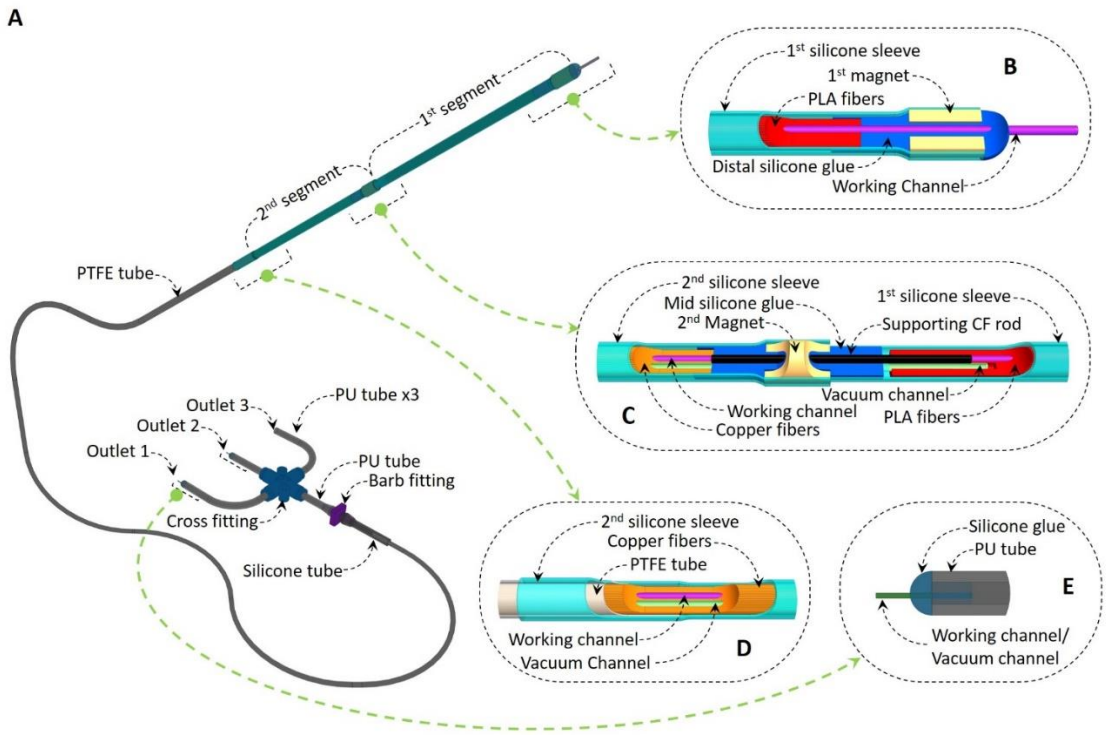

Figure 4.S 2 Anatomy of the two-segment FJ VS catheter with true proportions. a) Overview of the catheter with details of the rear tubing assembly. Near the rear tubing assembly, the PTFE tube is friction-fitted to a short silicone tube that is plugged into the 3.9-mm end of the barb fitting. The other end of the barb fitting (2.4mm) is connected to a short PU tube (ID: 2mm; OD: 4mm), which then goes to a cross fitting for tubing split into outlet 1, 2 and 3 for the placement of electric wire of the ablation tip, and vacuum application for the first and second FJ segments, respectively. b) Dissection view of the tip of the first segment. c) Dissection view of the middle connection between the two FJ segments. d) Dissection view of the rear connection between the second segment and the PTFE tube. e) Close-up view of the outlet showing that, to fully isolate outlet 1 and 2 from outlet 3, silicone glue is applied to block the PU tubes.

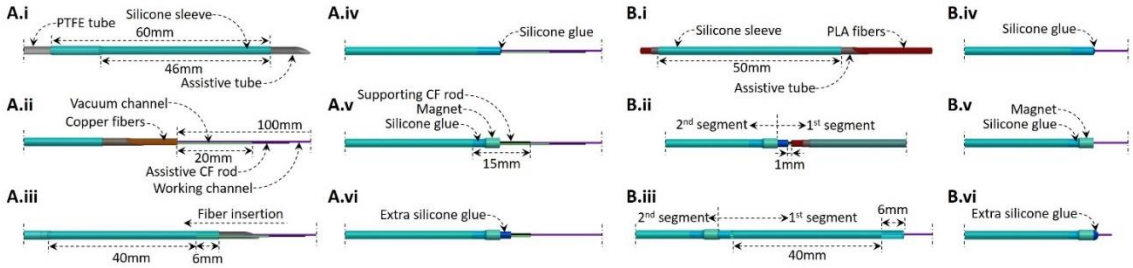

Figure 4.S 3 Fabrication of the two-segment catheter with true proportions and key dimensions.

a) Second segment fabrication. The PTFE tube is inserted into the 60mm long silicone sleeve by 14mm, leaving 46mm of the silicone sleeve for the second segment. The assistive tube with a wedged tip is then inserted (i). Copper fibers are inserted from the right, followed by the insertion of the working and vacuum channels with 100mm of the working channel and 20mm of the vacuum channel sticking out of the copper fibers (ii). Copper fibers are further pushed in with a 40mm length staying out of the PTFE tube and 6mm empty space at the tip of the silicone sleeve (iii). The assistive tube is then removed, followed by the silicone glue application at the tip of the silicone sleeve (iv). The magnet and the supporting CF rod (15mm long) are immediately inserted after glue application (v). Extra silicone glue is applied to seal the second segment (vi). b) First segment fabrication. The assistive tube with a wedged tip is inserted into the 50mm long silicone sleeve, followed by the insertion of the PLA fibers (i). The halfway first segment is inserted onto the tip of the second segment with a gap of around 1mm (ii). The silicone sleeve of the first segment is rubbed onto the tip of the second segment, followed by the removal of the assistive tube and trimming of the PLA fibers down to 40mm. The silicone sleeve is then fixed using a small amount of silicone glue to the tip of the second segment (iii). The tip of the first segment is filled with silicone glue to fix the PLA fibers (iv). The magnet is inserted immediately after the silicone glue application (v). Extra silicone glue is applied at the tip to seal the first segment, followed by the removal of the assistive CF rods in the working and vacuum channels (vi).

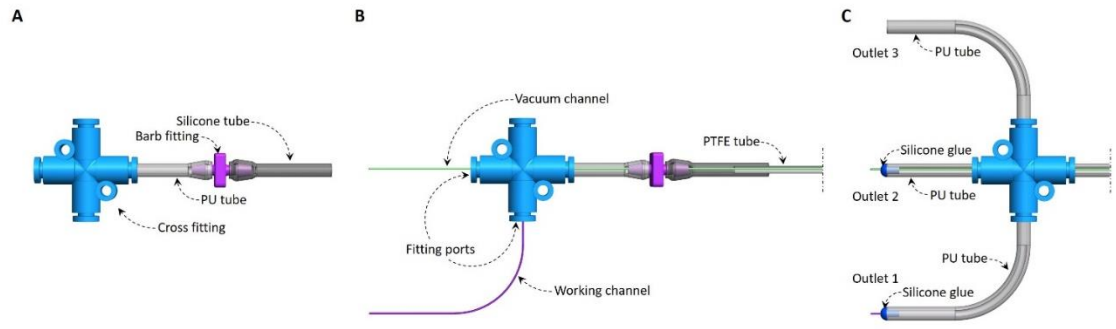

Figure 4.S 4 Rear tubing assembly.

a) The silicone tube, PU tube, barb fitting and the cross fitting are first assembled. b) The working and vacuum channels inside the PTFE tube are inserted through the silicone tube and, when they reach the cross fitting, the vacuum channel goes straight across the cross fitting, while the working channel is diverted to the fitting port pointing downwards,

followed by the PTFE tube insertion into the silicone tube. c) Another three PU tubes are then plugged into three fitting ports and the assembly is finished with silicone glue sealing the tip of outlet 1 and 2.

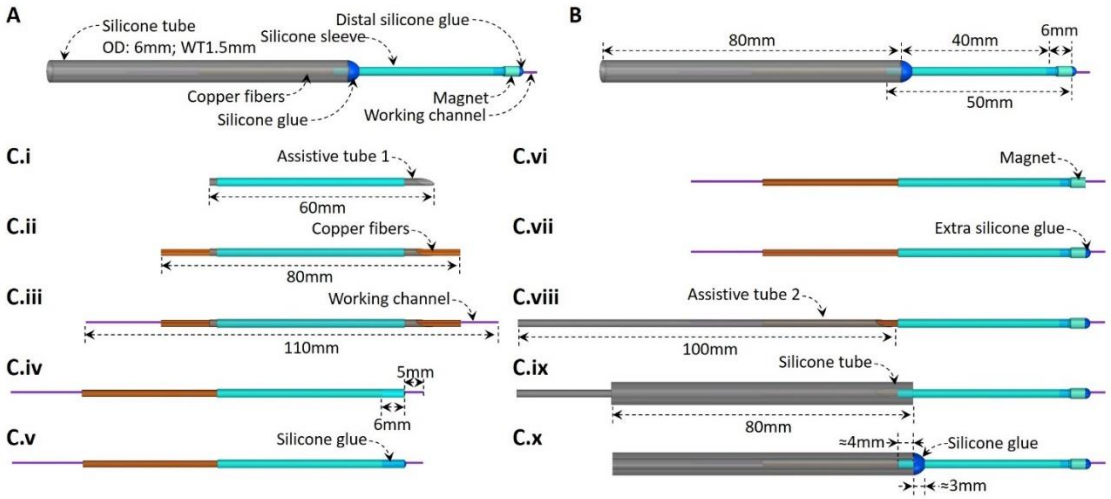

Figure 4.S 5 Fabrication of the single-segment catheter.
a) The components used in the single-segment catheter. b) Key dimensions for the single-segment catheter. c) The fabrication processes of the single-segment catheter with copper fibers. The assistive tube 1 with a wedged tip is inserted into the silicone sleeve (i), followed by the insertion of the copper fibers (ii). The working channel is then inserted (iii), and then the fibers and the working channel are repositioned to leave 6mm empty space at the tip of the silicone sleeve and 5mm of the working channel sticking out of the silicone sleeve (iv). Silicone glue is then applied to the tip of the silicone sleeve (v), followed by the immediate insertion of the magnet (vi). Extra glue is then applied to seal the tip (vii). The excessive copper fibers on the other end are inserted into the assistive tube 2 with a wedged tip (viii), which is then inserted into a silicone tube with 4mm of the silicone sleeve inside the silicone tube (ix). With the removal of the assistive tube 2 and the silicone glue application to fix the silicone sleeve with the silicone tube, the fabrication of the single-segment catheter is completed (x).

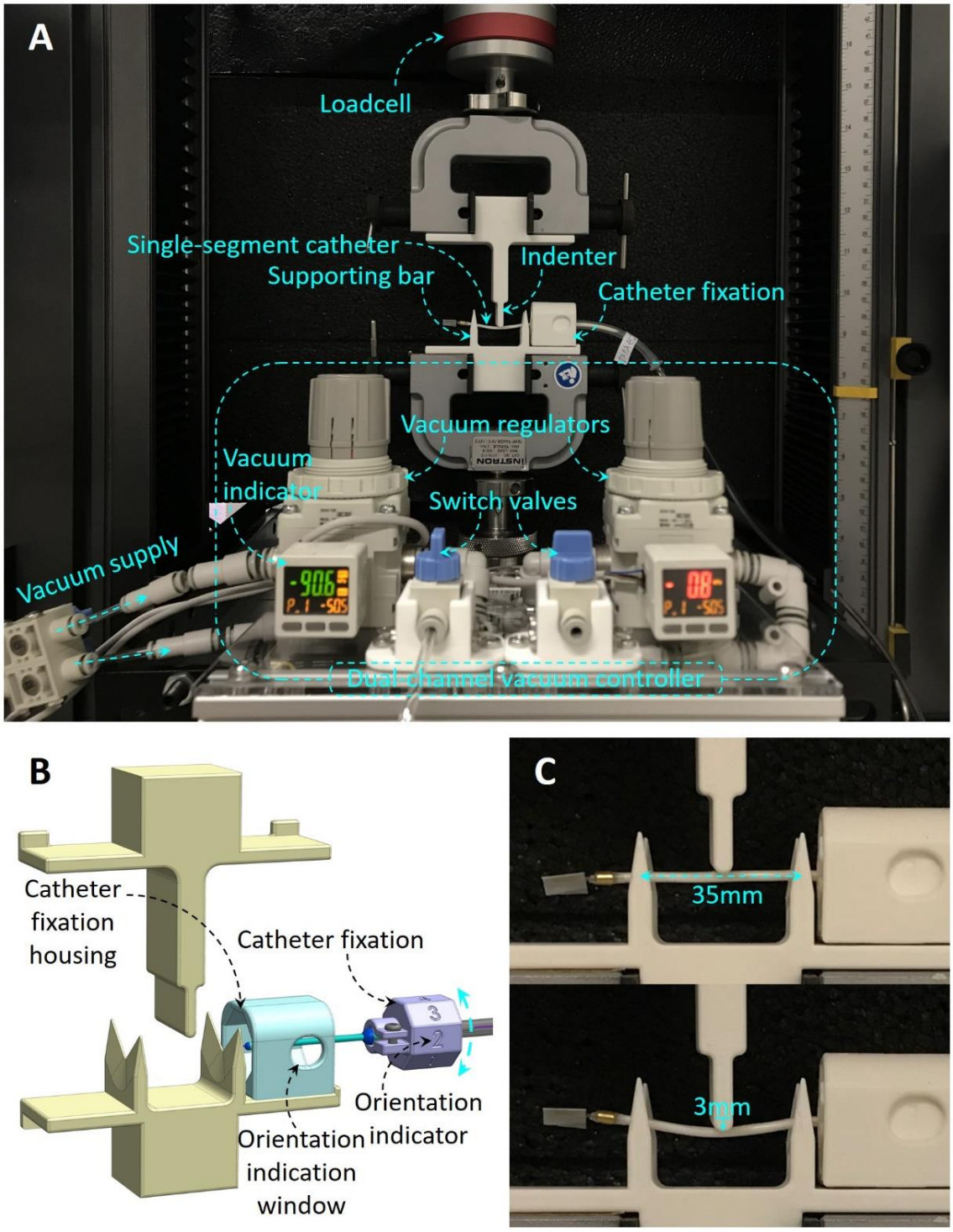

Figure 4.S 6 Characterization setup for the single-segment catheter.
a) 3-point bending test setup fixed on the Instron machine along with the dual-channel vacuum controller. b) Close-up view of the catheter fixation that allows bending tests at four orientations. After testing at one orientation, the catheter fixation will be drawn out, rotated by 45° to the next orientation, and then inserted in for testing. c) 3-point bending test process with 3mm deflection.

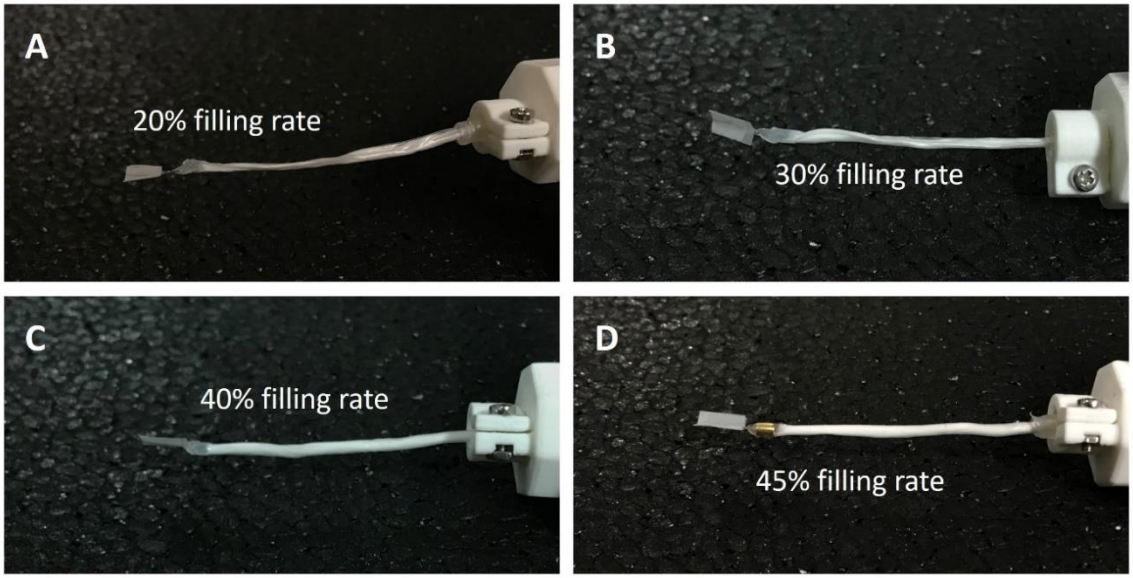

Figure 4.S 7 Vacuumed states of the single-segment catheters at different filling rates.
(a) 20%. (b) 30%. (c) 40%. (d) 45%.

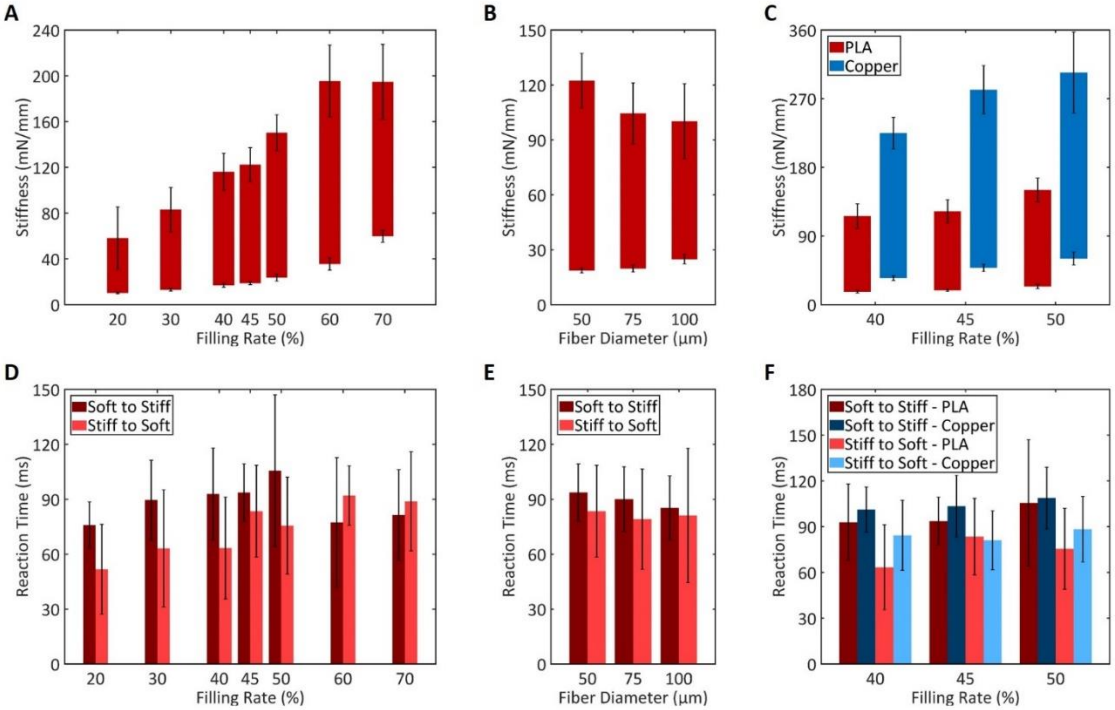

Figure 4.S 8 Additional FJ characterization results.
a) The stiffness ranges of FJ with Ø50μm PLA fibers at different filling rates. b) The stiffness ranges of FJ with PLA fibers of different diameters at 45% filling rate. c) The stiffness ranges of FJ with Ø50μm PLA and copper fibers at the optimal filling rates. d) FJ reaction times with Ø50μm PLA fibers at different filling rates. e) FJ reaction times

with PLA fibers of different diameters at 45% filling rate. f) FJ reaction times with Ø50μm PLA and copper fibers at the optimal filling rates. Please note that all error bars represent one SD.

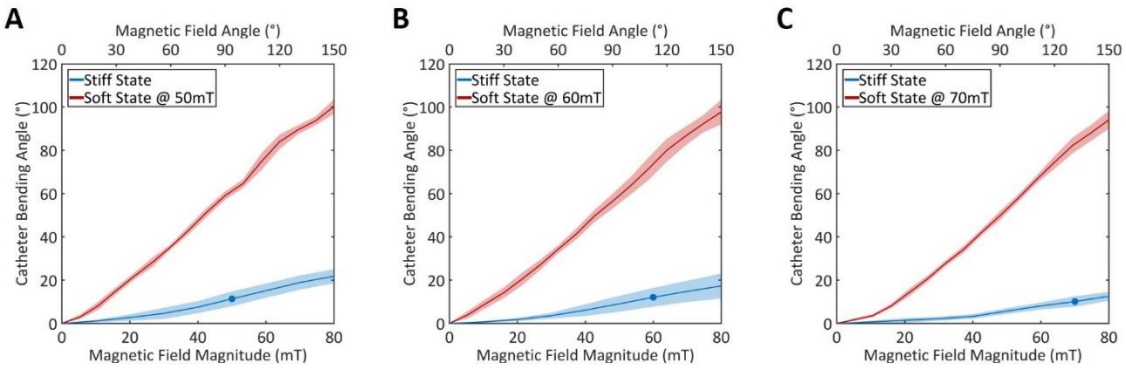

Figure 4.S 9 Bending results of the catheters with hybrid fiber bundles under the RMN system.
a) 75% PLA – 25% copper. b) 50% PLA – 50% copper. c) 25% PLA – 75% copper. The blue dots highlight the small deflections at the corresponding MFDs for their tests in the soft state.

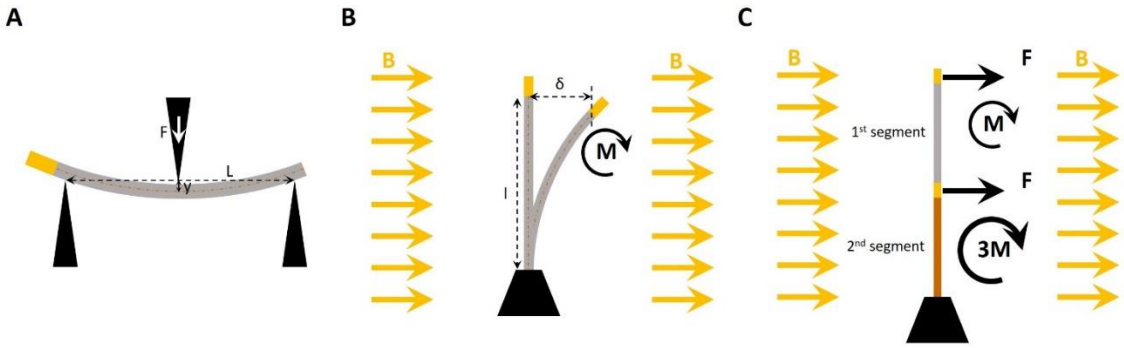

Figure 4.S 10 Different loading scenarios of the catheters.
a) The single-segment catheter in the 3-point bending test. b) The single-segment catheter in a magnetic field. c) The two-segment catheter in a magnetic field.

	Items	Material	Supplier	Outer diameter (mm)	Inner diameter (mm)	Wall thickness (mm)	Length (mm)	Elastic modulus (MPa)
Main components	1st Silicone sleeve	DragonSkin0020	Smooth-On, Inc.	2.3	2	0.15	50	0.34
	2nd Silicone sleeve						60	
	Silicone glue	Sil-poxy	Smooth-On, Inc.	NA	NA	NA	NA	2.7
	Working channel	Polytetrafluoroethylene (PTFE)	Zeus, Inc.	0.5842	0.4826	0.0508	450	400
	Vacuum channel							
	PTFE tube	PTFE	Zeus, Inc.	2.3114	2.0828	0.1143	200	400
	PLA fiber	Polylactide Acid (PLA)	Ultimaker B.V.	0.05	NA	NA	40	2763
	Supporting CF rod	Carbon fiber (CF)	Suter Kunststoffe AG	0.3	NA	NA	15	228000
	Copper fiber	Copper	Xinye Electric, Inc.	0.05	NA	NA	80	117000
	Silicone tube	Silicone	ROTIMA AG	4	2	1	30	4.3
	PU tube	Polyurethane (PU)	SMC. Ltd	4	2	1	30 & 70	2580
	Magnet	Neodymium+Iron+Boron (NdFeB)	HKCM Engineering e.K.	2.5	1.25	0.625	3.75	NA
						Dipole moment:	0.01187 Am^2	
	Barb fitting	Polypropylene (PP)	Foreshine. Ltd	Max diameter of two ends		2.4 mm	3.9 mm	NA
	Cross fitting	Polybutylene terephthalate (PBT)	SMC. Ltd	Port size		4 mm		NA
Assistive components	Assistive tube	PTFE	Zeus, Inc.	2.1	2	0.0508	70	400
	Assistive CF rod	Carbon fiber	Suter Kunststoffe AG	0.3	NA	NA	500	228000

Table 4.S 1 Information about the materials used in the catheter and the fabrication.

Spool spinning velocity (rad/s)	Spool edge linear velocity (mm/s)	Resultant fiber thickness (μm)
12.5π	1963.5	46.6
10π	1570.8	50.1
6.25π	981.75	60.8
3.968π	623.33	74.8

3.125π	490.875	85.5
2.294π	360.275	100.1
2.084π	327.25	104.4
1.5625π	245.44	115.1

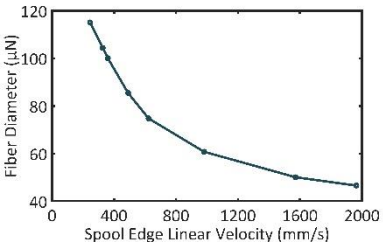

Table 4.S 2 Relation between spool spinning speed and fiber thickness.

Fiber composition	Stiffness state	Stiffness (N/m)	Flexural rigidity *EI* (×10-6 N·m2)	MFD (mT) needed to achieve a deflection of			Recommended MFDs (mT) for the soft states
				5mm	15mm	20mm	
100% PLA	soft	18.67	16.67	8.78	26.34	35.12	30*
0% copper	stiff	122.33	109.27	57.54	172.61	230.14	
75% PLA	soft	29.75	26.57	14	41.98	55.97	50
25% copper	stiff	154.25	137.78	72.55	217.64	290.19	
50% PLA	soft	36.58	32.68	17.21	51.62	68.82	60
50% copper	stiff	184.42	164.73	86.73	260.2	346.94	
25% PLA	soft	46.86	41.86	22.04	66.12	88.16	70
75% copper	stiff	232.64	207.8	109.41	328.24	437.66	
0% PLA	soft	48.08	42.95	22.61	67.84	90.46	80
100% copper	stiff	281.56	251.49	132.42	397.26	529.68	

Table 4.S 3 Calculation based on the hybrid fibre bundle characterization results.

D Scalable variable stiffness technology

D.1 Introduction

The field of smart fibers is advancing rapidly each year. Recent developments have seen the creation of smart fibers with functionalities such as sensing, actuation, variable stiffness, and energy generation.[18,19,24,36] Their potential application opportunities are quite broad from smart textiles and haptic devices to robots with multimodal locomotion and catheters for minimally invasive surgeries.[10,22,185]

However, at present, there are still a lot of design challenges associated with the integration of multiple functionalities in these smart fibers.[19,235–237] Specifically, a pertinent example is the integration of variable stiffness functionality, which implies a reversible change in the mechanical properties of the object when a certain trigger, for example heat or pressure, is applied.[18] Therefore, a variable stiffness fiber is already by default a multifunctional system with a variable stiffness substrate, stiffness change mechanism, and sensor that can read the current stiffness state of the fiber.[185]

Researchers have developed devices with multiple variable-stiffness fibers integrated into minimally invasive devices or drones.[10,185] They can already tune the geometrical, electrical, and mechanical parameters of these fibers for any specific application.[185] However, the connection strategy, which in all works implies the use of electrodes to supply power to each of the segments, limits the number of fibers involved. Each segment is connected to two electrodes that are then wound around the following segments all the way down to the base. Therefore, every new segment influences the geometry and stiffness of all the rest of the variable-stiffness fibers, making this particular connection strategy not scalable.

Here, we present a scalable approach to developing modular variable-stiffness fibers. Each of the modules has a plug design from one side and socket design from another side, which enables the connection of multiple segments without any influence on the mechanical or geometrical parameters of the rest modules. The main body of the module is made of conductive shape-memory polymeric material (CSMP), which changes its state

from rigid to soft and vice versa under thermal stimuli. Moreover, each module has a scalable in diameter design, which allows geometrical, mechanical, and electrical adjustment for a specific application.

D.2 Results and Discussion

D.2.1 Design and working principle of a variable stiffness module

Each module consists of the main tubular body made out of conductive shape-memory polymeric (CSMP) material surrounded by copper electrodes throughout the length at the equal distances from each other **(Figure D.1a)**. Two out of six electrodes are electrically and mechanically connected to the CSMP body to pass energy to it via direct Joule heating. The rest four electrodes are only mechanically connected to the SMP body and are used to pass current to the next module. Each module has a plug design from one side and socket design from another side. From the plug side, tips of electrodes protrude 5 mm from the edge to form a plug, which can be then inserted into the socket side of the next module. To form a socket at the second side of the module, all copper electrodes are inserted to the depth of 5 mm in PTFE tubes with a length of 10mm. The remaining 5 mm of PTFE tubes provides electrical connection between the electrodes. Electrodes and PTFE connecting tubes are encapsulated with an external silicone layer coated on top of the CSMP body. The mechanical connection between modules is provided via 20 mm in length carbon tube inserted into the SMP body from the plug side. Each module has a length of 100 mm, and an external diameter does not exceed 4 mm (Figure D.1b).

Modules stay in a rigid state at the room temperature (23 °C) and becomes significantly softer when heated up to 55 °C under thermal stimuli. The module becomes three times softer in 15 seconds under 1 W of power supplied to CSMP layer via direct Joule heating (Figure D.1c). CSMP-based variable stiffness substrate allows withstanding external forces while being in the rigid state and becoming compliant when the state is changed to soft (Figure D.1d).

D.2.2 Fabrication process of a variable stiffness module

Our variable stiffness module primarily uses a polyurethane-based SMP (SMP Technologies Inc., MM5520). We selected SMP material for its widespread use in biomedical fields like stents, drug delivery, and bone tissue engineering,[8,48,165] owing to its thermoplastic characteristics (stiffness alteration under thermal stimuli), affordability, high recoverable strain capacity (300% compared to 10% in other programmable materials like shape memory alloys), and manufacturability. This allows for the creation of scalable, complex soft medical devices. The fabrication process begins by creating a CSMP mixture, blending MM5520 with a solvent (dimethylformamide: DMF, Sigma–Aldrich) in a 1 to 4 weight ratio and stirring it at room temperature for 8 hours. Subsequently, 1.4 g of carbon black powder (Nouryon, Ketjenblack EC-600JD) and 36 g of DMF are added to 30 g of the uniform SMP mixture. This mixture is milled with 6

metal balls (10 mm diameter), which helps in breaking down carbon black powder clumps and evenly distributing them within the polymer matrix.[182,238]

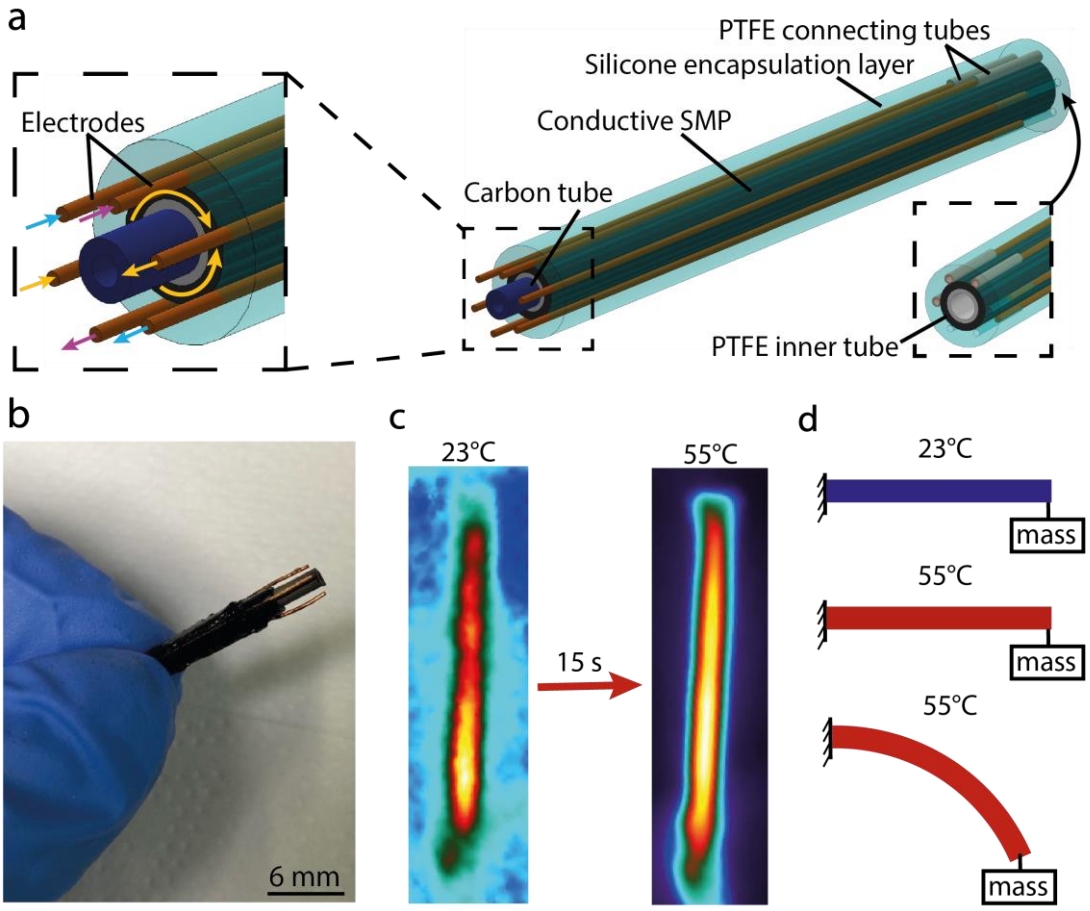

Figure D. 1 Structure and working principle of a variable stiffness module.
a) Structure of a module of the scalable variable stiffness fiber. It has a plug from one side and a slot from another side that allows electrical and mechanical connection of multiple modules. b) Picture of a fabricated module. c) Heating of the module via direct Joule heating of the conductive shape-memory polymeric material (CSMP). d) Working principle of variable stiffness module. It withstands applied force in a rigid state and becomes compliant as soon as the state changes to soft.

Next, we attach a PTFE tube with a 1.4 mm external diameter to a carbon rod and immerse it vertically into the CSMP mixture. Oven curing then leads to the formation of a CSMP layer on the tube **(Figure D.2a).** This immersion process can be repeated several times to attain the CSMP layer's required thickness (Figure D.2a-i,ii,iii). Our process employs an automated dipping mechanism (Figure D.2b), enabling precise CSMP thickness control by adjusting the number of dips, extraction, and spin speeds. Following extraction, the PTFE tube is sp un to evenly distribute the CSMP coating on its surface. The final thickness of the CSMP layer is determined by the dipping frequency and spin speed. After completing two dips, we place copper electrode wires and connecting PTFE tubes around the CSMP-coated tube (Figure D.2a-iv,v and Figure D.2c). The assembly is then

submerged in silicone for encapsulation and subsequently cured in the oven to hasten the solidification process.

D.2.3 Thermomechanical characterization of a variable stiffness module

To better understand the limitations of a variable stiffness module, we performed thermomechanical characterization, which consists of a stiffness characterization in both rigid and soft states and heating times characterization.

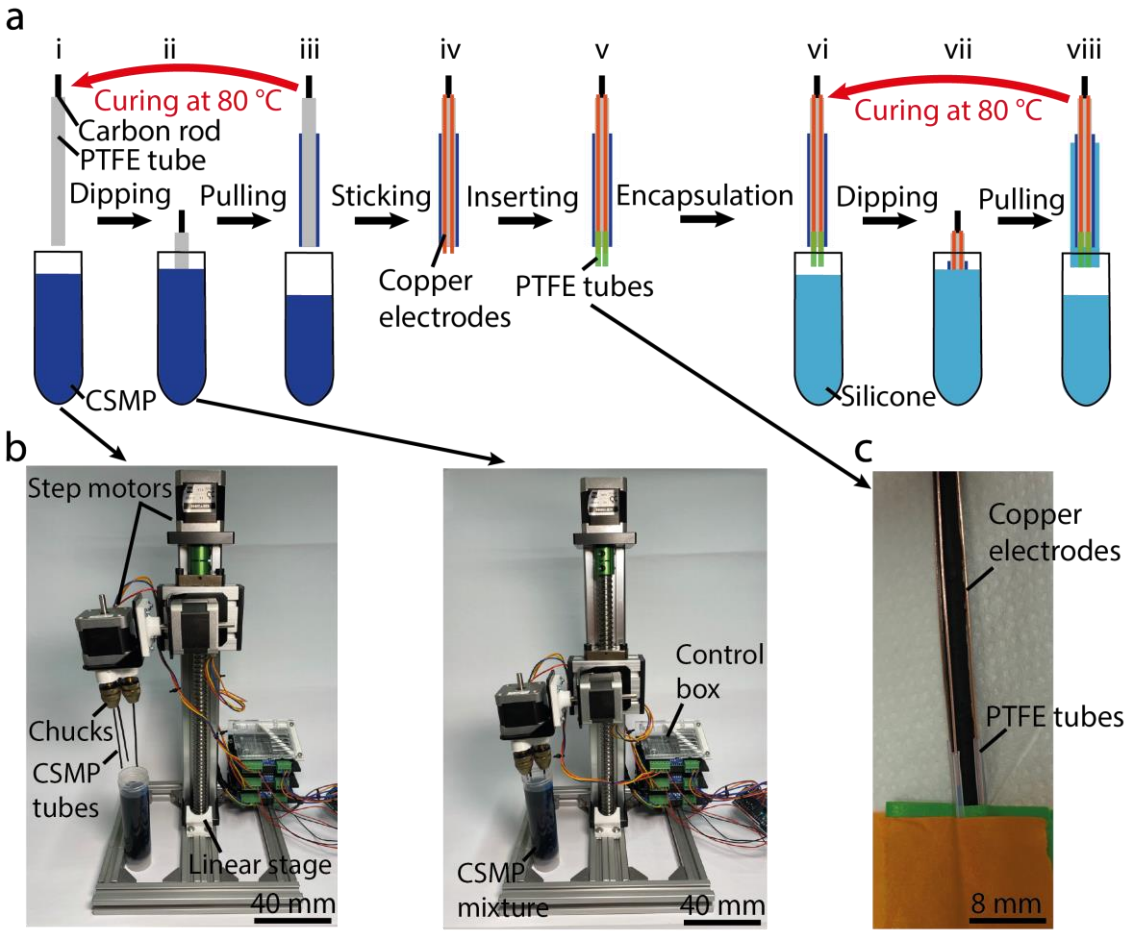

Figure D. 2 Fabrication process of a variable stiffness module.
a) Variable stiffness module's fabrication steps. b) Automated dipping process using custom-made dipping setup illustrates steps a-i and a-ii of the fabrication process. c) Picture of a module with installed four copper electrodes and connecting PTFE tubes.

To assess the stiffness variation in the variable stiffness module, we conducted a three-point bending test using a universal testing machine (Instron 5965) equipped with a temperature control unit. This machine included 3D printed supports made from acrylonitrile butadiene styrene (ABS) and a rail conforming to ISO178:2019 standards, which specify requirements for three-point bending tests in universal testing systems **(Figure D.3a).** The tests were carried out at two different temperatures: 23 °C (ambient

temperature) to evaluate the module in its rigid state, and 55 °C to assess it in its soft state. This was done to measure the device's deflection and reaction force. The reaction force data, plotted against forced displacement, were refined using the infinite impulse response (IIR) filter in Origin Pro 2016. We employed a Butterworth filter with a cutoff frequency of 400 Hz for this purpose. The findings show that the variable stiffness module exhibits a stiffness change factor of three (Figure D.3b). However, this performance is not as effective as the devices discussed in Chapters 2, 3, and 4. The primary reason for this is that the soft state of the variable stiffness module is approximately 15 times stiffer compared to the devices mentioned earlier, largely due to the incorporation of copper electrodes.

To analyze the heating duration, we recorded temperature data using a thermal camera (FLIR, E8xt) positioned 150 mm away from the variable stiffness module (Figure D.3c). We tested three samples, each with a CSMP wall thickness of 0.4 mm, at two different power settings of 1 W and 1.5 W. The variable stiffness module was returned to room temperature before each test. The heating patterns of the device were then analyzed using FLIR ResearchIR software. The results indicates that the variable stiffness module is heated up to 65 °C in less than 13 s under 1.5 W (Figure D.3d).

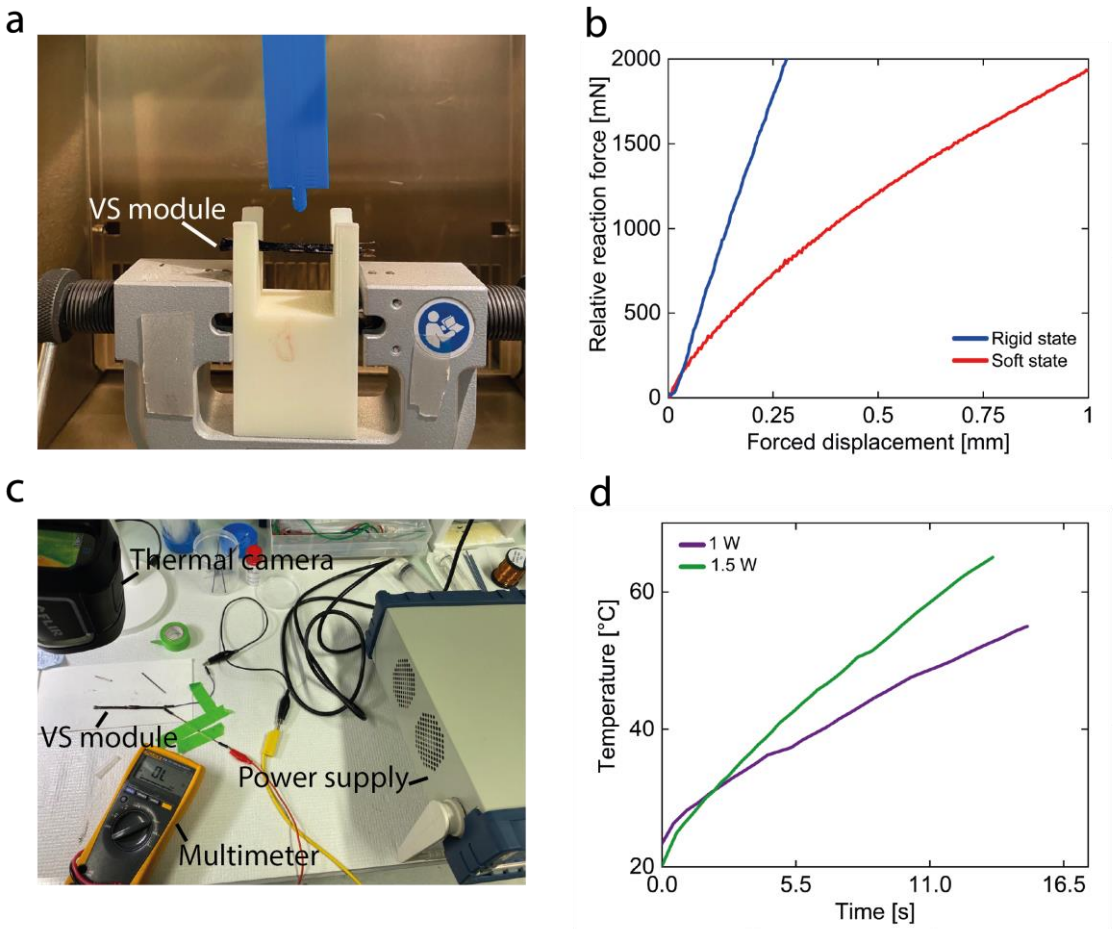

Figure D. 3 Variable stiffness (VS) module characterization.
a) Three-point flexural test setup inside the thermal camera, which enables precise control of environmental temature. b) Relative reaction force data as a function of forced

displacement for the VS module in a rigid and soft state. c) Heating times characterization setup. d) Heating times at different applied power.

D.3 Conclusion and Future work

In this chapter, we introduce a scalable method for creating variable-stiffness fibers using independent modules. Each module features a plug design on one end and a socket design on the other, allowing for the connection of multiple segments without affecting the mechanical or geometrical characteristics of the other modules. The core component of each module is a conductive shape-memory polymeric material (CSMP), capable of transitioning from a rigid to a soft state and back under thermal conditions. Additionally, the design of each module is scalable in diameter, facilitating adjustments in geometry, mechanics, and electrical properties to suit specific applications. Each module has stiffness change factor of three and can be heated up to 65 °C in less than 13 s under 1.5 W.

This actual piece of work still requires future work. First, the demonstration of scalable connection strategy has to be demonstrated by connecting together three variable stiffness modules. Last, the demonstrators of potential application have to be built to fascinate the benefits of the scalable approach.

E Publication List

Journal Papers

1. **Yegor Piskarev**, Yi Sun, Matteo Righi, Quentin Boehler, Christophe Chautems, Cedric Fischer, Bradley J. Nelson, Jun Shintake, and Dario Floreano, *Fast-response variable-stiffness magnetic catheters for minimally invasive surgery*, in Advanced Science, 2024, 2305537.
2. Yi Sun, **Yegor Piskarev**, Etienne H. Hofstetter, Cedric Fischer, Quentin Boehler, Bradley J. Nelson, and Dario Floreano, *Instant Variable Stiffness in Cardiovascular Catheters Based on Fiber Jamming*, in Science Advances (under major revision).
3. **Yegor Piskarev**, Antoine Devincenti, Vivek Ramachandran, Pierre-Etienne Bourban, Michael D Dickey, Jun Shintake, Dario Floreano, *A Soft Gripper with Granular Jamming and Electroadhesive Properties*, in Advanced Intelligent Systems, 2023, 2200409.
4. **Yegor Piskarev**, Etienne Desbouis, Vivek Ramachandran, Jiayi Yang, Neil Baugh, Jun Shintake, Michael D Dickey, Dario Floreano, *Enhancement of Pressure-Sensitive Adhesive by CO^2 Laser Treatment*, in Advanced Engineering Materials, 2022, 24 (10), 2200355.
5. **Yegor Piskarev**, Jun Shintake, Christophe Chautems, Jonas Lussi, Quentin Boehler, Bradley J Nelson, Dario Floreano, *A Variable Stiffness Magnetic Catheter Made of a Conductive Phase-Change Polymer for Minimally Invasive Surgery*, in Advanced Functional Materials, 2022, 32 (20), 2107662.
6. William Stewart, Luca Guarino, **Yegor Piskarev**, Dario Floreano, *Passive Perching with Energy Storage for Winged Aerial Robot*, in Advanced Intelligent Systems, 2021, 2100150.
7. Jun Shintake, **Yegor Piskarev**, *Liquid metal-based soft actuators and sensors for biomedical applications*, in Metal Oxides for Biomedical and Biosensor Applications, Elsevier, 2021.

8. Sungjune Park, Jun Shintake, **Yegor Piskarev**, Yuwen Wei, Ishan Joshipura, Ethan Frey, Taylor Neumann, Dario Floreano, Michael D Dickey, *Stretchable and Soft Electroadhesion Using Liquid-Metal Subsurface Microelectrodes*, in Advanced Materials Technologies, 2021 6 (9), 2100263.
9. **Yegor Piskarev**, Jun Shintake, Vivek Ramachandran, Neil Baugh, Michael D Dickey, Dario Floreano, *Lighter and Stronger: Cofabricated Electrodes and Variable Stiffness Elements in Dielectric Actuators*, in Advanced Intelligent Systems, 2020, 2 (10), 2000069.
10. Jiayi Yang, David Tang, Jinping Ao, Tushar Ghosh, Taylor V Neumann, Dongguang Zhang, **Yegor Piskarev**, Tingting Yu, Vi Khanh Truong, Kai Xie, Ying-Chih Lai, Yang Li, Michael D Dickey, *Ultrasoft liquid metal elastomer foams with positive and negative piezopermittivity for tactile sensing*, in Advanced Functional Materials, 2020, 30 (36), 2002611.
11. Jun Shintake, **Yegor Piskarev**, Seung Hee Jeong, Dario Floreano, *Ultrastretchable Strain Sensors Using Carbon Black-Filled Elastomer Composites and Comparison of Capacitive Versus Resistive Sensors*, in Advanced Materials Technologies, 2018 3 (3), 1700284.

Conference Papers

1. Jun Shintake, Harshal Sonar, **Yegor Piskarev**, Jamie Paik, Dario Floreano, *Soft Pneumatic Gelatin Actuator for Edible Robotics*, in 2017 IEEE/RSJ International Conference on Intelligent Robots and Systems (IROS) September 24–28, 2017, Vancouver, BC, Canada.

Patent Applications

1. **Yegor Piskarev**, Jun Shintake, Dario Floreano, *A variable stiffness magnetic catheter made of a conductive shape memory polymer for minimally invasive surgery*, WO Patent App. WO 2023/099949 A1.
2. Yi Sun, **Yegor Piskarev**, Etienne H. Hofstetter, Dario Floreano, *An approach to Instantly change stiffness in Cardiovascular Catheters and fabrication method*, WO Patent App. in preparation.

Conference Abstracts and Posters

1. **Yegor Piskarev**, Jun Shintake, Christophe Chautems, Jonas Lussi, Quentin Boehler, Bradley J Nelson, Dario Floreano, *A Variable Stiffness Magnetic Catheter Made of a Conductive Phase-Change Polymer for Minimally Invasive Surgery*, in Gordon Research Seminars, Ventura, California, 2022.
2. **Yegor Piskarev**, Jun Shintake, Christophe Chautems, Jonas Lussi, Quentin Boehler, Bradley J Nelson, Dario Floreano, *A Variable Stiffness Magnetic Catheter Made of a Conductive Phase-Change Polymer for Minimally Invasive Surgery*, in Gordon Research Conference, Ventura, California, 2022.

Bibliography

[1] V. Ramachandran, J. Shintake, D. Floreano, *Advanced Materials Technologies* **2019**, *4*, 1800313.

[2] W. H. Choi, S. Kim, D. Lee, D. Shin, *IEEE Robotics and Automation Letters* **2019**, *4*, 2539.

[3] A. Tonazzini, J. Shintake, C. Rognon, V. Ramachandran, S. Mintchev, D. Floreano, **2018**, pp. 485–490.

[4] S. Mintchev, J. Shintake, D. Floreano, *Science Robotics* **2018**, *3*, eaau0275.

[5] T. P. Chenal, J. C. Case, J. Paik, R. K. Kramer, IEEE, **2014**.

[6] M. C. Yuen, R. A. Bilodeau, R. K. Kramer, *IEEE Robot. Autom. Lett.* **2016**, *1*, 708.

[7] R. Zhao, Y. Yao, Y. Luo, *Journal of Medical Devices* **2016**, *10*.

[8] M. Han, L. Chen, K. Aras, C. Liang, X. Chen, H. Zhao, K. Li, N. R. Faye, B. Sun, J.-H. Kim, W. Bai, Q. Yang, Y. Ma, W. Lu, E. Song, J. M. Baek, Y. Lee, C. Liu, J. B. Model, G. Yang, R. Ghaffari, Y. Huang, I. R. Efimov, J. A. Rogers, *Nature Biomedical Engineering* **2020**.

[9] C. Potrich, L. Lunelli, M. Cocuzza, S. L. Marasso, C. F. Pirri, C. Pederzolli, *Talanta* **2019**, *193*, 44.

[10] A. Tonazzini, S. Mintchev, B. Schubert, B. Mazzolai, J. Shintake, D. Floreano, **2016**, *28*, 10142.

[11] R. Deimel, O. Brock, *The International Journal of Robotics Research* **2016**, *35*, 161.

[12] J. Shintake, S. Rosset, B. Schubert, D. Floreano, H. Shea, **2016**, *28*, 231.

[13] J. Shintake, B. Schubert, S. Rosset, H. Shea, D. Floreano, Ieee, In *2015 Ieee/Rsj International Conference on Intelligent Robots and Systems*, Ieee, New York, **2015**, pp. 1097–1102.

[14] R. L. Baines, J. W. Booth, F. E. Fish, R. Kramer-Bottiglio, **2019**, pp. 704–710.

[15] G. Y. Gu, J. Zou, R. K. Zhao, X. H. Zhao, X. Y. Zhu, *Sci. Robot.* **2018**, *3*, 12.

[16] Z. Liu, W. Sun, Z. Ren, K. Hu, T. Wang, L. Wen, In *2019 9th Ieee Annual International Conference on Cyber Technology in Automation, Control, and Intelligent Systems (ieee-Cyber 2019)*, Ieee, New York, **2019**, pp. 689–694.

[17] M. Cianchetti, C. Laschi, A. Menciassi, P. Dario, *Nat Rev Mater* **2018**, *3*, 143.

[18] T. L. Buckner, R. Kramer-Bottiglio, *Multifunctional Materials* **2018**, *1*, 012001.

[19] J. Xiong, J. Chen, P. S. Lee, *Advanced Materials* **2020**, 2002640.
[20] J. Cai, M. Du, Z. Li, *Advanced Materials Technologies* **2022**, *7*, 2101182.
[21] C. He, S. Korposh, F. U. Hernandez, L. Liu, R. Correia, B. R. Hayes-Gill, S. P. Morgan, *Sensors* **2020**, *20*, 1904.
[22] H. Banerjee, A. Leber, S. Laperrousaz, R. La Polla, C. Dong, S. Mansour, X. Wan, F. Sorin, *Advanced Materials* **2023**, *35*, 2212202.
[23] C. Dong, A. Leber, D. Yan, H. Banerjee, S. Laperrousaz, T. Das Gupta, S. Shadman, P. M. Reis, F. Sorin, *Science Advances* **2022**, *8*, eabo0869.
[24] M. Smith, V. Cacucciolo, H. Shea, *Science* **2023**, *379*, 1327.
[25] C. Chautems, A. Tonazzini, D. Floreano, B. J. Nelson, **2017**, pp. 181–186.
[26] H. M. Le, P. T. Phan, C. Lin, L. Jiajun, S. J. Phee, *Ann Biomed Eng* **2020**, *48*, 1837.
[27] C. Chautems, A. Tonazzini, Q. Boehler, S. Jeong, D. Floreano, B. Nelson, *Advanced Intelligent Systems* **Ноябрь 9**, 1900086.
[28] Q. Gao, Z. Sun, *Actuators* **2021**, *10*, 130.
[29] D. McCoul, S. Rosset, N. Besse, H. Shea, *Smart Materials and Structures* **2016**, *26*, 025015.
[30] C. Majidi, R. J. Wood, **2010**, *97*, 164104.
[31] E. Brown, N. Rodenberg, J. Amend, A. Mozeika, E. Steltz, M. R. Zakin, H. Lipson, H. M. Jaeger, **2010**, *107*, 18809.
[32] K. Myronidis, M. Kopec, M. Meo, F. Pinto, In *Bioinspiration, Biomimetics, and Bioreplication XII*, SPIE, **2022**, pp. 114–126.
[33] K. Fitch, T. Engel, A. Bochner, *Manag Care* **2015**, *24*, 40.
[34] D. Qeska, S. M. Singh, F. Qiu, R. Manoragavan, C. C. Cheung, D. T. Ko, M. Sud, M. Terricabras, H. C. Wijeysundera, *EP Europace* **2023**, *25*, euad074.
[35] A. Leber, S. Laperrousaz, Y. Qu, C. Dong, I. Richard, F. Sorin, *Advanced Science* **2023**, *10*, 2207573.
[36] A. Leber, C. Dong, S. Laperrousaz, H. Banerjee, M. E. M. K. Abdelaziz, N. Bartolomei, B. Schyrr, B. Temelkuran, F. Sorin, *Advanced Science n/a*, 2204016.
[37] A. Furuse, M. Hashimoto, In *Electroactive Polymer Actuators and Devices (EAPAD) 2017*, SPIE, **2017**, pp. 396–402.
[38] P. Chen, Y. Xu, S. He, X. Sun, W. Guo, Z. Zhang, L. Qiu, J. Li, D. Chen, H. Peng, *Advanced Materials* **2015**, *27*, 1042.
[39] T. Khudiyev, J. Clayton, E. Levy, N. Chocat, A. Gumennik, A. M. Stolyarov, J. Joannopoulos, Y. Fink, *Nat Commun* **2017**, *8*, 1435.
[40] Y. Guo, J. Guo, L. Liu, Y. Liu, J. Leng, *Extreme Mechanics Letters* **2022**, *53*, 101720.
[41] D. Ni, R. Heisser, B. Davaji, L. Ivy, R. Shepherd, A. Lal, *Microsyst Nanoeng* **2022**, *8*, 1.
[42] Y. Li, M. Guo, Y. Li, *J. Mater. Chem. C* **2019**, *7*, 12991.
[43] J. A. Lee, Y. T. Kim, G. M. Spinks, D. Suh, X. Lepró, M. D. Lima, R. H. Baughman, S. J. Kim, *Nano Letters* **2014**, *14*, 2664.
[44] I. Must, E. Sinibaldi, B. Mazzolai, *Nat Commun* **2019**, *10*, 344.
[45] S. He, P. Chen, X. Sun, H. Peng, In *Industrial Applications of Carbon Nanotubes* (Eds.: Peng, H.; Li, Q.; Chen, T.), Elsevier, Boston, **2017**, pp. 151–178.
[46] D. R. Higueras-Ruiz, M. W. Shafer, H. P. Feigenbaum, *Science Robotics* **2021**, *6*, eabd5383.
[47] F. Pilate, A. Toncheva, P. Dubois, J.-M. Raquez, *European Polymer Journal* **2016**, *80*, 268.
[48] J. Delaey, P. Dubruel, S. Van Vlierberghe, *n/a*, 1909047.
[49] J. Hu, H. Meng, G. Li, S. I. Ibekwe, *Smart Materials and Structures* **2012**, *21*, 053001.

[50] V. Sanchez, C. J. Payne, D. J. Preston, J. T. Alvarez, J. C. Weaver, A. T. Atalay, M. Boyvat, D. M. Vogt, R. J. Wood, G. M. Whitesides, C. J. Walsh, *Advanced Materials Technologies* **2020**, *5*, 2000383.
[51] K.-Y. Chun, S. Hyeong Kim, M. Kyoon Shin, C. Hoon Kwon, J. Park, Y. Tae Kim, G. M. Spinks, M. D. Lima, C. S. Haines, R. H. Baughman, S. Jeong Kim, *Nat Commun* **2014**, *5*, 3322.
[52] J. Yuan, W. Neri, C. Zakri, P. Merzeau, K. Kratz, A. Lendlein, P. Poulin, *Science* **2019**, *365*, 155.
[53] L. Ionov, G. Stoychev, D. Jehnichen, J. U. Sommer, *ACS Appl. Mater. Interfaces* **2017**, *9*, 4873.
[54] H. Kim, J. H. Moon, T. J. Mun, T. G. Park, G. M. Spinks, G. G. Wallace, S. J. Kim, *ACS Appl. Mater. Interfaces* **2018**, *10*, 32760.
[55] L. Blanc, A. Delchambre, P. Lambert, **2017**, *6*, 23.
[56] M. D. Lima, N. Li, M. Jung de Andrade, S. Fang, J. Oh, G. M. Spinks, M. E. Kozlov, C. S. Haines, D. Suh, J. Foroughi, S. J. Kim, Y. Chen, T. Ware, M. K. Shin, L. D. Machado, A. F. Fonseca, J. D. W. Madden, W. E. Voit, D. S. Galvão, R. H. Baughman, *Science* **2012**, *338*, 928.
[57] F. Lancia, A. Ryabchun, N. Katsonis, *Nat Rev Chem* **2019**, *3*, 536.
[58] M. R. Aguilar, J. San Román, In *Smart Polymers and their Applications (Second Edition)* (Eds.: Aguilar, M. R.; San Román, J.), Woodhead Publishing, **2019**, pp. 1–11.
[59] J. J. Wie, M. R. Shankar, T. J. White, *Nat Commun* **2016**, *7*, 13260.
[60] B. Xu, C. Zhu, L. Qin, J. Wei, Y. Yu, *Small* **2019**, *15*, 1901847.
[61] T. Yoshino, M. Kondo, J. Mamiya, M. Kinoshita, Y. Yu, T. Ikeda, *Advanced Materials* **2010**, *22*, 1361.
[62] A. H. Gelebart, M. Mc Bride, A. P. H. J. Schenning, C. N. Bowman, D. J. Broer, *Advanced Functional Materials* **2016**, *26*, 5322.
[63] F. H. Zhang, Z. C. Zhang, C. J. Luo, I.-T. Lin, Y. Liu, J. Leng, S. K. Smoukov, *J. Mater. Chem. C* **2015**, *3*, 11290.
[64] Y. Kim, H. Yuk, R. Zhao, S. A. Chester, X. Zhao, *Nature* **2018**, *558*, 274.
[65] M. Sitti, D. S. Wiersma, *Advanced Materials* **2020**, *32*, 1906766.
[66] S.-H. Jang, S.-H. Na, Y.-L. Park, *Materials* **2017**, *10*, 646.
[67] D. Y. Lee, Y. Kim, S.-J. Lee, M.-H. Lee, J.-Y. Lee, B.-Y. Kim, N.-I. Cho, *Materials Science and Engineering: C* **2008**, *28*, 294.
[68] D. Liu, A. Tarakanova, C. C. Hsu, M. Yu, S. Zheng, L. Yu, J. Liu, Y. He, D. J. Dunstan, M. J. Buehler, *Science Advances* **2019**, *5*, eaau9183.
[69] A. Le Duigou, M. Castro, R. Bevan, N. Martin, *Materials & Design* **2016**, *96*, 106.
[70] J. Deng, Y. Xu, S. He, P. Chen, L. Bao, Y. Hu, B. Wang, X. Sun, H. Peng, *Nat Protoc* **2017**, *12*, 1349.
[71] P. Chen, Y. Xu, S. He, X. Sun, S. Pan, J. Deng, D. Chen, H. Peng, *Nature Nanotech* **2015**, *10*, 1077.
[72] J. Mu, M. Jung de Andrade, S. Fang, X. Wang, E. Gao, N. Li, S. H. Kim, H. Wang, C. Hou, Q. Zhang, M. Zhu, D. Qian, H. Lu, D. Kongahage, S. Talebian, J. Foroughi, G. Spinks, H. Kim, T. H. Ware, H. J. Sim, D. Y. Lee, Y. Jang, S. J. Kim, R. H. Baughman, *Science* **2019**, *365*, 150.
[73] T. Xu, Q. Han, Z. Cheng, J. Zhang, L. Qu, *Small Methods* **2018**, *2*, 1800108.
[74] S. Kawamura, T. Yamamoto, D. Ishida, T. Ogata, Y. Nakayama, O. Tabata, S. Sugiyama, In *Proceedings 2002 IEEE International Conference on Robotics and Automation (Cat. No.02CH37292)*, **2002**, pp. 248–253 vol.1.
[75] G. Singh, G. Krishnan, *Soft Robotics* **2020**, *7*, 109.
[76] F. Connolly, P. Polygerinos, C. J. Walsh, K. Bertoldi, *Soft Robotics* **2015**, *2*, 26.

[77] J. Shintake, H. Sonar, E. Piskarev, J. Paik, D. Floreano, In *2017 Ieee/Rsj International Conference on Intelligent Robots and Systems* (Eds.: Bicchi, A.; Okamura, A.), Ieee, New York, **2017**, pp. 6221–6226.
[78] T. Wang, D. Qi, H. Yang, Z. Liu, M. Wang, W. R. Leow, G. Chen, J. Yu, K. He, H. Cheng, Y.-L. Wu, H. Zhang, X. Chen, *Advanced Materials* **2019**, *31*, 1803883.
[79] J. Lee, B. Llerena Zambrano, J. Woo, K. Yoon, T. Lee, *Advanced Materials* **2020**, *32*, 1902532.
[80] S. Chen, Z. Lou, D. Chen, K. Jiang, G. Shen, *Advanced Materials Technologies* **2016**, *1*, 1600136.
[81] J. Shintake, E. Piskarev, S. H. Jeong, D. Floreano, **2018**, *3*, 1700284.
[82] A. Frutiger, J. T. Muth, D. M. Vogt, Y. Mengüç, A. Campo, A. D. Valentine, C. J. Walsh, J. A. Lewis, *Advanced Materials* **2015**, *27*, 2440.
[83] B. Caglar, W. Esposito, T. Nguyen-Dang, S. Laperrousaz, V. Michaud, F. Sorin, *Advanced Materials Technologies* **2021**, *6*, 2000957.
[84] T. Q. Trung, S. Ramasundaram, B.-U. Hwang, N.-E. Lee, *Advanced Materials* **2016**, *28*, 502.
[85] H. Yang, D. Qi, Z. Liu, B. K. Chandran, T. Wang, J. Yu, X. Chen, *Advanced Materials* **2016**, *28*, 9175.
[86] Y. He, Q. Gui, S. Liao, H. Jia, Y. Wang, *Advanced Materials Technologies* **2016**, *1*, 1600170.
[87] J. Guo, B. Zhou, C. Yang, Q. Dai, L. Kong, *Advanced Functional Materials* **2019**, *29*, 1902898.
[88] T. Q. Trung, L. T. Duy, S. Ramasundaram, N.-E. Lee, *Nano Res.* **2017**, *10*, 2021.
[89] S.-J. Choi, H. Yu, J.-S. Jang, M.-H. Kim, S.-J. Kim, H. S. Jeong, I.-D. Kim, *Small* **2018**, *14*, 1703934.
[90] Z. Tang, S. Jia, F. Wang, C. Bian, Y. Chen, Y. Wang, B. Li, *ACS Appl. Mater. Interfaces* **2018**, *10*, 6624.
[91] M. M. Tousi, Y. Zhang, S. Wan, L. Yu, C. Hou, N. Yan, Y. Fink, A. Wang, X. Jia, *Polymers* **2019**, *11*, 1985.
[92] G. Zhou, J.-H. Byun, Y. Oh, B.-M. Jung, H.-J. Cha, D.-G. Seong, M.-K. Um, S. Hyun, T.-W. Chou, *ACS Appl. Mater. Interfaces* **2017**, *9*, 4788.
[93] B. Li, G. Xiao, F. Liu, Y. Qiao, C. M. Li, Z. Lu, *J. Mater. Chem. C* **2018**, *6*, 4549.
[94] D. Larcher, J.-M. Tarascon, *Nature Chem* **2015**, *7*, 19.
[95] M. Zhou, S. Dong, *Acc. Chem. Res.* **2011**, *44*, 1232.
[96] M. Grattieri, S. D. Minteer, *ACS Sens.* **2018**, *3*, 44.
[97] W. Jia, G. Valdés-Ramírez, A. J. Bandodkar, J. R. Windmiller, J. Wang, *Angewandte Chemie International Edition* **2013**, *52*, 7233.
[98] J. Lv, I. Jeerapan, F. Tehrani, L. Yin, C. A. Silva-Lopez, J.-H. Jang, D. Joshuia, R. Shah, Y. Liang, L. Xie, F. Soto, C. Chen, E. Karshalev, C. Kong, Z. Yang, J. Wang, *Energy Environ. Sci.* **2018**, *11*, 3431.
[99] N. Matsuhisa, M. Kaltenbrunner, T. Yokota, H. Jinno, K. Kuribara, T. Sekitani, T. Someya, *Nat Commun* **2015**, *6*, 7461.
[100] H. Jin, N. Matsuhisa, S. Lee, M. Abbas, T. Yokota, T. Someya, *Advanced Materials* **2017**, *29*, 1605848.
[101] J. Xiong, P. Cui, X. Chen, J. Wang, K. Parida, M.-F. Lin, P. S. Lee, *Nat Commun* **2018**, *9*, 4280.
[102] N. Yamamoto, H. Takai, *Electrical Engineering in Japan* **2002**, *140*, 16.
[103] F. Suarez, D. Parekh, C. Ladd, D. Vashaee, M. Dickey, M. Öztürk, *Applied Energy* **Январь 9**, *202*, 736.
[104] S. J. Kim, J. H. We, B. J. Cho, *Energy Environ. Sci.* **2014**, *7*, 1959.

[105] R. Feng, F. Tang, N. Zhang, X. Wang, *ACS Appl. Mater. Interfaces* **2019**, *11*, 38616.
[106] C. Zheng, L. Xiang, W. Jin, H. Shen, W. Zhao, F. Zhang, C. Di, D. Zhu, *Advanced Materials Technologies* **2019**, *4*, 1900247.
[107] C. S. Kim, H. M. Yang, J. Lee, G. S. Lee, H. Choi, Y. J. Kim, S. H. Lim, S. H. Cho, B. J. Cho, *ACS Energy Lett.* **2018**, *3*, 501.
[108] R. Li, X. Xiang, X. Tong, J. Zou, Q. Li, *Advanced Materials* **2015**, *27*, 3831.
[109] R. Simões, V. Neto, *Journal of Materials Research* **2016**, *31*, 1633.
[110] S. Pan, Z. Yang, P. Chen, J. Deng, H. Li, H. Peng, *Angewandte Chemie International Edition* **2014**, *53*, 6110.
[111] T. Chen, S. Wang, Z. Yang, Q. Feng, X. Sun, L. Li, Z.-S. Wang, H. Peng, *Angewandte Chemie International Edition* **2011**, *50*, 1815.
[112] Z. Chai, N. Zhang, P. Sun, Y. Huang, C. Zhao, H. J. Fan, X. Fan, W. Mai, *ACS Nano* **2016**, *10*, 9201.
[113] J. Chen, Y. Huang, N. Zhang, H. Zou, R. Liu, C. Tao, X. Fan, Z. L. Wang, *Nat Energy* **2016**, *1*, 1.
[114] M. Zhu, T. N. Do, E. Hawkes, Y. Visell, *Soft Robot* **2020**, *7*, 179.
[115] L. Liu, C. Yao, Y. Liu, P. Wang, Y. Chen, F. Ying, In *HCI International 2020 – Late Breaking Papers: Digital Human Modeling and Ergonomics, Mobility and Intelligent Environments* (Eds.: Stephanidis, C.; Duffy, V. G.; Streitz, N.; Konomi, S.; Krömker, H.), Springer International Publishing, Cham, **2020**, pp. 316–331.
[116] W. Shan, T. Lu, C. Majidi, *Smart Materials and Structures* **2013**, *22*, 085005.
[117] W. Wang, S.-H. Ahn, *Soft Robotics* **2017**, *4*, 379.
[118] W. Shan, S. Diller, A. Tutcuoglu, C. Majidi, *Smart Materials and Structures* **2015**, *24*, 065001.
[119] Y.-J. Kim, S. Cheng, S. Kim, K. Iagnemma, *IEEE Transactions on Robotics* **2013**, *29*, 1031.
[120] N. T. Srinivasan, R. J. Schilling, *Arrhythm Electrophysiol Rev* **2018**, *7*, 111.
[121] E. Bacha, D. Kalfa, *Nat Rev Cardiol* **2014**, *11*, 24.
[122] S. S. A. Y. Biere, M. I. van Berge Henegouwen, K. W. Maas, L. Bonavina, C. Rosman, J. R. Garcia, S. S. Gisbertz, J. H. G. Klinkenbijl, M. W. Hollmann, E. S. M. de Lange, H. J. Bonjer, D. L. van der Peet, M. A. Cuesta, *Lancet* **2012**, *379*, 1887.
[123] A. S. Mattingly, M. M. Chen, V. Divi, F. C. Holsinger, A. Saraswathula, *J Surg Res* **2023**, *281*, 33.
[124] T. Doenst, M. Diab, C. Sponholz, M. Bauer, G. Färber, *Dtsch Arztebl Int* **2017**, *114*, 777.
[125] T. P. Martens, A. F. G. Godier, J. J. Parks, L. Q. Wan, M. S. Koeckert, G. M. Eng, B. I. Hudson, W. Sherman, G. Vunjak-Novakovic, *Cell Transplant* **2009**, *18*, 297.
[126] T. J. Oxley, N. L. Opie, S. E. John, G. S. Rind, S. M. Ronayne, T. L. Wheeler, J. W. Judy, A. J. McDonald, A. Dornom, T. J. H. Lovell, C. Steward, D. J. Garrett, B. A. Moffat, E. H. Lui, N. Yassi, B. C. V. Campbell, Y. T. Wong, K. E. Fox, E. S. Nurse, I. E. Bennett, S. H. Bauquier, K. A. Liyanage, N. R. van der Nagel, P. Perucca, A. Ahnood, K. P. Gill, B. Yan, L. Churilov, C. R. French, P. M. Desmond, M. K. Horne, L. Kiers, S. Prawer, S. M. Davis, A. N. Burkitt, P. J. Mitchell, D. B. Grayden, C. N. May, T. J. O'Brien, *Nat Biotechnol* **2016**, *34*, 320.
[127] M. El Baba, D. Sabayon, M. M. Refaat, *J Innov Card Rhythm Manag* **2020**, *11*, 4234.
[128] Z. Li, L. Wu, H. Ren, H. Yu, *Mechanism and Machine Theory* **2017**, *107*, 148.
[129] A. AlTurki, R. Proietti, *Pacing and Clinical Electrophysiology* **2018**, *41*, 447.
[130] R. Ghadban, K. Gifft, Z. Luebbering, S. Sodhi, D. Cooper, T. Enezate, *J Interv Card Electrophysiol* **2021**, *62*, 95.
[131] A. Shauer, L. J. De Vries, F. Akca, J. Palazzolo, M. Shurrab, I. Lashevsky, I. Tiong, S. M. Singh, D. Newman, T. Szili-Torok, E. Crystal, *EP Europace* **2018**, *20*, ii28.

[132] C. Pappone, G. Vicedomini, F. Manguso, F. Gugliotta, P. Mazzone, S. Gulletta, N. Sora, S. Sala, A. Marzi, G. Augello, L. Livolsi, A. Santagostino, V. Santinelli, *J Am Coll Cardiol* **2006**, *47*, 1390.
[133] E. S. Gang, B. L. Nguyen, Y. Shachar, L. Farkas, L. Farkas, B. Marx, D. Johnson, M. C. Fishbein, C. Gaudio, S. J. Kim, *Circ Arrhythm Electrophysiol* **2011**, *4*, 770.
[134] E. Koutalas, L. Bertagnolli, P. Sommer, S. Richter, S. Rolf, O. Breithardt, A. Bollmann, G. Hindricks, A. Arya, *EP Europace* **2015**, *17*, 232.
[135] J. Rahmer, C. Stehning, B. Gleich, *Science Robotics* **2017**, *2*.
[136] C. Piorkowski, C. Eitel, S. Rolf, K. Bode, P. Sommer, T. Gaspar, S. Kircher, U. Wetzel, A. S. Parwani, L.-H. Boldt, M. Mende, A. Bollmann, D. Husser, N. Dagres, M. Esato, A. Arya, W. Haverkamp, G. Hindricks, *Circ Arrhythm Electrophysiol* **2011**, *4*, 157.
[137] P. Kanagaratnam, M. Koa-Wing, D. T. Wallace, A. S. Goldenberg, N. S. Peters, D. W. Davies, *J Interv Card Electrophysiol* **2008**, *21*, 19.
[138] L. Mantziari, I. Suman-Horduna, M. Gujic, D. G. Jones, T. Wong, V. Markides, J. P. Foran, S. Ernst, *Pacing Clin Electrophysiol* **2013**, *36*, 757.
[139] H. Dong, G. M. Walker, *Smart Mater. Struct.* **2012**, *21*, 042001.
[140] K. Ikuta, H. Ichikawa, K. Suzuki, D. Yajima, In *Proceedings 2006 IEEE International Conference on Robotics and Automation, 2006. ICRA 2006.*, **2006**, pp. 4161–4166.
[141] M. Brancadoro, M. Manti, F. Grani, S. Tognarelli, A. Menciassi, M. Cianchetti, *Frontiers in Robotics and AI* **2019**, *6*.
[142] M. Mattmann, C. De Marco, F. Briatico, S. Tagliabue, A. Colusso, X.-Z. Chen, J. Lussi, C. Chautems, S. Pané, B. Nelson, *Advanced Science n/a*, 2103277.
[143] J. Lussi, M. Mattmann, S. Sevim, F. Grigis, C. De Marco, C. Chautems, S. Pané Vidal, J. Puigmartí-Luis, Q. Boehler, B. Nelson, *Advanced Science* **2021**.
[144] M. Cianchetti, T. Ranzani, G. Gerboni, T. Nanayakkara, K. Althoefer, P. Dasgupta, A. Menciassi, *Soft Robotics* **2014**, *1*, 122.
[145] C. Chautems, A. Tonazzini, D. Floreano, B. J. Nelson, **2017**, pp. 181–186.
[146] J. K.-R. Chun, S. Ernst, S. Matthews, B. Schmidt, D. Bansch, S. Boczor, A. Ujeyl, M. Antz, F. Ouyang, K.-H. Kuck, *European Heart Journal* **2007**, *28*, 190.
[147] Q. Yang, J. Fan, G. Li, *Applied Physics Letters* **2016**, *109*, 183701.
[148] M. Manti, V. Cacucciolo, M. Cianchetti, *IEEE Robotics & Automation Magazine* **2016**, *23*, 93.
[149] B. Aksoy, H. Shea, *Advanced Functional Materials* **2020**, *30*, 2001597.
[150] K. Takashima, K. Sugitani, N. Morimoto, S. Sakaguchi, T. Noritsugu, T. Mukai, *Smart Materials and Structures* **2014**, *23*, 125005.
[151] I. Rajzer, E. Menaszek, L. Bacakova, M. Rom, M. Blazewicz, *Journal of Materials Science: Materials in Medicine* **2010**, *21*, 2611.
[152] A. Firouzeh, M. Salerno, J. Paik, *IEEE Transactions on Robotics* **Февраль 5**, *PP*, 1.
[153] B. Aksoy, N. Besse, R. J. Boom, B.-J. Hoogenberg, M. Blom, H. Shea, *Lab on a Chip* **2019**, *19*, 608.
[154] N. Besse, S. Rosset, J. J. Zarate, H. Shea, *Advanced Materials Technologies* **2017**, *2*, 1700102.
[155] S. Vlassov, S. Oras, M. Timusk, V. Zadin, I. Sosnin, R. Lõhmus, L. M. Dorogin, **2020**.
[156] A. H. A. Razak, A. L. Skov, *RSC Adv.* **2016**, *7*, 468.
[157] R. Groves, A. F. Routh, *Journal of Polymer Science Part B: Polymer Physics* **2017**, *55*, 1633.
[158] R. B. Arumathanthri, B. S. K. Abeygoonawardana, I. D. C. D. Kumarasinghe, D. S. Chathuranga, T. D. Lalitharatne, A. L. Kulasekera, **2018**, pp. 2082–2087.
[159] E. Rio, F. Boulogne, *Advances in Colloid and Interface Science* **2017**, *247*, 100.
[160] M. Barletta, G. Simone, V. Tagliaferri, *Progress in Organic Coatings* **2005**, *54*, 390.

[161] K. K. Sasidharan, R. Joseph, G. Rajammal, P. V. Pillai, K. S. Gopalakrishnan, *Journal of Applied Polymer Science* **2001**, *81*, 3141.
[162] L. de Nardo, S. Bertoldi, A. Cigada, M. C. Tanzi, H. J. Haugen, S. Farè, *Journal of Applied Biomaterials & Functional Materials* **2012**, *10*, 119.
[163] K. Pieri, *Dissertations - ALL* **2020**.
[164] J. Han, G. Fei, G. Li, H. Xia, *Macromolecular Chemistry and Physics* **2013**, *214*, 1195.
[165] Y.-J. Wang, U.-S. Jeng, S. Hsu, *ACS Biomater. Sci. Eng.* **2018**, *4*, 1397.
[166] S. H. Kim, J.-H. Moon, J. H. Kim, S. M. Jeong, S.-H. Lee, *Biomedical Engineering Letters* **2011**, *1*, 199.
[167] S.-J. Kim, D.-S. Lee, I.-G. Kim, D.-W. Sohn, J.-Y. Park, B.-K. Choi, S.-W. Kim, *The Kaohsiung Journal of Medical Sciences* **2012**, *28*, 123.
[168] N. P. Kim, *Polymers* **2020**, *12*, 1224.
[169] P. Lugoda, J. C. Costa, L. A. Garcia-Garcia, A. Pouryazdan, Z. Jocys, F. Spina, J. Salvage, D. Roggen, N. Münzenrieder, *Advanced Materials Technologies* **2021**, *6*, 2000780.
[170] M. Buaki-Sogó, L. García-Carmona, M. Gil-Agustí, M. García-Pellicer, A. Quijano-López, *Nanomaterials* **2021**, *11*, 2052.
[171] G. Panomsuwan, C. Chokradjaroen, R. Rujiravanit, T. Ueno, N. Saito, *Jpn. J. Appl. Phys.* **2017**, *57*, 0102BG.
[172] F. Keçe, K. Zeppenfeld, S. A. Trines, *Arrhythmia & Electrophysiology Review* **2018**, *7*, 169.
[173] E. Piskarev, J. Shintake, V. Ramachandran, N. Baugh, M. D. Dickey, D. Floreano, *Advanced Intelligent Systems* **2020**, 2000069.
[174] K. P. Sau, T. K. Chaki, D. Khastgir, *Journal of Applied Polymer Science* **1999**, *71*, 887.
[175] Z.-D. Xiang, T. Chen, Z.-M. Li, X.-C. Bian, *Macromolecular Materials and Engineering* **2009**, *294*, 91.
[176] N. C. Das, T. K. Chaki, D. Khastgir, *Carbon* **2002**, *40*, 807.
[177] Y. Ma, N. Gogin, P. Cathier, R. J. Housden, G. Gijsbers, M. Cooklin, M. O'Neill, J. Gill, C. A. Rinaldi, R. Razavi, K. S. Rhode, *Med Phys* **2013**, *40*, 071902.
[178] A. Loeve, P. Breedveld, J. Dankelman, *IEEE Pulse* **2010**, *1*, 26.
[179] S. Srisang, A. Boongird, M. Ungsurungsie, P. Wanasawas, N. Nasongkla, *Journal of Biomedical Materials Research Part B: Applied Biomaterials* **2021**, *109*, 496.
[180] Y.-F. Zhang, N. Zhang, H. Hingorani, N. Ding, D. Wang, C. Yuan, B. Zhang, G. Gu, Q. Ge, **2019**, *29*, 1806698.
[181] S. Rosset, O. A. Araromi, S. Schlatter, H. R. Shea, *J. Vis. Exp.* **2016**, 13.
[182] K. Awasthi, R. Kamalakaran, A. K. Singh, O. N. Srivastava, *International Journal of Hydrogen Energy* **2002**, *27*, 425.
[183] C.-K. Leong, D. D. L. Chung, *Carbon* **2003**, *41*, 2459.
[184] N. R. Grubb, S. Furniss, *BMJ* **2001**, *322*, 777.
[185] Y. Piskarev, J. Shintake, C. Chautems, J. Lussi, Q. Boehler, B. J. Nelson, D. Floreano, *Advanced Functional Materials n/a*, 2107662.
[186] M. Mattmann, Q. Boehler, X.-Z. Chen, S. Pané, B. J. Nelson, In *2022 IEEE/RSJ International Conference on Intelligent Robots and Systems (IROS)*, **2022**, pp. 9589–9595.
[187] B. Mazzolai, A. Mondini, E. D. Dottore, L. Margheri, F. Carpi, K. Suzumori, M. Cianchetti, T. Speck, S. K. Smoukov, I. Burgert, T. Keplinger, G. D. F. Siqueira, F. Vanneste, O. Goury, C. Duriez, T. Nanayakkara, B. Vanderborght, J. Brancart, S. Terryn, S. I. Rich, R. Liu, K. Fukuda, T. Someya, M. Calisti, C. Laschi, W. Sun, G. Wang, L. Wen, R. Baines, S. K. Patiballa, R. Kramer-Bottiglio, D. Rus, P. Fischer, F. C. Simmel, A. Lendlein, *Multifunct. Mater.* **2022**, *5*, 032001.

[188] V. Kanyanta, A. Ivankovic, *Journal of the Mechanical Behavior of Biomedical Materials* **2010**, *3*, 51.
[189] A. P. S. Selvadurai, *Journal of the Mechanics and Physics of Solids* **2006**, *54*, 1093.
[190] H. Lv, J. Leng, Y. Liu, S. Du, *Advanced Engineering Materials* **2008**, *10*, 592.
[191] M. Raja, S. H. Ryu, A. M. Shanmugharaj, *European Polymer Journal* **2013**, *49*, 3492.
[192] P. Prathumrat, S. Tiptipakorn, S. Rimdusit, *Smart Mater. Struct.* **2017**, *26*, 065025.
[193] M. Cabanlit, D. Maitland, T. Wilson, S. Simon, T. Wun, M. E. Gershwin, J. Van de Water, *Macromolecular Bioscience* **2007**, *7*, 48.
[194] W. S. Iv, T. S. Wilson, W. J. Benett, J. M. Loge, D. J. Maitland, *Opt. Express, OE* **2005**, *13*, 8204.
[195] S. Farè, V. Valtulina, P. Petrini, E. Alessandrini, G. Pietrocola, M. C. Tanzi, P. Speziale, L. Visai, *Journal of Biomedical Materials Research Part A* **2005**, *73A*, 1.
[196] M. Houmsse, E. G. Daoud, *Expert Review of Medical Devices* **2012**, *9*, 59.
[197] H.-W. Fang, K.-Y. Li, T.-L. Su, T. C.-K. Yang, J.-S. Chang, P.-L. Lin, W.-C. Chang, *Materials Letters* **2008**, *62*, 3739.
[198] H. Nakagawa, W. S. Yamanashi, J. V. Pitha, M. Arruda, X. Wang, K. Ohtomo, K. J. Beckman, J. H. McClelland, R. Lazzara, W. M. Jackman, *Circulation* **1995**, *91*, 2264.
[199] L. Capron, P. Bruneval, *Cardiovasc Res* **1989**, *23*, 941.
[200] K. Takashima, R. Shimomura, T. Kitou, H. Terada, K. Yoshinaka, K. Ikeuchi, *Tribology International* **2007**, *40*, 319.
[201] E. Nof, W. G. Stevenson, R. M. John, *Arrhythm Electrophysiol Rev* **2013**, *2*, 45.
[202] R. Yu, S. L. Charreyron, Q. Boehler, C. Weibel, C. Chautems, C. C. Y. Poon, B. J. Nelson, In *2020 IEEE International Conference on Robotics and Automation (ICRA)*, **2020**, pp. 9251–9256.
[203] K. Jia, Q. Jin, A. Liu, L. Wu, *J Electrocardiol* **2019**, *55*, 78.
[204] G. Bassil, S. M. Markowitz, C. F. Liu, G. Thomas, J. E. Ip, B. B. Lerman, J. W. Cheung, *Journal of Cardiovascular Electrophysiology* **2020**, *31*, 739.
[205] M. Brancadoro, M. Manti, S. Tognarelli, M. Cianchetti, *2018 IEEE International Conference on Soft Robotics (RoboSoft)* **2018**, 258.
[206] M. Brancadoro, M. Manti, S. Tognarelli, M. Cianchetti, *Soft Robotics* **2020**, *7*, 663.
[207] B. Aktaş, Y. S. Narang, N. Vasios, K. Bertoldi, R. D. Howe, *Advanced Functional Materials* **2021**, *31*, 2007554.
[208] L. Bai, H. Yan, J. Li, J. Shan, P. Hou, *Applied Sciences* **2022**, *12*, 3582.
[209] S. Jadhav, M. R. A. Majit, B. Shih, J. P. Schulze, M. T. Tolley, *Soft Robotics* **2022**, *9*, 173.
[210] L.-J. Gai, J. Huang, X. Zong, *IEEE/ASME Transactions on Mechatronics* **2023**, *28*, 2897.
[211] L. Arleo, L. Lorenzon, M. Cianchetti, *IEEE Trans. Robot.* **2023**, *39*, 4429.
[212] A. Blandino, F. Bianchi, A. Sibona Masi, A. Mazzanti, F. D'Ascenzo, S. Grossi, G. Musumeci, *Pacing and Clinical Electrophysiology* **2021**, *44*, 1102.
[213] W. Ullah, R. J. Schilling, T. Wong, *J Atr Fibrillation* **2016**, *8*, 1282.
[214] S. Schlögl, K. S. Schlögl, H. Haarmann, P. Bengel, L. Bergau, E. Rasenack, G. Hasenfuss, M. Zabel, *Pacing and Clinical Electrophysiology* **2022**, *45*, 14.
[215] F. Bessière, C. Zikry, L. Rivard, K. Dyrda, P. Khairy, *EP Europace* **2018**, *20*, ii1.
[216] Y. Litzistorf, F. Gorostidi, A. Reinhard, *Allergy Rhinol (Providence)* **2021**, *12*, 21526567211030889.
[217] J. Q. Zhang, R. H. Yu, J. B. Liang, D. Y. Long, C. H. Sang, C. S. Ma, J. Z. Dong, *Medicine* **2017**, *96*.
[218] S. Abbott, *undefined* **2015**.
[219] I. K. Mohammed, M. N. Charalambides, A. J. Kinloch, *Journal of Non-Newtonian Fluid Mechanics* **2015**, *222*, 141.

[220] L. Li, M. Tirrell, G. A. Korba, A. V. Pocius, *The Journal of Adhesion* **2001**, *76*, 307.
[221] S. Park, J. Shintake, Y. Piskarev, Y. Wei, I. Joshipura, E. Frey, T. Neumann, D. Floreano, M. D. Dickey, *Advanced Materials Technologies* **2021**, *6*, 2100263.
[222] G. Chen, J. Zheng, L. Liu, L. Xu, *Small Methods* **2019**, *3*, 1900688.
[223] P. Zhang, N. Shao, L. Qin, *Advanced Materials* **2021**, *33*, 2005944.
[224] T. T. Hoang, P. T. Phan, M. T. Thai, N. H. Lovell, T. N. Do, *Advanced Materials Technologies n/a*, 2000724.
[225] V. Subramaniam, S. Jain, J. Agarwal, P. Valdivia y Alvarado, *The International Journal of Robotics Research* **2020**, *39*, 1668.
[226] M. Li, A. Pal, A. Aghakhani, A. Pena-Francesch, M. Sitti, *Nat Rev Mater* **2022**, *7*, 235.
[227] C. J. Payne, I. Wamala, D. Bautista-Salinas, M. Saeed, D. Van Story, T. Thalhofer, M. A. Horvath, C. Abah, P. J. Del Nido, C. J. Walsh, N. V. Vasilyev, *Sci Robot* **2017**, *2*, eaan6736.
[228] A. Ghosh, C. Yoon, F. Ongaro, S. Scheggi, F. M. Selaru, S. Misra, D. H. Gracias, *Frontiers in Mechanical Engineering* **2017**, *3*.
[229] Y. Piskarev, E. Desbouis, V. Ramachandran, J. Yang, N. Baugh, J. Shintake, M. D. Dickey, D. Floreano, *Advanced Engineering Materials n/a*, 2200355.
[230] Y. Piskarev, A. Devincenti, V. Ramachandran, P.-E. Bourban, M. D. Dickey, J. Shintake, D. Floreano, *Advanced Intelligent Systems* **2023**, *5*, 2200409.
[231] M. S. Xavier, A. J. Fleming, Y. K. Yong, *Advanced Intelligent Systems* **2021**, *3*, 2000187.
[232] C. Tangwongsan, J. A. Will, J. G. Webster, K. L. Meredith, D. M. Mahvi, *IEEE Transactions on Biomedical Engineering* **2004**, *51*, 1478.
[233] C. Tangwongsan, L. Chachati, J. G. Webster, P. V. Farrell, *BioMedical Engineering OnLine* **2006**, *5*, 57.
[234] C. Tangwongsan, In *2007 IEEE/NIH Life Science Systems and Applications Workshop*, **2007**, pp. 81–84.
[235] J. Kim, W.-Y. Choi, S. Kang, C. Kim, K.-J. Cho, *IEEE Transactions on Robotics* **2019**, *35*, 1475.
[236] Y. H. Jung, B. Park, J. U. Kim, T. Kim, *Advanced Materials* **2019**, *31*, 1803637.
[237] J. Kim, A. S. Campbell, B. E.-F. de Ávila, J. Wang, *Nat Biotechnol* **2019**, *37*, 389.
[238] A. Mosteiro, S. Amaro, R. Torné, L. Pedrosa, J. Hoyos, L. Llull, L. Reyes, A. Ferrés, N. de Riva, R. Mellado, J. Enseñat, *Frontiers in Neurology* **2022**, *13*.

Yegor **Piskarev**

Ph.D. in Mechanical Engineering, EPFL · M.Sc. in Mechanical Engineering, EPFL

Av. Victor Ruffy, 1012 Lausanne, Switzerland

+41 78 225 12 52

yegor.piskarev@gmail.com | yegor-piskarev | yegorpiskarev

Profile: Mechanical engineer and researcher with 5 years of experience developing medical and robotics devices in a unique combination of the fields of metamaterials, rapid fabrication, and empirical characterization.

Achievements

- Led the development of three catheters for cardiac ablation procedures (class III medical devices) in accordance with FDA requirements.
- Developed and characterized eight soft grippers, actuators, and sensors.
- Filed two PCT patent applications for medical devices.
- Supervised a total of ten interns and graduate students in various soft and medical robotics projects.
- Initiated and managed collaborations with North Carolina State Unversity (NCSU), Tokyo University of Electro-Communications, and ETH Zurich.
- Received mulitple prestegious awards including "Editor's Choice in Advanced Intelligent Systems", "Advanced Materials Technologies: Top cited article 2018-2019", "EPFL 2022 Outstanding Performance Premium (6% Awarding Rate)", and "Fascination ETH Domain 2022".
- Authored ten scientific articles published in top-tier journals, including Advanced Functional Materials (Impact Factor 20, in the top 0.86% of all journals) and Advanced Materials Technologies.
- Participated in two industrial sustainability challenges, clinching victory in one (1 out of 100) and securing finalist status in the second (top 25 out of 250).

Experience

Swiss Federal Institute of Technology (EPFL) ***Lausanne, Switzerland***

Doctoral assistant at the Laboratory of Intelligent System ***from August 2019 - January 2024***

- Cardiac ablation catheter development
  - Developed, characterized, and experimentally verified three different cardiac catheters with variable stiffness capabilities in a hospital-compatible facility in accordance with FDA requirements (Solid Works, FEA with HPC, Abaqus MATLAB, polymer synthesis and labwork, thermomechanical testing, LabVIEW, FLIR).
  - Established an automated scalable fabrication process for catheters with precisely-controlled thickness and resistance of the coating (Arduino IDE, Inventor, Ultimaker Cura, rapid fabrication).
  - Performed an in-depth patent search, collaborated with a patent attorney, and filed two PCT patent applications.
- Soft Robotics Projects
  - Developed a versatile soft gripper based on granular jamming and electroadhesion with 35% enhanced grasping capabilities, which can lift objects of different geometries and material properties (Electroactive polymers (EAPs), elastomer fabrication, molding, laser micromachining, film coating, tensile testing).
  - Designed and characterized an approach to enhance the adhesion properties of pressure-sensitive elastomers by more than 50% for specific substrates using common equipment (Pressure-sensitive adhesives, laser etching, optical profilometry, Raman spectroscopy, peeling and viscosity testing).
- Leadership
  - Interviewed and supervised 10 interns and graduate students in soft robotics and medical robotics projects.

- Established and led collaborative projects on different soft robotics devices with North Carolina State University and the University of Electro-Communications in Tokyo.
- Teaching assistant for an artificial muscles class (physics, fabrication, characterization), guided and instructed 50 graduate students annually for four years.

North Carolina State University (NCSU) *Raleigh, United States*
Research assistant at the Dickey Group *from September 2018 - April 2019*

- Developed a 30% lighter and 2.6 times stronger variable stiffness actuator due to the integration of cofabricated electrodes and variable stiffness elements using polymers and liquid metal (Liquid metals, plasma bonding).
- Performed characterization of the actuator in terms of bending angle and applied force using a tensile machine.
- Supervised two undergraduate students in soft robotics semester projects.

Swiss Federal Institute of Technology (EPFL) *Lausanne, Switzerland*
Research assistant at the Laboratory of Intelligent System *from February 2017 - November 2017*

- Characterized the normal force of an electroadhesive liquid metal-based device under different prestrain ratio (System integration, applied force characterization, LabVIEW).
- Fabricated and characterized a smart glove and low-cost ultra stretchable sensors based on silicone and carbon black using layer-by-layer deposition in terms of strain, elongation, and repeatability(Silicone fabrication, film coating).

Extracurricular activities

Nespresso Swiss StartCup Challenge 2022 *Lausanne, Switzerland*
Circular economy challenge finalists *from July 2022 - November 2022*

- Introduced a zero-waste packaging strategy for Nespresso goods compatible with existing packaging facilities.
- Ranked in the top 25 as finalists in a 250-team challenge.

Ekipa, Innovate2030 challenge *Frankfurt am Main*
Sustainable consumption and production challenge winners *from June 2021 - October 2021*

- Developed an optimized, sustainable, and zero-waste concept for pallet delivery.
- Worked closely with different departments of a large intralogistic company KION Group to identify pain points and then validate our solution.
- Won 1st place in a 100-team challenge.

San Diego State University *San Diego, United States*
FDA and EMA regulations course *from August 2020 - October 2020*

- Learned the methodology for the FDA and EMA classification and certification of medical devices.
- Led Class 2 medical device certification project during coursework.

"The Future of Engineering", science and technology competition *Paris, France*
Challenge finalists *from June 2018 - October 2018*

- Developed a sustainable concept for large-scale cargo transportation in a megapolis.
- Ranked in the top 5 as finalists in a 70-team challenge.

Education

Swiss Federal Institute of Technology (EPFL) *Lausanne, Switzerland*
Ph.D. in Mechanical Engineering *from August 2019 - January 2024*
Ph.D. thesis: ”Filiform variable stiffness technologies for medical devices” supervised by Prof. D. Floreano.

Swiss Federal Institute of Technology (EPFL) *Lausanne, Switzerland*
M.Sc. in Mechanical Engineering - Grade: 5.3/6 *from August 2016 - March 2019*
Exchange M.Sc. thesis at North Carolina State University (NCSU): ”Lighter and stronger: Cofabricated electrodes and variable stiffness elements in dielectric actuators” supervised by Prof. D. Floreano and Prof. M. D. Dickey.

Bauman Moscow State Technical University (BMSTU) *Moscow, Russia*
B.Eng. in Robotics - Grade: 4.5/5 *from September 2012 - May 2016*
B.Eng. thesis: ”Development of a control algorithm for the B-SET lifting system (“Enerpak”, Holland) used in the installation of rectification columns.” supervised by Prof. S. Vorotnikov.

Skills and Languages

Workshop	3D printing | Laser Micromachining | Molding | Film Coating | Polymer Fabrication
Prototyping	SolidWorks | Inventor | Abaqus | FEA with HPC | Ultimaker Cura
Testing	tensile | three-point flexural | thermomechanical | fatigue | applied force | peel | bending
Analysis	deformation and stresses | hyperelasticity | electrostatics | soft sensors and actuators
Programming	Matlab | LabVIEW | Python | Arduino
Creative tools	Adobe Illustrator | OriginPro | Adobe Photoshop | Blender | HitFilm Express
Natural languages	English (C1) | Russian (native) | German (A2)

Referees

thesis supervisor
Prof. Dario Floreano
EPFL STI IMT LIS
MED 1 1026 Station 9
Vaud
CH-1015 Lausanne
dario.floreano@epfl.ch

industry supervisor
Mr. Igor Dimnik
SITA
26 Chemin de Joinville
Geneva
1216 Cointrin
idimnik@gmail.com

collaborator at NCSU
Prof. Michael Dickey
NCSU
911 Partners Way
Raleigh
NC 27695
mddickey@ncsu.edu

collaborator at Tokyo EC
Prof. Jun Shintake
University of Electro-Communications, Japan
1-5-1 Chofugaoka
Tokyo
shintake@uec.ac.jp

Publications and Patents

1. **A variable stiffness magnetic catheter made of a conductive shape memory polymer for minimally invasive surgery**
   Yegor Piskarev, Jun Shintake, Dario Floreano
   WO Patent App. WO 2023/099949 A1

2. **A Soft Gripper with Granular Jamming and Electroadhesive Properties**
   Yegor Piskarev, Antoine Devincenti, Vivek Ramachandran, Pierre-Etienne Bourban, Michael D Dickey, Jun Shintake, Dario Floreano
   Advanced Intelligent Systems, 2023, 2200409

3. **Biodegradable electrohydraulic soft actuators**
   Ryo Kanno, Fabio Caruso, Kazuma Takai, Yegor Piskarev, Vito Cacucciolo, Jun Shintake
   Advanced Intelligent Systems, 2023, 2200239

4. **Enhancement of Pressure-Sensitive Adhesive by CO2 Laser Treatment**
   Yegor Piskarev, Etienne Desbouis, Vivek Ramachandran, Jiayi Yang, Neil Baugh, Jun Shintake, Michael D Dickey, Dario Floreano
   Advanced Engineering Materials, 2022, 24 (10), 2200355

5. **A Variable Stiffness Magnetic Catheter Made of a Conductive Phase-Change Polymer for Minimally Invasive Surgery**
   Yegor Piskarev, Jun Shintake, Christophe Chautems, Jonas Lussi, Quentin Boehler, Bradley J Nelson, Dario Floreano
   Advanced Functional Materials, 2022, 32 (20), 2107662

6. **Passive Perching with Energy Storage for Winged Aerial Robots**
   William Stewart, Luca Guarino, Yegor Piskarev, Dario Floreano
   Advanced Intelligent Systems, 2021, 2100150

7. **Stretchable and Soft Electroadhesion Using Liquid-Metal Subsurface Microelectrodes**
   Sungjune Park, Jun Shintake, Yegor Piskarev, Yuwen Wei, Ishan Joshipura, Ethan Frey, Taylor Neumann, Dario Floreano, Michael D Dickey
   Advanced Materials Technologies, 2021 6 (9), 2100263

8. **Lighter and Stronger: Cofabricated Electrodes and Variable Stiffness Elements in Dielectric Actuators**
   Yegor Piskarev, Jun Shintake, Vivek Ramachandran, Neil Baugh, Michael D Dickey, Dario Floreano
   Advanced Intelligent Systems, 2020, 2 (10), 2000069

9. **Ultrasoft liquid metal elastomer foams with positive and negative piezopermittivity for tactile sensing**
   Jiayi Yang, David Tang, Jinping Ao, Tushar Ghosh, Taylor V Neumann, Dongguang Zhang, Yegor Piskarev, Tingting Yu, Vi Khanh Truong, Kai Xie, Ying-Chih Lai, Yang Li, Michael D Dickey
   Advanced Functional Materials, 2020, 30 (36), 2002611

10. **Ultrastretchable Strain Sensors Using Carbon Black-Filled Elastomer Composites and Comparison of Capacitive Versus Resistive Sensors**
    Jun Shintake, Yegor Piskarev, Seung Hee Jeong, Dario Floreano
    Advanced Materials Technologies, 2018 3 (3), 1700284

11. **Soft Pneumatic Gelatin Actuator for Edible Robotics**
    Jun Shintake, Harshal Sonar, Yegor Piskarev, Jamie Paik, Dario Floreano
    2017 IEEE/RSJ International Conference on Intelligent Robots and Systems (IROS) September 24–28, 2017, Vancouver, BC, Canada